AD_____

Award Number: DAMD17-99-1-9488

TITLE: Colloidal Stabilization of Neurofilaments and
        Microtubules

PRINCIPAL INVESTIGATOR: Jan H. Hoh, Ph.D.

CONTRACTING ORGANIZATION: The Johns Hopkins University,
                              School of Medicine
                           Baltimore, Maryland 21205-2196

REPORT DATE: June 2002

TYPE OF REPORT: Final

PREPARED FOR: U.S. Army Medical Research and Materiel Command
               Fort Detrick, Maryland 21702-5012

DISTRIBUTION STATEMENT: Approved for Public Release;
                         Distribution Unlimited

The views, opinions and/or findings contained in this report are
those of the author(s) and should not be construed as an official
Department of the Army position, policy or decision unless so
designated by other documentation.

20030923 045

REPORT DOCUMENTATION PAGE	*Form Approved* OMB No. 074-0188

Public reporting burden for this collection of information is estimated to average 1 hour per response, including the time for reviewing instructions, searching existing data sources, gathering and maintaining the data needed, and completing and reviewing this collection of information. Send comments regarding this burden estimate or any other aspect of this collection of information, including suggestions for reducing this burden to Washington Headquarters Services, Directorate for Information Operations and Reports, 1215 Jefferson Davis Highway, Suite 1204, Arlington, VA 22202-4302, and to the Office of Management and Budget, Paperwork Reduction Project (0704-0188), Washington, DC 20503

1. AGENCY USE ONLY (Leave blank)	2. REPORT DATE June 2002	3. REPORT TYPE AND DATES COVERED Final (1 Jun 99 – 31 May 02)

4. TITLE AND SUBTITLE Colloidal Stabilization of Neurofilaments and Microtubules	5. FUNDING NUMBERS DAMD17-99-1-9488

6. AUTHOR(S):
Jan H. Hoh, Ph.D.

7. PERFORMING ORGANIZATION NAME(S) AND ADDRESS(ES) The Johns Hopkins University, School of Medicine Baltimore, Maryland 21205-2196 E-MAIL: jhoh@jhmi.edu	8. PERFORMING ORGANIZATION REPORT NUMBER

9. SPONSORING / MONITORING AGENCY NAME(S) AND ADDRESS(ES) U.S. Army Medical Research and Materiel Command Fort Detrick, Maryland 21702-5012	10. SPONSORING / MONITORING AGENCY REPORT NUMBER

11. SUPPLEMENTARY NOTES

12a. DISTRIBUTION / AVAILABILITY STATEMENT Approved for Public Release; Distribution Unlimited	12b. DISTRIBUTION CODE

13. ABSTRACT *(Maximum 200 Words)*

The research supported by this award was based on the hypothesis that the interfilament distances between microtubules and neurofilaments are maintained by a polymer brush based mechanism, that results in what has been called colloidal stabilization. We suggest that failure of such stabilization may be related to neuropathologies such as ALS and Alzheimer's disease. To address this problem we used a set of biophysical methods, including atomic force microscopy, to investigate interfilament potentials. There are several main conclusions from the work under this award. First, microtubule associated proteins behave as though they are largely unstructured and can give rise to a long range repulsive force that is predominantly entropic in origin. This is an important finding that provides a biophysical mechanism that explains how microtubule spacing is maintained. Second, treating the unstructured proteins domains as polyelectrolytes shows how interfilament potentials between neurofilaments or micromicrotubules can be smoothly modulated by phosphorylation. Finally, the analysis of neurofilament distributions in axons shows that these can be recapitulated with a soft long range repulsion of the type generated by unstructured polymers. These findings support the main hypothesis and suggest a new way to think about axonal cytoskeleton and mechanisms of protein aggregation in neurodegeneration.

14. SUBJECT TERMS: neurotoxin	15. NUMBER OF PAGES 130
	16. PRICE CODE

17. SECURITY CLASSIFICATION OF REPORT Unclassified	18. SECURITY CLASSIFICATION OF THIS PAGE Unclassified	19. SECURITY CLASSIFICATION OF ABSTRACT Unclassified	20. LIMITATION OF ABSTRACT Unlimited

NSN 7540-01-280-5500

Standard Form 298 (Rev. 2-89)
Prescribed by ANSI Std. Z39-18
298-102

Table of Contents

Manuscripts:

1. Mukhopadhyay, R. and J. H. Hoh (2001). "AFM force measurements on microtubule associated proteins: the projection domain exerts a long-range repulsive force." FEBS Lett. 505: 374-378.

2. Bright, J. A., Stevens, M., Hoh, J. H. and T. B. Woolf (2001). "Characterizing the function of unstructured proteins: simulations of charged polymers under confinement." J. Chem. Phys. 117: 4909-4918.

3. Kumar, S., and J. H. Hoh (2001). "Probing the machinery of intracellular trafficking with the atomic force microscope." Traffic 2: 746-756.

4. Bright, J. A., Woolf, T. B., and J. H. Hoh (2001). "Predicting Properties of Intrinsically Unstructured Proteins." Prog. Biophys. Molec. Biol., 76:131-73

5. Kumar, S., Yin, X, Trapp, B. D., Paulaitis, M. E. and J. H. Hoh (2002). "Analysis and simulation of neurofilament distributions: implications for mechanisms of interfilament spacing." J. Neurosci. Res., 68: 681-90.

6. Kumar, S., Yin, X, Trapp, B. D., Hoh, J. H. and M. E. Paulaitis (2002). "Relating interactions between neurofilaments to the structure of axonal neurofilament distributions through polymer brush models." Biophys. J., 82: 2360-72.

Chapter 4 from S. Kumar's PhD Thesis

INTRODUCTION

The research supported by this award is based on the hypothesis that the interfilament distances between microtubules and neurofilaments are maintained by a polymer brush based mechanism, that results in what has been called colloidal stabilization. We suggest that failure of such stabilization may be related to, and even causal, in neuropathologies such as amyotrophic lateral sclerosis (ALS) and Alzheimer's disease. Thus focus of the research in this proposal is a series of experiments that test the polymer brush based mechanism. These experiments include atomic force microscopy, macromolecular exclusion measurements on isolated neurofilaments and microtubules and analysis of neurofilament distributions in electron micrographs. In addition we have pursued the general of functional properties of unstructured proteins, and how these are related to the protein sequence. With an understanding of the basic mechanism, conditions under which the colloidal stabilization fail will be examined. The results from this research will provide fundamental insight into the mechanism of neurodegeneration, and suggest new approaches to therapies and treatments for neuropathologies.

BODY OF REPORT

Below the approved statement of work is divided into four sections, and research progress associated with the tasks in each section is reported.

1. From Statement of work (verbatim): "The contractor will isolate microtubules, neurofilaments and associated proteins from bovine tissue. These proteins will be characterized by SDS-polyacrylamide gel electrophoresis, imaging by atomic force microscopy (AFM) and appropriate physical/biochemical methods. Isolation of these proteins will occur regularly throughout the three years of the proposed contract, as required for the specific experiments proposed. In the first year methods for immobilizing microtubules with microtubule associated proteins (MAPs) onto solid supports will be established. AFM force measurements will be performed on microtubules with MAPs to establish if the MAPs behave as an entropic brush. The data will be analyzed using isoforce difference mapping and fitting to appropriate theoretical models. Controls for these force measurements will include microtubules assembled in the absence of MAPs and microtubules for which MAPs have been chemically removed."

The main aim of this section was completed. The completed work differed from the proposed work only on relatively minor point. Above we proposed to examine forces of microtubule associated proteins while attached to microtubules. Instead, we developed a system in which the forces of microtubule associated proteins could be examined in the absence of microtubules. The results are described in detail in the attached manuscript (Mukhopadhyay and Hoh, 2001).

2. From statement of work (verbatim): "In the second year macromolecular exclusion experiments will be performed on microtubules with MAPs. The ability of the microtubules/MAPs to exclude macromolecules will be determined by a centrifugation-based approach. Fluorescent macromolecular probes will be used to determine the effective volume of the microtubules/MAPs, in order to establish if MAPs act as an entropic brush. The size dependency of the exclusion properties of the microtubules with MAPs will be determined by using a series of varying probe molecule size. Controls for these force measurements will include microtubules assembled in the absence of MAPs and microtubules for which MAPs have been chemically removed. If appropriate, similar experiments will be performed with neurofilaments."

Here we focused our efforts on neurofilaments. Neutron scattering was explored as a approach for getting interfilament spacing, however spacings could not be obtained from our scattering experiments. Subsequently we developed a centrifugation/pellet size assay for interfilament spacing, and this was used to examine the exclusion properties of neurofilaments. This approach the results are described in Chapter 4 of Sanjay Kumars PhD Thesis (Dr. Kumar was a PhD student with Dr. Hoh; appendix). The results are being prepared for publication.

We also developed alternative approach to the question raised was being pursued. The alternative approach is based on analysis of neurofilament distributions in electron micrographs, and using statistical mechanical approaches to probe the interaction forces. The results of this work shows that the organization of neurofilaments can be recapitulated using a long-range repulsive force of the type proposed, which supports the original hypothesis. Details of the work are described in the papers Kumar et al., 2002a (Appendix) and Kumar et al., 2002b (Appendix).

Work was initiated on macromolecular exclusion in microtubule/MAP gels. Initial experiments using fluorescently labled dextrans show that large dextrans are excluded from the proximity of microtubules with MAPs. These results are consistent with and support the proposed colloidal stabilization model. Given the effort directed at neurofilaments, the microtubule work remains in progress.

3. From statement of work (verbatim): "In year three the conditions and treatments that modulate the effect of the entropic brush of microtubules and neurofilaments will be established. The effect of varying concentrations of monovalent salt, divalent salt and pH on the entropic brush, as assayed by AFM force measurements and macromolecular exclusion experiments, will be determined. Using the results from these experiments appropriate combinations of ionic conditions, or new conditions, will be examined. The effect of phosphorylation state of neurofilaments on the entropic brush will be determined. Neurofilaments will be enzymatically dephosphorylated or hyperphosphorylated and the effect of the entropic brush will be examined as above. Neurofilaments will be treated with aluminum to determine if this metal directly effects the entropic brush."

The main goals of this aim have been completed for neurofilaments, and to a more limited extent microtubules. The neurofilament results are described in detail in Chapter 4 of Dr. Sanjay Kumar's PhD thesis (Appendix). This material is being prepared for publication. As #2 above, because of the focus on neurofilaments the work on MAPs remains in progress.

4. From Statement of work (verbatim): "The results from the work will be reported to the appropriate office at the USAMRMC at times specified by the USAMRMC. The results from the work will also be published in international peer reviewed scientific journals and presented at national meetings. The presentations will be on an annual basis, and the publication will be as appropriate with regard to content of the work."

The present document represents the required final report to the USAMRMC. In addition, the research supported by this award has been presented at several meetings and seminars as listed below under reportable outcomes. Six publications resulting from the research are attached (Appendix).

5. The work supported has lead to a new collaboration with Dr. Tom Woolf to simulate the behavior of the unstructured parts of neurofilaments and microtubule associated proteins. In the initial simulations, a highly simplified model and general model of unstructured polypeptides was

used. Results from these simulations are described in detail in the attached manuscript (Bright et al., 2000; Appendix). This work also prompted a thorough evaluation of the theory that underpins the colloidal forces, which was published as a review (Bright et al., 2001; Appendix).

KEY RESEARCH ACCOMPLISHMENTS

• Demonstration that Microtubule Associated Proteins behave as unstructured polymers (polyelectrolytes) and can generate a long range repulsive force, and that this force appears to be predominantly entropic in origin. This provides a biophysical mechanism for maintaining and regulating intertubular spacing, and supports the main hypothesis advanced in the proposal.

• Demonstration that the cytoskeletal (neurofilament) architecture can be recapitulated using an entropic exclusion model, while the more popular cross-bridge model can not. This supports the main hypothesis advanced in the proposal.

• Demonstration that phosphorylation alters the effective interaction potential between neurofilaments, suggesting a polyelectolyte behavior. This offers a mechanism for physiological regulation of interfilament spacing.

REPORTABLE OUTCOMES

Biobiography of Publications

1. Mukhopadhyay, R. and J. H. Hoh (2001). "AFM force measurements on microtubule associated proteins: the projection domain exerts a long-range repulsive force." FEBS Lett. 505:374-378.

2. Bright, J. A., Stevens, M., Hoh, J. H. and T. B. Woolf (2001). "Characterizing the function of unstructured proteins: simulations of charged polymers under confinement." J. Chem. Phys. 117:4909-4918.

3. Kumar, S., and J. H. Hoh (2001). "Probing the machinery of intracellular trafficking with the atomic force microscope." Traffic 2:746-756.

4. Bright, J. A., Woolf, T. B., and J. H. Hoh (2001). "Predicting Properties of Intrinsically Unstructured Proteins." Prog. Biophys. Molec. Biol., 76:131-73

5. Kumar, S., Yin, X, Trapp, B. D., Paulaitis, M. E. and J. H. Hoh (2002a). "Analysis and simulation of neurofilament distributions: implications for mechanisms of interfilament spacing." J. Neurosci. Res., 68:681-90.

6. Kumar, S., Yin, X, Trapp, B. D., Hoh, J. H. and M. E. Paulaitis (2002b). "Relating interactions between neurofilaments to the structure of axonal neurofilament distributions through polymer brush models." Biophys. J., 82:2360-72.

Seminars by Dr. Hoh on the Supported Work

National Institutes of Health
National Institute of Neurological Orders and Stroke
Analytical Cell Biology Department

North Carolina State University
Department of Material Science

The Johns Hopkins Protein Folding Meeting
Coolfont Resort, WV

Nanoscience and Nanotechnology Symposium
University of Pennsylvania

Tristate Biomedical Engineering Meeting
Drexel University

EMSL2000
Pacific Northwest National Laboratory
Environmental Molecular Sciences Laboratory

The Scripps Research Institute
La Jolla, CA

Mayo Clinic
Jacksonville, FL

North Carolina Microscopy Society
Wilmington, NC

National Institutes of Health
Physical Sciences Laboratory
Bethesda, MD

University of New England
Biddeford, ME

The Pittsburgh Conference on Analytical Chemistry
New Orleans, Louisiana

STM 2001 Meeting (Keynote Address)
Vancouver, Canada

Long Island University
Long Island, NY

Washington State University
Pullman, WA

Foresight Conference on Molecular Nanotechnology
Washington DC

MRS Meeting

University of North Carolina
Chapel Hill, NC

Arizona State University
Tempe, AZ

Poster Presentations

Poster Presentation
2001 Meeting of the Biophysical Society

Poster Presentation
Chesapeake Society for Microscopy

Nano-7 Meeting

Malmö, Sweden

Funding applied for based on work supported

Title: Protein-based polymer brushes: modeling and simulation of nanostructures
Source: National Science Foundation
Amount (total costs): $2,100,000
Duration: 3 years
Co-investigators: Dr. Michael Pauliatis; Dr. Thomas Woolf; Dr. William Russell
Submitted: 4/10/2000
The aim of this proposal is to develop a predictive theoretical framework for the protein based polymer brush model which is being studied experimentally in microtubules and neurofilaments in the supported work. This application was not successful.

Title: Unstructured polypeptides as materials with novel nanoscale properties
Source: National Science Foundation
Amount (total costs): $2,000,000
Duration: 4 years
Co-investigators: Dr. Mark Stevens; Dr. Michael Pauliatis; Dr. Thomas Woolf; Dr. William Russell
Submitted: 11/1/2000
The aim of this proposal is to develop new biomaterials based on unstructured polypeptides. Microtubule associated proteins and neurofilaments were major model systems in this proposal, and the proposal builds directly on the work supported here. This application was not successful.

Employment opportunities received on experiences supported by this award

• As a result of this award, we have established a collaboration with Dr. Terrone Rosenberry at the Mayo Clinic. In this collaboration we are using atomic force microscopy to support Dr. Rosenberry's research on the mechanisms of a-beta assembly and Alzheimer's disease. One publication has resulted from this work (Michael R. Nichols, Melissa A. Moss, Dana Kim Reed, Wen-Lang Lin, Rajendrani Mukhopadhyay, Jan H. Hoh and Terrone L. Rosenberry (2002). "Growth of beta-amyloid(1-40) protofibrils by monomer elongation and lateral association. Characterization of distinct products by light scattering and atomic force microscopy." Biochem., 41:6115-27).

• As a results of this award, we have established a collaboration with Dr. Anthony Brown at Ohio State University. In this collaboration we are using atomic force microscopy to visualize neurofilaments in preparations of splayed neurons, in an attempt to determine the number of filaments being transported in a fluorescence based transport assay developed by Dr. Brown.

• Dr. Jan Hoh was promoted to Associate Professor in part do to his activities associated with this award.

• Dr. Sanjay Kumar completed thesis research requirements with support from this award. Dr. Kumar is presently interviewing for faculty positions and postdoctoral positions on the basis of work supported by this award.

8

PERSONNEL SUPPORTED BY AWARD

Hoh, Jan
Mukhopadhyay, Rajendrani
Kumar, Sanjay
Marsh, Matthew
Ohsawa, Kazu.
Hodges, Alex
Bright, Joanne

CONCLUSIONS

There are several main conclusions from the work under this award. First, in agreement with main hypothesis, microtubule associated proteins behave as though they are largely unstructured and can give rise to a long range repulsive force that is predominantly entropic in origin. This is an important finding that provides a biophysical mechanism that explains how microtubule spacing is maintained. Second, treating the unstructured proteins domains as polyelectrolytes, shows how interfilament potentials between neurofilaments and between micromicrotubules (and probably between neurofilaments and microtubules) can be smoothly modulated by phosphorylation. Further, the analysis of neurofilament distributions in axons shows that these can be recapitulated with a soft long range repulsion of the type generated by unstructured polymers. This provides support for the main hypothesis of the proposal, and also demonstrates that the hypothesis has predictive power that extends from AFM force measurements to the cellular context. The methods developed for the neurofilament analysis will likely find use in analysis of neurofilaments and microtubules in a number of pathological conditions. Together, the findings provide evidence that the established cross-bridge model for neurofilament interactions is wrong, and suggests a new way to think about axonal mechanics and the mechanisms of protein aggregation in neurodegenerative disease.

AFM force measurements on microtubule-associated proteins: the projection domain exerts a long-range repulsive force

Rajendrani Mukhopadhyay[a], Jan H. Hoh[a,b,*]

[a]Department of Physiology, Johns Hopkins University School of Medicine, 725 N. Wolfe Street, Baltimore, MD 21205, USA
[b]Department of Chemical Engineering, Johns Hopkins University, Baltimore, MD 21218, USA

Abstract   Microtubule-associated proteins (MAPs) are thought to control spacing between microtubules. We propose that the projection domain is largely unstructured and exerts a long-range repulsive force that is predominantly entropic in origin, providing a physical mechanism for maintaining spacing. To test this hypothesis, we developed an experimental system where MAPs are electrostatically end-attached to a flat surface, such that the projection domains extend away from the surface. Atomic force microscopy force measurements on this system show that projection domains exert a long-range (> 100 nm) repulsive force. This force depends on the ionic strength of the solution in a way that is consistent with a polyelectrolyte polymer brush. © 2001 Published by Elsevier Science B.V. on behalf of the Federation of European Biochemical Societies.

Key words: Unstructured; Entropic exclusion; Microtubule-associated protein 2; Tau

1. Introduction

Microtubule-associated proteins (MAPs) are a class of proteins that bind to the surface of microtubules in a nucleotide-independent manner. These proteins are known to stabilize microtubules against depolymerization [1]. There is also evidence to suggest that MAPs play a role in maintaining spacing between adjacent microtubules [2,3]. However, the mechanism by which this spacing is created and maintained is not well understood.

There are two major classes of MAPs, type I and type II [4]. Here we are primarily concerned with type II MAPs which include MAP2, tau and MAP4. These MAPs are composed of two distinct domains: a C-terminal microtubule-binding domain and an N-terminal projection domain. The microtubule-binding domain is approximately 400 amino acids in length and is conserved among the type II MAPs. This domain is highly positively charged and electrostatically binds to the negatively charged surface of microtubules. The binding of MAPs is regulated by phosphorylation where phosphorylation causes MAPs to dissociate from the microtubule [5]. The pro-

jection domain is not as well conserved as the microtubule-binding domain, and varies in length, from ~ 300 amino acids in tau to ~ 1400 amino acids in the high molecular weight isoforms of MAP2. This domain is highly negatively charged; for instance, in MAP2b there are 287 acidic (D and E) and 138 basic (K and R) amino acids [6]. Phosphorylation of the projection domain further increases the amount of negative charge on this part of the molecule [7].

MAPs bound to microtubules produce a structure that resembles a bottle brush where the projection domains extend away from the surface of the microtubule [2,8]. When microtubules with MAPs are sedimented, they form a gel where microtubules are widely spaced [9]. For example, the center to center distance between microtubules with MAP2 bound is ~ 89 nm, while in the absence of MAPs, the distance is 44 nm [2]. The distance between microtubules is related to the size of the projection domain [10], but the mechanism by which the projection domain maintains this spacing is not known. One hypothesis is that the projection domain acts as a cross-bridge, essentially forming a strut between adjacent microtubules [3,11,12]. Alternatively, Mandelkow and colleagues describe MAPs as acting as 'soft' spacers, based on small angle X-ray scattering of MAP-microtubule gels [13]. A biophysical mechanism for such spacing activity has been proposed [14]. Here the projection domain is highly unstructured, in rapid Brownian motion, and produces a repulsive force that is primarily entropic in origin. This behavior is similar to that of unstructured, non-biological polymers that are widely used to stabilize colloidal suspensions [15]. Thus MAPs bound to the surface of a microtubule can be viewed as a polymer brush, and can maintain the distance between microtubules by entropic repulsion. This is similar to a proposed mechanism by which neurofilament side-arms maintain spacing between neurofilaments [16].

Consistent with this model, there are several lines of evidence that suggest that the MAP projection domain is unstructured. In [1]H [17] and [13]C [18] nuclear magnetic resonance studies of MAPs, the spectra have narrow resonance peaks that are typical of highly mobile and flexible molecules. Extensive biophysical characterization of MAP2, including circular dichroism, fluorescence spectroscopy and sedimentation equilibrium, has shown the protein to be mostly disordered [19]. In addition, recent analyses of sequences of intrinsically unstructured polypeptides have revealed several features that are characteristic of this class of polypeptides. In particular, unstructured polypeptides tend to be low complexity (i.e. contain a small number of different amino acids) with a high fraction of polar amino acids [20–22]. The projection domain

*Corresponding author. Fax: (1)-410-614 3797.
E-mail address: jhoh@jhmi.edu (J.H. Hoh).

of MAPs has a very high content of polar amino acids and the sequence is low complexity [23].

To test the hypothesis that the projection domain of MAPs is unstructured and forms a polymer brush on the surface of microtubules, we have developed a system to study forces produced by the projection domains of MAPs. This system exploits the positive charge on the microtubule-binding domains to electrostatically end-attach MAPs to a negatively charged substrate (mica). With the microtubule-binding domains attached to the mica, the projection domains extend away from the mica surface and, at sufficient density, form a polymer brush. Forces exerted by the projection domains can then be studied by direct atomic force microscopy (AFM) measurements (e.g. [16,24,25]). Our measurements demonstrate the presence of a long-range repulsive force that is consistent with a polyelectrolyte brush.

2. Materials and methods

2.1. Protein adsorption to mica

A whole MAP fraction from adult bovine brain (Cytoskeleton Inc., Denver, CO, USA), composed of 70% MAP2a/b and 30% other MAPs, including tau, was used. This preparation was restored from a lyophilized powder with water to a 1 mg/ml stock solution in 10 mM 1,4-piperazine-diethane-sulfonic acid (PIPES), 0.3 mM EGTA and 0.3% sucrose. 10 µl of the stock solution was added to 40 µl of 1 mM PIPES, pH 7.2 (Sigma Aldrich, St. Louis, MO, USA). The 50 µl aliquot was incubated on a freshly cleaved mica disk (Asheville-Schoonmaker, Newport News, VA, USA) for 30 min at room temperature. The mica was then thoroughly washed with 1 mM PIPES, pH 7.2. All solutions were prepared in deionized (>18 MΩ) and UV-treated water (Milli-Q UV, Millipore Corp., Bedford, MA, USA). Care was taken to keep the sample submerged in buffer during sample preparation and throughout the experiment.

Control proteins included bovine serum albumin (BSA; Sigma Aldrich), type II histone (Sigma Aldrich), skeletal muscle myosin (Sigma Aldrich) and an immunoglobulin G (IgG; Sigma Aldrich). A 1 mg/ml solution of each protein, in 1 mM PIPES, pH 7.2, was prepared. A 10 µl aliquot of the protein solution was added to 40 µl of 1 mM PIPES, pH 7.2. The 50 µl aliquot was incubated on freshly cleaved mica for 30 min, rinsed thoroughly and used in AFM force measurements.

3-Aminopropyl-triethoxy-silane (APTES)-modified mica surfaces were prepared essentially as previously described [26]. Briefly, 100 µl of neat APTES (Sigma Aldrich) was diluted into 10 ml of 1 mM acetic acid. The mica stubs were immersed in the APTES solution for 10 min, then thoroughly rinsed with distilled water and blown dry with compressed gas (Vari-Air, Peca Products, Janesville, WI, USA). These substrates were used in place of regular mica where indicated.

2.2. AFM

A Nanoscope III or IIIa controller equipped with a Multimode AFM, a J type scanner (*xy* scan range ~150 µm; *z* range ~6 µm) and conventional fluid cell (Digital Instruments, Santa Barbara, CA, USA) were used. Unsharpened 'D' type silicon nitride cantilevers (Microlevers; Thermomicroscopes, Sunnyvale, CA, USA) with a nominal force constant of 0.03 N/m were used. Cantilevers were cleaned for 20 min by exposure to high-intensity UV light (UVO-Cleaner, Jelight Co. Inc., Laguna Hills, CA, USA). Force curves were typically collected over 1–2 µm with 2048 data points per curve, at a rate of 0.1 Hz. Relative triggers of 0.3–3 nN were used to prevent the tip from gouging the surface. A closed fluid cell was used to allow for fluid exchange during an experiment. When exchanging solutions of different ionic strength, the fluid cell was rinsed with several ml (>20 times the fluid cell volume) of the new solution prior to a measurement.

2.3. Quantitation of MAPs bound to mica

To estimate the density of MAPs bound to the mica surface, known quantities of MAPs were adsorbed to mica and rinsed as described above. MAPs bound to mica in each sample were then solubilized in 33 µl Laemmli sample buffer (62.5 mM Tris–HCl, pH 6.8, 2% sodium

dodecyl sulfate, 25% glycerol, 0.01% bromophenol blue, 20% β-mercaptoethanol). A 25 µl aliquot of solubilized MAPs from each sample was run on a 7.5% acrylamide gel, together with MAPs of known amounts. The gel was silver-stained (Bio-Rad) and densitometry analysis was performed using Fujifilm LAS-1000 and Fuji Image Gauge V3.3 imaging software (Fujifilm Medical Systems USA, Inc., Edison, NJ, USA).

3. Results and discussion

To test the hypothesis that the projection domain of MAPs behaves as an unstructured polymer, we developed a system for studying forces exerted by the projection domain (Fig. 1). Our approach was to end-attach MAPs to mica via the microtubule-binding domain. This domain is highly positively charged and should electrostatically bind to the negatively charged surface of mica, leaving the projection domain free to extend away from the surface. At a sufficient density of proteins, a polymer brush should form. The properties of this brush could then be examined by direct AFM force measurements.

Force measurements on the MAP system showed a long-range repulsive force (Fig. 2). This long-range repulsive force could be detected 100–150 nm away from the surface. Within a given preparation, forces measured at different points on the surface did not vary significantly. When small compressive forces were used (<0.3 nN), the retracting curve retraced
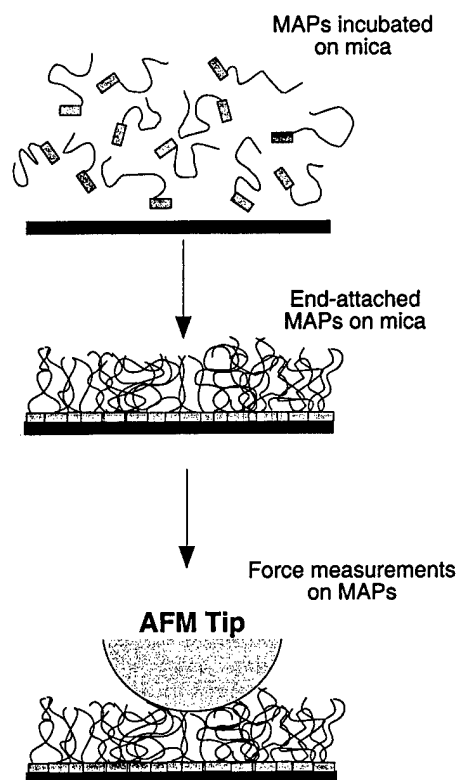

Fig. 1. Schematic of the experimental system of MAPs end-attached to mica. Positively charged microtubule-binding domains (rectangles) electrostatically interact with negatively charged mica (thick horizontal line). The MAPs self assemble into a polymer brush on the mica surface, with the projection domains extending away from the surface. The properties of the projection domain are investigated by direct AFM force measurements.
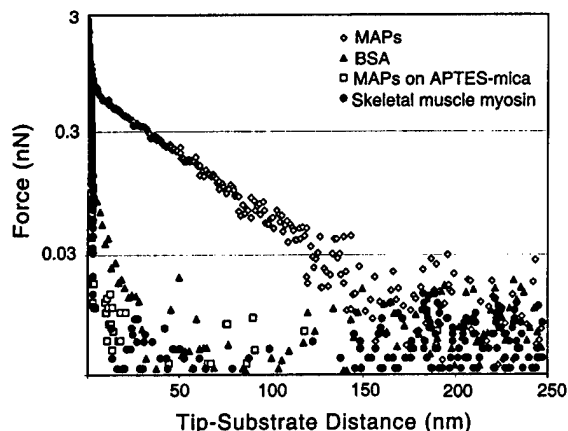
Fig. 2. Force measurement on the MAP polymer brush. A long-range, roughly exponential, repulsive force can be detected up to 150 nm away from the surface in the presence of MAPs. In each of the controls, BSA, type II histone, IgG and skeletal muscle myosin on mica, and MAPs bound to APTES mica, the long-range repulsive force is absent. For clarity, data for type II histone and IgG are not shown. In both those cases the measured forces were no greater than those for BSA.

the advancing curve exactly in >90% of the curves. In the remaining <10% a negative deflection away from the surface, typical of a trapped polymer, was observed. When high compressive forces were used, the approach curve overlapped the low force measurements but complex retracting curves were commonly observed. These retracting curves were highly irregular and suggested multiple interactions between molecules on the surface and the tip. Approach curves were reproducible for hundreds of measurements, suggesting that protein was not accumulating on the tip with time. These measurements are consistent with an entropic force originating from a polymer brush [16,24,25].

Several controls were performed to support this interpretation. First, different proteins that are thought to be well folded were adsorbed to mica and the forces measured. BSA and type II histone are known to be folded from X-ray crystallography [27,28]. Type II histone is positively charged and should bind electrostatically to mica, similar to the microtubule-binding domain. We note that a short stretch of type II histone has been proposed to be unstructured [20,21]; however the unstructured portion of the molecule is positively charged and should be immobilized on the mica. Other control molecules included skeletal muscle myosin and IgG. None of the control proteins exhibited the type of long-range repulsion seen for MAPs (Fig. 2). Second, forces from MAPs incubated on APTES-modified mica were measured. APTES modification of mica creates a positively charged surface [26]. This surface should bind the negatively charged projection domain and prevent the formation of a polymer brush. In agreement with that prediction, the APTES-bound MAPs did not produce a long-range force (Fig. 2).

The amount of MAPs bound to the surface was estimated by removing the MAPs from the surface and quantitating them by gel electrophoresis and densitometry. Samples, prepared identically to those used in the force measurements, had a MAP concentration on the mica surface of approximately 100 ng/cm^2. This corresponds to a monolayer of MAPs with an average intermolecular distance of 20 nm. For an ideal

polymer of the length of the MAP2 projection domain (~500 nm) in a theta solvent, the radius of gyration is ~22 nm. This is larger for a polymer in a good solvent, as would be the case for a polyelectrolyte in water. Thus the measured grafting density is well within the brush limit and is consistent with the picture presented in Fig. 1. In addition, the amount of protein bound to the mica saturates, with an increasing amount of protein used in the initial incubation, near 100 ng/cm^2, indicating that the protein does not form multilayers (data not shown).

Given the large net negative charge of the projection domain, it might be expected to behave as a polyelectrolyte. One characteristic property of polyelectrolyte polymer brushes is that the degree to which they are expanded is sensitive to the ionic strength of an aqueous medium [29]. Such sensitivity to ionic strength depends on ionic screening of intramolecular interactions. This prediction was supported by force measurements on the MAP polymer brush in solutions of different ionic strength (NaCl concentration), which show that as ionic strength increases, the measured force decreases (Fig. 3). The ionic strength sensitivity also demonstrates that the forces measured are not simply an electrostatic force between the layer of protein at the surface and the AFM tip. The decay length of the force measured in 100 mM NaCl is ~7 nm. This is a factor of seven larger than would be expected for a purely electrostatic interaction (e.g. [30,31]). It should be noted that changes in intramolecular interactions in a polyelectrolyte could also be achieved by modifying the intrinsic charge, which can be accomplished in a biological context by phosphorylation and dephosphorylation (discussed below).

One concern regarding the ionic strength sensitivity is that the decrease in force could result from loss of MAPs from the surface, due to ionic effects on the interaction of the microtubule-binding domain with the mica. Indeed, high ionic strength solutions are used to disrupt the interaction of the microtubule-binding domain with negatively charged chromatography media (phosphocellulose) during MAP purification [32,33]. To ensure that the change in force was not due to a loss in MAPs from the surface, we tested the reversibility of the ionic strength effect. Following an experiment where ionic strength had been increased from the 1 mM PIPES to 1 mM
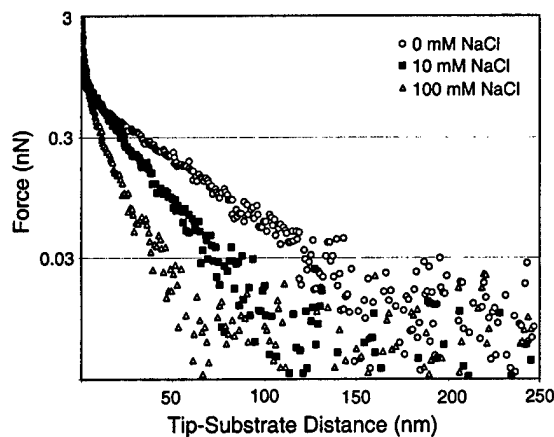
Fig. 3. Force measurement on the MAP polymer brush as a function of ionic strength. The long-range repulsive force decreases with increasing ionic strength. This sensitivity to ionic strength is consistent with a polyelectrolyte polymer brush.
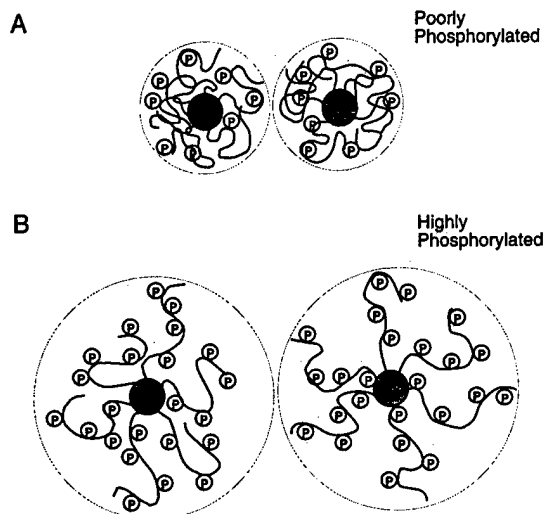
Fig. 4. Proposed regulation of MAP polymer brush by phosphorylation and dephosphorylation. A: Dephosphorylation reduces the intramolecular repulsion, causing the projection domains to become more compact and allows the microtubules to move closer. B: Phosphorylation of the projection domains causes the projection domains to expand due to an increase in intramolecular repulsion. This in turn causes the distance between adjacent microtubules to increase.

PIPES with 100 mM NaCl, the ionic strength was returned to 1 mM PIPES. This fully restored the original force, indicating that there was no detectable loss of MAPs from the surface (data not shown).

The focus of the work presented here is to provide evidence that the projection domains of MAPs behave as unstructured polymers, and can give rise to a long-range repulsive force that is predominantly entropic in origin. By predominantly entropic we mean that the protein is mostly unfolded, and that the force arises from restrictions to the space available for the protein to explore. This is not to exclude intramolecular interactions, such as electrostatic interactions, that are particularly critical in polyelectrolytes. Furthermore, it is not to say that some parts of the projection domain might not have some structure, but overall, the projection domain is sufficiently unstructured to give rise to the measured forces. The data presented clearly support this hypothesis, and provide a biophysical mechanism for MAPs maintaining spacing between microtubules. In this role, the polymer brush model for MAPs on microtubules advanced here suggests that MAPs should be highly compressible (compared to a folded protein). This is in agreement with the finding by Mandelkow and colleagues, who showed that MAPs behave as compressible spacers between microtubules [13]. However, the results presented here do not strictly exclude MAPs cross-linking microtubules. The free end of the projection domain could in principle bind to an adjacent microtubule, leaving the remainder of the projection domain unstructured and free to move. The results also do not exclude the binding of other molecules to the MAP projection domain, as has been proposed (e.g. [34]).

The polymer brush model for MAPs suggests a general mechanism for regulation of projection domain function and a specific mechanism for the effect of phosphorylation on microtubule packing (Fig. 4). Small angle X-ray scattering has been used to show that phosphorylation of MAPs in-

creases the distance between microtubules in MAP-microtubule gels [13]. Increasing the charge of a polyelectrolyte in a good solvent produces an increase in the radius of gyration through increased intramolecular repulsion [29]. Therefore, in the model presented here, phosphorylation of MAPs would increase the intramolecular repulsion and cause the MAP polymer brush to expand.

Beyond providing a mechanism for maintaining spacing between microtubules, the question of what the biological significance of the long-range force reported here might be arises. To begin with, the MAPs may contribute to cellular mechanics in a way identical to that proposed for neurofilaments [16]. The unstructured projection domain could act as an entropic spring between microtubules, or between microtubules and other cytoskeletal components (e.g. neurofilaments). This spring would resist mechanical compression and could serve to maintain cell shape. The unstructured projection domain would also occupy a very large volume, compared to folded protein of the same length, and tend to exclude other macromolecules in a size-dependent manner (the larger the molecule the more it would be excluded). This in turn could lead to a significant increase in the effective concentration of excluded molecules and thereby influence their intracellular biochemical activity. It should be noted that the presence of the polymer brush does not exclude the binding of other proteins to the surface of microtubules. For example, MAPs have been proposed to regulate motor protein interactions with microtubules [35]. Interestingly, Mandelkow and colleagues [36] have shown that tau affects the attachment and detachment of motor proteins but not the transport speed. Finally, unstructured polymers grafted to the surface of colloidal-sized particles are commonly used to prevent aggregation [15]. Microtubules themselves are highly soluble, and hence it would not appear that MAPs are involved in maintaining their solubility. However, it is interesting to note that some MAPs, in particular tau, are known to aggregate under pathological conditions [37,38]. Such aggregation might be expected if the polymer brush behavior of MAPs described here failed.

References

[1] Kreis, T. and Vale, R. (1999) pp. xx, 551, Oxford University Press, Oxford.
[2] Kim, H., Binder, L.I. and Rosenbaum, J.L. (1979) J. Cell Biol. 80, 266–276.
[3] Chen, J., Kanai, Y., Cowan, N.J. and Hirokawa, N. (1992) Nature 360, 674–677.
[4] Hyams, J.S. and Lloyd, C.W. (1994) in: Modern Cell Biology (Harford, J.B., Ed.), Vol. 13, Wiley-Liss, New York.
[5] Ainsztein, A.M. and Purich, D.L. (1994) J. Biol. Chem. 269, 28465–28471.
[6] Albala, J.S. and Kalcheva, N. (1993) Gene 136, 377–378.
[7] Sanchez, C., Diaz-Nido, J. and Avila, J. (2000) Prog. Neurobiol. 61, 133–168.
[8] Voter, W.A. and Erickson, H.P. (1982) J. Ultrastruct. Res. 80, 374–382.
[9] Brown, P.A. and Berlin, R.D. (1985) J. Cell Biol. 101, 1492–1500.
[10] Black, M.M. (1987) Proc. Natl. Acad. Sci. USA 84, 7783–7787.

[11] Aamodt, E.J. and Culotti, J.G. (1986) J. Cell Biol. 103, 23–31.
[12] Hirokawa, N., Hisanaga, S. and Shiomura, Y. (1988) J. Neurosci. 8, 2769–2779.
[13] Marx, A., Pless, J., Mandelkow, E.M. and Mandelkow, E. (2000) Cell. Mol. Biol. 46, 949–965.
[14] Hoh, J.H. (1998) Proteins 32, 223–228.
[15] Napper, D.H. (1983) in: Colloid Science, 3, pp. xvi, 428, Academic Press, London.
[16] Brown, H.G. and Hoh, J.H. (1997) Biochemistry 36, 15035–15040.
[17] Woody, R.W., Roberts, G.C.K., Clark, D.C. and Bayley, P.M. (1982) FEBS Lett. 141, 181–184.
[18] Ringel, I. and Sternlicht, H. (1984) Biochemistry 23, 5644–5653.
[19] Hernandez, M.A., Avila, J. and Andreu, J.M. (1986) Eur. J. Biochem. 154, 41–48.
[20] Romero, P., Obradovic, Z., Li, X.H., Garner, E.C., Brown, C.J. and Dunker, A.K. (2001) Proteins 42, 38–48.
[21] Uversky, V.N., Gillespie, J.R. and Fink, A.L. (2000) Proteins 41, 415–427.
[22] Dunker, A.K. et al. (2001) J. Mol. Graph. Model. 19, 26–59.
[23] Wootton, J.C. (1994) Curr. Opin. Struct. Biol. 4, 413–421.
[24] Kelley, T.W., Schorr, P.A., Johnson, K.D., Tirrell, M. and Frisbie, C.D. (1998) Macromolecules 31, 4297–4300.
[25] Overney, R.M. et al. (1996) Phys. Rev. Lett. 76, 1272–1275.
[26] Lyubchenko, Y.L., Gall, A.A., Shlyakhtenko, L.S., Harrington, R.E., Jacobs, B.L., Oden, P.I. and Lindsay, S.M. (1992) J. Biomol. Struct. Dyn. 10, 589–606.
[27] Brown, J.R. (1975) Fed. Proc. 34, 591.
[28] Burlingame, R.W., Love, W.E., Wang, B.C., Hamlin, R., Nguyen, H.X. and Moudrianakis, E.N. (1985) Science 228, 546–553.
[29] Pincus, P. (1991) Macromolecules 24, 2912–2919.
[30] Ducker, W.A., Senden, T.J. and Pashley, R.M. (1991) Nature 353, 239–241.
[31] Heinz, W.F. and Hoh, J.H. (1999) Biophys. J. 76, 528–538.
[32] Weingarten, M.D., Lockwood, A.H., Hwo, S.Y. and Kirschner, M.W. (1975) Proc. Natl. Acad. Sci. USA 72, 1858–1862.
[33] Kuznetsov, S.A., Rodionov, V.I., Gelfand, V.I. and Rosenblat, V.A. (1981) FEBS Lett. 135, 237–240.
[34] Morishima-Kawashima, M. and Kosik, K.S. (1996) Mol. Biol. Cell 7, 893–905.
[35] Sato-Harada, R., Okabe, S., Umeyama, T., Kanai, Y. and Hirokawa, N. (1996) Cell. Struct. Funct. 21, 283–295.
[36] Trinczek, B., Ebneth, A., Mandelkow, E.M. and Mandelkow, E. (1999) J. Cell Sci. 112, 2355–2367.
[37] Perez, M., Arrasate, M., de Garcini, E.M., Munoz, V. and Avila, J. (2001) Biochemistry 40, 5983–5991.
[38] Mann, D.M.A. and Pickering-Brown, S. (2001) Neurobiol. Aging 22, 109–111.

Characterizing the function of unstructured proteins: Simulations of charged polymers under confinement

Joanne N. Bright
Department of Physiology, Johns Hopkins University, School of Medicine, Baltimore, Maryland 21205

Mark. J. Stevens
Sandia National Laboratories, Albuquerque, New Mexico 87185

Jan Hoh and Thomas B. Woolf[a)]
Department of Physiology, Johns Hopkins University, School of Medicine, Baltimore, Maryland 21205

Experimental findings that some polypeptides may be unstructured and behave as entropically driven polymeric spacers in biological systems motivates a study of confined polymers. Here we examine the confinement of neutral, polyampholyte, and polyelectrolyte polymers between two parallel surfaces using course grained models and molecular dynamics. Forces between the confining surfaces are determined for different polymer classes and as a function of chain length, charge sequence (pattern) and degree of confinement. Changes in chain properties are also evaluated under these conditions. The results reinforce the significance of length and net charge for predicting chain properties. In addition the clustering of charge along the chain appears to be critical, and changes in cluster size and distribution produce dramatic changes in chain behavior. © *2001 American Institute of Physics.* [DOI: 10.1063/1.1392361]

I. INTRODUCTION

It is becoming increasingly clear that many proteins or regions of proteins are intrinsically unstructured, and that their function is directly related to being unstructured. A number of potential functions for unstructured polypeptides have been proposed.[1-3] One of these functions is based on the thermally driven motion of a polypeptide acting as a molecular spacer through primarily entropic forces. This type of entropic exclusion is common in nonbiological systems.[4] In biological systems there is evidence to suggest that unstructured polypeptides play an important role in stabilizing casein micelles,[5,6] maintaining interfilament spacing between neurofilaments,[7] and possibly a range of other functions.[3] Sequence analysis of unstructured polypeptides shows that these chains often have low sequence complexity and have an abundance of charged or hydrophilic amino acids.[2,8] This suggests that the extensive body of models and theory that have been developed to predict the behavior of nonbiological polymers might be productively applied to understand functional properties of unstructured polypeptides. In particular, the practice within the polymer community of using course grained (mesoscopic) models offers significant computational advantages over the detailed all atom representations commonly used in the protein simulation community. Within the course grained framework one can begin by categorizing polypeptides into one of three general polymer types, neutral, polyampholyte or polyelectrolyte. Here neutral polymers have no charged monomers, polyampholytes have charged monomers but a near net zero charge and polyelectrolytes have charged monomers and a net charge. It should

be noted that polymer theory has been extensively applied to biopolymers in other contexts, such as protein folding issues (e.g., Refs. 9 and 10), and polyelectrolyte systems such as DNA (e.g., Refs. 11 and 12). However, here our long-term aim is to obtain functionally relevant properties of intrinsically disordered polypeptides.

Polymer theory provides clear predictions for general chain behavior under certain limits. There is a substantial body of literature describing the properties of neutral polymers under a range of conditions.[13] Polyampholytes and polyelectrolytes have also been studied, but are less well understood.[14-19] However, making more detailed analytical predictions for charged polymer systems is challenging. This reflects the difficulties in approximating the interplay between long-range electrostatic effects and entropic effects. Some of these difficulties can be overcome using simulations.

Most studies on charged polymers have used either random or regularly alternating charge sequences, and have focused on average properties (e.g., the radius of gyration or the shape of chains). From such an analysis there is an understanding of chain behavior as a function of total charge,[16,20,21] for changes in solvent quality[16,22] or for the presence of an external field.[23,24] There has been much less work on the effect of a particular charge sequence[15,25-27] or on constrained (e.g., surface attached, adsorbed) chains or chains in confined geometries. Here we present molecular dynamics (MD) simulations of neutral, polyampholyte, and polyelectrolyte polymers under varying degrees of confinement, performed using the Large-scale Atomic/Molecular Massively Parallel Simulator (LAMMPS) molecular dynamics code.[28] In addition to confinement, we vary chain length, charge sequence, and net charge of the charged polymers. In

these simulations we use course grained bead representations of the polymer chain. Nonbonded interactions are treated by a strictly repulsive Lennard-Jones (LJ) potential. Bonds are simulated by a sum of the repulsive LJ potential and the finitely extensible, nonlinear elastic (FENE) potential. The solvent is treated implicitly using a continuum dielectric, and LJ parameters yield good solvent conditions for each chain. In addition, for charged polymers the simulations include explicit counterions. For these systems we compute full Coulombic interactions via the particle mesh Ewald algorithm. In all simulations, polymer chains are end-attached to a flat surface. For confinement, a second flat "probe" surface is moved to variable distances above the first. Both flat surfaces are purely repulsive, except for the anchoring bead. By examining the force on the probe surface as a function of the distance between the two surfaces, force-distance curves similar to those obtained experimentally by atomic force microscopy are produced. We also examine the confined polymer's structure.

We first present a brief background section discussing the initial expectations for polymer chains in the neutral, polyelectrolyte, and polyampholyte categories. We then describe simulations with confinement of neutral chains. We present the calculated confining force on the walls and chain properties for chains of varying length. In Sec. IV we present simulations of charged systems—i.e., simulations of polyelectrolytes and polyampholytes with variations in their charge sequence. In this section we use simulations with a fixed chain length and varying degrees of confinement. We conclude with a general discussion and possible future directions for these studies.

II. THEORETICAL BACKGROUND AND EXPECTATIONS

Polymer theory has been successfully applied to macromolecules with many individual bead components. The general approach is to compute properties as averages over the full statistical mechanical phase space of accessible conformations. For example, the average end-to-end distance of the chain is calculated by balancing entropic and excluded-volume effects to exhibit the classic scaling behavior: $R_F = \langle R^2 \rangle^{1/2} \sim aN^\nu$, where a is the segment or monomer size, N the number of monomers and ν is the Flory exponent, equal to 1/3, 1/2 and $\sim 3/5$ in poor, θ and good solvents in three dimensions, respectively.

For chains end-attached (grafted) to a surface the configurational space is reduced from the bulk, due to the additional constraint on the tether point of the chain. For high grafting densities interactions with other chains leads to strong stretching away from the surface (the polymer brush state). For sparse grafting (and sufficiently long) chains the surface is characterized by individual polymers occupying half "mushroom" spheres with radial dimensions following the same scaling behavior as dilute chains in bulk. The density profile of segments normal to the surface is predicted[29] to exhibit a maximum several monomer lengths from the surface and spread more in the radial direction parallel to the attachment plane than normal to it.
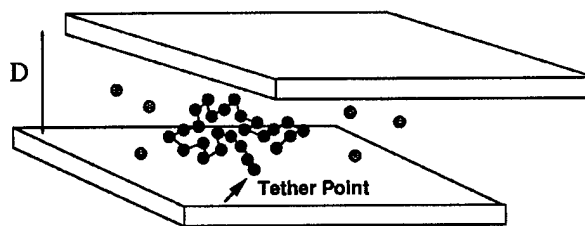

FIG. 1. Geometry of the simulations. The chain is permanently attached via the first neutral segment to the bottom surface. The top surface, modeling a probe or similar confining object, is held parallel to the bottom surface at a separation D. This separation D is varied in the simulations to individually collect force curves and chain properties for each simulation once equilibration has been obtained.

The presence of an additional confining surface will alter the unperturbed behavior of the chain. The simplest system to consider is the case of confinement between two parallel plates separated by a distance D in good solvent[30-32] (Fig. 1). For $D > R_F$ the chain is weakly confined and interacts with the surfaces through fluctuations in the chain beyond its average dimensions. For $D < R_F$ the chain may be described as a string of "blobs,"[13] with radius $D/2$, containing $(D/a)^{5/3}$ monomers exhibiting similar statistics to an unperturbed coil. The chain adopts a two dimensional pancake of radius $R_{F2} \sim aN^{3/4}(a/D)^{1/4}$. The total free energy of this type of system is determined by summing the contributions of the blobs $\sim kT$:

$$F = kTN \left(\frac{a}{D} \right)^{5/3},\tag{1}$$

for $a \ll R_F < D$ and the chain resists further compression by exerting a force scaling as

$$f = kTNa^{-1} \left(\frac{a}{D} \right)^{8/3},\tag{2}$$

on the confining plane. The force required to compress the polymer is predicted to increase linearly with the chain length and with a power law exponent of $-8/3$ with changes in D. For separation distances $D \gg R_F$ the force loses its dependence on chain length and becomes exponentially small.[33] For finite size compressing objects there is a possible escape transition by chains stretching to unconfined regions of space[34] or by arbitrary shape/misalignment,[35] however this is precluded by the geometry adopted in this paper.

The scaling laws for length and separation dependence have been tested by numerical SCF,[36] and MC and MD[31,32,37] studies for chains of varying finite length. Most studies find an exponent in excess of that predicted by Eq. (2) while retaining the predicted scaling behavior with chain length N. An analysis of the monomer distribution profiles via SCF confirms the "mushroom" configuration of the chain at large separations and the gradual transition to a two dimensional pancake with increasing confinement.

The properties of polymers bearing charged groups are less easily accessible to either simple theory or simulation. Analytic theory is complicated by the additional length scales of the system. Simulation is complicated by the diffi-

culty in accounting accurately for the full electrostatic interactions of the system while retaining computational efficiency.

The average properties of a polyampholyte (of which a polyelectrolyte may be considered a limiting case), will be controlled by the balance of electrostatic interactions and entropic degrees of freedom. For example, the electrostatic interactions in overall neutral chains promote collapse, while in the case of charge imbalance they promote swelling. In contrast, entropy promotes Gaussian-like configurations. Different regimes of behavior are dependent on the relative importance of these effects. Thus at high temperatures thermal effects dominate chain behavior and both chain dimensions and shape are relatively unperturbed by the presence of charged groups. At intermediate temperatures and with significant charge asymmetry (net overall charge) the chain behavior is dominated by electrostatic repulsion between uncompensated charged groups. Thus the chain is predicted to extend beyond its unperturbed dimension, reaching in the limit of infinite dilution and a strongly charged polyelectrolyte, a rodlike configuration. For intermediate temperatures and net neutrality the behavior is dominated by fluctuation induced attractions between unlike charges and the polyampholyte collapses to a globular configuration with dimensions less than that of the unperturbed chain. That is the charges screen each other in a Debye–Huckel-like fashion. At very low temperatures or very poor solvents the configuration may be frozen, resulting in "pearl-necklace" configurations of the chain.

External fields, added salt, charge sequence variation and excess charge may significantly influence the behavior of polyampholyte chains. An external field, for example, can lead to further frustration of the chain, due to an additional pull or repulsion on the charged groups. A similar situation is predicted for chains with a net overall charge $> \sim q\sqrt{fN^{1/2}}$ (q is the unit charge) where frustration may result in chains exhibiting both collapsed neutral and stretched highly charged portions.[38] The charge sequence may also play an important role in the balance of thermal and electrostatic effects producing variation in the chain dimensions for chains with similar total composition.[25] Chains with strictly alternating sequences of charge are not well described by Debye–Hückel theory since charge fluctuations over distances of the order of the screening length are generally not possible. They are predicted[26] to collapse in the same manner as neutral polymers in a poor solvent and may be described by an effective, negative second virial coefficient. Such chains are more soluble than polyampholytes with random sequences of charges, with decreasing solubility as the randomness or size of charged blocks along the chain increases.

Three important length scales can be identified for the description of polyampholyte chains. All our simulations are performed with charge separation along the backbone b equal to the monomer size a and we work with this latter parameter. The Bjerrum length, $\lambda_B = e^2/4\pi\epsilon\epsilon_0 kT$ is a measure of the distance over which charge groups interact. Under physiological conditions it has a value of ~ 7 Å. The relative importance of thermal and electrostatic interactions is characterized by the dimensionless coupling constant $\Gamma = \lambda_B/a$.

For polyampholytes with charge fraction $f=1$ (all segments charged) in good solvents and $\Gamma < N^{2/5}$ the thermal effects dominate while for $\Gamma > N^{2/5}$ the electrostatic interactions dominate behavior. Values of $\Gamma < 1$ imply the counterions are dispersed and results in neglible screening. For values of $\Gamma > 1$ this assumption is no longer appropriate and condensation of the counterions may occur, in order to preserve the threshold charge density of the chain, making theoretical analysis difficult. Finally the Debye screening length $\kappa^{-1} = (4\pi\lambda_B\rho)^{-1/2}$ where ρ is the ionic concentration (in our simulations $\sim$ monomer concentration) measures the length scale over which electrostatic interactions are screened. For very dilute solutions this screening effect is negligible.

III. SIMULATION DETAILS

Simulations are performed using the LAMMPS[28] code designed for the study of neutral and charged polymer systems. The code was modified to model the system of interest—end-grafted chains in the low density limit confined by inpenetrable surfaces in an infinite 2-dimensional geometry. As in many applications of polymer theory, we are interested in a general class of polymers–polypeptides. Thus we look for common trends across our set of simulations. Towards this end, we employ the representation of the system as a set of coarse grained bead-springs. In this representation each bead-spring/monomer represents several chemical bonds. Water molecules are not represented explicitly, however their stochastic effect is captured by coupling to a heat bath producing random thermal forces through the friction constant γ. At the length and timescales of interest that we consider, the precise nature of this coupling should not play a role. Additionally screening effects of water on electrostatics are captured with a continuum dielectric. Ions are included explicitly and the full Coulomb interactions are calculated with particle–particle–particle mesh Ewald. Use of this code to treat electrostatics is critical, since cutoff methods have been shown to lead to artifacts and several recent theoretical, numerical and experimental works[39–41] have indicated that ion fluctuations may significantly alter the electrostatic interactions of polyelectrolyte and polyampholyte chains. The two confining surfaces are modeled as homogeneous, flat, parallel surfaces exerting a short-range repulsive force on all monomers but the tether monomer. These surfaces are periodic with the boundaries of the simulation cell: the simulation approximates an infinite x-y periodic system with the z periodicity present, but adjusted to have a small effect on the planar energies and forces. We should also note that the x-y dimensions were chosen to enable a polymeric chain to remain confined with the central cell. The exact fraction of the cell confining the chains and ions is varied in different simulations, however the chains are always in the dilute limit. In other words, there are no LJ interactions between the polymer in the central cell and its periodic images.

The behavior and properties of any one given chain is determined by (i) excluded-volume type interactions with bead monomers, with explicit ions and with the two wall surfaces, (ii) the constraint of connectivity along the backbone, (iii) random thermal agitation and frictional drag due to the solvent (modeled through the Langevin equation), and

(iv) long-range Coulombic interactions between charged groups. The net potential is thus given by the summation

$$U_{TOT} = U_{LJ} + U_{CH} + U_{WALL} + U_{COUL}, \quad (3)$$

and the motion of any given bead i, with mass m and position $\mathbf{r}_i$ is described by the Langevin equation:

$$m\frac{d^2\mathbf{r}_i}{dt^2} = -\delta_i U - m\gamma\frac{d\mathbf{r}_i}{dt} + \mathbf{W}_i(t), \quad (4)$$

where γ is the friction constant and $\mathbf{W}_i(t)$ represents the random forces coupled to γ through the fluctuation-dissipation theorem.

We take into account excluded volume interactions for the monomers and ions via a standard Lennard-Jones potential:

$$U_{LJ} = 4\epsilon\left(\left(\frac{\sigma}{r}\right)^{12} - \left(\frac{\sigma}{r}\right)^6 - \left(\frac{\sigma}{r_c}\right)^{12} + \left(\frac{\sigma}{r_c}\right)^6\right), \quad r \leq r_c, \quad (5)$$

truncated at $r_c = 2^{1/6}\sigma$ so that the interactions are strictly repulsive and athermal good solvent conditions are reproduced. Since this work is the initial part of a general treatment, the ion size is identical. The effect of differing ion size will be treated later.

To model the effects of connectivity we employ a finite extensible nonlinear elastic (FENE) spring potential:

$$U_{CH}(r) = -\frac{1}{2}kR_0^2 \ln\left(1 - \left(\frac{r}{R_0}\right)^2\right), \quad (6)$$

which produces the required restoring force counterbalancing the excluded volume interactions of the chain. A spring constant of $k = 30\epsilon/\sigma^2$ and a maximum bond extension $R_0 = 1.5\sigma$ are adopted in all our simulations, following previous studies indicating this parameter set to be a good choice for tethered systems. For uncharged chains this leads to an average bond length $l_{av} = 0.97\sigma$[42] while for charged chains this is stretched slightly to $l_{av} = 0.98\sigma$.[43]

In the uncharged simulations each monomer in the chain is neutral and no ions are present. For the charged simulations each monomer of the chain is charged either positively or negatively to produce a polyampholyte with zero net charge, or a progressively greater net charge ending with the limiting case of a polyelectrolyte. The charge separation b along the chain backbone is given by the average bond length l_{av}. All charged chains have 32 charged monomers and one neutral tether monomer and are simulated at a fixed monomer density of $10^{-5}\sigma^{-3}$ (for the unconfined system) with 32 explicit counterions balancing the charge on the chain and 12 additional ions with net zero charge. The monomers and ions are always confined by the boundaries of the surfaces so that the effective density varies, depending on the surface–surface separation.

For all calculations with charges present (net neutral systems) we used particle–particle–particle mesh Ewald methods[44] within the LAMMPS code. This method is similar to the particle mesh Ewald method[45] in providing $N \log N$ performance. For our two-dimensional (2-D) periodic system, we also considered using 2-D Ewald methods,[46–49] but these are known to be an order of magnitude (or worse) slower than 3-D methods. We used the "parallel plate capaci-

tor" approximation developed by Spohr.[50] In this approximation, a large amount of empty space is allowed in the z-direction within the primary simulation cell. Spohr found that at least 5-times more distance in the z dimension should be used than present in the "matter-filled" regions. That is, with sufficient "empty-space" present, the coupling between the lattice spacing in the z-direction to the rest of the periodic images in the x-y plane is reduced to nearly zero. In our case the empty-space varied with the polymeric system, but generally was on the order of from five- to fifty-times larger than the primary "matter-filled" region of interest. The variability in this ratio reflects the position of the probe surface relative to the simulation box dimensions. With this choice of simulation conditions we have created a 2-D periodic system that represents the electrostatics of confinement.

The strength of the Coulomb interactions is set by the Bjerrum length λ_B. All our simulations adopted the value $\lambda_B = 0.833\sigma$, giving $\Gamma = 0.85$ and placing our simulations within the counterion condensation regime. We are thus modeling strongly charged polyelectrolyte and polyampholyte chains. The charge sequence variations along the chain backbone are systematically varied either by increasing the size of repeating blocks of charged monomers (for the net neutral chains) or by varying the net charge on a random sequence of charges (for the $Q_{TOT} > 0$ chains).

In all our simulations the first bead is neutral and fixed permanently to the bottom of two confining surfaces (see Fig. 1). These surfaces interact with all other monomers and ions in the system via the repulsive potential:

$$U_{WALL} = z^{-6}, \quad (7)$$

cut off at 2.2σ from the walls. The potential of mean force is calculated as a function of distance from the top surface. The bottom surface is maintained at a fixed position throughout all the simulations. Results for each D separation are collected individually and the potential of mean force reported as a function of D. The top surface is first rapidly brought from a large distance to the confinement distance and then held fixed while the chain is allowed to equilibrate. We monitored the approach to equilibrum of the chain with running averages of the potential of mean force and chain properties, e.g., R, R_g with a typical run time of 5×10^7 timesteps.

For the neutral chains, full force curves for four different chain lengths $N = 16, 32, 64, 128$ (excluding the tether monomer) were collected in this manner. For lengths varying between $N = 16$ and $N = 256$ the potential of mean force and chain properties were studied for several different separations. With charged chains the length was kept fixed and the charge sequence of the backbone varied—the potential of mean force and chain properties was then calculated for fixed separations of confinement.

The average end-to-distance R and radius of gyration R_g were calculated from

$$\langle R^2 \rangle = \langle (r_0 - r_{N-1})^2 \rangle, \quad (8)$$

and

TABLE I. The number of monomers is N, and the wall separation is D.

Class	N	Net charge	Repeat	D
Neutral	16	0		3.21–14.11, ∞
Neutral	32	0		3.21–14.11, ∞
Neutral	64	0		3.21–14.11, ∞
Neutral	128	0		3.21–14.11, ∞
Neutral	256	0		3.21–9.75, ∞
Polyampholyte	32	0	1–1, 2–2, 4–4, 8–8, 16–16	3.21, 5.39, 8.20, ∞
Polyampholyte	32	4	random	3.21, 5.39, 8.20, ∞
Polyampholyte	32	8	random	3.21, 5.39, 8.20, ∞
Polyampholyte	32	12	random	∞
Polyampholyte	32	16	random	∞
Polyelectrolyte	32	32		3.21, 5.39, 8.20, ∞

$$\langle R_g^2 \rangle = \frac{1}{N} \left\langle \sum_{j=0}^{N-1} (r_j - r_{CM})^2 \right\rangle, \tag{9}$$

where 0 denotes the first monomer after the tether and $N-1$ the last: there are N "chain monomers" and the tether point is excluded from the calculation. The ratio $r = R^2/R_g^2$, indicative of the chain asymmetry and the average position of the center of mass were monitored, and density profiles $n(r)$ of the chain segments calculated at different compression distances. Calculations in the charged systems determined the counterion distributions as well as the radial distribution functions of oppositely charge segments within the chain. The configurations of the chains over time were followed through visualization in GNUPLOT and typical snapshots collected and plotted using RASMOL.

In all simulations the timestep is $\Delta t = 0.0015\tau$, where $\tau = \sigma(m/\epsilon)^{1/2}$ is the LJ time and is set to 1. The temperature is maintained at $T = 1.2\epsilon$ and coupled to the heat bath via the friction constant $\gamma = \tau^{-1}$. This choice leads to good sampling while ensuring chain motion is not overdamped.

The force was calculated in a push–hold–equilibrate approach where the probe surface was shifted to a new position and the polymer system allowed to relax and equilibrate before data was collected on the average force exerted on the probe wall. The net force on the wall at a given position was then used to determine a relative free energy for motion of the probe wall by integration (potential of mean force).

A map of our system onto an experimental system is as follows: If we map $\lambda_B = 0.833\sigma$ onto the Bjerrum length of NaPSS in water, or alternatively physiological conditions we have $\lambda_B = 7.14\,\text{Å}$, so that $\sigma = 8.57\,\text{Å}$. Since our average bond length is 0.98σ this implies that a charge fraction $f = 0.3$. Alternatively, for an unstructured polypeptide with average residue size 3.6 Å our 32 monomers would correspond to approximately 75 residues of which approximately a fraction 0.4 bear a net charge.

The systems simulated are summarized in Table I.

IV. RESULTS AND DISCUSSION

We first present results for neutral chains and then for polyampholyte (and polyelectrolyte) chains. Because the set of polyampholyte simulations used a fixed chain of 32 beads,
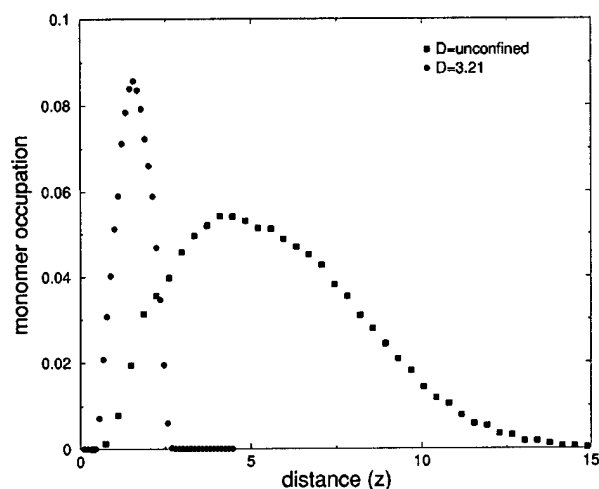
FIG. 2. A plot of the distribution of chain segments of a neutral chain of length $N = 32$ as a function of the distance from the bottom surface z for both an unconfined system (probe surface absent) and strong compression (surface separation $D = 3.21$). The chain preferentially occupies space in the proximity of the tether surface in the unconfined case, but is sharply peaked and exhibits a symmetric segment distribution in the case of strong confinement.

we will first present the results for a neutral chain of 32 beads. This is followed by an analysis, in the neutral chain case, for the effects of chain length.

A. Neutral chains

In the absence of a confining surface the conformation of our individual end-grafted chains is determined entirely by the monomer–solvent, the solvent–solvent interactions and the interactions of monomers of the chain with the attachment surface. Polymer theory predicts this to take the form of a "mushroom" occupying a pear shaped half sphere of radius $R \sim aN^{3/5}$,[29] with a distribution of R due to thermal fluctuations. For sufficiently long chains a maximal occupancy of monomers should occur several monomers from the vicinity of the surface and spread more in the x-y plane than the z dimension. In Fig. 2 we plot the monomer distribution in the direction normal to the surface for a chain of $N = 32$ monomers. The distribution exhibits a gradual increase in occupancy peaking at $\sim 5\sigma$ from the surface for the $N = 32$ chain and spreading significantly to a distance $\sim 15\sigma$ with greatest occupancy closer to the tether surface. The strongest compression $D = 3.21$ is also shown to illustrate how the configurational space of the confined chains is sharply reduced. The average end-to-end distance R distribution (not plotted) peaks at an average value 9.89 and has rms ($=R_g$) of 3.68. The ratio $r = R^2/R_g^2$ is just over 7 in both cases. For a neutral chain in a good solvent and in the absence of other constraints theory predicts $r \approx 6.3$. The chains are thus perturbed by the presence of the wall and the grafting constraint, exhibiting on average larger dimensions than unconstrained chains consistent with the predicted asymmetric shape of the chain. The average dimensions of the unconfined $N = 16$, $N = 64$, and $N = 128$ chains were measured to be $R = 6.20$, $R_g = 2.33$ ($N = 16$), $R = 14.48$ and $R_g = 5.57$ ($N = 64$) $R = 23.74$, $R_g = 8.70$ ($N = 128$).
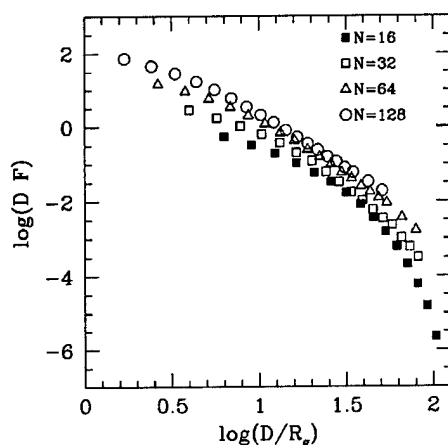
FIG. 3. The average force exerted by the tethered chains on the probe surface as a function of surface–surface separation D. Chain lengths of N = 16, 32, 64, and 128 are depicted.
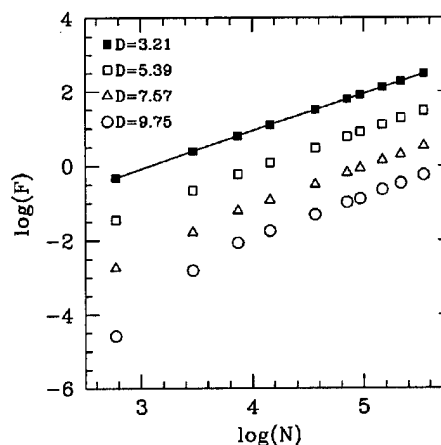

FIG. 4. The average force exerted by chains of length between $N = 16$ and 256 on a probe surface at four different separations. The curves are plotted on a log scale to make the power law more visible.

These values and figures are important for determining the onset and extent of confinement of the polymer chains in the presence of a second parallel probe surface. When the separation distance is $D \gtrsim R$ the chain interacts with the probe surface through relatively infrequent thermal fluctuations. Since the conformational space of the chain is not greatly reduced, the potential of mean force between the polymer and the surface is negligible, and the average dimensions of the chain are not significantly perturbed. Note that given that the chains are more spread in the direction parallel to the tethering plane, this range of weakly confined separations is likely to be larger than this estimate. For $D < R$ however the conformational space begins to be progressively reduced. Figure 2 illustrates this effect in the monomer distribution profile perpendicular to the surface. The confined polymer exerts a repulsive entropic force on the confining surface or object. Full force-distance curves that extend from unconfined to $D = 3.21$ for chains of $N = 16$, 32, 64, and 128 are presented in Fig. 3. In this case the force is a function of surface–surface separation D. We find good agreement with the predicted power law of $-8/3$ at close separations for all four chain lengths with a crossover to -3 at greater separations for the longest chains and a more rapid falloff for shorter chains. We are far from the limit of asymptopic chains and the $> -8/3$ power law is likely to be an effect of the finite length of our polymers. The rapid fall off for the shorter chains is similarly due to separations $D > R$. A comparison of the average end-to-end distance spread of the $N = 32$ chain for the unconfined system and for the smallest separation $D = 3.21$ indicates the progressive shift of R with increasingly smaller separation. At $D = 3.21$ it is peaked at 12.32 and skewed to higher values. The average center of mass of the chain in the z direction is measured to be ~ 1.5, i.e., approximately midway between the surfaces and the segment distribution more sharply peaked and symmetric around this value than for the unconfined chain. The chain is thus squashed into a pancake geometry constrained by the tethered monomer to a finite range of x-y exploration and constrained by the surfaces to a narrow slit in the z

dimension. Similar behavior was exhibited by the other chains.

To test our understanding of the chain length dependence of both the potential of mean force upon compression and the variation in the average dimensions of the chains, we analyzed data for chains of length $N = 16$ to $N = 256$ confined at 4 different separation lengths $D = 3.21$, 5.39, 7.57, and 9.75. The force exerted by the chains on the top surface is plotted as a function of the chain length in Fig. 4. The figure indicates linear behavior over all separations with minor deviations for the larger separations and very short chains. The results are thus in good agreement with both theory and simulation. As the chains are more strongly confined the chain dimensions are predicted to cross over to 2-dimensional behavior. In Fig. 5, we show how this is reflected in the average end-to-end distance of the chains. At the smallest separation the chains are pancakes with size increasing with a power law $\sim 3/4$ in agreement with the scal-
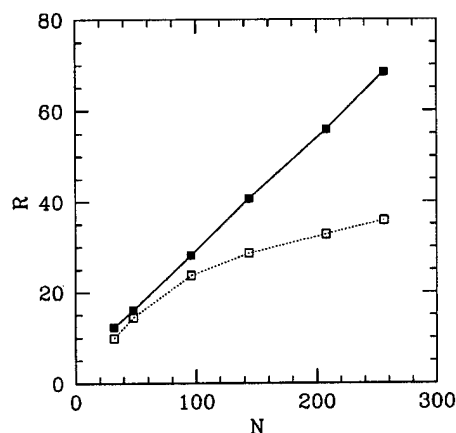

FIG. 5. The average end-to-end distance of chains of length $N = 16$ to 256 at compression $D = 3.21$ (open points) and in the absence of a confining surface (solid points). In the strongly confined case the chains are effectively two dimensional and the radius increases as for two-dimensional chains. A crossover to three-dimensional behavior occurs at larger separations.
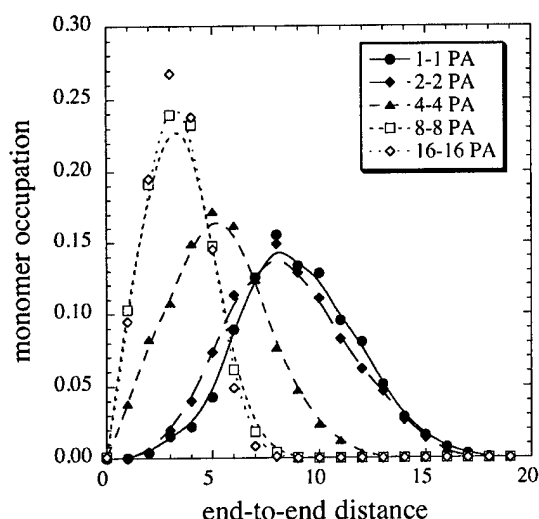
FIG. 6. The end-to-end distance spread as a function of charge block size for $N = 32$ in the polyampholyte sequence for chains of overall net neutrality. The top surface is absent in this system and the curves thus depict the unconfined dimensions of the chains. The curves peak sharply at small values for large charge blocks and approach the results of the equivalent neutral system for small repeating units.
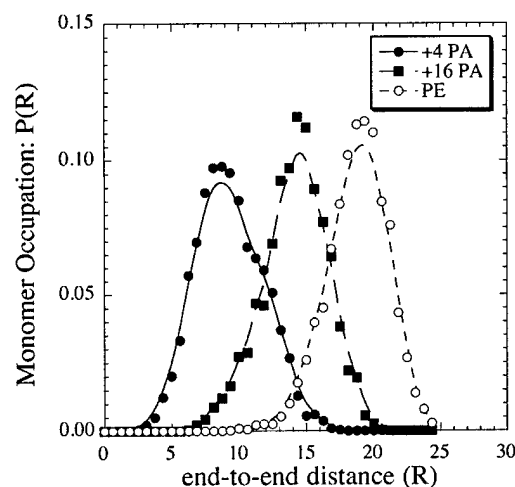

FIG. 7. The end-to-end distance spread as a function of net charge on polyampholytes with random charge sequences. Similar to Fig. 6(a), the chains are unconfined in this system. As the net charge on the chains is increased the curves are progressively shifted to larger values indicative of chain expansion.

ing of the average dimensions of a two-dimensional self-avoiding walk $bN^{3/4}$. As the separation distance increases the exponent becomes progressively weaker, indicative of the gradual crossover to 3-dimensional scaling.

B. Polyampholyte chains

In order to determine the effects of charge distribution and charge imbalance on the end-attached polyampholyte chains, we first studied the chain properties ($N = 32$) in the absence of the confining surface. In Fig. 6 we plot the average end-to-end distance spread of the net neutral chains with varying block size (listed in Table I). The sequences possessing the smallest repeat unit (1–1, 2–2) are negligibly perturbed from their neutral behavior, peaking at roughly the same value and demonstrating a similar spread. This is to be expected given that we are in a regime in which thermal effects dominate the electrostatic interactions along the chain at distances of the order of the charge separation. As the size of the charged blocks is increased, however, both the polyampholyte effect (promoting collapse) and the polyelectrolyte effect (promoting portions of chain stretching) are enhanced. Figure 6 depicts the resulting effects on the behavior of the chain. As the block size is increased the average end-to-end distance of the chain is shifted to smaller values and the distribution becomes less broad. This is indicative of the substantially reduced configurational space of the chain i.e., it adopts configurations maximizing block–block interactions, while being frustrated from complete collapse by thermal agitation. The behavior is further illustrated by the asymmetry parameter r, which is substantially reduced for the largest block sizes ($=3.23$ for the 16−16 sequence).

The effect of a charge imbalance on a random sequence under similar conditions is presented in Fig. 7. A small excess charge of $+4$ produces little deviation from neutral be-

havior. As the excess charge is increased, however, the average end-to-end distance is shifted to larger values and the distribution narrows. This is due to the increased tendency of segments to repel each other as a result of mainly repulsive electrostatic interactions. In the limit of a polyelectrolyte the chain is highly stretched with asymmetry parameter $r = 9.28$. These results are in qualitative agreement with the prediction of stretching from theory for chains with a charge imbalance ($\sim q\sqrt{fN^{1/2}}$).

In contrast to the neutral chains, confinement alters the behavior of the polyampholyte systems in several ways. First, in the same manner as in the neutral system, separations $D \lesssim R$ reduces the conformational space of the chain with a resultant loss in entropy and a potential of mean force between chain and surface. However in the polyampholyte systems, confinement may additionally enhance the polyampholyte (or alternatively polyelectrolyte effect) by increasing the electrostatic interactions. In our systems a decrease in the separation distance also leads to an increase in the effective density of ionic species. Screening effects will thus be enhanced, particularly in the polyelectrolyte (and polyelectrolyte-like) chains.

We first study the influence of confinement on the end-to-end distance of different net neutral sequences and for different net charge. Figure 8 plots the average value of R_g at 3 different separations as a function of sequence block size for the net neutral polyampholyte chains. A plot of the end-to-end distance produced similar results. R_g may in this case be a better gauge of the average dimensions of the chains since each PA has the first and last segments with charges of opposite sign. Over all separations the 1–1 and 2–2 repeating chains exhibit behavior very close to that of their neutral counterparts. The reduction in chain dimensions with separation distance is most pronounced for the smaller repeats (1–1, 2–2, 4–4) than for the 8–8 and 16−16 chains. This is in agreement with our earlier finding that even with the
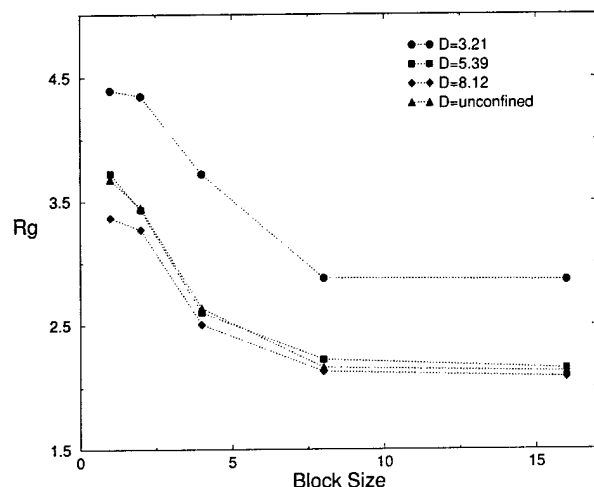
FIG. 8. The average radius of gyration of net neutral polyampholytes at different surface separations vs the block size of repeating charge units. As the block size is increased departures from the behavior of the neutral system become more apparent indicative of the tendency of collapse of the chains.

absence of a confining surface the polyampholyte effect is sufficient to cause the polyampholyte to adopt collapsed dimensions.

Further evidence for a behavior change for polyampholytes with different charge sequence distributions is shown by Fig. 9. In this figure the end-to-end distance spread is plotted for the strongest compression $D=3.21$ This can be compared with Fig. 6 (unconfined). While the average value of R and its spread are similar for the 8–8 and 16–16 chains, a substantial shift occurs for the smaller repeats to larger values and wider spread in a similar manner as for the neutral system. Similar results were found for polyam-
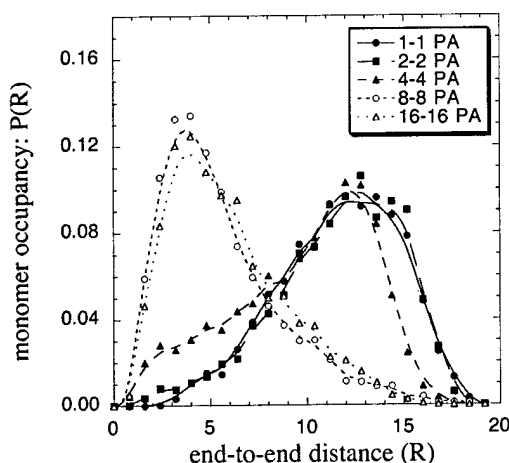

FIG. 9. The end-to-end distance spread as a function of block size for the strongest compression $D=3.21$. The results are similar to those of unconfined chains for the chains with largest repeating units while for the chains with smaller repeats the curves are shifted to higher values in the same manner as for the identical neutral system. Note that only a block size of 8 is necessary for significant pairing and collapse.
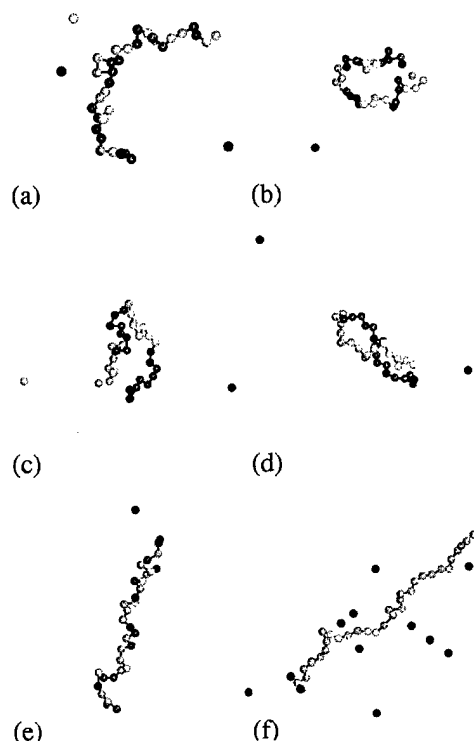
FIG. 10. Snapshots typical of polyampholyte configurations at the strongest compression distance $D=3.21$ for different charge sequences. (a) Corresponds to a 2–2 repeating chain, while (b), (c), (d) correspond to 4–4, 8–8, 16–16 repeats and (e) and (f) to chains with a net charge of $+8$ and $+32$ (polyelectrolyte). Different segment charge types are depicted with different shades.

pholytes with charge imbalance although the shift in this case was less pronounced.

These results are in qualitative agreement with the Monte Carlo (MC) simulations of Ref. 25 in which the average dimensions of polyampholytes with varying degrees of blockiness (measured in terms of the intrachain energies) were found to be sequence dependent. It is also consistent with theoretical studies on the effects of correlations in polyampholytes sequences,[15] in which it has been shown that sequence correlations become important when the correlation is sufficiently large to produce polyelectolyte behavior within the chain. This may be important in some unstructured protein sequences in which the charge sequence is predetermined and may exhibit such low complexity.[51]

The potential of mean force differs very little from that of the neutral chain at the two smaller separation distances but shows a marked drop for the larger block repeat sequences at weaker separation, indicative of the decreased tendency of the chain to thermally explore conformations resulting in an interaction with the surface. This suggests that while the smallest block chains may map well onto the neutral force curve, substantial deviations are to be expected at moderate to weak separations for chains with polyelectrolyte portions. A further confirmation of this finding was seen in the distributions $n(z)$ for the different sequences which peaked at larger values for the smaller repeat chains.

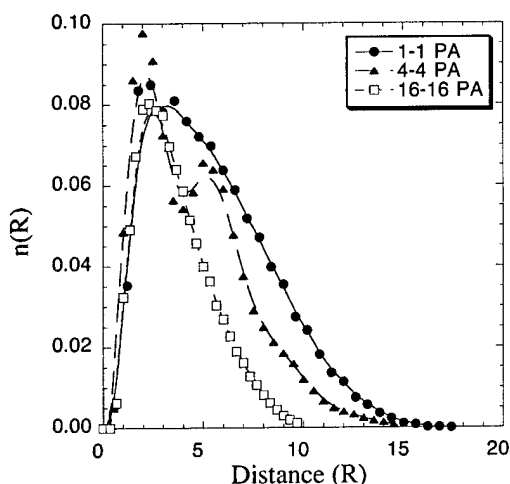Figure 10 depicts typical snapshots of different repeat

FIG. 11. Radial distribution function of segments of opposite charge in repeating polyampholyte chains at a surface separation of $D = 3.21$, i.e., strong compression. Large repeat block chains exhibit the sharpest distributions while the smaller repeats produce typically broader distributions. An interesting double peak is found for the 4–4 repeating chain.
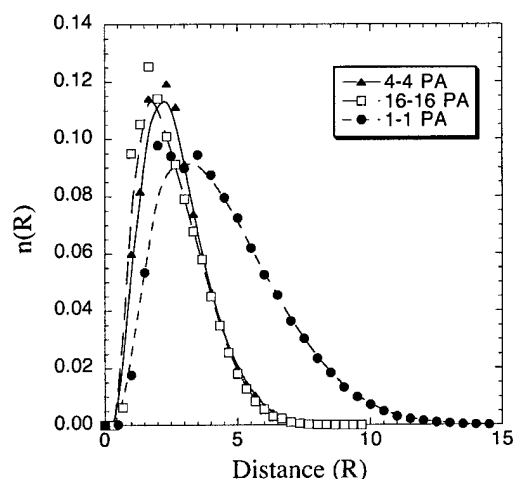
FIG. 12. The radial distribution function of segments of opposite charge in repeating polyampholyte chains at a surface separation $D = 8.12$, i.e., weakly confined. The double peak in Fig. 11 for the 4–4 repeating chain is absent.

chains and different chains with net charge at a surface separation of $D = 3.21$. The smallest repeat unit chains behaved in a manner very similar to uncharged chains, consistent with our chain property results and a thermally dominated system. For the larger repeating unit chains, however, typical configurations located oppositely charged portions of the chain in proximity and involved stretched portions of chain involving the same charge type. The 4–4 repeat chain was most frustrated in its attempts to balance thermal and polyelectrolyte/polyampholyte effects and exhibited more diverse configurations than the larger repeat chains. A net charge of +4 resulted in behavior not dissimilar from a neutral chain, while a larger excess charge resulted in predominantly stretched configurations.

We studied the typical configuration space of the different repeating chains more explicitly by calculating the radial distribution function of oppositely charged segments of the chains. Bonded segments were excluded from the calculation. Figure 11 plots the distributions of three of the repeating chains at the surface separation $D = 3.21$ corresponding to the snapshots in Fig. 10. The 2–2 and 8–8 repeating chains (not shown) exhibited behavior very close to the 1–1 and 16–16, respectively. All sequences peak at a small distance at about $2-3\sigma$, however the distribution broadens for the smaller repeat chains. The 4–4 sequence exhibits two maxima, one at $\sim 2.5\sigma$ and the other at about 6σ. The secondary peak is absent for the weakly confined case $D = 8.12$ shown in Fig. 12, in which its available configurational space is increased and may be a result of two energetically favorable configurations for the chain under strong confinement.

V. CONCLUSIONS

We have performed MD simulations of neutral, charged and polyampholyte polymers within a confined geometry. Our neutral polymer simulations provide a good test of poly-

mer predictions for finite length chains. Our polyampholyte simulations suggest a previously unexplored dependence of the properties of a tethered, confined polyampholyte on the charge sequence of the chain.

To summarize, the simulations varied the length of the polymers, the charge distribution along the polymer chain, and the distance between a tethered wall and a probe wall. For neutral chains of varying length we obtained force curves in good agreement with theoretical predictions for compressed neutral polymer chains, with some deviations for the smallest chain lengths simulated. The chain properties such as the average end-to-end distance and radius of gyration and segment distribution functions were also in good agreement with theory and MC simulation. Our study is one of the few MD simulations of compressed end-attached neutral chains. The agreement with similar MC studies is thus encouraging.

For chains bearing charged groups we found an interesting dependence of chain properties on the charge sequence of the chain. For polyampholytes bearing an excess charge our results are in agreement with predictions for similar chains in bulk: for an excess charge above a critical value, the chains expand beyond their neutral dimensions and in the limit of a polyelectrolyte result in an almost fully extended chain. For polyampholytes with equal numbers of positive and negative charged segments (net neutral) our results indicate that while thermal dominance was sufficient to maintain near neutral dimensions and chain properties for small repeating block chains, the enhancement of both the polyelectrolyte (promoting chain expansion) and polyampholyte (promoting chain collapse) effects was sufficient to promote local stretching and overall collapsed configurations of the chains. The extent to which the chain was frustrated in balancing the different constraints and interactions was sequence dependent, being determined by the size of the repeating blocks. Further studies employing longer chain lengths and further systematic sequence variation would be

interesting to pursue this point. Given that exclusion properties of unstructured polypeptide domains[3] may be closely related to their biological function, and the possibility of exploring such a mechanism via experimental techniques such as atomic force microscopy, an understanding of the properties of polyampholyte systems such as we have studied here is highly desirable. Here we have taken the first steps toward this end.

ACKNOWLEDGMENTS

[1] P. E. Wright and H. J. Dyson, J. Mol. Biol. **293**, 321 (1999).
[2] A. K. Dunker, J. D. Lawson, C. J. Brown *et al.*, J. Mol. Graphics **19**, 26 (2001).
[3] J. Hoh, Proteins: Struct., Funct., Genet. **32**, 223 (1998).
[4] W. B. Russel, D. Saville, and W. R. Schowalter, *Colloid Dispersions* (Cambridge University Press, New York, 1989), Chap. 6.
[5] P. Walstra, V. A. Bloomfield, G. Wei, and R. Jenness, Biochim. Biophys. Acta **669**, 258 (1981).
[6] C. G. de Kruif, J. Colloid Interface Sci. **185**, 19 (1997).
[7] H. G. Brown and J. H. Hoh, Biochemstry **36**, 15035 (1997).
[8] V. Uversky, J. Gillespie, and A. Fink, Proteins **41**, 415 (2000).
[9] E. G. Timoshenko, Y. A. Kuznetsov, and K. A. Dawson, Phys. Rev. E **53**, 3886 (1996).
[10] K. A. Dill, Biochemistry **29**, 7133 (1990).
[11] J. Ubbink and T. Odijk, Biophys. J. **68**, 54 (1995).
[12] V. A. Bloomfield, Biopolymers **31**, 1471 (1991).
[13] P.-G. deGennes, *Scaling Concepts in Polymer Physics* (Cornell University Press, Ithica, 1971).
[14] S. Edwards, P. R. King, and P. A. Pincus, Ferroelectrics **30**, 3 (1980).
[15] P. G. Higgs and J.-F. Joanny, J. Chem. Phys. **94**, 1543 (1991).
[16] A. V. Dobrynin and M. Rubinstein, J. Phys. II **5**, 677 (1995).
[17] P.-G. deGennes, P. Pincus, R. M. Velasco, and F. Brochard, J. Phys. (France) **37**, 1461 (1976).
[18] J. C. Barrat and J.-F. Joanny, Adv. Chem. Phys. **44**, 1 (1996).
[19] P. Pfeuty, J. Phys. (Paris), Colloq. **149**, C2–149 (1978).
[20] T. Soddemann, H. Schiessel, and A. Blumen, Phys. Rev. E **57**, 2081 (1998).
[21] M. Tanaka, A. Y. Grosberg, V. S. Pande, and T. Tanaka, Phys. Rev. E **56**, 5798 (1997).
[22] Y. Kantor and M. Kardar, Europhys. Lett. **27**, 643 (1994).
[23] D. Loomans, H. Schiessel, and A. Blumen, J. Chem. Phys. **107**, 2636 (1997).
[24] D. Long, A. V. Dobrynin, M. Rubinstein, and A. Ajdari, J. Chem. Phys. **108**, 1234 (1998).
[25] D. Srivastava and M. Muthukumar, Macromolecules **29**, 2324 (1996).
[26] J. Wittmer, A. Johner, and J. F. Joanny, Europhys. Lett. **24**, 263 (1993).
[27] M. Tanaka, A. Y. Grosberg, and T. Tanaka, J. Chem. Phys. **110**, 8176 (1999).
[28] S. Plimpton, J. Comput. Phys. **117**, 1 (1995).
[29] P. G. deGennes, Macromolecules **13**, 1069 (1980).
[30] M. Daoud and P. G. deGennes, J. Phys. (France) **38**, 85 (1977).
[31] A. Milchev and K. Binder, Eur. Phys. J. B **3**, 477 (1998).
[32] J. deJoannis, J. Jiminez, R. Rajagopalan, and I. Bitsanis, Europhys. Lett. **51**, 41 (2000).
[33] E. Eisenriegler, Phys. Rev. E **55**, 3116 (1997).
[34] G. Subramanian, D. R. M. Williams, and P. A. Pincus, Macromolecules **29**, 4045 (1996).
[35] I. Szleifer and M. Carignano, Macromol. Rapid Commun. **21**, 423 (2000).
[36] B. M. Steels, J. Koska, and C. A. Haynes, J. Chromatogr. B **743**, 41 (2000).
[37] J. Jiminez and R. Rajagpolan, Langmuir **14**, 2598 (1996).
[38] S. Wolfling and Y. Kantor, Phys. Rev. E **57**, 5719 (1998).
[39] M. J. Stevens and K. Kremer, J. Chem. Phys. **103**, 1669 (1995).
[40] R. Podgornik and V. A. Parsegian, Phys. Rev. Lett. **80**, 1560 (1998).
[41] B.-Y. Ha and A. J. Liu, Phys. Rev. Lett. **79**, 1289 (1997).
[42] M. Murat and G. S. Grest, Phys. Rev. Lett. **63**, 1074 (1989).
[43] F. S. Csajka and C. Seidel, Macromolecules **33**, 2728 (2000).
[44] R. Hockney and J. Eastwood, *Computer Simulation Using Particles* (McGraw-Hill, New York, 1981).
[45] T. Darden, D. York, and L. Pedersen, J. Chem. Phys. **98**, 10089 (1993).
[46] D. Parry, Surf. Sci. **49**, 433 (1975).
[47] D. Parry, Surf. Sci. **54**, 195 (1976).
[48] D. Heyes, M. Barber, and J. Clarke, J. Chem. Soc., Faraday Trans. 2 **73**, 1485 (1977).
[49] S. de Leeuw and J. Perram, Mol. Phys. **37**, 1313 (1979).
[50] E. Spohr, J. Chem. Phys. **107**, 6342 (1997).
[51] J. C. Wooton, Curr. Opin. Struct. Biol. **4**, 413 (1994).

Review

Probing the Machinery of Intracellular Trafficking with the Atomic Force Microscope

Sanjay Kumar[1] and Jan H. Hoh[1,2,*]

[1]Department of Physiology, Johns Hopkins University School of Medicine, Baltimore, MD 21205, USA
[2]Department of Chemical Engineering, Johns Hopkins University, Baltimore, MD 21218, USA
*Corresponding author: Jan H. Hoh, jhoh@jhmi.edu

Atomic force microscopy has emerged as a powerful tool for characterizing single biological macromolecules, macromolecular assemblies, and whole cells in aqueous buffer, in real time, and at molecular-scale spatial and force resolution. Many of the central elements of intracellular transport are tens to hundreds of nanometers in size and highly dynamic. Thus, atomic force microscopy provides a valuable means of addressing questions of structure and mechanism in intracellular transport. We begin this review of recent efforts to apply atomic force microscopy to problems in intracellular transport by discussing the technical principles behind atomic force microscopy. We then turn to three specific areas in which atomic force microscopy has been applied to problems with direct implications for intracellular trafficking: cytoskeletal structure and dynamics, vesicular transport, and receptor–ligand interactions. In each case, we discuss studies which use both intact cellular elements and reconstituted models. While many technical challenges remain, these studies point to several areas where atomic force microscopy can be used to provide valuable insight into intracellular transport at exquisite spatial and energetic resolution.

Key words: atomic force microscopy, AFM, cell mechanics, cytoskeleton, force measurements, imaging, membrane fusion, receptors, vesicles

Received and accepted for publication 27 July 2001

As cell biology advances into the postgenomic era, increasing attention will be paid to the physical and chemical details of the macromolecular interactions that determine cell physiology. Gaining insight into these interactions will require thorough study of both the structure of macromolecular complexes and the forces that govern their assembly. This need is particularly acute in the area of intracellular trafficking, where macromolecular assemblies such as receptor-ligand complexes, cytoskeletal fibers, and lipid vesicles play a central role, but where our knowledge of molecular biology far outstrips our understanding of the underlying physical chemistry.

Clearly, these questions require tools which allow one to probe the structure and physical chemistry of a cell under conditions which are both biologically relevant and easily manipulated. Atomic force microscopy (AFM) is emerging as one such technique. AFM enables imaging and mechanical interrogation of single molecules and macromolecular complexes under near-physiological conditions. Less than two decades after its invention, AFM has begun to contribute to the characterization of systems of biological macromolecules, ranging from single molecules to intact cells.

Here, we review the use of AFM in the study of intracellular trafficking. We begin by briefly discussing the technical aspects of the method, including the components of the instrument, common modes of operation, and how it complements traditional forms of microscopy. We then focus on three central problems in intracellular transport in which there has been particularly intense effort to apply AFM: cytoskeletal structure and dynamics, vesicular transport, and receptor–ligand interactions. While we clearly do not present an exhaustive review of the application of AFM to problems in cell biology, these selected examples should help illustrate some of the insights AFM can provide into the molecular and submolecular details of the machinery of intracellular trafficking.

Principles and Modes of Operation

Instrumentation

The central measurement in atomic force microscopy is the interaction force between a sample surface and a probe (tip) affixed to a weak spring cantilever (Figure 1). These cantilevers are typically microfabricated from silicon or silicon nitride and measure between several microns and hundreds of microns in length. The size of the tip apex, which may range from a few nanometers (carbon nanotube tips) to tens of microns (colloidal particles), places fundamental limits on the imaging resolution and plays a dominant role in determining the tip–sample interaction force. The sample is mounted on a piezoelectric ceramic scanner that enables sample movement in the lateral (x,y) and vertical (z) directions. In some instruments, the cantilever is completely stationary during an AFM experiment; all movement is made by the sample via control of the scanner (Figure 2A). AFM has also been combined with optical microscopy into a single instrument; here, in order to provide an optical path, the cantilever is mounted
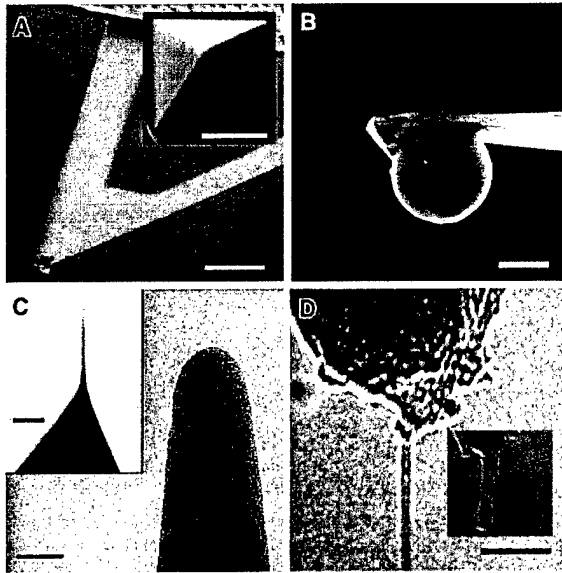
trace of the piezo's motion is a topographic map of the surface.

In tapping mode (Figure 3B), the cantilever is actively vibrated at around its resonance frequency (typically several kHz to hundreds of kHz) using a piezoelectric actuator. The tip–sample separation distance is set such that the cantilever lightly taps the surface at the lowest point of its oscillation. Here, instead of static deflections, interactions with the sample lead to changes in the amplitude of oscillation of the cantilever. As with contact mode, these changes are measured by a reflected laser beam and fed back to the piezoelectric scanner, which adjusts in z to maintain a constant amplitude. Again, the scanner trace yields the topography of the surface. Because the tip does not maintain constant contact with the surface, tapping mode has also been called 'intermittent contact mode.' There are at least two other important imaging modes in which the cantilever is oscillated. In noncontact (attractive) mode, the tip is vibrated at lower amplitude and senses topography primarily through the influence of noncontact forces that predominate above the sample (1). In magnetic alternating current imaging, the cantilever is magnetically coated and its vibration is driven by an applied, oscillating magnetic field instead of a piezoelectric device (2).

Perhaps the greatest advantage of tapping mode over contact mode is that it minimizes potentially destructive shear and adhesive forces on the sample, a particularly valuable property when imaging cells or biological macromolecules. One disadvantage is that conventional cantilevers tend to have low or poorly defined resonances in aqueous solution, making high-resolution tapping mode imaging a technical challenge. While in principle tapping mode tends to minimize tip–sample interaction forces, in practice, contact mode often provides higher resolution for a given application.

Several other sources of imaging contrast besides topography have been exploited. As a particularly simple example, the error signal (deflection or amplitude) is often useful, particularly in samples in which edges and other topographic gradients are of interest. In tapping mode, the difference in phase of oscillation between the motor driving the cantilever and the cantilever itself may be used as a basis for contrast. These phase differences have been interpreted in terms of energy dissipation by the cantilever and correlated with the viscoelastic properties of the sample (3) and electrostatic interactions between tip and sample (4). In lateral or friction force microscopy (LFM), the torsion of the cantilever is monitored as it scans across the surface, revealing regions of frictional contrast. While we do not review them extensively here, these nontraditional imaging modes are expected to play an increasingly important role in the characterization of biological surfaces by AFM.

Force spectroscopy

In force spectroscopy, the sample is cycled vertically (in z) with respect to the tip while the lateral (x,y) position is fixed. The cantilever deflection is then measured as a function of

Figure 1: AFM cantilever and tips. (A) Standard pyramidal silicon nitride cantilever (bar is 10 μm), with high-magnification image of tip (inset, bar is 1 μm) (Image courtesy of Eric Henderson). (B) Colloidal particle glued to AFM tip (bar is 5 μm). These tips are widely used for force measurements. (C) Electron-beam deposited (EBD) tip (11) at low magnification (inset, bar is 300 nm) and high magnification (bar is 30 nm) (reprinted with permission, © 2000, American Chemical Society). (D) Carbon nanotube-modified tips of diameter 0.9 nm (main panel) and 2.8 nm (inset) (bar is 10 nm for both) (12) (reprinted with permission, © 2001, American Chemical Society).

on and translated by a piezoelectric scanner while the sample remains stationary (Figure 2B).

Imaging

There are two canonical classes of AFM experiments: imaging and force spectroscopy. The two most commonly used modalities for imaging are contact mode and tapping mode. In contact mode (Figure 3A), the tip is brought into a light but stable contact with the sample, which is then raster-scanned in the x–y plane relative to the cantilever. In this regime, contrast originates from van der Waals repulsion, which dominates the tip–sample interaction force. Topographic variations along the surface lead to deflections of the cantilever; these deflections are monitored by a laser beam which reflects off the back of the cantilever onto a position sensor. Since the cantilever behaves as a linear spring, the deflection is proportional to the interaction force, where the constant of proportionality is the spring constant. Typical spring constants for contact mode AFM cantilevers fall in the range 0.01–1 N/m, allowing the measurement of forces on the order of piconewtons (10^{-12} N). By feeding the signals from this photodiode back to the piezo scanner, the sample's vertical position may be adjusted during the scan so as to maintain a constant deflection (imaging force). Thus, the
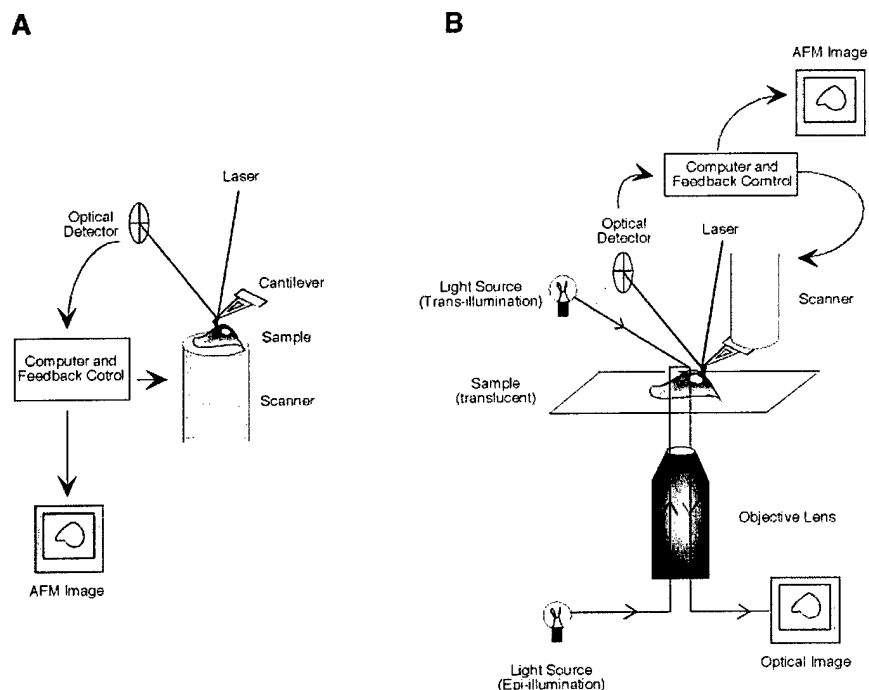
A

B

Figure 2: AFM instrumentation. (A) Schematic of stationary-probe AFM. The sample is mounted on a piezoelectric scanner which enables sample manipulation in x, y, and z. The z-position of the cantilever is monitored by a laser beam which reflects onto a position sensor. This position signal is continuously fed back to the scanner, which adjusts to maintain a constant cantilever static deflection (contact mode) or amplitude (tapping mode). The scanner trace thus yields the topography signal. (B) Schematic of a combined AFM/optical microscope. A number of modifications are needed to permit optical access. First, the sample is held stationary and the cantilever is scanned. Second, the sample and substrate must be translucent. Finally, the presence of the scanner in the optical path means that the light source must often be placed out of line with the sample and objective, although this may be overcome by placing a mirrored surface on the scanner (not shown).

piezo scanner (sample) z-position (Figure 4). The data describing deflection vs. sample position, or force curve, may be readily converted to a curve of force vs. tip-sample separation distance which reveals the dominant physical forces between the tip and sample. The portion of the curve in which the probe approaches the sample reveals information about long- and medium-ranged forces such as electrostatic and steric exclusion forces. The portion in which the tip and sample deform one another reflects sample elasticity, and the portion of the curve in which the sample retracts from the tip illustrates tip-sample adhesion and unbinding forces (5). Perhaps most effort in force spectroscopy in biological systems has been directed towards characterizing receptor-ligand interactions, including measurements of binding specificity and strength. Since specific receptor-ligand interactions lie at the heart of virtually all intracellular trafficking and signal transduction pathways, we pay special attention to these studies in this review.

Two emerging areas of force spectroscopy are force mapping and single-molecule stretching. In force mapping, force curves are obtained in an array covering many points on a surface. Each curve is then analyzed to reveal some property of interest, leading to a two-dimensional 'map' of that prop-

erty (5). In single-molecule stretching experiments, an individual macromolecule is tethered between the tip and surface. As the tip is pulled away from the surface, the macromolecule is stretched and, if it is a protein, unfolded. Each unfolding event produces a characteristic sawtooth-like feature in the force curve, corresponding to unfolding of different domains of the protein. Since the mechanical unfolding of titin was reported in 1997 (6), this method has been applied to many natural and synthetic proteins and extended to polysaccharides (7) and nucleic acids (8). We refer the reader to an excellent review of these experiments (9).

Comparison to other microscopies

The most striking differences between AFM and more traditional types of microscopy lie in three areas: origin and degree of contrast, resolution, and sample preparation. In light and electron microscopy (EM), contrast is based on the ability of a sample to scatter radiation (i.e. a beam of light or electrons). Contrast in AFM originates from forces experienced by the probe as it is scanned across the surface, and may consist of several components (e.g. electrostatics, van der Waals). The degree of contrast is also significantly higher in AFM. While EM has atomic resolution and therefore possesses sufficient power to resolve single biological macro-
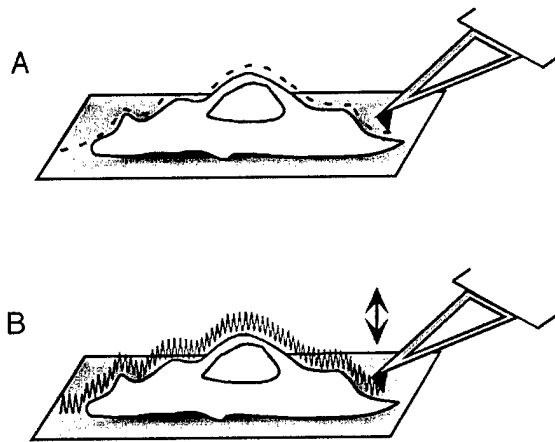
Figure 3: Standard AFM imaging modes. (A) Contact mode imaging. The cantilever is scanned over a sample, and static deflections produce a height signal. (B) Tapping mode imaging. The cantilever is actively vibrated as it scans the sample, and changes in topography produce changes in the amplitude of oscillation.
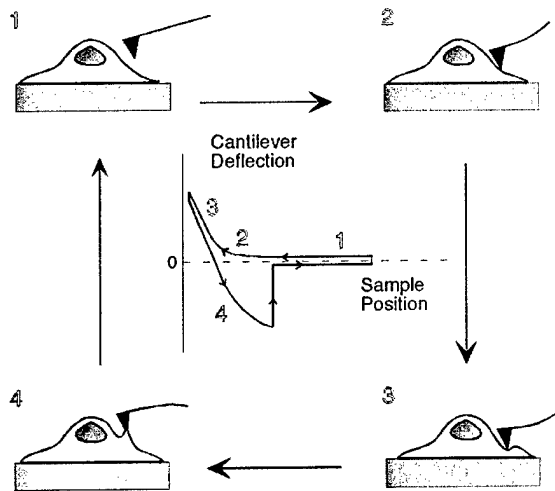

Figure 4: Force curves. 1) At large separation distances, the cantilever and sample do not interact and there is zero deflection. 2) As the sample approaches the tip, the tip deflects; a soft sample (such as a living cell) will likely deform. 3) Further approach leads to greater cantilever deflection and sample deformation. 4) As the tip retracts, the sample adheres to the tip, causing the cantilever to under-deflect. This adhesion results from a complex combination of nonspecific (e.g. electrostatics, van der Waals interactions) and specific (receptor–ligand interactions) forces. When the tip and sample separate, the cycle is completed. Note this schematic illustration of a force curve is rather simplistic. For highly complex samples and tip chemistries, one observes a rich variety of fine structure which results from several superimposed types of tip–sample interaction forces. The approach and retract curves in the noncontact region (1) are slightly separated for clarity.

molecules, contrast is in general poor without the addition of enhancing agents. By comparison, it is routine to image single, unstained protein and nucleic acid molecules by AFM with excellent contrast. Next, because of diffraction effects, the lateral resolution of traditional far-field light microscopy is fundamentally limited to approximately half the wavelength of the imaging radiation. In AFM, images are not produced by diffraction; instead, lateral (x–y) resolution limits are set by the probe size, cantilever z-sensitivity, and sample properties and typically fall within 0.2–50 nm. Vertical (z) resolution limits are instrumental in origin and typically lie around 0.01 nm. Methods have been developed to sharpen tips beyond the abilities of microfabrication. Electron beam deposition may be used to construct tips with end-radii of 5–10 nm (Figure 1C) (10,11). This limit may be pushed even further by affixing a carbon nanotube to the tip (Figure 1D) (12,13). A final distinguishing feature relates to sample preparation. For biological samples, EM typically requires fixation and staining or cryogenic preparation and imaging under vacuum. Conversely, AFM typically requires no staining, and sample preparation is often accomplished simply by physically adsorbing the sample onto a substrate. AFM therefore combines resolution that approaches EM with sample preparation features that more closely resemble light microscopy, with contrast better than both. With a sample chamber that is accessible for buffer exchange over the course of an experiment, these powerful properties allow one to conduct studies in which soluble factors (ions, ATP, regulatory proteins, pharmacological agents) are introduced to the sample and dynamics are monitored in real time.

AFM carries clear limitations relative to traditional microscopies, as well. First, unlike light microscopy, AFM is a surface characterization technique that cannot directly visualize the interior of a cell. Second, even at its fastest, AFM image acquisition is markedly slower than light microscopy. Third, the scanning process can be invasive, and the imaging forces may damage the sample. Finally, the sample must be immobilized onto a surface, and this may either damage the sample or significantly alter its properties. For these and other reasons, instruments that combine AFM with a second imaging modality have become increasingly widely used. Perhaps the best example of this is combined AFM and light microscopy. Using hybrid instruments, this approach has been taken to concurrently visualize intracellular structures with AFM and fluorescence microscopy (14). Some of these studies are discussed in more detail later in the review.

Cytoskeletal Structure and Dynamics

Understanding the structure and function of cytoskeletal polymers is of direct relevance to intracellular transport. First, transport vesicles utilize the cytoskeleton for directional transport, often through kinesin and other motor proteins (15). Second, the cytoskeleton is critical to the maintenance of cell polarity, which in turn supports directional transport of solutes (16). Third, the cytoskeleton is absolutely critical to cell mo-

tility and cytokinesis (17). Given that the substructural features of these cytoskeletal elements are typically on the order of nanometers, and given the interest in correlating cytoskeletal architecture in cells with external mechanical stimuli, the AFM is well suited to address structural and mechanical questions about the cytoskeleton. We first consider studies with isolated cytoskeletal filaments before moving on to studies performed in the context of whole cells.

Purified cytoskeletal filaments

The three major classes of cytoskeletal polymers, actin, microtubules, and intermediate filaments, have all been successfully imaged *in vitro* by AFM. Of these three, microtubules (MTs) have received the most attention in the published literature (Figure 5A). Despite the presence of several estab-

lished purification protocols, high-resolution imaging of MTs has posed a formidable challenge. Much of this challenge results from difficulty finding substrates and imaging conditions under which the MTs are immobilized but do not significantly deform or rupture, forcing investigators to take creative approaches to substrate and sample preparation. By crosslinking MTs with glutaraldehyde and using glass substrates coated with polylysine, Vater and coworkers were among the first to successfully image MTs in air and solution (18). Later, Vinckier and colleagues induced and arrested MT polymerization at different times and presented AFM images of the resulting structures. These images showed progressive polymerization and growth over 20–30 min; the authors also used force spectroscopy to estimate the elastic moduli of individual microtubules (19). Importantly, both papers recog-
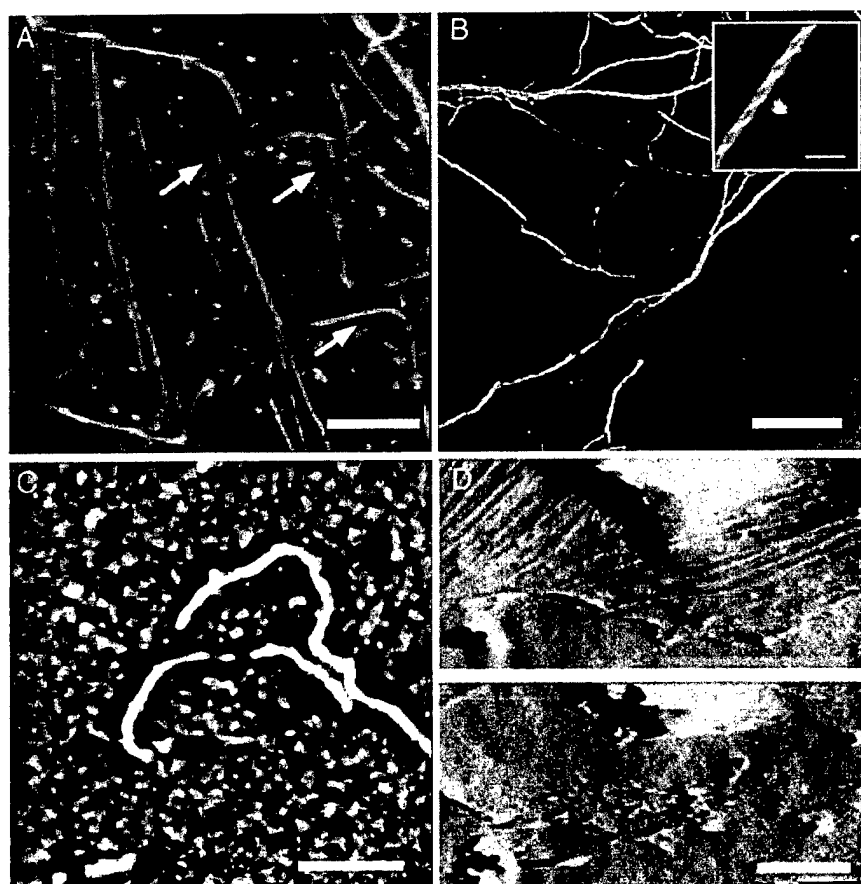
Figure 5: AFM and the cytoskeleton. (A) Microtubules. This image shows microtubules adsorbed to a lipid bilayer in buffer (bar is 2 μm) (20) (reprinted with permission, © 2000 Springer-Verlag, Figure 2A from cited reference). (B) Actin filaments. This image was acquired by cryo-AFM (25). Single filaments associate longitudinally to form rafts which are in turn connected by branching structures (bar is 400 nm). Higher magnification imaging shows the packing of single filaments within rafts (inset, bar is 50 nm) (reproduced with permission, © 2000, Biophysical Society). (C) Intermediate filaments. This image of native neurofilaments (NFs) under buffer shows zones around the filament backbone from which contaminant particles are excluded (bar is 500 nm) (26) (reprinted with permission, © 1997, American Chemical Society). (D) Cytoskeletal imaging *in situ*. In the deflection image of an untreated glial cell (top), a prominent network of filamentous structures is observed in the cytoplasm. When the cell is treated with cytochalasin B, an inhibitor of actin polymerization, this network disappears (bottom) and the cell membrane is rendered labile to repeated scanning (bar is 25 μm) (29) (reproduced with permission, © 1992, American Association for the Advancement of Science).

nized that AFM overestimates microtubule diameters by as much as a factor of four when compared to EM (i.e. 110 nm vs. 25–30 nm). This discrepancy results from the finite size of the tip, which causes apparent broadening of structures that are small relative to the tip. More recent efforts have focused on identifying MT substructures such as protofilaments and attempting to capture MT interactions with accessory motor proteins (20).

Efforts to study actin filaments *in vitro* by AFM have faced similar technical challenges. Several groups have attempted to use AFM to image actin filaments in ambient and aqueous conditions (21–24), although resolution of filament substructure has been limited. Using a custom-built AFM which operates at cryogenic temperatures, Shao and coworkers markedly improved the resolution of individual filaments (Figure 5B) (25). They obtained images of ribbon- and raft-like structures containing several single actin filaments each. The images also clearly show the right-handed helicity of the filaments and a well-defined intrahelical repeat of 35–40 nm, both in excellent agreement with EM. One finding not previously seen by EM was 'branching' junctions in which single filaments formed bridges between two actin rafts. These bridges may help account for the high viscoelasticity of pure, dilute actin gels. Later, Shao et al. presented images of actin paracrystals adsorbed to cationic lipid bilayers (23). This study provided further insight into the packing of actin filaments within rafts, and provides a foundation for AFM characterization of complexes of actin and actin binding proteins.

Intermediate filaments (IF's) are the least well studied of the three types of cytoskeletal fibers by AFM. Neurofilaments (NFs) provide an example of the application of AFM imaging and force spectroscopy to IF's (Figure 5C). NFs are the primary cytoskeletal components of large, myelinated neurons. Through interfilament interactions mediated by their C-terminal 'sidearm' domains, NFs form an ordered intracellular framework which helps maintain neuronal polarity and patency. The structure of the sidearms and thus the origin of interfilament interactions remains controversial. While imaging native NFs purified from bovine spinal cord, Brown and Hoh observed 100–200-nm-wide zones surrounding the backbone of each NF from which contaminants in the preparation were excluded (26). Using direct force measurements, they also found that the NFs generate a long-range repulsive force that persists in the presence of high salt concentration. They interpreted these findings to mean that the sidearm domains are unstructured polypeptides that generate long-range repulsion through thermally driven motion and steric exclusion. This suggests that NFs function by acting as aligned, mutually repulsive, cylindrical 'springs' in the neuron, a hypothesis supported by analysis and simulation of NF distributions from whole neurons (Kumar S, Yin X, Trapp BD, Paulaitis ME, Hoh JH, unpublished data). This approach has also recently been extended to microtubule-associated proteins, which are believed to contribute to microtubule spacing through a similar mechanism (27). AFM has also been used to characterize the structural and mechanical properties of

keratin, lending insight into the microstructural origin of the great tensile strength of hair (28).

Cytoskeletal filaments in situ and cell mechanics

The ability of AFM to image samples in aqueous environments and without fixation or staining has been exploited to interrogate living cells and measure changes in cytoskeletal structure and mechanics. The pioneering work of Henderson and colleagues demonstrated that the actin cytoskeleton and subcellular organelles may be imaged without apparent harm to the cell (Figure 5D) (29). The first of these studies used AFM to image a meshlike network in the cell, demonstrating that this was the actin cytoskeleton by correlating it with fluorescence signals from rhodamine-phalloidin stained cells. A later study focused specifically on glial cells, demonstrating that the AFM tip could be used to mechanically manipulate glia and even sever glial processes without killing the cells (30). It also pushed the limits of resolution for subcellular structures, presenting images of the nucleus and mitochondria. Additional studies have examined cytoskeletal dynamics. In one such study (31), the authors used time-lapse imaging to observe extension and withdrawal of lamellipodia, changes in cell shape, and vesicle-like structures traveling along cytoskeletal fibers. Perhaps most strikingly, the authors observed ripple-like cytoskeletal rearrangements propagating both radially outward from the nucleus and around the edge of the cell.

In addition to its importance in trafficking, the cytoskeleton also forms the structural framework which determines cell shape and mechanical properties. Therefore, using AFM to examine cell mechanics can provide insight into cytoskeletal properties. There are many published attempts to use both force curves and spatially resolved force mapping to extract cellular elasticity (32). The recent work of Radmacher and colleagues combines AFM imaging, fluorescence microscopy, and elasticity mapping. Two reports focused on stress fibers and the formation of lamellipodial extensions. The first showed that relative to stably adhered regions of the cell, the active edges of migrating fibroblasts showed greater height fluctuations and higher elasticity with time (33). A more recent study examined the effect of cytoskeletal drugs on cell mechanics. Addition of actin-targeted drugs (cytochalasins B and D and latrunculin A) softened the cell and caused disruption of stress fibers, whereas microtubule targeted drugs (colchicine, colcemide, taxol) produced no morphological or mechanical changes (34). These results illustrate that AFM can be used both to manipulate cells nondestructively and to record cytoskeletal dynamics in real time. Future studies should continue to sharpen spatial and force resolution as well as the biochemical specificity of perturbations and measurements.

Vesicular Transport

The interaction of a transport vesicle with its target membrane is thought to proceed through an orderly series of

events that includes docking, membrane apposition, and ultimately fusion. In many cases, fusion is triggered by discrete events of short time scale such as intracellular calcium release (35). Thus, there is significant interest in learning about vesicle structure at different stages of fusion as well as structural changes induced by soluble effectors. While much valuable insight into the molecular structure of these vesicles has been gained from EM (36), mechanical properties and dynamics are not directly accessible. Here, AFM has yielded new insight, complementing the contributions of established technologies. We again divide AFM studies in this area into two groups: studies with reconstituted systems, and studies with intact biological vesicles.

Reconstituted vesicle systems

Much effort has been devoted to using AFM to study vesicles reconstituted from phospholipids. The underlying paradigm is that reconstituted lipid vesicles serve as well-understood and readily manipulated models of cellular transport vesicles. In one of the first AFM studies of lipid vesicles in buffer, phosphatidylcholine/cholesterol vesicles presenting human IgG were adsorbed onto a gold surface coated with antihuman IgG (37). Contact-mode AFM imaging revealed a heterogeneous surface coated with 80–120-nm-high protrusions interpreted to be individual vesicles. A key finding to emerge from this work was that the lateral resolution of vesicles depends strongly on tip–vesicle contact pressure and lateral shear force, which in turn depends on imaging force and probe dimensions. This complication presents a central technical challenge to AFM imaging of vesicles. In a later study, biotinylated vesicles were adsorbed to an avidin-coated mica surface (38). This study further defined the relationship between imaging forces and observed vesicle morphology and also showed that with increasing vesicle biotinylation, the vesicles may be induced to spread, flatten, and ultimately rupture.

Other studies have focused on characterizing both vesicle substructure and interactions between vesicles. For example, two recent reports presented images of adsorbed, flattened vesicles containing central protrusions. In the first, these structures were detected as transient intermediates in the formation of planar supported bilayers (39). In the second, they were found adsorbed to planar supported bilayers, suggesting that such structures might form during the early stages of vesicle-bilayer fusion (40). The latter study used elasticity mapping to show that the adsorbed vesicles were substantially softer than the underlying bilayer, and also showed the characteristic flat contact interface formed by coadsorbed vesicles, a structural feature previously appreciated only by EM (Figure 6A). Finally, several studies have addressed the mechanism of formation of supported lipid bilayers from the adsorption of small unilamellar vesicles (41–43).

Intact biological vesicles

The properties of biological transport vesicles are less well understood than those of reconstituted vesicles, and the literature of AFM studies of these systems is more limited. Nonetheless, several important strides have been made towards using AFM to characterize these vesicles. In one early report, the authors performed contact mode imaging on cholinergic synaptic vesicles isolated from *Torpedo californica* in air and in buffer (44). In addition to providing valuable proof of principle, this study also showed that one could induce and measure height changes in the vesicles by changing the osmolarity of the solution. Another group performed force spectroscopy and mapping on these vesicles (Figure 6B) (45). Here, the authors showed that the centers of the vesicles were considerably stiffer than their peripheries, and that this center stiffness increases with calcium concentration. EM had already established the presence of 'electron-dense' features at the center of these vesicles, and biochemical studies had established that the centers are proteoglycan-rich. Based on this finding, the authors hypothesized that the calcium binds and cross-links these proteoglycans, producing a stiff, centrally located network.

In addition to simple changes in ionic strength and calcium concentration, vesicular shape changes in response to nucleoside triphosphates have also been studied (46). Here, the authors used zymogen granules (ZGs), secretory vesicles which fuse with the plasma membrane in a GTP-dependent manner. When GTP was added *in situ* to ZGs, the authors observed a 15–25% increase in vesicle height. The authors then hypothesized that the GTP triggers activation of ion channels through heterotrimeric G-proteins.

Receptor–Ligand Interactions

Vesicle docking and fusion *in vivo* require the presence of specific receptor–ligand interactions. Indeed, protein trafficking, antigen processing and presentation, and virtually all other processes of intracellular transport depend on the recognition of ligands by their receptors. The AFM is capable of measuring forces on the piconewton scale, a property that has been exploited to examine receptor–ligand interactions. Molecular recognition is also increasingly being explored as a mechanism of imaging contrast. The vast majority of work in this area has addressed interactions between purified and reconstituted binding partners; an emerging body of literature attempts to extend the application of AFM to measure and characterize these interactions in the context of whole cells.

Pure component receptor-ligand systems

A wide range of receptor-ligand pairs have been studied by AFM. The first studies focused on very high-affinity interactions, particularly that between biotin and avidin (47–49). Typically, streptavidin is anchored to the AFM tip, often by pretreating the tip with biotinylated bovine serum albumin (BSA-biotin). Correspondingly, the substrate is coated with biotin, often as BSA-biotin or by adsorbing biotinylated agarose beads. One then obtains and analyzes force curves. Upon tip–sample approach, the tip and surface bind one another through biotin-avidin recognition. When the tip is re-
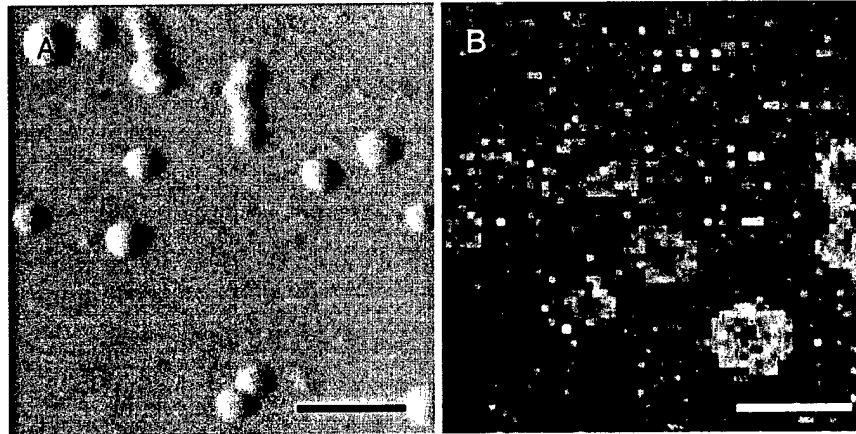
Figure 6: AFM of vesicles. (A) Reconstituted vesicles. This deflection image shows phospholipid-cholesterol vesicles adsorbed to a planar bilayer (40). Where vesicles have coadsorbed, a flat contact interface is seen, characteristic of mutually deformed vesicles (bar is 250 nm) (reprinted with permission, © 2000, American Chemical Society). (B) Cholinergic synaptic vesicles (45). This elasticity map was acquired by taking an array of force curves over the surface, analyzing each curve to obtain the local elastic modulus, and mapping the resulting values (bar is 250 nm). In this map, lighter values correspond to areas of low elasticity (stiffness). Each circular region is a single vesicle; the dark vesicular centers imply that the core is stiffer than the periphery (reproduced with permission, © 1997, Biophysical Society).

tracted, it detaches from the surface in a series of discrete jumps, each corresponding to breakage of one or more biotin-avidin contacts (Figure 7A). Soluble binding inhibitors are often used to demonstrate binding specificity; if the measured adhesion is indeed due to receptor–ligand interactions, addition of an inhibitor to the AFM sample chamber should significantly reduce the binding frequency. The total jump-off force is expected to consist of an integral multiple of the single-pair rupture force. Therefore, by constructing a histogram of rupture forces and determining its period, the single-pair unbinding force may be obtained (50).

As understanding and interpretation of these experiments has improved, attention has shifted away from these model systems to a wide variety of binding partners. Antigen–antibody interactions have served as a particular point of interest. By probing a human serum antigen (HSA)-covered surface with an anti-HSA-functionalized tip, Hinterdorfer and coworkers spatially mapped the location of single surface-bound HSA molecules through adhesion measurements (51). Ros and colleagues used a similar approach to study the effect of point mutations on the binding affinity of fluorescein to the variable region of its cognate antibody (52). Other examples of receptor–ligand pairs under study include ferritin/antiferritin (53), P-selectin/ligand (54) and cadherin/cadherin (55) (Figure 7B). While AFM is clearly a useful tool for detecting the presence of bonds and changes in binding strength, the measured force and energy of bond breakage depend strongly on the rate at which the bond is loaded, as well as a host of other complicating factors (56). Thus, great care must be taken in extracting thermodynamic parameters of bonds from AFM measurements. Willemsen et al. provide an extensive overview of AFM binding studies in which they address such issues and describe many of the other receptor-ligand systems under study (57).

Whole-cell systems

A growing body of research seeks to translate *in vitro* AFM measurements of receptor-ligand binding to systems of whole cells. One of the first of these studies, conducted by Gad et al., sought to map the distribution of polysaccharides on the cell walls of yeast (58). Here, the authors used gold-thiol chemistry to functionalize AFM tips with concavalin A (conA), a lectin which recognizes mannose residues on the yeast cell wall. They then obtained force curves on yeast cells under buffer. While they were unable to spatially resolve the distribution of receptors, they did measure 100–500 pN adhesive forces over cells that could be abolished by adding free mannose. Later work with the conA system showed that chemical cross-linking of the receptors produced marked increases in unbinding forces to an extent that is consistent with cooperative binding (59). Another effort from Lehenkari and Horton (60) took this approach to map integrin distributions on osteoclasts using AFM tips modified with various Arg-Gly-Asp (RGD)-containing peptides. This study showed that RGD-integrin binding depends on a highly specific manner on the peptide context in which the RGD tripeptide is presented, confirming long-standing results from solution assays. A long-term technological goal of receptor-ligand measurements on cells is to develop nondestructive methods for cell identification and sorting. An excellent example of such a study used AFM to type red blood cells (61). The authors probed a mixed monolayer of type-A and O blood cells using a lectin which binds the glycolipids on type-A erythrocytes. Using force mapping, the authors successfully discriminated between the two cell types based on forces of adhesion.

Conclusions and Future Directions

AFM has already demonstrated its utility as a way of acquiring high-resolution images and force measurements of bio-
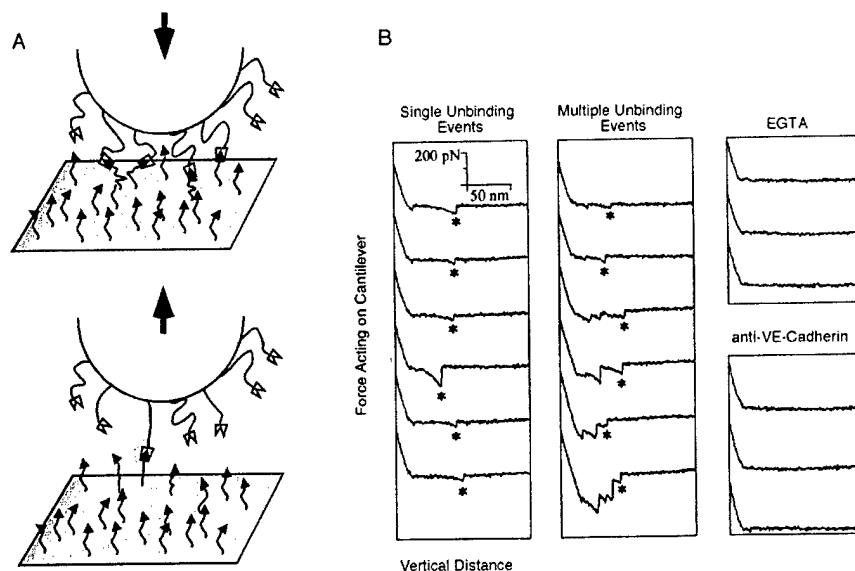
Figure 7: AFM measurements of receptor–ligand interactions. (A) Schematic of typical experiment. A receptor is covalently linked to the AFM probe (shown here as a sphere), often via a flexible linker. Similarly, the cognate ligand is anchored to the substrate. On tip–sample approach (top), several bonds are formed between the two surfaces. On retraction (bottom), each bond is broken in sequence, producing a discrete sawtooth-like deflection of the cantilever. When only one bond is formed, a single sawtooth is observed; when multiple bonds are formed, multiple events are observed, with the final sawtooth corresponding to rupture of the final bond (highlighted). This final deflection provides information about single receptor–ligand interactions. (B) Experimental data for cadherin dimerization. Here, cadherin monomers were adsorbed to the tip and substrate, and many force curves were obtained. The left panel depicts instances in which only one bond formed and ruptured, and the middle panel depicts cases in which multiple bonds formed and ruptured. The asterisks (*) correspond to single pair interactions. The right panel shows that these sawtooth features are attenuated in the presence of EGTA or an anticadherin antibody, implying that these events are specifically due to cadherin–cadherin interactions (55) (Figure reproduced with permission, © 2000 National Academy of Sciences, USA).

logical structures in a near-native environment. In some cases, this rapidly growing body of work has served to verify long-standing results from traditional methods; in others, it has uncovered novel phenomena that provide new insight. This is certainly true in areas relevant to intracellular transport. Here, we have reviewed recent efforts to apply AFM to the study of intracellular trafficking, with a particular focus on cytoskeletal structure and dynamics, vesicular transport, and receptor–ligand interactions. It should be clear that while AFM holds enormous potential to contribute in these areas, much room for improvement remains. First, more effort will likely be devoted to improving the integration of AFM with other techniques, particularly light microscopy. Efforts to combine the power of single molecule fluorescence with single molecule force spectroscopy are particularly exciting. Second, there is ongoing work aimed at developing increasingly versatile and sophisticated tools for the analysis of AFM images and force curves. Third, in terms of improving canti-lever performance, much attention continues to be paid to the microfabrication of smaller cantilevers with much higher resonance frequencies (62,63). Much effort has also been put into establishing robust and efficient methods of chemi-cal functionalization of tips. Fourth, improvements in instru-mental design are proceeding rapidly. There is a particularly intense focus on developing instruments with faster and

more convenient sample transfer and exchange of solutes, with a long-term emphasis on automation. Finally, to fully harness its potential in the biological sciences, more exten-sive efforts are needed to train life scientists in the theory, practice, and data analysis of AFM. As these areas continue to be addressed, AFM should become more widely used to directly investigate cells and subcellular elements. These ef-forts will help narrow the gap between our knowledge of the identities of the molecules that drive cell biological phenom-ena and the physical forces that govern their actions.

Acknowledgments

References

1. Martin Y, Williams CC, Wickramasinghe HK. Atomic force microscope force mapping and profiling on a sub 100-Å scale. J Appl Phys 1987;61:4723–4729.
2. Raab A, Han WH, Badt D, Smith-Gill SJ, Lindsay SM, Schindler H,

Hinterdorfer P. Antibody recognition imaging by force microscopy. Nat Biotechnol 1999;17:902–905.

3. Cleveland JP, Anczykowski B, Schmid AE, Elings VB. Energy dissipation in tapping-mode atomic force microscopy. Appl Phys Lett 1998;72:2613–2615.

4. Czajkowsky DM, Allen MJ, Elings V, Shao ZF. Direct visualization of surface charge in aqueous solution. Ultramicroscopy 1998;74:1–5.

5. Heinz WF, Hoh JH. Spatially resolved force spectroscopy of biological surfaces using the atomic force microscope. Trends Biotechnol 1999;17:143–150.

6. Rief M, Gautel M, Oesterhelt F, Fernandez JM, Gaub HE. Reversible unfolding of individual titin immunoglobulin domains by AFM. Science 1997;276:1109–1112.

7. Marszalek PE, Pang YP, Li HB, El Yazal J, Oberhauser AF, Fernandez JM. Atomic levers control pyranose ring conformations. Proc Natl Acad Sci USA 1999;96:7894–7898.

8. Clausen-Schaumann H, Rief M, Tolksdorf C, Gaub HE. Mechanical stability of single DNA molecules. Biophys J 2000;78:1997–2007.

9. Fisher TE, Oberhauser AF, Carrion-Vazquez M, Marszalek PE, Fernandez JM. The study of protein mechanics with the atomic force microscope. Trends Biochem Sci 1999;24:379–384.

10. Keller DJ, Chou CC. Imaging steep, high structures by scanning force microscopy with electron-beam deposited tips. Surf Sci 1992;268: 333–339.

11. Skarman B, Wallenberg LR, Jacobsen SN, Helmersson U, Thelander C. Evaluation of intermittent contact mode AFM probes by HREM and using atomically sharp CeO_2 ridges as tip characterizer. Langmuir 2000;16:6267–6277.

12. Hafner JH, Cheung CL, Oosterkamp TH, Lieber CM. High-yield assembly of individual single-walled carbon nanotube tips for scanning probe microscopies. J Phys Chem B 2001;105:743–746.

13. Wong SS, Woolley AT, Odom TW, Huang JL, Kim P, Vezenov DV, Lieber CM. Single-walled carbon nanotube probes for high-resolution nanostructure imaging. Appl Phys Lett 1998;73:3465–3467.

14. Mathur AB, Truskey GA, Reichert WM. Atomic force and total internal reflection fluorescence microscopy for the study of force transmission in endothelial cells. Biophys J 2000;78:1725–1735.

15. Kamal A, Goldstein LSB. Connecting vesicle transport to the cytoskeleton. Curr Opin Cell Biol 2000;12:503–508.

16. Okamoto CT, Forte JG. Vesicular trafficking machinery, the actin cytoskeleton, and H+-K+-ATPase recycling in the gastric parietal cell. J Physiol (Lond) 2001;532:287–296.

17. Schmidt A, Hall MN. Signaling to the actin cytoskeleton. Annu Rev Cell Dev Biol 1998;14:305–338.

18. Vater W, Fritzsche W, Schaper A, Bohm KJ, Unger E, Jovin TM. Scanning force microscopy of microtubules and polymorphic tubulin assemblies in air and in liquid. J Cell Sci 1995;108:1063–1069.

19. Vinckier A, Dumortier C, Engelborghs Y, Hellemans L. Dynamical and mechanical study of immobilized microtubules with atomic force microscopy. J Vac Sci Technol B 1996;14:1427–1431.

20. Kacher CM, Weiss IM, Stuart RJ, Schmidt CF, Hansma PK, Radmacher M, Fritz M. Imaging microtubules and kinesin decorated microtubules using tapping mode atomic force microscopy in fluids. Eur Biophys J 2000;28:611–620.

21. Buguin A, Du Roure O, Silberzan P. Active atomic force microscopy cantilevers for imaging in liquids. Appl Phys Lett 2001;78:2982–2984.

22. Fritz M, Radmacher M, Cleveland JP, Allersma MW, Stewart RJ, Gieselmann R, Janmey P, Schmidt CF, Hansma PK. Imaging globular and filamentous proteins in physiological buffer solutions with tapping mode atomic force microscopy. Langmuir 1995;11:3529–3535.

23. Shi D, Somlyo AV, Somlyo AP, Shao Z. Visualizing filamentous actin on lipid bilayers by atomic force microscopy in solution. J Microsc 2001;201:377–382.

24. Bustamante C, Erie DA, Keller D. Biochemical and structural applications of scanning force microscopy. Curr Opin Struct Biol 1994;4: 750–760.

25. Shao ZF, Shi D, Somlyo AV. Cryoatomic force microscopy of filamentous actin. Biophys J 2000;78:950–958.

26. Brown HG, Hoh JH. Entropic exclusion by neurofilament sidearms: a mechanism for maintaining interfilament spacing. Biochemistry 1997;36:15035–15040.

27. Mukhopadhyay R, Hoh JH. AFM force measurements on microtubule-associated proteins: the projection domain exerts a long-range repulsive force. FEBS Lett 2001;in press.

28. Parbhu AN, Bryson WG, Lal R. Disulfide bonds in the outer layer of keratin fibers confer higher mechanical rigidity: correlative nano-indentation and elasticity measurement with an AFM. Biochemistry 1999;38:11755–11761.

29. Henderson E, Haydon PG, Sakaguchi DS. Actin filament dynamics in living glial cells imaged by atomic force microscopy. Science 1992;257:1944–1946.

30. Parpura V, Haydon PG, Henderson E. 3-dimensional imaging of living neurons and glia with the atomic force microscope. J Cell Sci 1993;104:427–432.

31. Schoenenberger CA, Hoh JH. Slow cellular-dynamics in MDCK and R5 cells monitored by time-lapse atomic force microscopy. Biophys J 1994;67:929–936.

32. Vinckier A, Semenza G. Measuring elasticity of biological materials by atomic force microscopy. FEBS Lett 1998;430:12–16.

33. Rotsch C, Jacobson K, Radmacher M. Dimensional and mechanical dynamics of active and stable edges in motile fibroblasts investigated by using atomic force microscopy. Proc Natl Acad Sci USA 1999;96: 921–926.

34. Rotsch C, Radmacher M. Drug-induced changes of cytoskeletal structure and mechanics in fibroblasts: an atomic force microscopy study. Biophys J 2000;78:520–535.

35. Brunger AT. Structural insights into the molecular mechanism of calcium-dependent vesicle-membrane fusion. Curr Opin Struct Biol 2001;11:163–173.

36. Mironov AA, Polishchuk RS, Luini A. Visualizing membrane traffic *in vivo* by combined video fluorescence and 3D electron microscopy. Trends Cell Biol 2000;10:349–353.

37. Shibata-Seki T, Masai J, Tagawa T, Sorin T, Kondo S. *In situ* atomic force microscopy study of lipid vesicles adsorbed on a substrate. Thin Solid Films 1996;273:297–303.

38. Pignataro B, Steinem C, Galla HJ, Fuchs H, Janshoff A. Specific adhesion of vesicles monitored by scanning force microscopy and quartz crystal microbalance. Biophys J 2000;78:487–498.

39. Jass J, Tjarnhage T, Puu G. From liposomes to supported, planar bilayer structures on hydrophilic and hydrophobic surfaces: an atomic force microscopy study. Biophys J 2000;79:3153–3163.

40. Kumar S, Hoh JH. Direct visualization of vesicle-bilayer complexes by atomic force microscopy. Langmuir 2000;16:9936–9940.

41. Egawa H, Furusawa K. Liposome adhesion on mica surface studied by atomic force microscopy. Langmuir 1999;15:1660–1666.

42. Muresan AS, Lee KYC. Shape evolution of lipid bilayer patches adsorbed on mica: an atomic force microscopy study. J Phys Chem B 2001;105:852–855.

43. Reviakine I, Brisson A. Formation of supported phospholipid bilayers from unilamellar vesicles investigated by atomic force microscopy. Langmuir 2000;16:1806–1815.

44. Parpura V, Doyle RT, Basarsky TA, Henderson E, Haydon PG. Dynamic imaging of purified individual synaptic vesicles. Neuroimage 1995;2:3–7.

45. Laney DE, Garcia RA, Parsons SM, Hansma HG. Changes in the elastic properties of cholinergic synaptic vesicles as measured by atomic force microscopy. Biophys J 1997;72:806–813.

46. Jena BP, Schneider SW, Geibel JP, Webster P, Oberleithner H, Sritharan KC. G$_i$ regulation of secretory vesicle swelling examined by atomic force microscopy. Proc Natl Acad Sci USA 1997;94:13317–13322.

47. Florin EL, Moy VT, Gaub HE. Adhesion forces between individual ligand-receptor pairs. Science 1994;264:415–417.

48. Moy VT, Florin EL, Gaub HE. Intermolecular forces and energies between ligands and receptors. Science 1994;266:257–259.

49. Lee GU, Kidwell DA, Colton RJ. Sensing discrete streptavidin biotin interactions with atomic-force microscopy. Langmuir 1994;10:354–357.

50. Hoh JH, Cleveland JP, Prater CB, Revel JP, Hansma PK. Quantized adhesion detected with the atomic force microscope. J Am Chem Soc 1992;114:4917–4918.

51. Hinterdorfer P, Baumgartner W, Gruber HJ, Schilcher K, Schindler H. Detection and localization of individual antibody-antigen recognition events by atomic force microscopy. Proc Natl Acad Sci USA 1996;93:3477–3481.

52. Ros R, Schwesinger F, Anselmetti D, Kubon M, Schafer R, Pluckthun A, Tiefenauer L. Antigen binding forces of individually addressed single-chain Fv antibody molecules. Proc Natl Acad Sci USA 1998;95:7402–7405.

53. Allen S, Chen XY, Davies J, Davies MC, Dawkes AC, Edwards JC, Roberts CJ, Sefton J, Tendler SJB, Williams PM. Detection of antigen-antibody binding events with the atomic force microscope. Biochemistry 1997;36:7457–7463.

54. Fritz J, Katopodis AG, Kolbinger F, Anselmetti D. Force-mediated kinetics of single P-selectin/ligand complexes observed by atomic force microscopy. Proc Natl Acad Sci USA 1998;95:12283–12288.

55. Baumgartner W, Hinterdorfer P, Ness W, Raab A, Vestweber D, Schindler H, Drenckhahn D. Cadherin interaction probed by atomic force microscopy. Proc Natl Acad Sci USA 2000;97:4005–4010.

56. Merkel R, Nassoy P, Leung A, Ritchie K, Evans E. Energy landscapes of receptor-ligand bonds explored with dynamic force spectroscopy. Nature 1999;397:50–53.

57. Willemsen OH, Snel MME, Cambi A, Greve J, De Grooth BG, Figdor CG. Biomolecular interactions measured by atomic force microscopy. Biophys J 2000;79:3267–3281.

58. Gad M, Itoh A, Ikai A. Mapping cell wall polysaccharides of living microbial cells using atomic force microscopy. Cell Biol Int 1997;21:697–706.

59. Chen A, Moy VT. Cross-linking of cell surface receptors enhances cooperativity of molecular adhesion. Biophys J 2000;78:2814–2820.

60. Lehenkari PP, Horton MA. Single integrin molecule adhesion forces in intact cells measured by atomic force microscopy. Biochem Biophys Res Commun 1999;259:645–650.

61. Grandbois M, Dettmann W, Benoit M, Gaub HE. Affinity imaging of red blood cells using an atomic force microscope. J Histochem Cytochem 2000;48:719–724.

62. Walters DA, Cleveland JP, Thomson NH, Hansma PK, Wendman MA, Gurley G, Elings V. Short cantilevers for atomic force microscopy. Rev Sci Instrum 1996;67:3583–3590.

63. Hodges AR, Bussmann KM, Hoh JH. Improved atomic force microscope cantilever performance by ion beam modification. Rev Sci Instrum 2001;in press.

Review

Predicting properties of intrinsically unstructured proteins

Joanne N. Bright[a], Thomas B. Woolf[a,b,c], Jan H. Hoh[a,d,*]

[a] *Department of Physiology, School of Medicine, Johns Hopkins University, 725 N. Wolfe Street,
Baltimore, MD 21205, USA*
[b] *Department of Biophysics, School of Medicine, Johns Hopkins University, 725 N. Wolfe Street,
Baltimore, MD 21205, USA*
[c] *Department of Biomedical Engineering, School of Medicine, Johns Hopkins University, 725 N. Wolfe Street,
Baltimore, MD 21205, USA*
[d] *Department of Chemical Engineering, Johns Hopkins University, Baltimore, MD 21218, USA*

Abstract

There is increasing evidence that intrinsically unstructured proteins or protein domains have important biological functions. These types of proteins may be productively analyzed using polymer theory developed to predict global physical properties of polymers. In these theories molecular detail is "coarse grained" out of the models, and replaced with a small number of parameters that characterize the polymer. This reduction in complexity allows extremely large systems to be studied. In the case of simulations, the time scales accessible also increase significantly. Here we discuss the application of polymer theory to unstructured proteins, and consider how to classify proteins within a polymer framework. We then review polymer theory that is relevant to predicting functionally important properties, such as radius of gyration, height of a polymer brush and force required to compress a polymer brush. © 2001 Elsevier Science Ltd. All rights reserved.

Keywords: Polymer theory; Protein structure

Contents

*Corresponding author. Tel.: +1-410-614-3795; fax: +1-410-614-3797.
E-mail address: jhoh@jhmi.edu (J.H. Hoh).

Nomenclature

α	expansion factor
b	bead size (also B)
c	polymer segment concentration (context dependent)
c_s	added salt concentration (context dependent)
C_∞	long time correlation between beads
$C(r)$	local segment concentration (function of r)
χ	Flory interaction parameter
D_P	protein diffusion constant
d	grafting distance between molecules in a brush
e	charge (valence)
ε_{crit}	critical concentration
ε	dielectric constant
f	fraction of segments with net charge
f_c	critical charge fraction (for collapse)
F	free energy
G	intrinsic screening length
γ	semi-flexible angle (depends on context)
γ	surface tension (depends on context)

Γ	ratio of electrostatic to thermal effects
H	brush height
h	distance between two brush surfaces
k_B	Boltzmann constant
κ	inverse Debye screening length
κ_b	inverse screening length in the bulk
L	fully extended length of chain
l_p or l_{p0}	persistence length
l_B	Bjerrum length
l_{pe}	electrostatic persistence length
N	number of segments (also n)
v	2nd virial coefficient
μ	solvent dependent exponent
Π	osmotic pressure
P	probability distribution of the end-to-end vector
P_p	pressure
ω	3rd virial coefficients
ω_{PB}	grand Poisson–Boltzmann free energy
ϕ	site occupation fraction
r	position along chain
R_g	radius of gyration
R_N	end-to-end distribution (N; index for polymer length)
R_{probe}	radius of probing surface
s	contour length along chain
σ	charge asymmetry parameter (depends on context)
σ	grafting density ($\sigma^{-1/2} = d$) (depends on context)
T	temperature (also t for effective temperature)
Θ	sequence order parameter
ξ	electrostatic blob size
z	excluded volume parameter
ψ	electrostatic potential (reduced units)

1. Introduction

In recent years there has been an increased interest in intrinsically unstructured proteins, that is proteins that in their natural state do not adopt stable, folded structures. This interest arises in part from recent suggestions that unstructured proteins may have functions that derive from the lack of structure. Such proteins, or protein domains, may be usefully described by the well-established theories of polymer physics, developed for the description of large macromolecules by means of their statistical properties. Here we review some of the existing polymer theory that is relevant to unstructured proteins. The theory is presented in a general biophysical framework that is intended to be accessible to the protein biochemistry community and also presents problems that represent an important area for polymer theory development. We do not attempt to be

exhaustive, rather our purpose is to be illustrative. It is hoped that this will provide a suitable basis for further experimental and theoretical efforts in describing the properties of intrinsically unstructured proteins.

Early studies of proteins often focused on their general colloidal and polymeric properties, such as monomer composition, viscosity and hydrodynamic radii. However, the ability to crystallize proteins and the subsequent emergence of highly detailed three-dimensional structures from crystallographic data deflected interest from these approaches and led to the structure–function paradigm. That paradigm, in which the function of a protein is directly related to its folded structure, has dominated thinking about protein function for more than 50 years. The structure–function paradigm has been extraordinarily successful in revealing precise mechanisms of action for thousands of proteins. Unstructured proteins and protein domains were known to exist from a range of early biophysical studies (see review in Dunker, 2001). However, such unstructured proteins were widely ignored from a functional standpoint. One of the rare early examples, with which we are familiar, where a function was directly attributed to a protein being unstructured was in the case of casein, where the unstructured κ-casein molecule was thought to colloidally stabilize casein micelles (Walstra et al., 1981; Walstra and Jenness, 1984; De Kruif and Zhulina, 1996).

More recently there have been a number of functions proposed for unstructured polypeptide domains (Dunker et al., 2001; Wright and Dyson, 1999; Hoh, 1998). For example, Dunker and colleagues have proposed that fd phage penetration involves a disordered state of the coat protein (Dunker et al., 1991), and Wright and colleagues have proposed that unstructured regions of the p21 protein confer molecular plasticity with regard to binding partners (Kriwacki et al., 1996). Our interest in this area is motivated by the finding that parts of neurofilament proteins give rise to a very long-range force that is consistent with a polymer brush like force that is predominantly entropic in origin (Brown and Hoh, 1997), and a similar finding for microtubule associated proteins (Mukhopadhyay and Hoh, 2001). This suggests that these protein domains are largely unstructured, and provides a mechanism by which neurofilament and microtubule spacing is maintained. In analogy to an end-attached (grafted) polymer, the unstructured chain would be expected to rapidly explore a large conformational space and exert a repulsive entropic force on incoming molecules: a mechanism capable of being both size and charge selective depending upon the properties of the chain and the approaching particle. That in turn leads to the notion that the unstructured neurofilament protein domains might contribute functionally important mechanical properties to axons. The term entropic bristle (Hoh, 1998) was used to denote an individual unstructured protein domain of the type proposed for neurofilaments, based on the idea that many bristles make up a brush (Fig. 1). For such systems chain flexibility would be highly desirable, while backbone polarity and charge could be instrumental in success or failure of the mechanism (e.g. through collapse of the chain). It was further noted that entropic bristles might be very widespread, and that the ability to regulate bristles could be involved in controlling protein–protein interactions (Hoh, 1998).

Polymer models have significant advantages in the characterization of unstructured proteins/ polypeptides (UPs). The highly detailed calculations commonly used to understand the structure of folded proteins are limited by existing computational capabilities and are intractable to analytic solution. Polymer theories (Flory, 1969; de Gennes 1971; Doi and Edwards, 1986) are based on models with significantly less detail and lend a degree of simplicity, in the sense that the global properties may be extracted in a more intuitive manner (Fig. 2). Moreover, polymer theories have
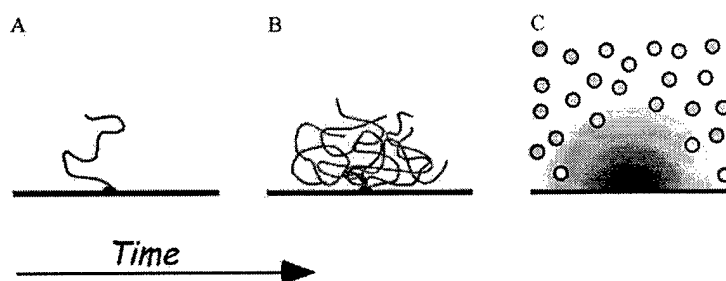
Fig. 1. Schematic representation of an entropic bristle. The notion of an entropic bristle domain in a protein is based on the idea that part of the protein is largely unstructured, and has properties in common with an unstructured polymer chain attached to a surface. Such a polymer has a random configuration at any point in time (A), but is in rapid Brownian motion and quickly explores a large number of the configurations available to it (B). This rapid motion allows the polymer to exclude many molecules (such as proteins) and large structures (such as an AFM tip) that impinge on it, through what is effectively an entropic force (C).

been developed to determine common properties applicable to a given class. The properties of a given polymer chain may be determined via a few universal properties, rather than attempting to account for specific and sometimes unknown characteristics for each system of study. While less detailed than an all-atom model, polymer theories do provide the ability (within limits) to add detail at the desired level of complexity. There is thus the possibility of models ranging from an extremely coarse-grained bead-spring level to those incorporating some of the specific details (e.g. through angle constraints, segmental shape and size, explicit solvent, etc). Simulations and other numerical approaches in particular have flexibility in balancing runtime with the required level of detail.

Theoretical approaches of the kind considered here have already proved useful in many areas of biology, contributing to our understanding of DNA (Grosberg, 1979; Ubbink and Odijk, 1995; Bloomfield, 1991), colloidal stabilization (Napper, 1983; Leermakers et al., 1996; Dickinson and Stainsby, 1982), biomembranes (Lipowsky, 1995; Goulian et al., 1993) and chromosomal systems (Marko and Siggia, 1997). Polymer frameworks have also been widely applied to gain insights into the protein folding problem (Timoshenko et al., 1996; Creighton, 1992; Dill, 1990; Sfatos et al., 1993). They have been applied rarely to the description of intrinsically or natively unstructured proteins, where the focus has been on a structured native state and the manner in which it is achieved. Where polymer theories have proved most instructive is in the reduction of complex systems possessing many variables and parameters to comparatively simple ones that still reproduce the behavior of the system as a whole. As with all theoretical efforts, their validity rests on reproducibility of experimentally observed results. In many cases good qualitative and quantitative agreement can be found, when the global properties of the system reflect non-specific effects. In others, particularly in the achievement of specific folded structures, they have been less successful. In the description of unstructured proteins, however, there is much to be gained.

The most important characteristic of the proteins at which this paper is aimed is that they are intrinsically unstructured (unfolded) and have persisted through the evolutionary process due to the properties they possess in their unstructured state. Studies of the sequences of unstructured proteins suggest that they may have common features that account for their properties. Dunker, Obradovic and colleagues trained a neural network based computer program on a set of
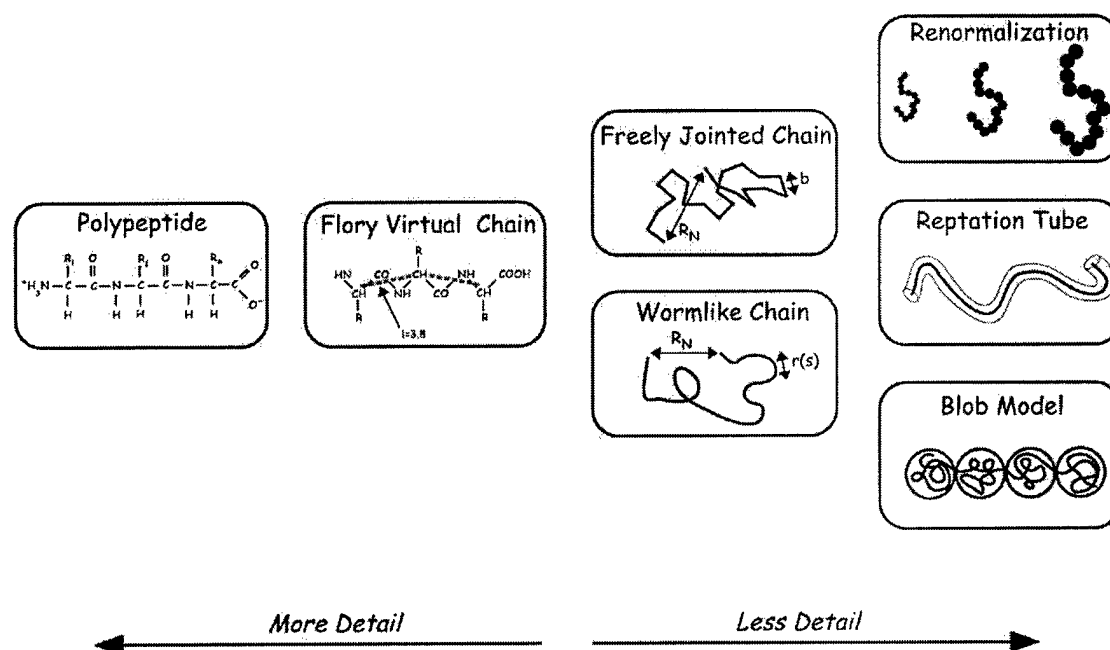
Fig. 2. Treating a protein chain in a general polymer framework. The sequence of amino acids in the protein chain are first converted into a virtual chain, where detailed information about the atoms in each amino acids is reduced to a small number of aggregate properties in a virtual monomer. Such virtual chains then form the basis for basic polymer models such as the freely jointed chain and the wormlike chain. These basic models are in turn the basis for higher order models and methods for treating the statistical properties of polymers.

unstructured sequences selected based on their absence in protein crystal structures, and used this program to predict that there are more than 1000 proteins with long unstructured regions in the SWISS-PROT protein data base (Romero et al., 1998). Analysis of these sequences reveal that they tend to be of low complexity. Furthermore, they show a tendency to be over-represented in polar or charged amino acids and under-represented in hydrophobic amino acids (Garner et al., 1998). This is consistent with an analysis of an independent set of unstructured protein sequences identified by considering a range of biophysical measurements (Uversky et al., 2000).

This paper presents a review of polymer theories relevant to unstructured polypeptides. The first section is directed at the characterization of a given polypeptide chain in solution under various external conditions (such as pH, temperature, solution properties) within polymeric models, while the latter parts of the paper deal with exclusion properties of tethered proteins and interaction events. We conclude with a brief summary.

2. Polymer classification of a protein sequence

Polypeptides are characterized by the repeating structural motif: the chain is made up of repeating α-amino acid residues (monomers) –NH–CHR–CO– and terminated by amino and

carboxyl groups at the two ends (Fig. 2). A detailed representation of the conformations of the polypeptide chain (for example, one leading to a native folded structure) would thus incorporate all the permitted C–C bond (ψ) and C_α–N bond (φ) angles, the rigid planar peptide bonds, the number, size, charge and polarity of the –R groups, etc. This approach is analytically intractable and computationally highly expensive. The aim in applying polymer theory to the problem is to overcome this complexity, and for a given a sequence of amino acid residues "coarse grain" out all but those details which alter the average properties of the sequence as a whole. This amounts to an increasing primary length scale as the complexity is reduced and a corresponding gain in the time scales accessible in simulations. The number of length scales is determined by the system, ranging from a single primary scale for the simplest neutral systems, to several for systems involving electrostatic and other long-range forces. Three intrinsic properties of the chain that are particularly important for an appropriate description via polymer principles are flexibility, charge and chemical interaction with solvent (e.g. hydrophobicity), properties determined by the nature of the –R groups.

There are several general polymer categories for which theory has been developed. One division of theories considers primarily charge, classifying polymers as neutral, polyelectrolyte or polyampholyte. Another major division deals with the monomer order and classifies polymers as homopolymers, co-polymers, block co-polymers or heteropolymers. To apply the theory appropriately, different proteins must be mapped into these categories based on their sequence. Such a mapping is shown in Fig. 3. There we fabricate a number of hypothetical protein sequences and show the appropriate classification of those sequences. Each sequence is given a tag "UP" representing "unstructured protein", indicating the focus of our interest. However, this is not to claim that the sequences listed in fact are unstructured. One important assumption made in the table is that the persistence length of a protein is about 5 amino acids (see Section 4.4), and thus the bead size is 5 amino acids. Thus a sequence that is heterogeneous at the amino acid level at lengths of 5 amino acids or shorter can in some cases be classified as a homopolymer, when there is a short repeating unit. We note that this is a fairly coarse mapping with several shortcomings for considering proteins, and eventually it may be necessary to develop new polymer categories to accommodate properties of unstructured proteins. However, our purpose here is to consider polypeptides within the existing framework of polymer theory.

3. Neutral polypeptides

3.1. Basic polymer models

We first follow the approach of Flory (1969), introducing virtual bonds (Fig. 2) connecting the α-carbon atoms. One virtual bond thus corresponds to 3.8 Å and is the smallest structural unit to be considered (Creighton, 1993; Miller and Goebel, 1968). The properties of the –R group (charge, etc.) are then assumed to be distributed uniformly over this bond. We then proceed to apply statistical arguments valid for long chains of N repeating chemical units (monomers) of size b. Such an approach is reasonable given our interest in the global properties of the chain pertinent to the unstructured state. There are many different models for polymer chains that may be adopted. We discuss here only two, the freely jointed chain model and the wormlike chain model.

Classification	Polypeptide	Polymer Type	Representation
UP1	NNNNNNNNNNNNNN... SGSGSGSGSGSGSGSGSG...	Homopolymers	
UP2	$(N)_n(SG)_m$ $(N)_n(SG)_m(QN)_o$	Block Homo-copolymers	
UP3	$(SGGNNGNSGF)_n$		
UP4	KRPERRGEKKGDKRGERKPD...	Heteropolymers	
UP5	QAWSEDCRFVTGYHNMIK...		
UP6	NNNNNNNFVTGYHNMIK...	Block Hetero-copolymers	
UP_N	NNNNNNNNNNNNNNNN...	Neutral	
UP_E	RNRNRNRNRNRNRNRN...	Polyelectrolyte	
UP_A	RENRENRENRENRENREN... REDREDREDREDREDRED...	Polyampholytes	

(Left margin, top section: "Monomer Distribution"; bottom section: "Charge Distribution")

Fig. 3. Classification of polypeptide sequences into established polymer categories. This classification considers two properties, the general pattern of monomers and the charge. Homopolymers are the simplest type of chain molecules. Some polymers have more than one monomer type, and hence are heteropolymers from a chemical view point, can still be treated as homopolymers from an analytical point of view. In particular, a repeating polymer where each repeat is smaller than the bead size used in the polymer model, can be treated as a homopolymer (UP1). Here we assume a bead size of 5 amino acids for proteins. Attaching two or more homopolymers produces block copolymers (UP2). From a polymer theory point of view, a repeating polymer where the repeat unit is larger than the bead size (UP3) or where the repeat varies significantly (UP4) is a heteropolymer. Polymers where there is no discernable order are also considered heteropolymers (UP5). Fusions of UP1 with UP3, UP4 or UP5 produces a block hetero-copolymer (UP6). With respect to charge there are three categories. Neutral polymers with no charge (UP_N), polyelectrolyte, which have multiple occurrences of one charged type (UP_E) and polyampholytes, which have multiple occurrences of monomers with either charge (UP_A). Most, if not all, intrinsically unstructured proteins will be of type UP_E or UP_A.

Unstructured polypeptides with sequences of chemically identical, neutral amino acid residues classified here as $UP1_N$, are referred to as neutral homopolymers.

3.1.1. The freely jointed chain

The simplest model of a homopolymer chain is the freely jointed chain due to Flory (1969). In this model the UP chain is divided into N statistical segments or virtual bonds (beads) of size b. In the absence of effects other than the thermally driven motion and the connectivity requirement, the chain performs a "random walk", with mean squared distance between units separated by N segments $\langle \mathbf{R}_N^2 \rangle = b^2 N$ (note that if the virtual bonds differ in length, b^2 would represent the mean square value). This leads to a simple expression for the radius of
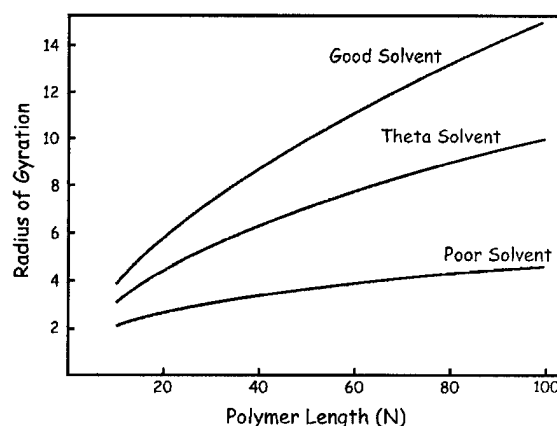
Fig. 4. Scaling of radius of gyration for neutral polymers. The scaling of the radius of gyration is from the freely jointed chain model. In the ideal (theta) case the exponent μ is 0.5. In a poor solvent μ = 0.33 and the molecule tends to collapse. In a good solvent μ = 0.588 and the molecule is expanded.

gyration (Fig. 4):

$$R_{\mathrm{g}} = \frac{1}{6} b N^{1/2}.$$ (1)

The segment assignment requires formally that orientional correlations along the chain are lost and that each segment behaves independently of others. That is, mathematically $\langle \mathbf{b}_i \cdot \mathbf{b}_j \rangle = 0$ for all $i \neq j$, where $\mathbf{b}_i$ denotes the vector associated with the ith bond. For real chains this is in general not the case. The characteristic ratio C_∞ is commonly used to characterize a chain and is given by:

$$C_\infty = \frac{\langle R_N^2 \rangle}{Nb^2}.$$ (2)

For a freely jointed chain $C_\infty = 1$, while for polypeptides the value is typically several times this. Note that if C_∞ is known (by scattering or viscosity experiments for example) then the chain can be modeled via a rescaling of the statistical segment size so that the chain is made up of n_{s} segments of size $b_{\mathrm{s}} = C_\infty b$. A unique assignment of n_{s} and b_{s} is demanded by the requirements $n_{\mathrm{s}} = b_{\mathrm{s}} L$, where L denotes the fully extended length of the chain, and $n_{\mathrm{s}} b_{\mathrm{s}}^2 = \langle R_N^2 \rangle$. An unstructured polypeptide might consist of 100 residues and have a total length of 380 Å. If $\langle R_N^2 \rangle$ is measured as 290 Å then the segment size follows as ≈ 2 residues i.e. 7.6 Å. Such a description assumes the probability distribution of the end-to-end vector is Gaussian i.e. that:

$$P(R, N) = \left(\frac{3}{2\pi N b^2} \right)^{3/2} \exp\left(-\frac{3 R_N^2}{2 N b^2} \right)$$ (3)

an assumption that holds true in the limit of infinitely long chains but must be corrected for chains of finite length. An exact expression for P may be found in Flory (1969), but is mathematically complex to handle. The freely jointed chain model breaks down where $\langle R_N^2 \rangle / (nL)^2$ plateaus off as a function of the number of monomers, which happens as molecules become relatively stiff or too short.

3.1.2. Wormlike chain

Here we draw attention to a common model adopted to describe chains of finite length and flexibility. We define first a quantity referred to as the persistence length l_p (Porod, 1949; Kratky and Porod, 1949), corresponding to the average sum (in the limit $n \to \infty$) of the projection of bond $j \to i$ on bond i, where $1 \ll i \ll n$ such that $\langle \mathbf{R}_n \rangle = 2nbl_p - nb^2$, or

$$l_p = (1 + C_\infty)\frac{b}{2}. \tag{4}$$

The most commonly employed model is that due to Kratky and Porod (Porod, 1949; Kratky and Porod, 1949) and often referred to as the wormlike chain model (although more often this term is used for so-called semi-flexible chains) (Grosberg, 1979; Ubbink and Odijk, 1995, 1996; Bloomfield, 1991).

In the Kratky–Porod model the chain has a constant contour length that undergoes a continuous change in direction described by $u(s) = \delta r/\delta s$, where $r(s)$ denotes the position along the chain at contour length s. For the persistent or wormlike chain the average square end-to-end distance and average square radius of gyration become

$$\left\langle R_N^2(L) \right\rangle = 2l_p L - 2l_p^2 \left(1 - \exp\left(-\frac{L}{l_p}\right) \right) \tag{5}$$

and

$$\left\langle R_g^2(L) \right\rangle = \frac{1}{3} l_p L - l_p^2 + \frac{2l_p^3}{L}\left(1 - \frac{l_p}{L}\left(1 - \exp\left(-\frac{L}{l_p}\right) \right) \right). \tag{6}$$

3.2. Accounting for backbone heterogeneity

Variations in the local stiffness of a polypeptide induced by the constraints on the individual residues along the chain, or alternatively resulting from events such as binding of other molecules, may be of interest in some cases. Within the polymer framework this can be thought of as a locally changing bending constant or a persistence length that varies along the chain. Most models for homopolymers are based on the assumption that deviations from the average persistence length are negligible, while pronounced differences are taken into account by modeling the chain as a copolymer, consisting of groups of rod-like or coil-like character. Significant heterogeneity must have repercussions for the conformational properties of the chain as a whole. The measured radius of gyration of a rod–coil mixture, for example, is obviously expected to deviate significantly from that of both a purely rod-like chain and a purely flexible one, and its properties will accordingly be intermittent between the two. A discussion of this problem may be found in Flory (1969). A well-known area in which such chains are found is in the helix or helix-to-coil transition regions where the chain possesses both helical and random chain components (Poland and Scheraga, 1970; Zimm and Bragg, 1959; Hong and Schellman, 1992). Two approaches that have been employed to describe the chain for these cases are the Zimm and Bragg theory (Zimm and Bragg, 1959) and the broken rod-like chain model (Muroga, 1988, 1992, 2000), and these have proved successful in predicting quantities such as the average helical content of the chain, the average number of residues per helix and the radius of gyration. Although our interest here is in a

class of proteins which may perform their function in a purely random coil state (i.e. in the absence or near absence of secondary structure), some of the results of these theories may be usefully employed in some cases. In the broken rod-like chain model, for example, the chain is assumed to consist of $N_s - 1$ rods alternating with N_s sections of small rods or flexible coils, containing m_k segments so that

$$N_{tot} = \sum_{k=1}^{N_s} m_k + \sum_{l=1}^{N_s-1} n_l. \tag{7}$$

The average fraction of flexible components is $\langle f \rangle$ and the average number of flexible coil segments is $\langle n \rangle$, where $\langle f \rangle = (\sum_{l=1}^{N_s-1} n_l)/(N_{tot})$ and $\langle n \rangle = (N_{tot}\langle f \rangle)/(N_s - 1)$. Note that $\langle f \rangle = 1$ reproduces the fully flexible chain. The derivation of the particle scattering function and radius of gyration of the broken rod-like chain leads to complicated analytic expressions which may be found in Muroga (1988). The theory predicts a smooth increase in the ratio as flexible content increases. The model may be usefully applied to interpret the conformations of a chain measured at high scattering vectors. This is an important issue, given that a measured radius of gyration sheds no direct light on the local conformations of the chain and relies on the employment of an appropriate polymer model.

Finally, events such as ligand binding and interactions with proteins are known to result in static bends or locally altered flexibility in DNA molecules, which in turn are reflected, for example, in the hydrodynamic properties, and have motivated studies into the implications of defects or flexibility heterogeneity in semi-flexible or wormlike chains (Hakansson and Elvingson, 1994). For the special case of a random distribution of non-uniformities $\gamma = \langle \cos \theta \rangle$ occurring with probability p, the usual expression for the (long chain limit) persistence length: $b/(1 - \langle \cos \vartheta \rangle) = b/(1 - \alpha_a)$ becomes: $b/(1 - (1 - p)\alpha_a - p\gamma)$, where θ is the small angle made by a segment with the previous one (i.e. for $\theta \to 0$ continuous curvature). With fixed average flexibility along the chain (e.g. regularly spaced defects), the persistence length of the chain as a whole is reduced, resulting in expanded dimensions when compared to its random counterpart. The effects of defects or static bends is likely to be most pronounced for rod-like chains and is less pertinent for more flexible cases.

3.3. Accounting for volume exclusion and solvent quality

The models, in their simplest form (as we have introduced them above), neglect long-range effects, accounting for only neighbor and near neighbor interactions. They thus ignore treatment of encounters between segments far separated along the chain backbone but in close proximity spatially. Such encounters may involve a number of possible interactions, including steric (volume) exclusion, van der Waals forces, and chemically and electrostatically governed interactions with molecules and ions in solution. In explicit models of local behavior the nature and precise magnitude of the different contributions is of great importance. For global properties however, properties such as radius of gyration, end-to-end distance and probability of segment–segment distances may be extracted from the polymeric models through theories such as Flory–Huggins (mean field) theory and excluded volume theory, valid at high and at intermediate to low concentration of polymer, respectively. As before the chain is characterized by segments of size b

and the volume interactions are accounted for at this level, consistent with the assumption of independent segments.

The low segment density in a coil ($<6\%$ of the volume pervaded) justifies over a wide range of concentrations the assumption of small local segment concentration $c(\mathbf{r})$. The interaction energy of the chain may be written in the form of a virial expansion:

$$U = k_{\mathrm{B}}T \int \mathrm{d}r \frac{1}{2} vc(r)^2 \frac{1}{6} \omega c(r)^3 + \cdots, \tag{8}$$

where $k_{\mathrm{B}}T$ represents units of energy, and v and ω (referred to as the second and third virial coefficients, respectively), denote the effect of 2-body and 3-body interactions. In practice ω is relatively insensitive to external conditions and may usually be taken as constant or ignored. The behavior of v to a great extent governs the behavior of the chain. $v < 0$ indicates an effective attraction between segments and a tendency for global collapse (prevented by higher order terms), $v > 0$ corresponds to repulsive interactions and results in an overall swelling of the chain beyond its predicted Gaussian dimensions, and $v = 0$ reproduces the ideal walk discussed above with minor contributions from higher order terms. The radius of gyration, for example, exhibits the following scaling behavior:

$$\left\langle R_{\mathrm{g}}^2 \right\rangle^{1/2} \approx bN^\mu, \tag{9}$$

where the exponent μ is equal to 1/3, 1/2 and 0.588 for $v < 0$, $= 0$ and > 0 in the different solvent regimes. In the polymer literature these regimes are generally classified as poor, θ and good solvent conditions, respectively. Note that the expansion (contraction) of the coil due to excluded volume interactions is often written in terms of an expansion factor $\alpha(z)$ where $z = (3/2\pi)^{3/2} \times (\mu/b^w)N^{1/2}$ is the excluded volume parameter and

$$\left\langle R_{\mathrm{g}}^2 \right\rangle^{1/2} = \frac{1}{6}\alpha(z)^2 bN^{1/2}. \tag{10}$$

Fig. 5 indicates the manner in which the segment density (calculated from the radial distribution function) varies about the center of mass of the chain in the various cases.

At high concentrations the applicability of excluded volume theory breaks down, while Flory–Huggins mean field theory (Flory, 1942; Huggins, 1942) becomes valid. In the Flory–Huggins description, the chain is represented as a random walk on a lattice with each site corresponding to a single unit. The site occupation fraction ϕ is related to the segment concentration through $\phi = cb^3$ and is used to describe the chain. The total free energy consists of an entropic contribution describing arrangements of the chain on the lattice (often written as an entropy of mixing) and an energetic contribution describing interactions between monomers and molecules in the solution (often written as an energy of mixing). For the simple case of UP plus low molecular weight solvent and under the mean field assumption of independent segments (i.e. uncorrelated interactions) this leads to

$$\frac{F}{k_{\mathrm{B}}T} = \frac{\phi}{N}\ln\phi + (1-\phi)\ln(1-\phi) + \chi\phi(1-\phi), \tag{11}$$

where $\chi = \chi_{\mathrm{PS}} - \frac{1}{2}(\chi_{\mathrm{PP}} + \chi_{\mathrm{SS}})$ is the Flory interaction parameter describing polypeptide–solvent (PS), polypeptide–polypeptide (PP) and solvent–solvent (SS) interactions. At low concentrations a
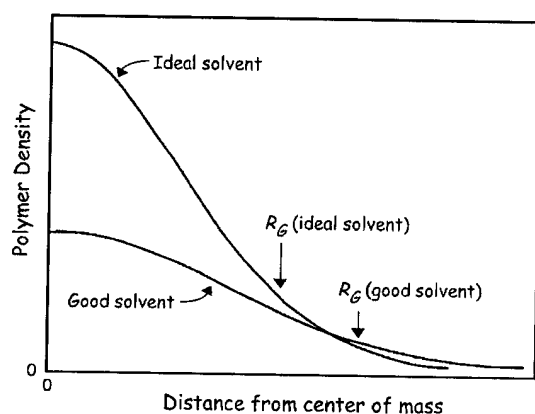
Fig. 5. Segment density of a polymer in ideal (theta) and good solvent. As solvent quality is improved, the attractive interactions between the solvent and the chain cause the polymer to effectively swell. This is effectively the same as having positive intrachain interactions. The polymer then spends more time at larger distances from the center of mass, which is reflected in the segment density profile.
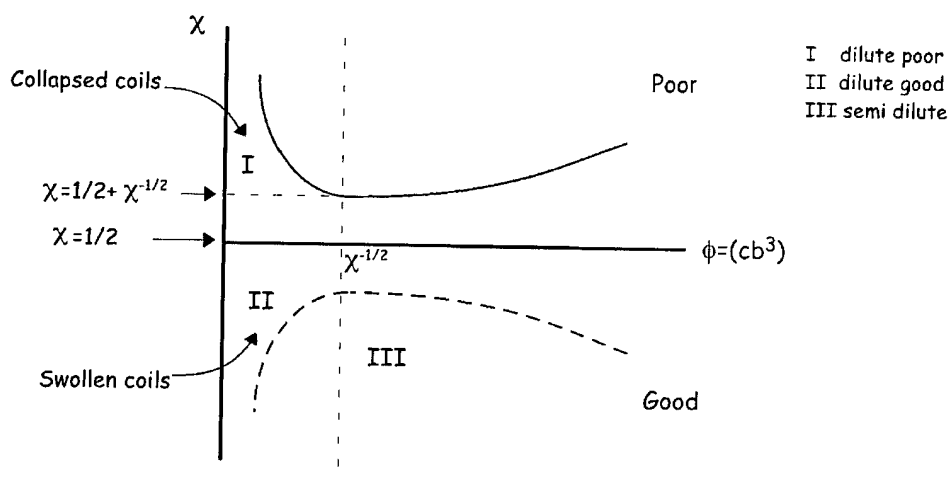
Fig. 6. Phase diagram for polymers as function of the Flory interaction parameter (χ) and the site occupation fraction (ϕ; related to segment density). Adapted from Daoud and Jannink (1976) and de Gennes (1979).

virial expansion with respect to ϕ: $F/(k_B T) = (\phi/N) \ln \phi + \frac{1}{2}\phi^2(1 - 2\chi) + \frac{1}{6}\phi^2 + \cdots$ is directly related to Eq. (11) through $\phi = cb^3$ such that $v = b^3(1 - 2\chi)$. Good solvents then correspond to $\chi < 1/2$ and poor solvents to $\chi > 1/2$ with theta (ideal) behavior being recovered for $\chi = 1/2$.

The typical behavior of a UP–solvent system may thus usually be described via a phase diagram such as that depicted in Fig. 6 (Daoud and Jannink, 1976; Schaefer et al., 1980). Region I here corresponds to a system of collapsed dilute coils (poor solvent, $v < 0$), while regions II and III depict dilute and semi-dilute solutions for good solvents ($v > 0$). The applicability of the

Flory–Huggins and excluded volume theories is reflected in the inset (shown here for good solvent conditions). Low segment concentrations imply large fluctuations so that the mean-field description breaks down. Flory–Huggins validity is thus reserved for relatively concentrated solutions. The critical concentration for overlap of coils is approximately given by $c_{\text{crit}} \approx N/R_{\text{g}}^3 \approx N^{-4/5}b^{-3}$. Note that c_{crit} decreases with N so that for long chains the critical crossover concentration may be quite low. Renormalization group methods (Freed, 1987) and scaling arguments (de Gennes, 1971) have been successfully employed in the semi-dilute regime to incorporate the effects of both inter- and intra-chain interactions. The mean squared end-to-end distance for instance can be shown to become

$$\left\langle R_N^2 \right\rangle \approx Nb^2 c^{2(2v-1)/(3v-1)} \tag{12}$$

which scales as the inverse of the concentration in the ideal limit (i.e. $v = 0$). For the concentrated regime the critical crossover concentration and mean squared end-to-end distance are given by: $c_{\text{crit}} \approx v/b^6$ and $\left\langle R_N^2 \right\rangle \approx Nb^2(1 + (12/\pi)(v\sqrt{12cv})/b^5)$. In a poor solvent phase separation (Huggins, 1942) may occur due to the attractive interactions between UP segments. For most polymeric systems the phase diagram is usually plotted as a function of temperature T, reflecting the dependence. $\chi(T) \approx 1/T$ which generally holds. However, in a biological system the temperature is essentially fixed ($T \approx 20-37°C$), as are the pH and concentration, although the latter properties are often varied in experimental situations.

3.4. Accounting for chemical heterogeneity

We have discussed briefly the effects of a variation in flexibility due to the given sequence of amino acid groups along the chain backbone. Another possibility is variation in the χ parameters for the different residues; i.e. the polypeptide is rightly a heteropolymer and different parts of the chain may interact with molecules in the solution in very different manners (for example hydrophobic versus hydrophilic behavior). However, most of the discussion here is directed at the case of homopolymers i.e. to sequences of amino acid groups for which the interaction with the solvent may be reasonably represented by an average interaction parameter. Heterogeneity may be incorporated into polymer models such as diblock, triblock and higher order block copolymers through self-consistent analysis. Balazs and coworkers (Balazs et al., 1985) have considered the effect of a specific distribution or sequence of segments (i.e. sequence specific χ variation) on miscibility of homopolymer/copolymer mixtures. This is done by introducing a parameter Θ, the value of which indicates blockiness, randomness or alternating character in the sequence (a similar parameter may be used to identify the relative blockiness/randomness of a charged chain) (Wittmer and Joanny, 1993a). The free energy of mixing using the Flory–Huggins formalism in terms of individual parameters associated with the interactions between interacting segment type pairs, i.e. for an A–B UP2 chain mixing with a C UP1 Eq. (11) becomes

$$\frac{F}{k_{\text{B}}T} = \frac{\phi_1}{N_1}\ln \phi_1 + \frac{\phi_2}{N_2}\ln \phi_2 + \phi_1\phi_2(f\chi_{\text{AC}} + 1 - f)\chi_{\text{BC}} - f(1-f)\chi_{\text{AB}} \tag{13}$$

where ϕ_1 and ϕ_2 correspond to the volume fractions of A–B UP2 and C UP1, respectively, and f and $(1 - f)$ describe the composition of the UP2 chain. χ in Eq. (13) thus corresponds to $\chi_{\text{blend}} = f\chi_{\text{AC}} + (1 - f)\chi_{\text{BC}} - f(1 - f)\chi_{\text{AB}}$ and $\chi_{\text{blend}} > 0$ indicates immiscibility, while $\chi_{\text{blend}} < 0$ indicates

miscibility. $\chi_{\text{blend}} > 0$ varies with_ and the authors show that miscibility can be controlled through this variable. A blocky UP2 chain in this description corresponds to $0 < \Theta < \frac{1}{2}$, a random chain to $\Theta = \frac{1}{2}$ and a UP$_2$ chain containing alternating patterns to $\frac{1}{2} < \Theta < \Theta_{\text{max}}$. Average block lengths of A and B segments are determined by the symmetry and the relative probability of, for example, AB, A, B, AA, BB, etc. pairs along the chain, and the different pairs may vary in the relative energetics of their interaction with the C UP1 chain. A detailed discussion of the appropriate analysis and the implications of different sequence types may be found in Balazs and DeMeuse (1989).

4. Charged polypeptides

An important aspect of the polypeptide system is the presence of charged amino acid groups in various combinations and fractions through the presence of the –R groups along the chain backbone. Under physiological conditions (pH ≈ 7 and $T = 20$–37°C) four of the naturally occurring amino acids carry a net charge of significance. Aspartate (D) and Glutamate (E) carry a net negative charge, while Lysine (K) and Arginine (R) are positively charged. Histidine (H) also carries a small net positive charge. Thus in practice, a large number of polypeptides must be classified as either polyelectrolytes (Barrat and Joanny, 1996; de Gennes et al., 1976; Pfeuty, 1978), or polyampholytes (Dobrynin and Rubinstein, 1995; Higgs and Joanny, 1991; Edwards et al., 1980), following the polymeric designations for polymer chains bearing a single charge type and both charge types, respectively.

Most of the simpler polymeric models and studies of polyelectrolytes and polyampholytes are based on the application of Debye–Huckel (D–H) theory, whereby the non-linear Poisson–Boltzmann equation is linearized under the assumption of spherically symmetric charge distributions with Boltzmann density statistics and the approximations of pair-wise interactions and small electrostatic potentials. D–H theory is most valid at low ionic concentrations where the average distance between ions in solution is large and produces a small average potential. Theories for simple electrolytes however do not necessarily carry over to the description of charged long chain macromolecules, due to the complications associated with the accumulation of charges in the solution and the interplay of long-range and short-range interactions of the chain itself. Despite these and other issues, simple models have been developed to describe the conformational properties in the same manner as for neutral chains and should be applicable to a number of polypeptides. An alternative approach to computing salt effects is used in computer simulations, where the salt is treated explicitly using Ewald summation methods. This enables the accurate computation of polymeric properties for both simple and complex systems (Darden et al. 1993; Hockney and Eastwood, 1981).

4.1. Polyelectrolyte polypeptides

Polypeptides carrying charged groups with a significant predominance of one sign over the other are most appropriately classified as polyelectrolytes (UP$_E$) and the conformational properties of the chains can be extracted from polymer theory developed to describe such macromolecules. Three important length scales must be identified for this purpose: the screening length κ^{-1} defining the range of the electrostatic interactions, the Bjerrum length l_B defining the

scale at which these interactions become equal to the thermal energy, and the dimensionless coupling parameter Γ characterizing the strength of interactions. Clearly the presence of charged groups must affect the average properties: expansion of the chain will increase the average distance between charged groups but must compete with the effects of connectivity and thermal agitations. The effective statistical segment size or the persistence length should thus increase due to an increasing average stiffness of the chain as the average conformational space is reduced by unfavorable penalties for charge proximity. These effects can be described for a given unstructured polypeptide, satisfying certain criteria, in terms of κ^{-1}, l_B and Γ.

In the D–H approximation the interaction energy between elementary charges separated by a distance r_{ij} may be written:

$$U(r_{ij}) = \frac{e^2}{4\pi\varepsilon_0\varepsilon r_{ij}}\exp(-r_{ij}\kappa). \tag{14}$$

For $r_{ij} > \kappa^{-1}$ the interaction is effectively screened. In terms of the ionic strength of the solution I this length scale is given by

$$\kappa^{-1} = (4\pi I l_B)^{1/2}. \tag{15}$$

The Bjerrum length, $l_B = e^2/4\pi\varepsilon_0\varepsilon kT$, is essentially a fixed parameter for any given charge under specific conditions. For example, under physiological conditions, the value for sodium is $\approx 7\,\text{Å}$. This value indicates that the Coulombic interaction between unscreened charges is balanced by the thermal energy at relatively short distances. Indeed Eq. (15) yields a screening length $\approx 9\,\text{Å}$. Experimentally κ^{-1} can be varied by solutions of differing dielectric constants and ionic strengths over a wide range. The meaning of these distances for a given polypeptide may be characterized by the parameter $\Gamma = l_B f/b$, where f is the fraction of segments carrying a net charge. For small Γ the Coulombic interaction is dominated by the thermal agitation and the chain is only expected to be weakly perturbed by electrostatic interactions. Polyelectrolytes falling into this category are often referred to as "weakly charged" and are generally distinguished by a small charge fraction f and may be described by "blob" arguments (Barrat and Joanny, 1996; de Gennes et al., 1976; Khokhlov, 1980). For a UP with statistical segment size as large as 6 of which a fraction 0.5 are charged, for example, $\Gamma = 0.5$. Normally $\Gamma > 1.0$ is taken as large and $\Gamma < 1$ as small. Blob arguments are based on the introduction of a new length scale ξ which describes the length scale below which the electrostatic effects are negligible in comparison to the thermal energy (i.e. in the same manner as for l_B, the scale at which the electrostatic energy balances $k_B T$). For distances $r > \xi$ the chain stretches out as a string of blobs, so that (for $v > 0$) the end to end distance is given by

$$R \approx Nv^{1/3}f^{2/3}\Gamma^{2/3}. \tag{16}$$

Here $v = \omega$ and the temperature dependence of the virial coefficients is ignored.

For strongly charged unstructured polypeptides the application of the blob arguments breaks down. For such cases $\xi \approx b$ and the chain assumes a rod-like configuration. The concept of electrostatic blobs also breaks down for screening lengths less than the blob size. In this case the screened Coulombic interactions are more appropriately represented by an effective excluded volume between monomers, which is described by a second virial coefficient of $v_{\text{eff}} \approx 4\pi\Gamma/\kappa^2$. In general, the same conclusion holds for intrinsically stiff chains in general, i.e. where b is a

significant fraction of the total chain length. In this case the theory of an electrostatic wormlike chain, due to Odijk, Skolnick and Fixman (Odijk, 1977; Skolnick and Fixman, 1977) is appropriate and most commonly employed. In this limit the chain backbone is stiff and resistant to local bending. Odijk and Fixman introduced for this regime the concept of an electrostatic persistence length in analogy to that developed for a neutral wormlike chain:

$$l_{PE} = \frac{l_B}{4\Gamma^2}\left(\frac{f^2}{b\kappa}\right)^2 \tag{17}$$

such that, (for $l_p \gg \kappa^{-1}$), $l_p = l_{p0} + l_{PE}$: the total persistence length is the sum of the intrinsic (bare) value and an electrostatic contribution. For $v = 0$ the radius of gyration is given by

$$\left\langle R_g^2 \right\rangle = \frac{Ll_p}{3} - l_p^2 + \frac{2l_p^3}{L} - \frac{2l_p^4}{L^2}\left(1 - \exp\left(\frac{-L}{l_p}\right)\right) \tag{18}$$

which becomes $bL/6$ and $L^2/12$ in the limits of a fully flexible chain and rigid rod, respectively. Note that the expansion of the chain beyond its neutral dimensions reflects an effective excluded volume interaction between segments due to the electrostatic effects. This has been estimated by Odijk (1977) as $v_e \approx 8\pi l_p^2\kappa^{-1}$ and is responsible for the observed experimental swelling parameter: $\alpha = \left\langle R_g^2 \right\rangle / \left\langle R_g^2 \right\rangle_0$. For a string of blobs in the flexible limit an equivalent expression for the end-to-end distance may be obtained (Haronska et al., 1997):

$$R(N) \cong \left(\frac{be^2}{\kappa}\right)^{1/2} N. \tag{19}$$

Theories for polyelectrolytes have been less successful in describing the crossover region for which b/f, b and l_B are of the same order of magnitude. We do not consider those unstructured polypeptides falling into this class here and the description of such polyelectrolytes currently remains a source of controversy.

4.2. Polyampholyte polypeptides

The majority of naturally occurring polypeptides of course consist of amino acid residues with varying properties. In many cases, at a given pH, the chain consists of both positively and negatively charged groups in similar proportions and is considered a polyampholyte (UP$_A$). The first theoretical studies of polyampholytes within the polymer community were initiated by Edwards et al. (1980), who argued that a unique property of a polyampholyte consisting of equal numbers of positively and negatively charged groups, is that at low temperatures the average net attraction between segments can lead to its collapse into a microelectrolyte. In contrast to the globular states achieved by neutral chains with $v \ll 0$ (very poor solvents), collapse should occur at a point governed by the length, charge fraction, Bjerrum length and temperature and should result in a globular state which is not dominated by the short range forces. Since this early work significant effort has been directed at the description of polyampholytes under varying conditions, including small net charge (Soddemann et al., 1998; Tanaka et al., 1997), salt variation (Diehl et al., 1996), charge distribution (Srivastava and Muthukumar, 1996), chain rigidity (Ha and Thirumalai, 1997) and influence of external forces (Loomans et al., 1997; Schiessel et al., 1995; Schiessel and Blumen, 1996; Long et al., 1998). We summarize some of these results here, with

reference to the limiting charge distributions on flexible unstructured polypeptides at a given pH. It should be noted that variation of the pH can significantly alter the charge distribution and degree of ionization of the –R groups on the backbone of the chain. The sites, in this sense are fixed (or "quenched" in the language commonly employed to distinguish fixed charge distributions from those which are mobile or "annealed" (Raphael and Joanny, 1990; Mandel, 1988), while the degree of ionization is annealed and governed by the pH and properties of the solution. To explicitly consider this distinction requires extensive calculation, or alternatively, simulation. However, more general results may be obtained by a simpler classification of the chain, in which the net charge of a segment is calculated by assuming uniform ionization of potential charged sites along the backbone and taking the net charge on a segment as the sum the charges on all residues contributing to that segment moved to its center. This approximation should be reasonable for some asymmetric charge distributions on the individual segments and where portions of the chain consisting of uncharged segments (we refer to these as X portions) is greater than b. The size of X may of course vary along the backbone of the chain, but again, global behavior may be in a first approximation predicted by taking $X = \langle X \rangle$.

Consider first the scenario in which the chain consists of positively and negatively charged in random positions (i.e. no regularly repeating motif). Two different possibilities can immediately be identified: (1) net neutrality, such that $n_+ = n_-$ and $Q_{tot} = 0$ or (2) net charge $n_+ \neq n_-$. In the former case the segments are on average attracted to other segments in the chain which carry on average a small compensating opposite charge. This average attraction is increased further by the fluctuations in the charge distribution due to the conformations of the chain. Note that the fluctuations are more pronounced for the random case than for the alternative scenario of an alternating sequence. For large Q_{tot} the chain stretches in the same manner as a UP_E chain (polyelectrolyte) and is relatively insensitive to the distribution of charges along the backbone in most cases (Srivastava and Muthukumar, 1996), but responsive to the net charge carried by the chain.

Many recent studies, both theoretical and computational (Soddemann et al., 1998; Tanaka et al., 1997) have been devoted to an understanding of the influence of a net charge. A simple two parameter Flory theory for flexible chains (Dobrynin and Rubinstein, 1995) summarizes the important results for random, flexible chains, while alternative treatments have been proposed also for the relatively rigid case (Ha and Thirumalai, 1997). We expect that many of those polypeptides at which this paper is directed should satisfy the criteria of these approaches.

For the flexible case, characterizing a chain by the fractions of positive and negative segments f_+ and f_-, Dobrynin and Rubinstein (1995) introduced a charge asymmetry parameter:

$$\sigma = \frac{(f_+ - f_-)^2}{f_+ + f_-} \tag{20}$$

and effective temperature:

$$t = \frac{1}{u(f_+ + f_-)}, \tag{21}$$

where $u = l_B/b$ is used to distinguish different regimes of behavior for the chain. For a given pH and temperature we treat σ and t as fixed for the polypeptide under consideration. Note that for a fully charged chain, $t = 1/\Gamma$. Large values of t correspond to the dominance of thermal effects

over electrostatic contributions while large σ corresponds to large charge asymmetry, reproducing a neutral polyampholyte and polyelectrolyte for $\sigma = 0$ and $\sigma = 1$, respectively. When t is very large the dimensions of the chain are determined by the solvent and average properties are similar to those of a neutral chain (UP$_N$). For intermediate t the behavior may be polyelectrolyte like or polyampholyte like depending upon the charge asymmetry. Consider the case for which the second virial v is zero (θ solvent). At high effective temperatures the chain is unperturbed and has dimensions $\langle R \rangle \approx N^{1/2}$ as for a neutral chain. At $t = t_1 \approx N^{3/2}$ however, the electrostatic repulsion between segments becomes appreciable and stretches the chain. The configuration is then determined by the balance of the electrostatic interactions with the chain elasticity. As for pure polyelectrolytes, an effective "blob" size ξ, determined by equating the electrostatic energy of γ segments with uncompensated charge $e(f_+ - f_-)$ with the thermal energy ($k_B T$), can be identified at which scale the electrostatic effects perturb the chain. In terms of the new parameters the conformation of the chain is then that of an elongated cigar of length $N(\sigma/t)^{1/3}$, consisting of electrostatic blobs of size $\xi \approx b(t/\sigma)^{1/3}$ and containing $(t/\sigma)^{2/3}$ segments. As before, the model requires $t/\sigma = 1/(u(f_+ + f_-)^2) > 1$ for the representation in terms of blobs to be relevant. At still lower t, $t < t_2 \approx \sigma^{-1/2}$, the attraction between segments due to the spatially correlated charge fluctuations may lead to a polyampholyte regime. The chain then takes the form of an asymmetric globule with aspect ratio $L/\xi \approx N\sigma^2$ for which the blob size and segments number per blob are given by $(t/\sigma)^{1/3}$ and σ^{-1}, respectively. For $\sigma \approx 0$ (negligible charge asymmetry and $Q_{tot} \approx 0$) collapse occurs with no stretched conformation exhibited. For non-zero second virial (good and poor solvents) the same qualitative behavior is reproduced with different scaling.

From the above discussion it is clear that the charge asymmetry is an important parameter in classifying an unstructured polypeptide; the more so due to the possibility for large changes in σ and hence conformation, with changes in the pH. Another relevant parameter is the intrinsic stiffness of the backbone and its magnitude compared to the total contour length of the chain. Stiff polyampholyte chains have received comparatively little attention. An alternative approach is required to their flexible counterparts and we briefly discuss this case here. When the backbone of the chain is intrinsically stiff (i.e. large persistence length or short chain length) so that the chain is best described by a wormlike chain model, fluctuations in the chain configuration are small and interactions of the excluded volume kind do not significantly contribute. Moreover the application of Debye–Huckel theory gains greater credibility since the relevant length scales are more likely to exceed the Bjerrum length and thus satisfy the criteria for approximations of the Debye form.

For weakly charged, wormlike chains with mean squared charge σ^2 and mean squared fluctuations $\delta\sigma^2$ small and $l_p/L \approx 1$, Ha and Thirumalai (1997) write the effective (two body) interaction between randomly distributed charged sites along the chain as a sum of a polyelectrolyte (repulsive) term and a polyampholyte (attractive) term scaling with the magnitude of the charge fluctuations:

$$v_{ij} = kT\sigma^2 l_B \frac{\exp(-\kappa r_{ij})}{r_{ij}} - \frac{kT}{2}(\delta\sigma)^4 l_B^2 \frac{\exp(-2\kappa r_{ij})}{r_{ij}}. \tag{22}$$

Three body interactions are unimportant when L is not too small but may lead to an increase in chain flexibility. From such an analysis it is then possible to extract a total persistence length for the chain incorporating a polyampholyte term in the same manner as was described earlier for a

polyelectrolyte contribution, i.e.: $l_p = l_{p0} + l_{PA}$ so that:

$$l_p = l_{p0} + \frac{l_B \sigma^2}{4b^2 \kappa^2} - \frac{l_B^2 (\delta\sigma)^4}{8b^2 \kappa}, \tag{23}$$

where $l_p \approx L$, which incorporates both the polyelectrolyte induced expansion and polyampholyte induced contraction of the chain. Note that the polyelectrolyte and polyampholyte terms vary with κ^{-2} and κ^{-1}, respectively and that $(\delta\sigma)^4 > \kappa^{-1}\sigma^2/l_B$ is required for the latter contribution to dominate. The scaling moreover applies to a random charge distribution. However for large "blocks" of charges of the same sign along the backbone i.e. correlations between charges over a distance L_c, then the polyelectrolyte effect may be enhanced. For $L_c \gg \kappa^{-1}$ the relevant equation becomes

$$l_p = l_{p0} + \frac{l_B}{b^2 \kappa^2} \left(\sigma^2 + (\delta\sigma)^2 - \frac{L_c l_B}{b^2} ((\delta\sigma)^2 \sigma^2 + (\delta\sigma)^4) \right) \tag{24}$$

and for $(\delta\sigma)^2 \leqslant (b^2/l_B L_c)$ the overall behavior is that of a polyelectrolyte, even for $\sigma = 0$ (neutral chain). The sequences of correlated charge thus exhibit independent polyelectrolyte behavior. This may be important for some stiff polypeptides with a propensity of acidic or basic –R groups at regions along the chain backbone.

4.3. Specific charge sequences in polyelectrolytes and polyampholytes

The above discussions have all dealt with non-specific charge distributions. In many cases, however, the distribution of charged groups may be important. Consider a UP with a strictly alternating sequence of positively and negatively charged segments with net charge of zero. For this particular case simulations and theoretical treatments (Wittmer and Joanny, 1993a) indicate that the chain behaves like a neutral polymer with an effective, negative second virial coefficient. The interactions between segments are thus short range and attractive. This result may be explained by the restriction of charge fluctuations to a range of the order of the chain self-screening length. Except for very high polymer concentrations, such that the self-screening length is less than the average spatial distance between charges (of the order of the globule size), the criteria for fluctuations is not satisfied and collapse occurs as for a chain in a poor solvent, with the replacement of $\nu = 0$ with $\nu_{eff} \approx (-bl_B^2/X^2)$. As the distribution of charges along the backbone is made more random there is a smooth crossover to the behavior discussed above, while in the opposite limit, in which large blocks of charge characterize the sequence, the chain may be polyelectrolyte like or alternatively aggregation may occur if there is a strong attraction between blocks.

Inhomogenities in the charge distribution along the chain backbone may significantly effect the shape of unstructured polypeptides (Khokhlov, 1980; Dobrynin et al., 1996; Kantor and Kardar, 1994) (this is to be distinguished from R and R_g which describe the overall size). A chain carrying a net charge may exhibit a radius of gyration closely corresponding to its unperturbed (neutral) dimensions, while locally exhibiting highly stretched and collapsed portions. The shape of the chain is determined by the balance of the surface energy of those blobs exposed to the solvent ($\approx k_B T$/blob), described by a surface tension $\gamma \approx k_B T \xi^2 \approx k_B T \kappa^2$, with the perturbing influences, such as net charge and external fields. For $Q_{tot} = 0$, in the absence of other forces, a spherical

shape is thus adopted as this minimizes the exposed surface area and hence the surface energy. For smaller γ the surface energy is more likely to be strongly influenced by perturbations (such as the need to minimize electrostatic energy) and a deviation from spherical geometry may occur. An analogy has been drawn with a charged droplet which becomes unstable at a critical value of the net charge. Connectivity prevents a chain from completely expelling charges as for a droplet, however the chain can lower its energy by expelling "fingers" of charge so that its shape is that of a collapsed globule with highly stretched charged strings. This effect is most pronounced for very poor solvents, very low temperatures and very asymmetric charge distributions. In these cases the segment rearrangements possible for small net charges and/or higher temperatures, by which segments preferentially surround themselves with segments of the opposite charge, is precluded by local energy barriers. Theoretical studies and simulations indicate that the chain consists of portions of chain in which loose aggregates have formed and highly charged stretched portions, depending upon the charge distribution. In some situations the shape can be frozen in i.e. the relative positions of the segments are effectively fixed, as for a folded protein. This can occur only on length scales larger than the self-screening length of the chain and requires high charge or very low temperatures. Dorbrynin et al. (1996) have derived a scaling theory to describe the effects of solvent and charge on the necklace configuration of a polyelectrolyte for which some predictions follow. A globular geometry becomes unstable as the solvent is made poorer and deforms to an elongated cylinder of length: $L_c \approx (bN/\tau)(\Gamma f^2)^{2/3}$ and width: $D \approx b(\Gamma f^2)^{-1/3}$, where τ describes the deviation from the θ point (i.e. solvent quality) and Γ is the coupling parameter introduced previously. The transition occurs when the charge on the chain, fN exceeds a critical value, $(N\tau/\Gamma)^{1/2}$. When $\tau > (\Gamma f)^{1/3}$ however, the cylindrical shape in turn becomes unstable and is no longer the configuration which minimizes the free energy. Instead the chain is predicted to take the form of a necklace of total length $L_n = (N_{\text{bead}} - 1)l_{\text{str}} + N_{\text{bead}}d_{\text{bead}}$, where $d_{\text{bead}} \approx \tau^{-1/3}$ and $l_{\text{str}} \approx b(\tau/\Gamma f^2)^{1/2}$ so that $L_n \approx b(\Gamma/\tau)^{1/2}fN$, i.e. the length of the necklace is proportional to the total charge on the chain. The number of segments contributing to each bead is $\approx \tau/\Gamma f^2$ and the number of beads is an integer defined by: $N_{\text{bead}} \approx \Gamma(N/\tau)f^2$. Variation of the fraction of charged sites or the solvent through f and τ can thus lead to transitions between states involving beads of varying size and number. The scaling analysis holds as long as the electrostatic blob size remains larger than the thermal blob size i.e. the solvent must be sufficiently poor. Analysis of necklaces in polyampholytes may be found in Kantor and Kardar (1994, 1995), Kantor et al. (1998).

4.4. Polypeptide persistence lengths

The calculation of persistence length assumes knowledge of the relative probability of different conformations for the polymer domain. The most common assumption is that each conformation is equally weighted and that each bond rotation is independent of the other bond rotations. That is, for

$$p = \sum_{j=i}^{\infty} \frac{\langle l_i \cdot l_j \rangle}{l_i} \tag{25}$$

the ensemble weights each conformation uniformly and assumes that rotation about each bond is independent of the others. These simplifying assumptions lead to compact analytic formulae, but are not likely to be sufficient for all UP domains which are of interest here. Even within the

context of simple synthetic homopolymers, the analytic models often only provide moderate agreement with experiment. For polyethylene, experiments give a characteristic ratio (C_∞; Eq. (2)) of 6.7 while the freely jointed chain suggests 2.0 (Boyd and Phillips, 1993). This is improved by assuming that perpendicular component of independent bonds do not vanish, with a resulting characteristic number of 3.4.

An alternative to estimating persistence length is numeric computation using a more detailed potential function and conformational sampling. The resulting sampled conformations are then weighted by their relative probability and the persistence length is directly computed. To perform this calculation, the projection of the bond vector onto an initial bond vector (chosen near the center of the chain) is used (e.g. Zhang and Mattice, 1992, 1993). The idea here is that as the bond vector projections become less correlated with distance they will fall to zero, and the persistence length then reflects the length scale for which there is memory of the orientation of a previous segment. Within a rod-like polymer (e.g. polyelectrolyte) Eq. (25) yields a much longer persistence length than for neutral polymer. Computation is made easier by defining a transformation matrix that connects the orientation of an initial bond vector with the following bond vectors. Thus the transformation matrix defines the coordinate system transformation that brings the vectors into alignment:

$$l_i = T_i l_{i+1} \tag{26}$$

where

$$T_i = \begin{pmatrix} \cos\theta_i & \sin\theta_i & 0 \\ \sin\theta_i \cos\phi_i & -\cos\theta_i \cos\phi_i & \sin\phi_i \\ \sin\theta_i \sin\phi_i & -\cos\theta_i \sin\phi_i & -\cos\phi_i \end{pmatrix}. \tag{27}$$

The iterative application of the transformation allows the computation of the projection of distant bond vectors onto the original bond vector.

$$l_j = T_i T_{i+1} \dots T_{j-1} l_j^0. \tag{28}$$

Thus the persistence length can be defined by the ensemble averaged set of projections, as seen through the transformation matrix, connecting all bond vectors back to the reference vector.

$$p = \frac{1}{l_j} \sum_{j=i}^{\infty} \left\langle l_i^0 \cdot T_i T_{i+1} \dots T_{j-1} l_j^0 \right\rangle. \tag{29}$$

A common assumption, even numerically, is that the individual transformations are independent (Zhang and Mattice, 1992, 1993). This enables a more rapid computation and is equivalent to the claim that each bond vector is an independent location for rotation, not influenced by other rotations.

$$\left\langle T_i T_{i+1} \dots T_{j-1} \right\rangle = \left\langle T_i \right\rangle \left\langle T_{i+1} \right\rangle \dots \left\langle T_{j-1} \right\rangle. \tag{30}$$

Within this computational framework, the ability to predict persistence lengths is improved relative to analytic approaches. However, recently, Pappu et al. (2000) have shown that for peptide units the independence assumption breaks down. That is, for more detailed atomic models of protein units, the assumption that each phi–psi angle is independent of neighboring dihedral

angles does not hold. In a polymer framework this becomes less of an issue for very long molecules (many persistence lengths). Nonetheless, it points to an important problem in using computational or analytical methods for determining persistence lengths.

In this context we note that there have been a number of experimental measurements of the persistence length of proteins. Methods used include atomic force microscopy, optical tweezers, static light scattering, quasielastic light scattering, small angle neutron and/or small angle X-ray scattering, and nuclear magnetic resonance. A commonly used value is 5 amino acids, but experimental measurements vary depending on the protein. For example, experimental determination shows $l_p \sim 7$–10 amino acids for the fibronectin binding protein from *Staphylococcous aureus* (Penkett et al., 1998), $l_p \sim 7$ amino acids for lysozyme (Schwalbe et al., 1997), $l_p \sim 2$ amino acids for myelin associated protein (Mueller et al., 1999), $l_p \sim 4$–5 amino acids for titin (Kellermayer et al., 2000) and $l_p \sim 8$ amino acids for phosphoglycerate kinase (Damaschun et al., 1999, 1993).

5. Unstructured polypeptides at surfaces

Above we have been primarily concerned with bulk properties i.e. in the absence of tethering or anchoring constraints and extra-chain interactions with all but solution molecules. In this section we cover some of the most important properties of unstructured polypeptides attached to surfaces. This includes attachment to non-biological surfaces, but also biological surfaces such as membranes or folded protein domains. Most of the important concepts of the previous section, such as flexibility and chemical properties carry over directly to systems involving unstructured polypeptides at surfaces.

For chains end-attached (grafted) to a surface the configurational space is reduced from bulk, due to the additional constraint on the tether point of the chain. For high grafting densities interactions with other chains leads to strong stretching away from the surface (the polymer brush state). For sparse grafting (and sufficiently long) chains the surface is characterized by individual polymer occupying half "mushroom" spheres with radial dimensions following the same scaling behavior as dilute chains in bulk. The density profile of segments normal to the surface is predicted to exhibit a maximum several monomer lengths from the surface and spread more in the radial direction parallel to the attachment plane than normal to it (de Gennes, 1980; Steels et al., 2000).

We begin with the simple case of a single "bristle" and discuss different classes of surface attachment, implications of the surface constraint. The discussion is then extended to include many attached closely attached polymers (bristles), referred to as a "brush" in polymer theories, for which inter-chain interactions may lead to stretching of the attached layer. Scaling theories for neutral brushes (UP_N) at surfaces of different curvature and steric stabilization are presented. We then consider the possibility of electrosteric stabilization produced by sequences such as UP_E and the influence of salt and pH on such a brush and its stabilization properties. Finally there is a discussion of the interaction of bristles and brushes with finite objects, such as particles in the solution or experimental probes (e.g. AFM tip) and the influence on hydrodynamic properties. Most of the discussion presents the scaling arguments as these permit relatively simple and intuitive analytic predictions for the average properties, however we more

generally discuss the results and predictions of more sophisticated analyses, including numerical treatments.

5.1. Modes of attachment

We draw attention here to three different common classes of surface (Cates and Brooks, 1993; Patel and Tirrell, 1989; Russel et al., 1989): (i) adsorption, (ii) chemical grafting and (iii) block copolymer attachment (Fig. 7).

5.1.1. Adsorbed polypeptides

At the simplest level, adsorption (de Gennes, 1969; Milchev and Binder, 1998; Johner and Joanny, 1991; Johner et al., 1990) of a UP to a surface can be thought of as a preference of the surface for contact with the polypeptide (or certain segments of the chain) over contact with the solvent that leads to a free energy gain for polypeptide–surface contacts. As a result, segments of the polypeptide may "stick" to the surface and form a layer, which may in turn effectively convey stabilizing properties (e.g. preventing flocculation). The thickness of the layer may be estimated by simple arguments (de Gennes et al., 1976). A UP in a good solvent (i.e. $v > 0$, $\chi < \frac{1}{2}$) has an average end to end distance $R_N \approx bN^{3/5}$ determined by the balance of chain entropy and excluded volume considerations as discussed earlier. However, when a segment of the polypeptide makes contact with the surface there is a free energy gain $\Delta F \approx -kT\gamma$, where $kT\gamma$ is an energy representing the adsorption and is determined by the relative energies associated with UP–solvent, UP–surface, surface–solvent, etc. contacts. If a fraction f of the UP sticks and forms a layer at the surface of thickness $H \approx b/f$ then the total free energy will consist of a term representing the energetic gain in surface contact and the entropic cost for reducing the configurational space of the polypeptide:

$$\frac{F}{kT} \approx \left(\frac{b}{H}\right)^{3/5} N - \gamma \frac{b}{H} N \tag{31}$$

so that at equilibrium $F/kT \approx -N\gamma^{5/3}$ and the average thickness is $H_{av} \approx b\gamma^{-3/2}$. The actual configuration of the chain may consist of many "loops" and "tails" corresponding to portions of the UP attached to the surface and extending into the solution, respectively. Dynamically, since
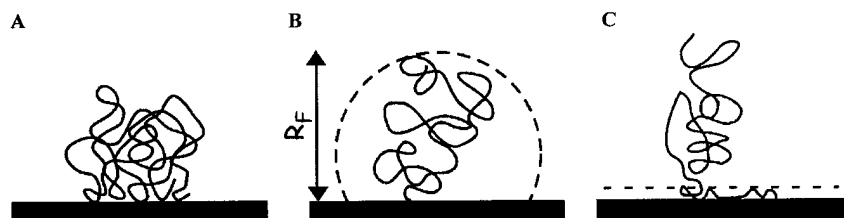
Fig. 7. Modes of attachment of a protein to a surface. (A) Adsorption to a surface can occur through relatively non-specific chemical and physical interactions at several points along the chain. (B) End attachment (end-grafting) typically employs specific chemistry by which the end of the molecule forms a covalent or other strong bond with the substrate. (C) Block copolymer attachment exploits strong interactions between one of the blocks in the polymer with the surface, leaving the other block(s) to behave as though they were end-grafted.

adsorption is reversible, segments may attach and detach while maintaining the same average thickness.

5.1.2. Chemically grafted polypeptides

In contrast to adsorbed UPs, chemically grafted (Alexander, 1977; de Gennes, 1980; Milner, 1991; Napper, 1983) UPs are tethered at one end (the –N or –C terminal for example) to the surface and consist of segments which have no affinity for the surface or tend to avoid it. The chain may be considered irreversibly attached for this case (although this assumption may need to be relaxed for fluid-like interfaces) due to the strong chemical bond. In a good solvent a single UP chain is thus confined to a half sphere of $R \approx bN^{3/5}$ determined by a balance of chain entropy with excluded volume interactions as covered earlier. The segment density profile is altered by the presence of an impenetrable wall (de Gennes, 1980) even for the case of a single chain.

5.1.3. Diblock polypeptide adsorption

The case of a neutral or charged diblock ($UP2_N$ or $UP2_E$) is in many ways intermediate between cases (i) and (ii) above. Here one of the blocks plays the role of an anchor and is strongly physically or chemically adsorbed to the surface, while the remainder of the UP chain avoids the surface and extends into the solution. The concept is not restricted to adsorption at a surface, but may result from, for example, the formation of a micellar closely packed core consisting of insoluble segments with a corona of extended segments or "hairs" corresponding to the soluble portion of the UP; i.e., a "star" configuration. Polymer stars (Daoud and Cotton, 1982; Shusharina et al., 1996; Wittmer and Joanny, 1993b) have been the subject of many studies both for neutral and charged systems and many of the results carry over to homopolymer systems at curved surfaces. Since our interest here is in the behavior of the soluble portion of the chain, either at an independent surface or in the corona of such a micelle (consider the globule micelle as the folded portion of a protein), we will treat this case as identical to (ii) above and ignore the insoluble block, excepting when the micellar state results in a change in the effective surface geometry.

5.2. Unstructured polypeptide brushes

5.2.1. Polypeptides in the brush limit

In many cases it is not the behavior of a single, isolated, surface attached UP which is of interest, but rather many polypeptides attached in close proximity to form a layer or brush in which the UPs are stretched beyond their average dimensions in the absence of other chains. Consider two UPs end-attached at some separation $d \approx \sigma^{-1/2}$ where σ is the number of chains per unit area of surface, in a good solvent where d is sufficiently large that the chains do not interact. Then each UP forms a half-sphere of radius $R \approx bN^{3/5}$ and is essentially independent. When the distance between attachment points is of the order of R however, the chains overlap significantly (some interaction may occur at $d > R$ due to fluctuations beyond the average dimensions) resulting in an increase in the excluded volume interactions of each chain so that the UPs stretch away from the surface. In stretching a chain must pay an entropic penalty $F_{str}/kT \approx (\pi^2/24) \times (H^2/2Nb^2)$ which must be balanced with the excluded volume interactions $F/kT \approx vN^2b\sigma/2H$. It has been assumed here that all chains stretch to the same height (i.e. no free UP ends located within the brush) and that they do so elastically, so that the entropy of δn segments stretching a

distance z is $\delta F_{str} \approx (3kT/2)(\delta z)^2/\delta n$. At equilibrium, one obtains an average height for the brush (Milner, 1991): $H_{av} \approx N\sigma^{1/3}$. Each UP chain in this simple picture may be thought of a string of blobs (Alexander, 1977) of size ξ, containing $g = c^{-5/4} = (\xi/b)^{5/3}$ segments, which fill space completely. At scales $r < \xi$ the chain is thus unperturbed, while for $r > \xi$ it is stretched perpendicular to the surface so that $H_{av} \approx (N/g)\xi \equiv Nb(b/\xi)^{2/3}$.

5.2.2. Effect of surface curvature

The curvature of the surface to which the UP is attached may also vary, either due to the intrinsic geometry (e.g. spherical, cylindrical) of the folded region of the protein or macromolecule from which it extends or the experimental surface employed. The geometry of the brush may influence the properties of the UP dramatically (Daoud and Cotton, 1982; Birshtein and Zhulina, 1984; Dan and Tirrell, 1992; Ball et al., 1991; Murat and Grest, 1991; Grest et al., 1987). For a planar interface the concentration of segments is essentially independent of distance from the surface. However, for a positive curvature (e.g. the outside of a sphere) leads to a concentration which, to a first approximation, decreases as a power law, so that the excluded volume interactions within the brush effectively decrease with distance. We have seen how scaling theories predict a step function profile for the segment density in the planar case i.e. $\phi(r) \approx \sigma^{2/3}$. For cylindrical and spherical geometries similar arguments lead to: $\phi(r) \approx \sigma^{2/3}(R_s/r)^{2/3}$ and $\phi(r) \approx \sigma^{2/3}(R_s/r)^{4/3}$, respectively, where R_s denotes the radius of curvature of the surface. The average brush height $H_{av} \approx bN\sigma^{1/3}$ found for a flat surface becomes $H_{av} \approx bN^{3/4}\sigma^{1/4}(R_s/r)^{1/4}$ for a cylindrical geometry and $H_{av} \approx bN^{3/5}\sigma^{1/5}(R_s/r)^{2/5}$ for a sphere. In the cases of surface curvature the average distance to which the UPs extend is thus reduced, reflecting the rapid fall off of the effects of excluded volume interactions between adjacent UPs which stretch the chains (Fig. 8).

5.2.3. Critique of the scaling approach

While scaling methods have been successful in predicting the asymptotic behavior and global properties such as H_{av}, a detailed description of the concentration within the attached layer more
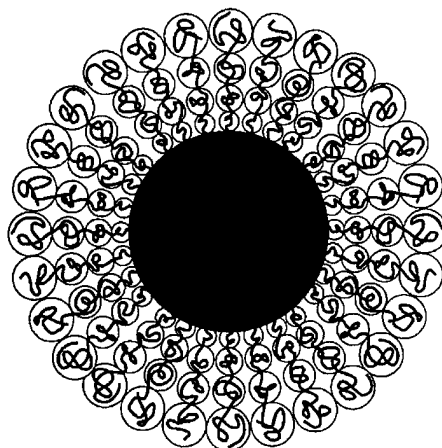

Fig. 8. Polymer brush on a sphere. The curvature of the surface results in fewer chain–chain interactions further away from the sphere. Thus the blob size increases as a function of distance from the surface, as strength of interchain interactions decrease.

rightly requires models with fewer approximations. In particular, one failing of the scaling models is the assumption that all chains stretch to the same height and do not fluctuate in their extension. In contrast, self-consistent field (SCF) models (Milner et al., 1988; Dolan and Edwards, 1975), working upon the assumption that the chains are strongly stretched, place no such constraint on the distribution of chain ends or segment density and calculate the configurations of each segment by introducing a potential field due to the configurations of all other segments. The random walk of an ideal UP chain introduced earlier in the paper thus becomes a random walk in a potential field consisting of a short range wall contribution and a long-range contribution proportional to the concentration profile. The analysis then leads to a parabolic density profile and pressure within the layer. The parabolic profile becomes concave as the curvature of the interface increases. Agreement with the scaling model exponents is found for the planar and spherical geometries, however a $-2/3$ power law is predicted for the density profile in the cylindrical case, while producing the same H_{av} as the scaling approach.

The self-consistent field method neglects fluctuations of the chains about their most probable paths and is thus inappropriate when the density of grafting is low so that the chains are not stretched. One of the most important implications of the SCF analysis is that the force required to compress the brush (or alternatively the force exerted on a particle or object in its vicinity) is reduced so that the SCF brush is effectively "softer" than that of the scaling analysis (discussed further below).

5.2.4. Potential of mean force and brush–brush interactions

The steric repulsion on molecules and objects imposed by the surface attached UPs may be described in terms of the potential of mean force. This describes the interaction of the surface attached chains with other molecules and, in addition to the van der Waals interactions, determines the force at a given separation. Colloidal stability, for example, relies on the balance of the van der Waals attractions between coated particles in solution and the repulsive force, which can be thought of as an osmotic pressure, that arises due to the reduction in entropy within the layer as particles are brought together. Similar effects give rise to forces on an AFM tip as it impinges on the brush (Fig. 9).

The system can be theoretically described in the following manner. Consider a layer of UP, consisting of N segments/chain of size b, end-attached (grafted) to a planar surface (or surface of very low curvature) with distance between attachment points $b \ll \sigma^{-1/2} \ll R$, in a θ solvent ($v = 0$). Scaling analysis then predicts an average height $H_{av} \approx b^{5/6} \sigma^{-1/3} N$ with concentration profile $c \approx Nb^3/\sigma H_{av} \approx b^{4/3} \sigma^{-2/3}$ everywhere within the layer and $c = 0$ else. The UPs are stretched relative to their unperturbed dimensions in the direction normal to the surface and undergo a random walk laterally of size $\approx bc^{-3/4}$. The layer may thus be thought of as consisting of chains of blobs of size $\xi_0 \approx bc^{-3/4}$ close packed and stretching to an average distance H_{av}. Upon compression to $H < H_{av}$ the osmotic pressure within the brush (ignoring the bulk contribution) is given by $\Pi < \Pi_0 \approx kT/\xi^3 \approx kTc^{9/4}/b^3$ due to the entropic cost of confining the chains. In the blob picture, ξ is reduced as the chains are compressed and more closely pack space, so that as a function of distance from the surface:

$$\frac{\Pi}{kT} \approx \left(\frac{H}{H_{av}}\right)^{-9/4} \sigma^{-1/2}. \tag{32}$$

There is also a van der Waals interaction energy (note that for non-identical surfaces this may in some cases result in a repulsive interaction) between the incoming particle/object and the surface. For two planar surfaces separated by a distance D this is given by (per unit area): $F_{van} \approx -A/12\pi D^2$, while for sphere–sphere (radius R_{P1} and R_{P2} and sphere–particle this becomes: $F_{van} \approx (-A/8D)(R_{P1}R_{P2}/(R_{P1} + R_{P2}))$ and $F_{van} \approx -AR_P/6D$, respectively. The variable A here is the Hamaker constant and is typically of the order of 10^{-20} J. These and other simple geometries and the effect of surfaces and media are discussed by Israelachvili (1991). In situations where the van der Waals attractions may be safely ignored Eq. (32) is equivalent to the force exerted on an approaching object. Note that the above holds for a θ solvent (i.e. $v = 0$). A particularly simple relationship between two planar brushes, where d is the distance between grafted molecules, interacting over a distance D (with $D < 2L$ where L is brush thickness) was derived by de Gennes (1985, 1987):

$$P_p(D) \approx \frac{kT}{d^3}\left[\left(\frac{2L}{3D}\right)^{9/4} - \left(\frac{D}{2L}\right)^{3/4}\right]. \tag{33}$$

Consider the interaction of two UPs each tethered by one end to one of two parallel surfaces. The UPs first interact at a separation $H \approx R$ and the interaction leads to a confinement penalty per chain of $F/kT \approx (b/H)^{5/3}$ and an entropic force of $f/kT \approx H^{-8/3}$. For many UPs end-attached to the surfaces at a density σ a similar prediction can be derived, only now with a dependence on σ. Two such brushes interpenetrate each other insignificantly due to the large penalty required by chains on penetration which produces increased local stretching and excluded volume interactions. As a result the brushes may be considered independently and the disjoining pressure in the region between the surfaces is given by Eq. (32). A more sophisticated analysis using the self-consistent field approach (Milner et al., 1988) yields a free energy per unit area for a planar brush:

$$\frac{F}{AkT} \approx Nb^2\sigma\left(\frac{\pi^2}{12}\right)^{1/3}\left(v\sigma b^2\right)^{2/3}\left(\frac{H_{av}}{2H} + \frac{H^2}{2H_{av}^2} - \frac{H^5}{10H_{av}^5}\right) \tag{34}$$

and a disjoining pressure:

$$\frac{\Pi}{kT} \approx \frac{Nb^2\sigma}{H_{av}}\left(\frac{\pi^2}{12}\right)^{1/3}\left(v\sigma b^2\right)^{2/3}\left(\frac{H_{av}^2}{2H^2} - \frac{H}{H_{av}} + \frac{H^4}{2H_{av}^4}\right). \tag{35}$$

Recent work on quenched polyelectrolyte brush–brush interactions has provided a prediction for the types of energies and forces in these systems (Tamashiro et al., 2001). The approach involves application of the non-linear Poisson–Boltzmann equation for ion concentrations and electrostatics balanced with the entropic elastic energy of ideal Gaussian chains for the surface attached polyelectrolytes. The system geometry is flat on flat with the two brush surfaces separated by a distance 2D and with brush surface heights H. The Poisson–Boltzmann equation is solved analytically with continuity of the electrostatic potential at the two grafting surfaces and at the edges of the brush. The resulting free energy for flat on flat surfaces is then converted into an expression for the force between two-crossed cylinders or a sphere on flat interaction using the Derjaguin approximation (Israelachvili, 1991).

$$\frac{F}{R_{probe}} = 4\pi\kappa^{-1}c_s k_B T\Delta\omega_{PB}, \tag{36}$$
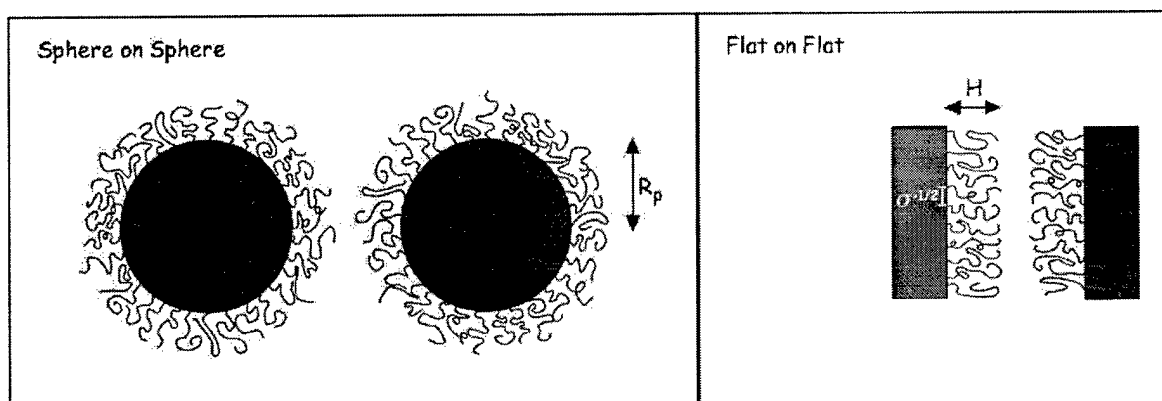
Fig. 9. Interaction geometries of polymer brushes. (A) Two UP-protein coated spheres interacting. (B) Two UP-protein coated flat surfaces interacting.

where $\Delta\omega_{PB} \equiv \omega_{PB}(d) - \overline{\omega_{PB}}$ and

$$-\omega_{PB} = 4d \sinh^2 \frac{\psi_d}{2} + \frac{4}{\lambda}\psi_h + 2\int_{\phi_0}^{\phi_h} d\psi \Delta_1(\psi_0, \psi) - 4\Delta_0(\psi_d, \psi_h)\cosh\frac{\psi_h}{2}$$
$$- 8\varepsilon(\psi_d, \psi_h)\cosh\frac{\psi_d}{2} \tag{37}$$

is the reduced Poisson–Boltzmann grand potential with

$$\Delta_n(\psi_1, \psi_2) \equiv \sqrt{2\cosh\psi_2 - 2\cosh\psi_1 + \frac{4n}{\lambda h}(\psi_2 - \psi_1)} \tag{38}$$

and

$$\varepsilon(\psi_1, \psi_2) \equiv E\left(\arccos\left[\frac{\sinh\frac{\psi_1}{2}}{\sinh\frac{\psi_2}{2}}\right], \frac{1}{\cosh\frac{\psi_1}{2}}\right) \tag{39}$$

and $E(\psi, k)$ is the elliptic integral of the second kind. The resulting predictions of this theory were tested against surface forces apparatus experiments for poly(ter-butyl styrene)-sodium-sodium poly(styrene sulfonate) [PtBS/NaPss] and found to perform well. To compare the theory against the experiments the grafting area per chain was used as an adjustable parameter.

5.2.5. Effect of solvent quality

Solvent quality significantly effects the structure of the UP brush and may be responsible for the success or failure of an UP exclusion mechanism. Earlier in the paper it was shown that an isolated chain in a θ solvent (i.e. $v = 0$) has average dimensions $R_N \approx bN^{1/2}$ i.e. a random walk, reflecting the exact balance of excluded volume interactions with chain entropy, while in a poor solvent ($v < 0$) the effective two body interaction is attractive due to the unfavorable segment–solvent contacts and produces a collapse of the chain so that $R_N \approx bN^{1/3}$. When the surface

attached UP chains overlap to form a layer it is a reasonable assumption that the average brush height should decrease as the mechanisms driving the chains to stretch compete with the tendency toward collapse. Indeed analysis shows that not only is the average height reduced as the solvent quality is reduced, but so is the segment density within the brush (Birshtein and Zhulina, 1984; Grest and Murat, 1993; Halperin and Zhulina, 1991; Milner, 1991). In a poor solvent the density profile decreases less rapidly as the edge of the brush is approached and the free ends are located preferentially at the edge of the brush, reproducing the step profile of the scaling analysis in the case of an extremely poor solvent.

Scaling predictions can easily be obtained by simple Flory energy arguments in which the effect of solvent quality is expressed by the coefficients v and ω introduced earlier for two- and three-body interactions, respectively. It was shown in previous sections that the free energy of a solution with UP present at some volume fraction ϕ could be written as a virial expansion: $F/kT = -\frac{1}{2}(v/b^3)\phi^2 + \frac{1}{6}(\omega/b^6)\phi^3$, resulting in an osmotic pressure: $\Pi/kT = \phi(\delta F/\delta\phi) - F = -\frac{1}{2}(v/b^3)\phi^2 + \frac{1}{3}(\omega/b^6)\phi^3$, ignoring higher order terms. In a brush in a θ solvent $v = 0$ and the three body interactions are balanced by the penalty for chain stretching $\approx kT/Nb^2$. Assuming a uniform density of segments throughout the brush this yields an average height $H_{av} \approx Nb^2\sigma^{1/2}$. In a good solvent, in contrast, the second virial term dominates and leads to a greater contribution from the osmotic pressure and hence a more swollen brush i.e. $H_{av} \approx Nbv^{1/3}\sigma^{1/3}$. In a poor solvent, stretching of the chains is negligible in comparison to the energies associated with the favorable inter segment interactions driving collapse. Here the attractive two body interactions compete with the three body repulsive exclusion term and the average height is $H_{av} \approx b\sigma N/3v$.

In biological systems one is often interested in surfaces with finite curvature, for example the interaction between two roughly spherical proteins or macromolecular assemblies with attached UPs. Consider two such proteins/assemblies separated by a distance $r > R$ where R is the radius of a single (identical) UP attached at one end to one of the proteins (under good solvents conditions $R \approx bN^{3/5}$). The potential of mean force at a separation r can be shown to be: $U(r) \approx (\gamma - 1/v)\ln(R/r)$ where $\gamma = \frac{7}{6}$ and $v \approx \frac{3}{5}$ in a good solvent. For n such UPs attached to each protein at a density $\sigma \approx n/b^2$ the problem may be approached via a blob description in which the fall off in the segment concentration with increasing distance from the surface is captured by an increase in the blob size $\xi(r)$ so that the blobs fill space. Each blob contains $g \approx (\xi/b)^{1/v}$ segments such that $c(r) \approx ng(r) \approx (R_Pb^2/n^{1/2}r)^{4/3}b^{-3}$ and there are $vR_P\sigma^{1/2}\ln(N/R_P\sigma^{1/2})^{5/3}$ blobs per chain. The size of the attached UP layer is: $H_{av} \approx N^{3/5}\sigma^{1/5}R_P^{2/5}$. The scaling approach (Daoud and Cotton, 1982; Dan and Tirrell, 1992; Misra et al., 1989; Miklavic and Marcelja, 1988) is most valid for systems in which $H_{av} \gg R_P$ and is useful in gaining a qualitative picture. It is based on the assumption of high surface curvature and the step function segment density profile obtained for the scaling analysis of a planar brush. However, the interaction potential calculated by this means, $U(r)/kT \approx 4\pi R_P^3\sigma^{3/2}\ln(r/R_T)$, where $R_T = R_P + H_{av}$, is not reproduced by a SCF analysis (Ball et al., 1991; Dan and Tirrell, 1992), which also takes into account the internal structure of the brush and the effect of brush interpenetrations, indicating that the interaction is much steeper so that the repulsion is much stronger.

5.2.6. Charged unstructured polypeptide brushes

Finally, it is necessary to consider the effect of charge on the properties of a UP brush (Pincus, 1991; Misra et al., 1989; Miklavic and Marcelja, 1988; Wittmer and Joanny,

1993b; Zhulina et al., 2000a; Tran et al., 1999; Lyatskaya et al., 1995; Hariharan et al., 1998). We noted earlier that many UPs may possess charged residues and that this may have profound implications on the average properties of the chain. In particular, a UP_E was found to be stretched in comparison to its neutral counterpart, and the introduction of several new length scales (e.g. Γ, κ^{-1}, etc.) was necessary in order to describe the properties of the UP chain.

Analogous to the neutral case discussed above, the average dimensions of a single surface attached UP may be calculated by balancing energy due to chain stretching: $F_{str}/kT \approx R^2/Nb^2$ with the electrostatic energy: $F_{el}/kT \approx (l_B f^2 N^2)/R$ to give $R \approx Nf^{2/3}(l_B/b)^{2/3}$ where it is assumed that the electrostatic interactions are sufficiently strong to stretch the chain beyond its Gaussian dimensions. When the attachment density σ is sufficiently low that interactions between neighboring UPs are negligible, R thus defines a half sphere occupied by the chain. Given the interplay of forces of both electrostatic and non-electrostatic origin it is not surprising that attached UP_Es may lead to "electrosteric stabilization".

5.2.6.1. Effect of polypeptide charge. When considering the behavior of polyelectrolyte brushes, four regimes can be identified (Pincus, 1991; Tran et al., 1999; Wittmer and Joanny, 1993b; Zhulina et al., 2000b). Two of these regimes consider only counter ions to the polymer, while the other two include considerations for added salt. In case one (osmotic or strongly charged regime), with no added salt, the brush height is much greater than the intrinsic screening length and is given by

$$H \cong f^{1/2} Nb. \tag{40}$$

The screening length is the characteristic distance over which a test charge is neutralized, and for this case is:

$$G \equiv d\left(b/4\pi l_B f^{1/2}\right)^{1/2}. \tag{41}$$

Here the disjoining pressure between two flat polyelectrolyte brushes (separated by h), when the brushes are compressed, is

$$\Pi \cong fNT/d^2 h. \tag{42}$$

In the second case (Pincus or weakly charged regime), with no added salt, the brush height is much smaller than the intrinsic screening length and given by

$$H \cong 2\pi l_B N^3 \left(fb/d^2\right). \tag{43}$$

For brushes of this type, the counter ion distribution extends beyond the brush. Here the intrinsic screening length is given by the Gouy–Chapman length, and is $G \equiv d^2/2\pi l_B f$. The disjoining pressure again is Eq. (42).

In the third case (weak screening regime), with added salt, the intrinsic screening length is smaller than κ_b^{-1} (screening due to the added salt) and the brush height is dominated by the intrinsic screening length. In this case the disjoining pressure decays exponentially to zero with increasing salt, as

$$\Pi \cong T\left(\kappa_b/2\pi l_B\right) \exp\left(-\kappa_b h\right). \tag{44}$$
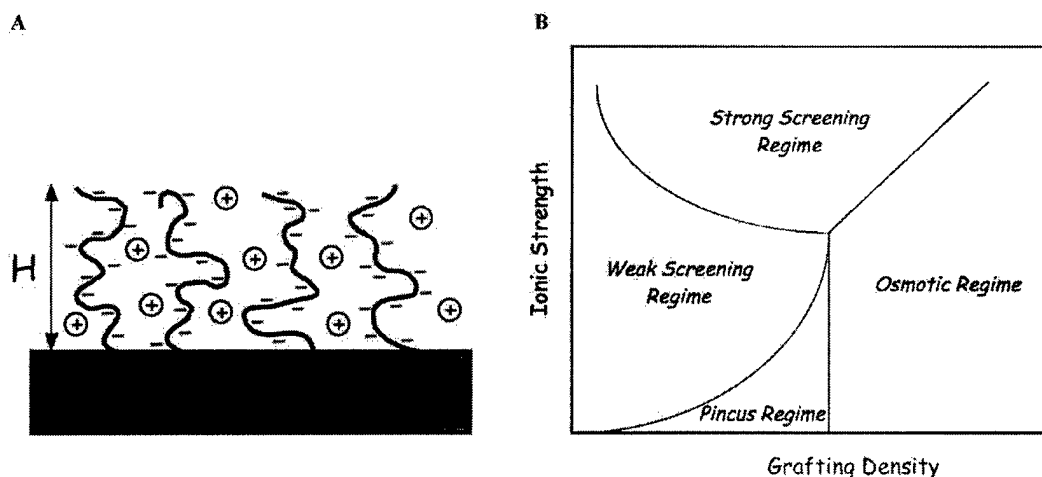
Fig. 10. Behavior of a charged polymer brush. (A) Schematic of a polyelectrolyte brush. (B) States of a polyelectrolyte brush as a function of ionic strength and grafting density. (Adapted from Tran et al., 1999.)

In the fourth case (strong screening regime) the κ_b^{-1} is smaller than the intrinsic screening length, and the brush height is now dependent on the added salt and given by

$$H \cong Nb\left(2bd^2 c_s\right)^{-1/3}. \tag{45}$$

Now the expression for the disjoining pressure has several forms depending on the distance between the brushes. For large distances ($h > H$) the pressure falls off exponentially (as above). For intermediate distance where the $H \geqslant h \geqslant h^*$, and $h^* \equiv N(2d^2 c_s)^{-1}$, the pressure is given by

$$\Pi \cong \left(1/2\right)\left(T/c_s\right)\left(N/d^2 h\right)^2. \tag{46}$$

When $h < h^*$ then disjoining pressure again becomes Eq. (42). Note that all four cases discussed above are electrically neutral, and that the definition of the intrinsic screening length (G) due to counter ion alone may change with regime. The different regimes considered are summarized in Fig. 10.

5.2.6.2. Effect of solvent quality on a charged polypeptide brush. To illustrate the general effect of solvent quality on a polyelectrolyte UP brush (Ross and Pincus, 1992; von Goeler and Muthukumar, 1996; Leermakers et al., 1996; De Kruif and Zhulina, 1996) we take the simplest scenario in which it is assumed that the behavior of the UPs is dominated by contributions from the residues of a single charge type and to the limit of strong charging, with screening dominated by counterions in the layer i.e. $\rho_{\text{cbrush}} > \rho_{\text{cbulk}}$ (Fig. 10). This case is applicable to UPs for which a fraction $f > (N^2 b l_B \sigma)^{-2/3}$ of segments that are charged i.e. if $N \approx 50$ segments of size ~ 2 amino acids and $l_B \approx b$ (physiological), and the UPs are attached at a separation $\sim 3b$ for example, this requires $f > \approx 0.024$ charged and is easily satisfied. The free energy consists of an electrostatic contribution, dominated by the entropic cost of localizing counterions: $F_{en}/kT \approx f\rho_{\text{cbrush}} \approx f\phi \approx fNb^3\sigma/H$, where ϕ is the volume fraction of segments, a segment interaction contribution, characterized by the virial coefficients v and ω: $F_{\text{int}}/kT \approx -\frac{1}{2}(v/b^3)\phi^2 + \frac{1}{6}(\omega/b^6)\phi^3$,

and the entropic cost associated with chain stretching: $F_{str}/kT \approx H\sigma/2Nb^2$. Assuming a step function segment density profile as in all our earlier discussions $\phi \approx Nb^3\sigma/H$ we then obtain a total free energy:

$$\frac{F}{kT} = N\sigma\left(f \ln \phi - \frac{1}{2}\tilde{v}\phi + \frac{1}{6}\tilde{\omega}\phi^2 + \frac{1}{2}\frac{b^4\sigma^2}{\phi^2}\right), \tag{47}$$

where the tildas denote a scaling by b^3. Three limits can immediately be identified:

(i)　strong charge fractions and weak excluded volume interactions,
(ii)　small charge fractions and weak excluded volume interactions,
(iii)　small charge fractions and strong excluded volume interactions.

Case (i) corresponds to a charged UP brush in a good solvent. $-\frac{1}{2}\tilde{v} < 0$ so that the coefficient of two body interactions $v > 0$ and interactions with solvent molecules are favorable. The average properties of the brush are determined by the balance of the first and last terms in Eq. (47) (electrostatic energy and stretching) to give an average brush height $H_{av} \approx f^{1/2}Nb$. In case (ii) counterion entropy is less significant than the three body interactions and the average dimensions are determined by the balance of the last two terms in Eq. (47): $H_{av} \approx Nb^2\sigma^{1/2}$. The situation thus reproduces the result for a neutral brush in a θ solvent. In case (iii) the unfavorable solvent–segment interactions provide a driving force toward collapse which is ultimately balanced by the three body terms of volume exclusion to give $H_{av} \approx Nb^2\sigma/v$. In this case electrostatics and chain stretching play relatively minor roles.

From the expressions for the average dimensions of the charged brush given above it is clear that by varying either the charge fraction or solvent–segment interaction parameters, the relative strength of the excluded volume as opposed to electrostatic interactions may be altered, resulting in swelling or contraction of the brush. For a UP brush attached at a fixed density, consisting of many charged segments for which the majority experience unfavorable solvent interactions, this has the important implication that collapse may be induced by a sudden change in charge fraction. It is the electrostatic interactions which promote chain stretching in this case: the UPs would otherwise assume collapsed dimensions to minimize segment–solvent contact. The critical charge fraction at which collapse occurs may be estimated to scale as $f_c \approx v^2$. In the collapsed regime the disjoining pressure is substantially reduced: $\Pi/kT \approx \frac{-1}{2}(vN^2\sigma^2/H^2) + \frac{1}{3}(N^3\sigma^3/H^3)$, where $\phi \approx N\sigma/H$, from that in an electrostatically dominated brush: $\Pi/kT \approx fN\sigma/H$ for $d < H$ and $\Pi/kT \approx (2\pi l_B H^2)^{-1}$ for $d > H$, i.e. the UP exclusion mechanism may fail.

5.2.6.3. Effect of added salt on a charged polypeptide brush. The above collapse transition was predicted for the case of a strongly charged brush with screening dominated by the counterions in the UP layer. From the manner in which salt changed the internal structure and dimensions of the brush discussed earlier, it is clear that the presence of salt should also play an important role in a collapse transition of this nature, if present at sufficiently high concentrations. As previously discussed, the effect of the salt ions is to screen the electrostatic interactions on the scale of the Debye screening length κ^{-1}. In contrast to its role in the bulk, the salt only significantly alters an UP brush's behavior when $\kappa^{-1} < L_C$. When this is the case (strong screening) the osmotic pressure due to the counterions, promoting UP stretching, is reduced and the brush collapses as the

salt concentration is increased. In the presence of salt the osmotic pressure is given by: $\Pi/kT = C(\kappa_C/(\kappa_C^2 + \kappa_S^2)^{1/2})^2$. For $\kappa_S \gg \kappa_C$ this corresponds to an effective excluded volume $v_{\text{eff}} = 4\pi l_B/\kappa_S^2$ and $\Pi/kT \approx c^2/2c_s$, i.e. the mechanism promoting brush swelling is reduced. Some of the predictions of the above scaling treatments and those of numerical analysis (e.g. SCF) have been tested by comparison with experiments (Hariharan et al., 1998; Tran et al., 1999) and good agreement with the theories is found.

5.2.6.4. Interaction with proteins and other finite objects. The interaction of isolated tethered polymers and polymer brushes with finite objects and particles has attracted a great deal of interest and analysis via scaling (Jeon et al., 1991; Subramanian et al., 1996; Martin and Wang, 1995; Halperin, 1999, SCF (Szleifer, 1997; Szleifer and Carignano, 2000; Steels et al., 2000) and simulation (Grest and Murat, 1993, 1989; Jiminez and Rajagopalan, 1998; Milchev et al., 1999) studies. Interaction events are of particular interest in biological situations where the function of surface attached UPs may be to exclude certain foreign objects (e.g. based on their size) and also in experiments on such systems where the experimental probe, such as an AFM tip, has a finite diameter and geometric and alignment issues. For biocompatability (Elbert and Hubbell, 1998; Woodle and Lasic, 1992) one requires prevention of protein adsorption to the surface. Thrombosis, for example, may be induced by adsorption of plasma proteins when blood is exposed to foreign materials. Such adsorption may be prevented by the attachment of polymers (Horbett et al., 1986) and there is now a growing amount of literature aimed at obtaining simple theories for these events. Similarly, the constraints and interpretation of the experimental systems (particularly force measurements) have motivated simulations and theoretical studies of common systems. We shall discuss here two scenarios: (1) penetration of (or alternatively exclusion from) UP brushes by small proteins, and (2) deformation and compression by objects such as an AFM tip. In the former we are interested primarily in the size determined capability of an object to penetrate the brush and the resultant rate of approach to the surface if penetration occurs, while in the latter we are motivated primarily by the experimental setting and discuss briefly force measurements and UP deformation.

Case (1) has been studied in recent years via numerical, experimental and theoretical methods. As we have done in the majority of this paper we will focus here on a relatively simple theoretical model (Alexander, 1977; Halperin, 1999) for illustrative purposes. The treatment is applicable to flexible polypeptides. The backbone is considered homogeneous and solvent–UP interactions favorable (good solvent). The protein interaction with the UPs is similarly devoid of structure: a densely packed sphere for example.

The potential of interaction of the approaching protein with the UPs consists of the van der Waals attraction between a sphere and a flat surface, $U_V = -AR_P/6H$, where R_P is the protein radius and H is the distance from the surface, and a repulsive potential arising from the entropic penalty for penetrating the brush, manifested in the osmotic pressure as discussed earlier. U_V is fixed by the protein size while the brush potential U_B is determined by the attachment density σ and the average height of the brush H_{av} and its range and strength may be controlled by variation of these parameters. The ratio R_P/H_{av} however is what critically determines the success/failure of protein exclusion. Fig. 11 is a schematic illustration of the manner in which attached UPs could exclude large proteins and other macromolecules while allowing permeation of smaller molecules such as water. The larger protein (R_{P1}) is prevented access to the surface but may compress the
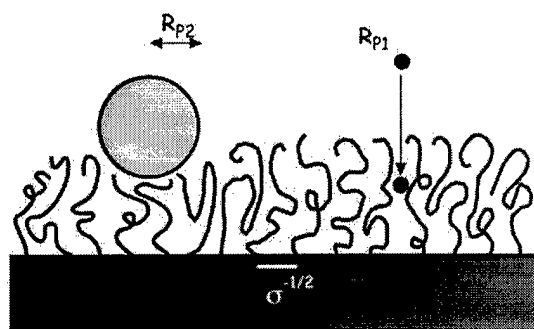
Fig. 11. Exclusion of molecules from a surface by a polymer brush. The brush behaves like an entropic spring and excludes large molecules or particles. Molecules that are small relative to the brush height can penetrate.

layer, in order to gain an increased free energy benefit by proximity to the surface, until the force imparted by the "entropic springs" prevents closer approach. In contrast, the smaller protein/ molecule (R_{P2}) can permeate the layer.

The size of the correlation blobs of the unperturbed brush $\xi \approx \sigma^{1/2}$ is also the length scale at which the proteins rate of passage suffers due to the presence of the UP chains i.e. the osmotic repulsion mechanism becomes significant. Using Kramers theory (Kramers and Wannier, 1941) Halperin (1999) shows that for $\xi < R_P \ll H_{av}$, the rate constant k_{ads} is given by

$$k_{ads} \approx \frac{kT}{\eta_S R_P H_{av}^2} \left(\frac{\sigma^{1/2}}{R_P}\right)^3 \exp\left(-\left(\frac{R_P}{\sigma^{1/2}}\right)\right)^3 \tag{48}$$

i.e. as the ratio $R_P/\sigma^{1/2}$ increases, the rate of approach of the protein to the surface is decreased and the protein's diffusion constant: $D_P \approx kT/\eta R_P \approx kT/\eta_S R_P(\sigma^{1/2}/R_P)^3$ is much less than in the absence of the brush: $D_{P0} \approx kT/\eta_S R_P$. When $R_P/\sigma^{1/2} < 1$ the UP chains are sparsely attached relative to the size of the protein and passage is unperturbed. In contrast, when $R_P/H_{av} \ll 1$ the protein may approach the surface and perturbation of the brush is small. Approach is then opposed by the hydrodynamic drag force $f \approx \eta R_P v$ where η is the effective viscosity and v is the velocity of the protein. As the surface–protein separation is decreased and the van der Waals attraction becomes very strong adsorption at the surface rather than the outer edge of the brush becomes possible.

Case (2) has a few simple limits that have proved insightful. One of the first of these is for a single polymer attached to a flat surface with a second probe surface (such as an AFM tip) approaching from above. The resulting prediction for the free energy penalty is readily derived by a collisional argument for interactions between the polymer and a wall (Grosberg and Khokhlov, 1994):

$$\frac{F}{k_B T} = \frac{Nb^2}{H^2}, \tag{49}$$

where b is the bead size, H is the distance between the grafting surface and the wall, and N is the chain length. When the interaction is between a cylindrical probe surface of cross-sectional area A_1 approaching a surface with neutral brush height of H_0, then the free energy change with

compression can be defined by the change between those parts of the brush compressed by the cylinder and those parts not compressed. This leads to the following expression:

$$\frac{F}{kT} = Af_0 \left[1 + \frac{5}{3}\left(\frac{A_1}{A}\right)\left(\frac{c}{H_0}\right)^3 + \frac{2}{3}\left(\frac{A_1}{A}\right)\left(\frac{c}{H_0}\right)^5 + \frac{5}{9}\left(\frac{A_1}{A}\right)\left(\frac{c}{H_0}\right)^6 \left(\frac{1}{1 - (c/H_0)}\right) \right], \tag{50}$$

where c is the extent of compression of the brush (deviation from equilibrium) and f_0 is the unperturbed energy per unit area (Subramanian et al., 1996).

One of the most interesting predictions for an UP–object interaction is found for the simple case of a cylinder of diameter D held at a distance H above a planar surface to which the UP of length bN is end-attached. In both good (Subramanian et al., 1995, 1996) and θ (Guffond et al., 1997) solvents a first order escape transition, and hysterisis upon retraction of the object for a uniformly compressed to a partially escaped state, has been predicted. The prediction rests on energy balance arguments: when the UP in a good solvent for example is compressed by an object (assumed to be of size $D > \approx bN^{3/5}$) to a height H less than its unperturbed dimensions it suffers a confinement penalty. If the object is very large then compression is uniform and a force $f/kT \approx Nb^{5/3}H^{-8/3}$ must be applied to further reduce H. If, however, the object is finite it may be possible for some segments of the UP to avoid confinement by the chain stretching as a tether to the edge of the confinement region. As was the case in a UP brush, stretching requires a penalty in the free energy which must be balanced with the benefits of entropic gain. Simple arguments lead to a critical object-surface distance $H_{av} \approx N^{3/2}b^{5/2}/D^{3/2}$. Since escape corresponds to sudden drop in the chain dimensions, the transition is reflected in a sudden decrease in the force required to compress the UP. In a θ solvent ($v = 0$) the UP escapes at $H \approx Nb^2/D$ i.e. roughly the ratio of the mean squared end to end distance of the chain to the object diameter. In both cases a large energy barrier is present at weak compressions, leading to the possibility for hysterisis in the force curve. When the object is misaligned with the surface so that H is non-uniform (e.g. a step) there is a competition between escape under strong compression with a relatively short tether and weak compression with a long tether (Guffond et al., 1997). This competition leads to the possibility of multiple transitions and corresponding drops in the force curve.

In the brush limit the scaling approach is based upon the assumption that the object compresses only those segments directly beneath it, leaving the remainder of the brush unperturbed. For a brush of total area A, attached at density σ to the surface, the force exerted on the incoming object is (in the limit of small D/A): $f \approx (-D^2/A)((H_{av} - H)^2/h^3)$ and is repulsive at all distances. Simulations in contrast indicate that the assumption of uniform compression of chains under the tip is inappropriate, and that in fact the chains splay in order to avoid compression (Grest and Murat, 1993), resulting in a less sharp rise in the force required to compress the chain as the surface-object distance is decreased. This "splaying" effect is more pronounced for smaller objects and is reflected in a local decrease in the segment density under the object. The implications of "splaying" are further addressed in recent SCF calculations in which the full segment density profile within the brush have been considered (Dan and Tirrell, 1992).

Not all neutral UPs will fall into the range of the predictions above. Some UPs may be intrinsically stiff so that the chains tend not to compress elastically but rather undergo a bending deformation in the presence of the approaching object. For a rod-like UP (l_p/L) the energy associated with bending the rod (assuming small deformation) is $F/kT \approx (l_p(1 - (H/L))/2L)$ and

Table 1
Summary of important equations presented. See main text for details

Property	Equation	Notes
Radius of gyration	$R_g = \dfrac{1}{6} b N^{1/2}$	Freely jointed chain model Neutral homopolymer, No chain interactions
Radius of gyration	$\left\langle R_g^2 \right\rangle^{1/2} \approx b N^{\mu}$	Accounts for solvent and volume effects μ is $1/3$, $1/2$ and 0.588 in poor, theta and good solvents, respectively
Radius of gyration	$\left\langle R_g^2(L) \right\rangle = \dfrac{1}{3} l_p L - l_p^2$	Wormlike chain model Finite length and flexibility
Radius of gyration	$\left\langle R_g^2 \right\rangle = \dfrac{L l_p}{3} l_p^2 + \dfrac{2 l_p^3}{L} - \dfrac{2 l_p^4}{L^2}\left(1 - \exp\left(-\dfrac{L}{l_p}\right)\right)$ $+ \dfrac{2 l_p^3}{L}\left(1 - \dfrac{l_p}{L}\left(1 - \exp\left(-\dfrac{L}{l_p}\right)\right)\right)$	Polyelectrolytes
Brush height	$H_{av} \approx b\gamma^{-3/2}$	Single neutral polymer Balance energy of contact adsorption and entropic loss in configurations
Brush height	$H_{av} \approx N\sigma^{1/3}$	Neutral polymer brush Balance of enthalpic and entropic terms
Brush height	$H_{av} \cong Nb\left(2bd^2 c_s\right)^{-1/3}$	Polyelectrolyte brush Strong screening limit
Brush height	$H_{av} \cong 2\pi l_B N^3 \left(fb/d\right)^2$	Polyelectrolyte brush Weakly charged (no added salt)
Brush: brush compression	$P_P(D) \approx \dfrac{kT}{d^3}\left[\left(\dfrac{2L}{3D}\right)^{9/4} - \left(\dfrac{D}{2L}\right)^{3/4}\right]$	Neutral brushes on flat surfaces $D < 2L$ (interacting)
Brush: brush compression	$\dfrac{F}{R_{Probe}} = 4\pi K^{-1} n_s k_B T \Delta\omega_{PB}$	Quenched polyelectrolyte brushes
Single chain compression	$\dfrac{F}{kT} = \dfrac{Nb^2}{H^2}$	Free energy penalty Single (neutral) chain between two surfaces
Brush compression	$\dfrac{F}{kT} = Af_0\left[1 + \dfrac{5}{3}\left(\dfrac{A_1}{A}\right)\left(\dfrac{c}{H_0}\right)^3 + \dfrac{2}{3}\left(\dfrac{A_1}{A}\right)\left(\dfrac{c}{H_0}\right)^5 \right.$ $\left. + \dfrac{5}{9}\left(\dfrac{A_1}{A}\right)\left(\dfrac{c}{H_0}\right)^6\left(\dfrac{1}{1 - (c/H_0)}\right)\right]$	Cylinder of area A_1 compressing a neutral polymer brush

results in a force for compression $f/kT \approx l_p/2L^2$. If the approaching object is sufficiently small that the rod can bend to its edge then an escape transition may be found at a critical deformation angle, with a sharper drop in the force required to compress the UP than in the flexible chain case. In a brush of stiff chains end-attached with density σ as before, the force required for compression is more sensitive to the extent of deformation of the chains and may result in all chains escaping from the vicinity of the object for strong compressions.

6. Summary

Here we have taken the position that intrinsically unstructured proteins have functionally important properties that can be understood and predicted using polymer theory developed to describe average properties of molecules and molecular assemblies, such as radius of gyration, height of a polymer brush and force required to compress a polymer brush. Thus we have reviewed polymer theory that we believe is relevant to the problem of predicting properties of unstructured proteins. To provide an overview of some of the central equations discussed we present a summary table (Table 1). The polymer theory presented has to a limited extent been applied to proteins, although it remains to be seen how well it will perform when more widely used. It is likely that many shortcomings will become apparent, and we hope that this will prompt the development of polymer models and theories that are directed at understanding properties of intrinsically unstructured proteins.

Acknowledgements

References

Alexander, S., 1977. Adsorption of chain molecules with a polar head—a scaling description. J. Phys. (Paris) 38, 983–987.

Balazs, A.C., DeMeuse, M.T., 1989. Miscibility in ternary mixtures containing a copolymer and two homopolymers—effect of sequence distribution. Macromolecules 22, 4260–4267.

Balazs, A.C., Sanchez, I.C., Epstein, I.R., Karasz, F.E., MacKnight, W.J., 1985. Effect of sequence distribution on the miscibility of polymer/copolymer blends. Macromolecules 18, 2188–2191.

Ball, R.C., Marko, J.F., Milner, S.T., Witten, T.A., 1991. Polymers grafted to a convex surface. Macromolecules 24, 693–703.

Barrat, J.L., Joanny, J.-F., 1996. Theory of polyelectrolyte solutions. Adv. Chem. Phys. 94, 1–66.

Birshtein, T.M., Zhulina, E.B., 1984. Conformations of star-branched macromolecules. Polymer 25, 1453–1461.

Bloomfield, V.A., 1991. Condensation of DNA by multivalent cations—considerations on mechanism. Biopolymers 31, 1471–1481.

Boyd, R.H., Phillips, P.J., 1993. The science of polymer molecules. Cambridge Solid State Science Series, p. 197

Brown, H.G., Hoh, J.H., 1997. Entropic exclusion by neurofilament side-arms: a mechanism for maintaining interfilament spacing. Biochemistry 36, 15035–15040.

Cates, M.E., Brooks, J.T., 1993. Non-equilibrium effects in polymeric stabilization. Polymer Surf. Interf. II, 49–70.

Creighton, T. E., 1992. Proteins: Structures and Molecular Properties, 2nd Edition. W.H. Freeman, New York, pp. 512.

Damaschun, G., Damaschun, H., Gast, K., Misselwitz, R., Muller, J.J., Pfeil, W., Zirwer, D., 1993. Cold denaturation-induced conformational changes in phosphoglycerate kinase from yeast. Biochem. 32, 7739–7746.

Damaschun, G., Damaschun, H., Gast, K., Zirwer, D., 1999. Proteins can adopt totally different folded conformations. J. Mol. Biol. 291, 715–725.

Dan, N., Tirrell, M., 1992. Polymers tethered to curved interfaces. A self-consistent-field analysis. Macromolecules 25, 2890–2895.

Daoud, M., Cotton, J.P., 1982. Star shaped polymers: a model for the conformation and its concentration dependence. J. Phys. II 43, 531–538.

Daoud, M., Jannink, G., 1976. Temperature–concentration diagram of polymer solutions. J. Phys. (Paris) 37, 973–979.

Darden, T., York, D., Pedersen, L., 1993. Particle mesh ewald—an $N. \log(N)$ method for ewald sums in large systems. J. Chem. Phys. 98, 10089–10092.

de Gennes, P.-G., 1969. Some conformation problems for long macromolecules. Rep. Prog. Phys. 32, 187.

de Gennes, P.-G., 1971. Scaling Concepts in Polymer Physics, Cornell University Press, New York, pp. 324.

de Gennes, P.-G., 1980. Conformations of polymers attached to an interface. Macromolecules 13, 1069–1075.

de Gennes, P.-G., 1985. Films of polymer solutions. C. R. Acad. Sci. (Paris) 300, 839–843.

de Gennes, P.-G., 1987. Polymers at an interface—a simplified view. Adv. Coll. Interf. Sci. 27, 189–209.

de Gennes, P.-G., Pincus, P., Velasco, R.M., Brochard, F., 1976. Remarks on polyelectrolyte conformation. J. Phys. (Paris) 37, 1461–1473.

De Kruif, C.G., Zhulina, E.B., 1996. Kappa-casein as a polyelectrolyte brush on the surface of casein micelles. Colloids Surfaces A 117, 151–159.

Dickinson, E., Stainsby, G., 1982. Colloids in Food. Applied Science, London, pp. 533.

Diehl, A., Barbosa, M.C., Levin, Y., 1996. Neutral polyampholyte in an ionic solution. Phys. Rev. E 54, 6516–6525.

Dill, K.A., 1990. Dominent forces in protein folding. Biochem. 29, 7133–7155.

Dobrynin, A.V., Rubinstein, M., 1995. Flory theory of a polyampholyte chain. J. Phys. II 5, 677–695.

Dobrynin, A.V., Rubinstein, M., Obukhlov, S.P., 1996. Cascade of transitions of polyelectrolytes in poor solvents. Macromolecules 29, 2974–2979.

Doi, M., Edwards, S. F., 1986 The Theory of Polymer Dynamics. Clarendon Press, Oxford, pp. 391.

Dolan, A.K., Edwards, S.F., 1975. Effect of excluded volume on polymer dispersant action. Proc. Royal Soc. London A 343, 427–442.

Dunker, A.K., Ensign, L.D., Arnold, G.E., Roberts, L.M., 1991. Proposed molten globule intermediates in fd phage penetration and assembly. FEBS Lett. 292, 275–278.

Dunker, A.K., Lawson, J.D., Brown, C.J., Williams, R.M., Romero, P., Oh, J.S., Oldfield, C.J., Campen, A.M., Ratliff, C.M., Hipps, K.W., Ausio, J., Nissen, M.S., Reeves, R., Kang, C., Kissinger, C.R., Bailey, R.W., Griswold, M.D., Chiu, W., Garner, E.C., Obradovic, Z., 2001. Intrinsically disordered protein. J. Mol. Graph. Model. 19, 26–59.

Edwards, S.F., King, P.R., Pincus, P., 1980. Phase changes in polyampholytes. Ferroelectrics 30, 3–6.

Elbert, D.L., Hubbell, J.A., 1998. Self-assembly and steric stabilization of heterogeneous biological surfaces using adsorbing block copolymers. Chem. Biol. 5, 177–183.

Flory, P.J., 1942. Thermodynamics of high polymer solutions. J. Chem. Phys. 10, 51–61.

Flory, P.J., 1969. Statistical Mechanics of Chain Molecules. Wiley, New York, pp. 432.

Freed, K. F., 1987. Renormalization Group Theory of Macromolecules. J. Wiley, New York, pp. 361.

Garner, E., Cannon, P., Romero, P., Obradovic, Z., Dunker, A.K., 1998. Predicting disordered regions from amino acid sequence: common themes despite differing structural characterization. Genome Informatics 9, 201–213.

Goulian, M., Bruinsma, R., Pincus, P.A., 1993. Long-range forces in heterogeneous fluid membranes. Europhys. Lett. 22, 145–150.

Grest, G.S., Murat, M., 1989. Structure of a grafted polymer brush—a molecular dynamics simulation. Macromolecules 22, 4054–4059.

Grest, G.S., Murat, M., 1993. Structure of grafted polymeric brushes in solvents of varying quality: a molecular dynamics study. Macromolecules 26, 3108–3117.

Grest, G.S., Kremer, K., Witten, T.A., 1987. Structure of many-arm star polymers—a molecular-dynamics simulation. Macromolecules 20, 1376–1383.

Grosberg, A.Y., 1979. Certain possible conformational states of a uniform elastic polymer chain. Biofizaka 24, 32–37.

Grosberg, A.Y., Khokhlov, A. R., 1994. Statistical Physics of Macromolecules. AIP Press, New York, pp. 350.

Guffond, M.C., Williams, D.R.M., Sevick, E.M., 1997. End-tethered polymer chains under AFM tips: compression and escape in theta solvents. Langmuir 13, 5691–5696.

Ha, B.Y., Thirumalai, D., 1997. Persistence length of intrinsically stiff polyampholyte chains. J. Phys. II 7, 887–902.

Hakansson, C., Elvingson, C., 1994. Semiflexible chain molecules with nonuniform curvature. 1. Structural-properties. Macromolecules 27, 3843–3849.

Halperin, A., 1999. Polymer brushes that resist adsorption of model proteins: design parameters. Langmuir 15, 2525–2533.

Halperin, A., Zhulina, E.B., 1991. Stretching polymer brushes in poor solvents. Macromolecules 24, 5393–5397.

Hariharan, R., River, C., Mays, J., Russel, W.B., 1998. Ionic strength and curvature effects in flat and highly curved polyelectrolyte brushes. Macromolecules 31, 7506–7513.

Haronska, P., Wilder, J., Vilgis, T.A., 1997. On the elastic behavior of a single polyelectrolyte chain. J. Phys. II 7, 1273–1285.

Higgs, P.G., Joanny, J.-F., 1991. Theory of polyampholyte solutions. J. Chem. Phys. 94, 1543–1554.

Hockney, R.W., Eastwood, J.W., 1981. Computer Simulation using Particles. McGraw-Hill, New York, pp. 540.

Hoh, J.H., 1998. Functional protein domains from the thermally driven motion of polypeptide chains: a proposal. Proteins 32, 223–228.

Hong, Q., Schellman, J.A., 1992. Helix-coil theories—a comparative-study for finite length polypeptides. J. Phys. Chem. 96, 3987.

Horbett, T.A., Cheng, C.M., Ratner, B.D., Hoffman, A.S., Hanson, S.R., 1986. The kinetics of baboon fibrinogen adsorption to polymers: in vitro and in vivo studies. J. Biomed. Mater. Res. 20, 739–772.

Huggins, M.L., 1942. Thermodynamic properties of solutions of long-chain compounds. Ann. New York Acad. Sci. 41, 1–32.

Israelachvili, J. N., 1991. Intermolecular Forces. Academic Press, San Diego, pp. 450.

Jeon, S.I., Lee, J.H., Anderade, J.D., de Gennes, P.-G., 1991. Protein-surface interactions in the presence of polyethylene oxide. J. Coll. Interf. Sci. 142, 149–158.

Jimenez, J., Rajagopalan, R., 1998. A new simulation method for the determination of forces in polymer/colloid systems. Eur. Phys. J. B 5, 237–243.

Johner, A., Joanny, J.-F., 1991. Polymer adsorption in a poor solvent. J. Phys. II 1, 181–194.

Johner, A., Brochard, F., Daoud, M., 1990. Stretching of a polymer by an attractive wall. J. Phys. (Paris) 51, 495–502.

Kantor, Y., Kardar, M., 1994. Excess charge in polyampholytes. Europhys. Lett. 27, 643–648.

Kantor, Y., Kardar, M., 1995. Instabilities of charged polyampholytes. Phys. Rev. E 51, 1299–1312.

Kantor, Y., Kardar, M., Ertas, D., 1998. Necklace model of randomly charged polymers. Physica A 249, 301–306.

Kellermayer, M.S., Smith, S., Bustamante, C., Granzier, H.L., 2000. Mechanical manipulation of single titin molecules with laser tweezers. Adv. Exp. Med. Biol. 481, 111–126.

Khokhlov, A.R., 1980. Collapse of weakly charged poly-electrolytes. J. Phys. A 13, 979–987.

Kramers, H.A., Wannier, G.H., 1941. Statistics of the two-dimensional ferromagent. Phys. Rev. 60, 252.

Kratky, O., Porod, G., 1949. Rontgenuntersuchung geloster fadenmolekule. Recl. Trav. Chim. 68, 1106–1122.

Kriwacki, R.W., Hengst, L., Tennant, L., Reed, S.I., Wright, P.E., 1996. Structural studies of p21 Waf1/Cip1/Sdi1 in the free and Cdk2-bound state: conformational disorder mediates binding diversity. Proc. Natl. Acad. Sci. USA 93, 11504–11509.

Leermakers, F.A.M., Atkvison, P.J., Dickinson, E., Horne, D.S., 1996. Self consistent field modeling of adsorbed beta-casein: effects of pH and ionicstrength on surface coverage and density profile. J. Coll. Interf. Sci. 178, 681–693.

Lipowsky, R., 1995. The morphology of lipid membranes. Curr. Opin. Struct. Biol. 5, 531–540.

Long, D., Dobrynin, A.V., Rubinstein, M., Adjari, A., 1998. Electrophoresis of polyampholytes. J. Chem. Phys. 108, 1234–1244.

Loomans, D., Schiessel, H., Blumen, A., 1997. Biased reptation of polyampholytes: trapping and enhancement effects. J. Chem. Phys. 107, 2636–2642.

Lyatskaya, Y.V., Leermakers, F.A.M., Fleer, G.J., Zhulina, E.B., Birshtein, T.M., 1995. Analytic self-consistent-field model of weak polyacid brushes. Macromolecules 28, 3562–3569.

Mandel, M., 1988. Polyelectrolytes. In: Kroschwitz, J.I. (Ed.), Encyclopedia of Polymer Science and Engineering, Vol. 11. Wiley, New York.

Marko, J.F., Siggia, E.D., 1997. Polymer models of meiotic and mitotic chromosomes. Mol. Biol. Cell 8, 2217–2231.

Martin, J.I., Wang, Z.G., 1995. Polymer brushes: scaling, compression forces, interbrush penetration and solvent size effects. J. Phys. Chem. 99, 2833–2844.

Miklavic, S.J., Marcelja, S., 1988. Interaction of surfaces carrying grafted poly-electrolytes. J. Phys. Chem. 92, 6718–6722.

Milchev, A., Binder, K., 1998. A polymer chain trapped between two parallel repulsive walls: a Monte-Carlo test of scaling behaviour. Eur. Phys. J. B 3, 477–484.

Milchev, A., Yamakov, V., Binder, K., 1999. Escape transition of a polymer chain: phenomological theory and MC simulations. Phys. Chem. Chem. Phys. 1, 2083–2091.

Miller, W.G., Goebel, C.V., 1968. Dimensions of protein random coils. Biochem. 7, 3925–3935.

Milner, S.T., 1991. Polymer brushes. Science 251, 905–914.

Milner, S.T., Witten, T.A., Cates, M.E., 1988. A parabolic density profile for grafted polymers. Europhys. Lett. 5, 413–418.

Misra, S., Varanasi, S., Varanasi, P.P., 1989. A poly-electrolyte brush theory. Macromolecules 22, 4173–4179.

Mueller, H., Butt, H.J., Bamberg, E., 1999. Force measurements on myelin basic protein adsorbed to mica and lipid bilayer surfaces done with the atomic force microscope. Biophys. J. 76, 1072–1079.

Mukhopadhyay, R., Hoh, J.H., 2001. AFM force measurements on microtubule-associated proteins: the projection domain exerts a long-range repulsive force. FEBS Lett. 505, 374–378.

Murat, M., Grest, G.S., 1991. Polymers end-grafted onto a cylindrical surface. Macromolecules 24, 704–708.

Muroga, Y., 1988. Conformational-analysis of broken rodlike chains. 1. Scattering function of rods joined together by flexible coils. Macromolecules 21, 2751–2755.

Muroga, Y., 1992. Particle scattering function and the radius of gyration for a broken rodlike chain having a length distribution of constituents. Macromolecules 25, 6063–6065.

Muroga, Y., 2000. Applicability of broken-rodlike chain model to conformational analysis of polypeptide chain. Biopolymers 54, 58–63.

Napper, D.M., 1983. Polymeric Stabilization of Colloidal Dispersions. Academic Press, New York, pp. 428.

Odijk, T., 1977. Polyelectrolytes near rod limit. J. Polym. Sci. Phys. 15, 477–483.

Pappu, R.V., Srinivasan, R., Rose, G.D., 2000. The flory isolated-pair hypothesis is not valid for polypeptide chains: implications for protein folding. Proc. Natl. Acad. Sci. USA 97, 12565–12570.

Patel, S.S., Tirrell, M., 1989. Measurement of forces between surfaces in polymer fluids. Ann. Rev. Phys. Chem. 40, 597–635.

Penkett, C.J., Redfield, C., Jones, J.A., Dodd, I., Hubbard, J., Smith, R.A., Smith, L.J., Dobson, C.M., 1998. Structural and dynamical characterization of a biologically active unfolded fibronectin-binding protein from staphylococcus aureus. Biochem. 37, 17054–17067.

Pfeuty, P., 1978. Conformations des polyelectrolytes ordre dans les solutions de polyelectrolytes. J. Phys. France 39, C2–149.

Pincus, P.A., 1991. Colloid stabilization with long grafted polyelectrolytes. Macromolecules 24, 2912–2919.

Poland, D., Scheraga, H.A., 1970. Theory of Helix-coil Transitions in Biopolymers: Statistical Mechanical Theory of Order–Disorder Transitions in Biological Macromolecules. Academic Press, New York, pp. 797.

Porod, G., 1949. Zusammenhang zwischen mittlerem endpunktsabstand und kettenlange bei fadenmolekulen. Monatsh. Chem. 80, 251–255.

Raphael, E., Joanny, J.-F., 1990. Annealed and quenched polyelectrolytes. Europhys. Lett. 13, 623–628.

Romero, P., Obradovic, Z., Kissinger, C.R., Villafranca, J.E., Garner, E., Guilliot, S., Dunker, A.K., 1998. Thousands of proteins likely to have long disordered regions. Pac. Symp. Biocomput. 3, 437–448.

Ross, R.S., Pincus, P.A., 1992. The polyelectrolyte brush: poor solvent. Macromolecules 25, 2177–2183.

Russel, W.B., Saville, D., Schowalter, W.R., 1989. Chapter 6. In Colloidal Dispersions. Cambridge University Press, Cambridge, (Chapter 6) pp. 525.

Schaefer, D.W., Joanny, J.-F., Pincus, P., 1980. Dynamics of semiflexible polymers in solution. Macromolecules 13, 1270–1289.

Schiessel, H., Blumen, A., 1996. Instabilities of polyampholytes in external electrical fields. J. Chem. Phys. 105, 4250–4256.

Schiessel, H., Oshanin, G., Blumen, A., 1995. Dynamics and conformational properties of polyampholytes in external electrical fields. J. Chem. Phys. 103, 5070–5074.

Schwalbe, H., Fiebig, K.M., Buck, M., Jones, J.A., Grimshaw, S.B., Spencer, A., Glaser, S.J., Smith, L.J., Dobson, C.M., 1997. Structural and dynamical properties of a denatured protein. Heteronuclear 3D NMR experiments and theoretical simulations of lysozyme in 8M urea. Biochem. 36, 8977–8991.

Sfatos, C.D., Gutin, A.M., Shakhnovich, E.I., 1993. Phase-diagram of random copolymers. Phys. Rev. E 48, 465–475.

Shusharina, N.P., Nyrkova, I.A., Khokhlov, A.R., 1996. Diblock copolymers with a charged block in a selective solvent: micellar structure. Macromolecules 29, 3167–3174.

Skolnick, J., Fixman, M., 1977. Electrostatic persistence length of a wormlike polyelectrolyte. Macromolecules 10, 944–948.

Steels, B.M., Koska, J., Haynes, C.A., 2000. Analysis of brush-particle interactions using self-consistent-field theory. J. Chromatogr. B 743, 41–56.

Soddemann, T., Schiessel, H., Blumen, A., 1998. Molecular-dynamics simulations of polyampholytes: instabilities due to excess charges and external fields. Phys. Rev. E 57, 2081–2090.

Srivastava, D., Muthukumar, M., 1996. Sequence dependence of conformations of polyampholytes. Macromolecules 29, 2324–2326.

Subramanian, G., Williams, D.R.M., Pincus, P.A., 1995. Escape transitions and force laws for compressed polymer mushrooms. Europhys. Lett. 29, 285–290.

Subramanian, G., Williams, D.R.M., Pincus, P.A., 1996. Interaction between finite-sized particles and polymers. Macromolecules 29, 4045–4050.

Szleifer, I., 1997. Protein adsorption on surfaces with grafted polymers: a theoretical approach. Biophys. J. 72, 595–612.

Szleifer, I., Carignano, M.A., 2000. Tethered polymer layers: phase transitions and reduction of protein adsorption. Macromol. Rapid Comm. 21, 423–448.

Tamashiro, M.N., Hernandez-Zapata, E., Schorr, P.A., Balestre, M., Tirrell, M., Pincus, P., 2001. J. Chem. Phys. 115, 1960–1969.

Tanaka, M., Grosberg, A.Y., Pande, V.S., Tanaka, T., 1997. Molecular dynamics study of the structure and organization in a strongly coupled chain of charged particles. Phys. Rev. E 56, 5798–5808.

Timoshenko, E.G., Kuznetsov, Y.A., Dawson, K.A., 1996. Gaussian self-consistent method for the kinetics of heteropolymers: a direction in studying the protein folding problem. Phys. Rev. E 53, 3886–3899.

Tran, Y., Auroy, P., Lee, L.-T., 1999. Determination of the structure of polyelectrolyte brushes. Macromolecules 32, 8952–8964.

Ubbink, J., Odijk, T., 1995. Polymer-induced and salt-induced toroids of hexagonal DNA. Biophys. J. 68, 54–61.

Ubbink, J., Odijk, T., 1996. Deformation of toroidal DNA condensates under surface stress. Biophys. J. 33, 353–358.

Uversky, V.N., Gillespie, J.R., Fink, A.L., 2000. Why are "natively unfolded" proteins unstructured under physiologic conditions? Proteins 41, 415–427.

von Goeler, F., Muthukumar, M., 1996. Stretch-collapse transition of polyelectrolyte brushes in a poor solvent. J. Chem. Phys. 105, 11335–11346.

Walstra, P., Jenness, R., 1984. Dairy Chemistry and Physics. Wiley, New York, pp. 467.

Walstra, P., Bloomfield, V.A., Wei, G.J., Jenness, R., 1981. Effect of chymosin action on the hydrodynamic diameter of casein micelles. Biochim. Biophys. Acta 669, 258–259.

Wittmer, J., Joanny, J.-F., 1993a. Random and alternating polyampholytes. Europhys. Lett. 24, 263–268.

Wittmer, J., Joanny, J.-F., 1993b. Charged diblock copolymers at interfaces. Macromolecules 26, 2691–2697.

Woodle, M.C., Lasic, D.D., 1992. Sterically stabilized liposomes. Biochim. Biophys. Acta 1113, 171–199.

Wright, P.E., Dyson, H.J., 1999. Intrinsically unstructured proteins: re-assessing the protein structure–function paradigm. J. Mol. Biol. 293, 321–331.

Zhang, R., Mattice, W.L., 1992. Evaluation of the persistence length of the rigid-rod polymers poly(benzobisoxazole) and poly(benzobisthiazole) using molecular dynamics simulations. Macromolecules 25, 4937–4941.

Zhang, R., Mattice, W.L., 1993. Flexibility of a new thermoplastic polyimide studied with molecular simulations. Macromolecules 26, 6100–6105.

Zhulina, E.B., Borisov, O.V., Birshtein, T.M., 2000a. Static forces in confined polyelectrolyte layers. Macromolecules 33, 3488–3491.

Zhulina, E.B., Wolterink, J.K., Borisov, O.V., 2000b. Screening effects in a polyelectrolyte brush: self-consistent-field theory. Macromolecules 33, 4945–4953.

Zimm, B.H., Bragg, W., 1959. Theory of the phase transition between helix and random coil in polypeptide chains. J. Chem. Phys. 31, 526–535.

Role of Long-Range Repulsive Forces in Organizing Axonal Neurofilament Distributions: Evidence From Mice Deficient in Myelin-Associated Glycoprotein

Sanjay Kumar,[1] Xinghua Yin,[2] Bruce D. Trapp,[2] Michael E. Paulaitis,[3] and Jan H. Hoh[1,3]*

[1]Department of Physiology, Johns Hopkins University School of Medicine, Baltimore, Maryland
[2]Department of Neurosciences, Lerner Research Institute, Cleveland Clinic Foundation, Cleveland, Ohio
[3]Department of Chemical Engineering, Johns Hopkins University, Baltimore, Maryland

When the axon of a motor neuron is sectioned and visualized by electron microscopy, a two-dimensional distribution of neurofilaments (NFs) with nonrandom spacing is revealed; this ordered arrangement implies the presence of physical interactions between the NFs. To gain insight into the molecular basis of this organization, we characterized NF distributions from mouse sciatic nerve cross sections using two statistical mechanical measures: radial distribution functions and occupancy probability distributions. Our analysis shows that NF organization may be described in terms of effective pairwise interactions. In addition, we show that these statistical mechanical measures can detect differences in NF architecture between wild-type and myelin-associated glycoprotein null mutant mice. These differences are age dependent, with marked contrast between the NF distributions by 9 months of age. Finally, using Monte Carlo simulations, we compare the experimental results with predictions for models in which adjacent NFs interact through rigid cross bridges, deformable cross bridges, and long-range repulsive forces. Among the models tested, a model in which the filaments interact through a long-range repulsive force is most consistent with the results of our analysis. © 2002 Wiley-Liss, Inc.

Key words: cytoskeleton; intermediate filaments; unstructured proteins; phosphorylation; interaction forces; amyotrophic lateral sclerosis

Neurofilaments (NFs) are the most abundant cytoskeletal element of large, myelinated axons. These type IV intermediate filaments have contour lengths of several micrometers and run in parallel along the axon. When the axon is cut in cross section and the transected NFs are visualized by electron microscopy (EM), the NF distribution appears nonrandomly arranged, suggesting that the filaments interact with one another to maintain order. One metric for this order is the distribution of nearest-neighbor spacings, which typically reveals that most nearest-neighbor separation distances fall within a relatively narrow range (e.g., 33–47 nm for adult rats; Hsieh et al., 1994). Experimental nearest-neighbor spacings have also been compared with simulated distributions of highly ordered and randomly positioned particles; based on this study, it was concluded that NF distributions lie intermediate between completely random and highly ordered (Hsieh et al., 1994). Other approaches have been used to characterize structure in NF distributions, including the use of tile-counting methods (Price et al., 1988, 1993).

Much attention has been paid to the biochemistry of interfilament interactions. NFs are composed of three polypeptide subunits: a light chain (NF-L; 61 kD in humans), a medium chain (NF-M; 90 kD), and a heavy chain (NF-H; 110 kD). The amino termini of the monomers contain rod domains, which associate to form the filament backbone, and the carboxy termini of NF-M and -H form "sidearms" that protrude from the filament backbone to give the isolated NF a bottle-brush appearance (Geisler and Weber, 1981; Willard and Simon, 1981; Hisanaga and Hirokawa, 1988; Leapman et al., 1997). The sidearms, which are heavily phosphorylated (Lee et al., 1988), are thought to mediate interactions between NFs and allow them to form a structural framework that maintains axonal patency and protects the bore of the axon from compressive stress (Brown and Hoh, 1997; Gou et al., 1998). There are several hypotheses for the nature of these interactions. One proposed mechanism is electrostatic repulsion between the phosphorylated sidearms; this is supported by several observations, including a correlation between regional NF phosphorylation level and interfilament spacing distance (Carden et al., 1987; de Waegh et

al., 1992). A second model is interfilament cross bridging mediated by the sidearms, which is based primarily on the observation of connecting structures between NF backbones by EM (Chen et al., 2000) and rheological measurements (Leterrier et al., 1996). In a third model, the sidearms lack a stable three-dimensional structure and move rapidly to occupy a large effective volume, giving rise to an entropic repulsion upon compression. This model is supported by atomic force microscopy (AFM) measurements, which demonstrate molecular exclusion in the proximity of NFs; independent experiments have detected a long-range repulsive force between individual NFs and the AFM probe even in high-salt buffer (Brown and Hoh, 1997). Consistent with this finding, Dunker and colleagues screened the Swiss-Prot database with a neural network predictor trained to identify long disordered regions of proteins and found that the mouse NF-H sidearm domain received the sixth-highest score among more than 59,000 total sequences (Romero et al., 1998).

Anterograde axonal transport of NFs is also the subject of much controversy, with some groups favoring a model in which fully assembled NF polymers are transported along the axon and others favoring one in which individual NF subunits or short oligomers are transported and then added into existing mature filaments (Terada et al., 1996; Galbraith et al., 1999; Brown, 2000). Moreover, there is disagreement among proponents of the former model regarding whether NFs are transported as single filaments or as bundles (Wang et al., 2000; Yabe et al., 2001). Understanding the physical nature of NF–NF interactions in the axon bears obvious implications for each of these models.

To understand better the relationship between interfilament interaction mechanisms and observed interfilament spacing in vivo, we have applied statistical mechanical methods to analyze NF distributions from sciatic nerve cross sections. To determine the utility of this approach for studying phenotypic changes in interfilament interactions, we have compared NF distributions from wild-type mice with those from myelin-associated glycoprotein (MAG) –/– mice. MAG is a heavily glycosylated type I integral membrane protein that is enriched in the myelin internode membrane that apposes the axon. The MAG –/– phenotype was chosen as a comparison because it has been characterized extensively and includes marked reductions in nearest-neighbor NF spacing, mean axonal diameter, and NF phosphate content. MAG directly or indirectly serves, based on these findings, as an axonal ligand that influences the phosphorylation state of NFs, which, in turn, regulates interfilament spacing and axonal diameter (Yin et al., 1998). To explore which models of interfilament interaction might account for the results of the analysis, we performed Monte Carlo (MC) simulations of two-dimensional NF distributions in which we imposed interfilament potentials designed to model different sidearm interactions.
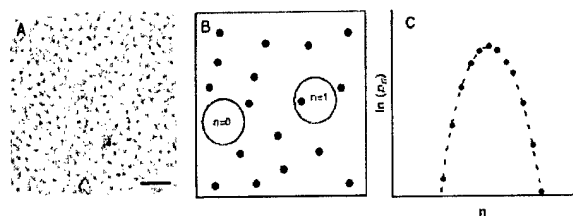

Fig. 1. Schematic diagram of information theory approach. **A:** Electron microscopy of a motor neuron axon cut in cross section; the punctate structures are NFs. **B:** Schematic representation (at higher magnification) of NFs and observation circles. Observation circles of a fixed diameter are placed in the field, and the numbers of NFs observed in the circle (*n*) are recorded. **C:** Occupancy numbers are converted into a probability distribution (*p_n*) by constructing a histogram and normalizing by the number of observations. The dashed line represents a Gaussian fit, which appears parabolic on these semilogarithmic axes. Scale bar = 100 nm.

MATERIALS AND METHODS

Theory

The potential of mean force (PMF) provides a means of connecting interaction potentials between particles with their arrangement in space. One recently developed approach to connecting the PMF to the structural arrangement of particles involves the application of information theory (IT; Hummer et al., 1996). The central quantity in this approach is the occupancy probability distribution, defined in the context of NF organization as the distribution of probabilities p_n of finding n NFs in an axon cross-sectional area of defined size and shape. To calculate the occupancy probability distribution for an ensemble of axon cross sections, we place a spherical observation "area" at a large number of random positions within the cross section (Fig. 1A) and count the number of NFs that fall within each area (Fig. 1B). A normalized histogram is then constructed to yield the distribution of probabilities of finding a given number of NFs in the observation area (Fig. 1C). The moments of this distribution are directly related to the cross-sectional density and radial distribution function of NFs in the ensemble of axon cross sections. The PMF is directly related to the radial distribution function.

The p_n distribution shown in Figure 1C is analyzed be defining an information entropy (η) in terms of p_n:

$$\eta = - \sum_{n=0}^{N} p_n \ln(p_n/\hat{p}_n).$$

Here, the set $\hat{p}_n$ is a set of prior distributions, which we chose to be unbiased (constant $\hat{p}_n$ for $n = 0 \dots N$), and N is large compared with the average of n. The most likely p_n distribution is obtained by maximizing η under constraints of the available information, i.e., that satisfy conditions imposed by the moments of the distribution. In particular, for the zeroth moment,

$$\langle n^0 \rangle = \sum p_n = 1,$$

and, for the first moment,

$$\langle n^1 \rangle = \sum np_n = \rho \Delta A,$$

where ρ is the number density of NFs in cross section and ΔA is the observation area, and, for the second moment,

$$\langle n^2 \rangle = \sum n^2 p_n = \langle n \rangle + \rho^2 \int_{\Delta A} dr \int_{\Delta A} g|(r-r')| \, dr.$$

Here $g(r)$ is the radial distribution function characterizing spatial correlations between pairs of NFs and, as such, is related to the PMF through the expression PMF $= -kT\ln[g(r)]$. Radial distribution functions have been used to quantify structure and interaction potentials between connexins in gap junctions (Braun et al., 1984, 1987) and immunoglobulin receptors (Perelson, 1978) and bacteriorhodopsin proteins in membrane arrays (Pearson et al., 1983). The statistical descriptors obtained from IT have been used successfully to relate intermolecular structure and intermolecular interactions in water (Hummer et al., 1996) and polymeric fluids (Garde et al., 2000). Maximizing η subject to the three moment constraints leads to a Gaussian distribution for p_n, which has several implications. Most significantly, a Gaussian probability distribution indicates that the organization of the system may be described in terms of pair correlations alone, i.e., the PMF calculated directly from the radial distribution function. Descriptions of higher order correlations among three or more NFs are not required. The first moment or mean of this Gaussian distribution corresponds to the NF number density in cross section, and the variance, which is related to the second moment, provides a measure of the interfilament PMF or, equivalently, the strength of interfilament interactions. For a given density, the smaller the variance about the mean, the stronger the pair correlations between NFs.

Analysis of Electron Micrographs

Electron micrographs were obtained from wild-type and MAG $-/-$ mice at ages 14 days, 3 months, and 9 months. The procedures for perfusion and fixation of tissue as well as microscopy have been described elsewhere (Yin et al., 1998). Micrographs were then scanned and digitized (6–12 EMs for each cohort); a region containing 200–1,000 NFs and relatively free of organelles and other cytoskeletal structures was chosen, and the coordinates of each NF within the region were identified by hand and recorded. These coordinates were used to calculate radial distribution functions and probability curves. Computer code for this analysis and for the MC simulations described below were written in Fortran. Gaussian fits for both experimental and simulation results were performed as quadratic fits to $\ln(p_n)$ which adds statistical weight to the extremes of the distribution.

MC Simulations

NF cross sections were represented as two-dimensional disks in canonical ensemble MC simulations carried out at 300K (Allen and Tildseley, 1987). An initial configuration was gen-erated by placing the disks at the nodes of a square lattice. Metropolis MC moves were made one randomly chosen particle at a time until the system reached equilibrium, as determined by a constant average total energy and radial distribution function. After equilibration, the simulation run was continued to obtain the occupancy probability distributions, which were calculated as averages over 30–50 structures sampled at fixed intervals (approximately every 10–15 MC cycles).

Interactions between the disks were modeled using an analytical potential function representing pair interactions between polymer brushes. Specifically, we used a potential function based on an expression for gelatin-coated hard spheres (Likos et al., 2000). This spherical interaction potential is taken to be a reasonable approximation for the interaction potential between pairs of parallel cylinders, as would be the case for NFs aligned in the axon. To our knowledge, the latter potential function is not available. In this model, the NF–NF interaction potential, $U(r)$, is a function of center-to-center separation distance between NF cylinders or disks in cross section. The NF sidearms will occupy a diffuse volume that extends a distance, L, from the filament backbone, which has radius R_c. The NF backbones are not allowed to overlap, so that $U(r) = \infty$ for $r < 2R_c$. When the NFs are sufficiently far apart that the sidearm layers do not overlap (i.e., $r > 2R_c + 2L$), the NFs do not interact and $U(r) = 0$. At intermediate distances, the potential is given by:

$$U(y) = kT\alpha \frac{16\pi R_c L^2}{35s^3}$$

$$\times \alpha \left[28(y^{-1/4} - 1) + \frac{20}{11}(1 - y^{11/4}) + 12(y - 1) \right],$$

where $y = (r - 2R_c)/(2L)$. Here, kT is the thermal energy, s is the distance between sidearms along the NF backbone, and α is a scaling factor empirically determined to be 0.01. Based on estimates from EM of isolated NFs (Geisler and Weber, 1981), we took $R_c = 5$ nm and $s = 3$ nm. We used a square-well potential to represent rigid cross bridging and a soft repulsive potential of the above-described form superimposed on a square-well potential to represent deformable cross bridging.

RESULTS

We first determined the occupancy probability distributions and radial distribution functions for wild-type and MAG $-/-$ mice at 9 months of age (Fig. 2). The radial distribution function has a direct structural interpretation and can provide insights not apparent in the probability distributions. This being the case, direct calculations of radial distribution functions complement their more indirect representation in the IT approach. The occupancy probability curves for wild-type and MAG $-/-$ are Gaussian (Fig. 2A), consistent with the IT prediction for a system whose organization is governed by a collection of pairwise interactions. Insight into the physical properties of the two NF architectures may be obtained by comparing the statistical descriptors of the two distributions. The means of the wild-type and MAG $-/-$ distributions are
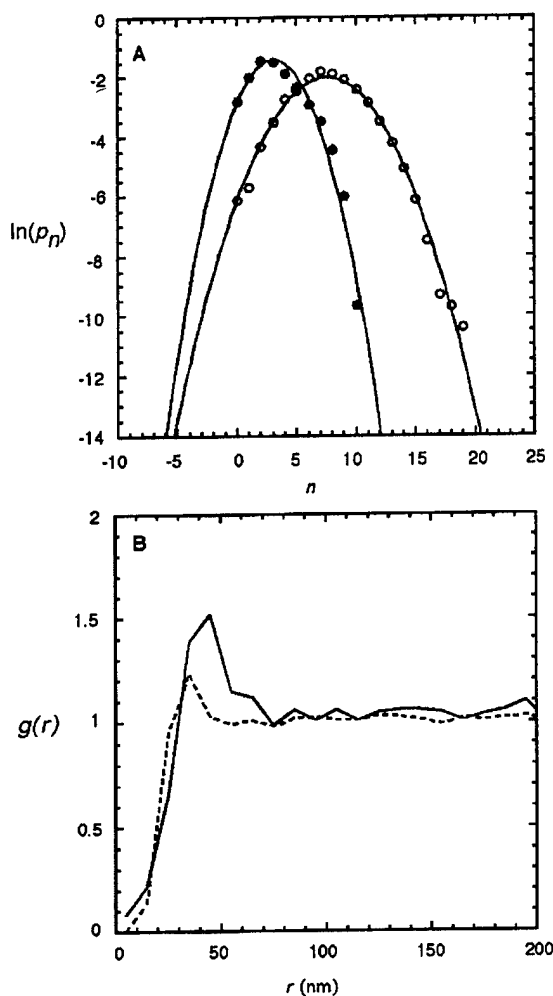
Fig. 2. **A:** Experimental probability distributions at 9 months. Points are experimental values for wild-type mice (solid circles) and MAG −/− mice (open circles) using an observation circle radius of 60 nm, with Gaussian fits. **B:** Experimental radial distribution functions at 9 months. Wild type is represented by a solid line and MAG −/− by a dashed line.

Fig. 3. Mean (**A**) and standard deviation (**B**) of wild-type (solid circles) and MAG −/− (open circles) probability distributions over time. *$P <$ 0.01 by Student's t-test. Note that here we used an 80-nm-radius window (rather than 60 nm as for Fig. 2) for all ages to obtain more meaningful p_n statistics for the smaller NF densities of the 14-day-old mice. This change in window size has no qualitative effect on the results.

approximately 2.6 and 7.4, respectively, reflecting the fact that the NFs are more densely packed in the axons of the MAG −/− animals than in those of the wild type. In addition, the standard deviations of the curves differ substantially at approximately 1.7 for the wild-type group and 2.5 for the MAG −/− group (a fractional difference of 0.47 times the wild-type value). Within the IT framework, this difference demonstrates weaker pair correlations and greater disorder in the MAG −/− NF distributions. This, in turn, suggests that interfilament interaction forces are weaker in the MAG −/− mice than in wild-type mice. This is seen more readily through direct measurement of the radial distribution functions (Fig. 2B). The wild-type NFs show greater interfilament spacing as evidenced by
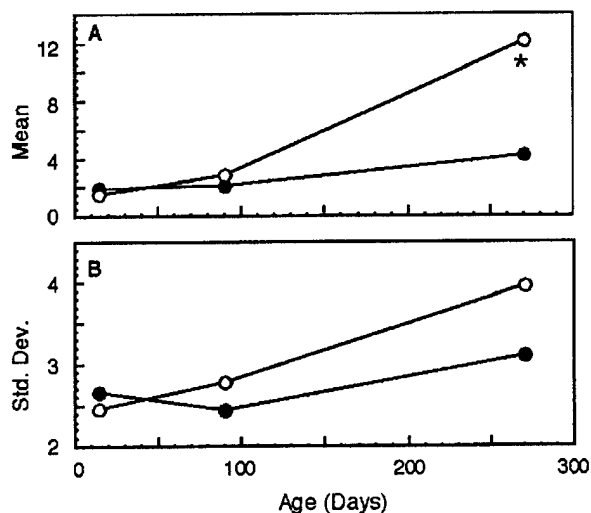
the right-shifted peak; they also show greater structure on this length scale as evidenced by a higher first peak value in $g(r)$.

The IT approach was further tested by examining changes in NF distributions during development (Fig. 3). We performed IT analysis on axonal cross sections from wild-type and MAG −/− at ages 14 days and 3 months, in addition to the 9-month-old mice described above. In this analysis, the densities of the two populations track one another closely through 3 months but diverge significantly by 9 months (Fig. 3A). Similar developmental changes are observed in the width of the probability distributions (Fig. 3B).

An attractive feature of the statistical mechanical approach described here is that it provides measurable quantities (p_n and $g(r)$) that change with interaction potentials. To determine whether proposed models of interfilament interaction are capable of accounting for the trends observed in the experimental data (Fig. 2), we conducted MC simulations on two-dimensional arrays of particles representing NF cross sections. In these simulations, we fixed the density, volume, and temperature of the system, imposed a pairwise interaction potential representing a physical model, and assessed the resulting configurations using IT and radial distribution functions. We tested three models: a rigid cross-bridging model (Chen et al., 2000), a soft cross-bridging model, and an entropic repulsion model (Brown and Hoh, 1997). In each case, we simulated two NF densities, one corresponding to the NF density of the wild-type mice at 9 months and the other
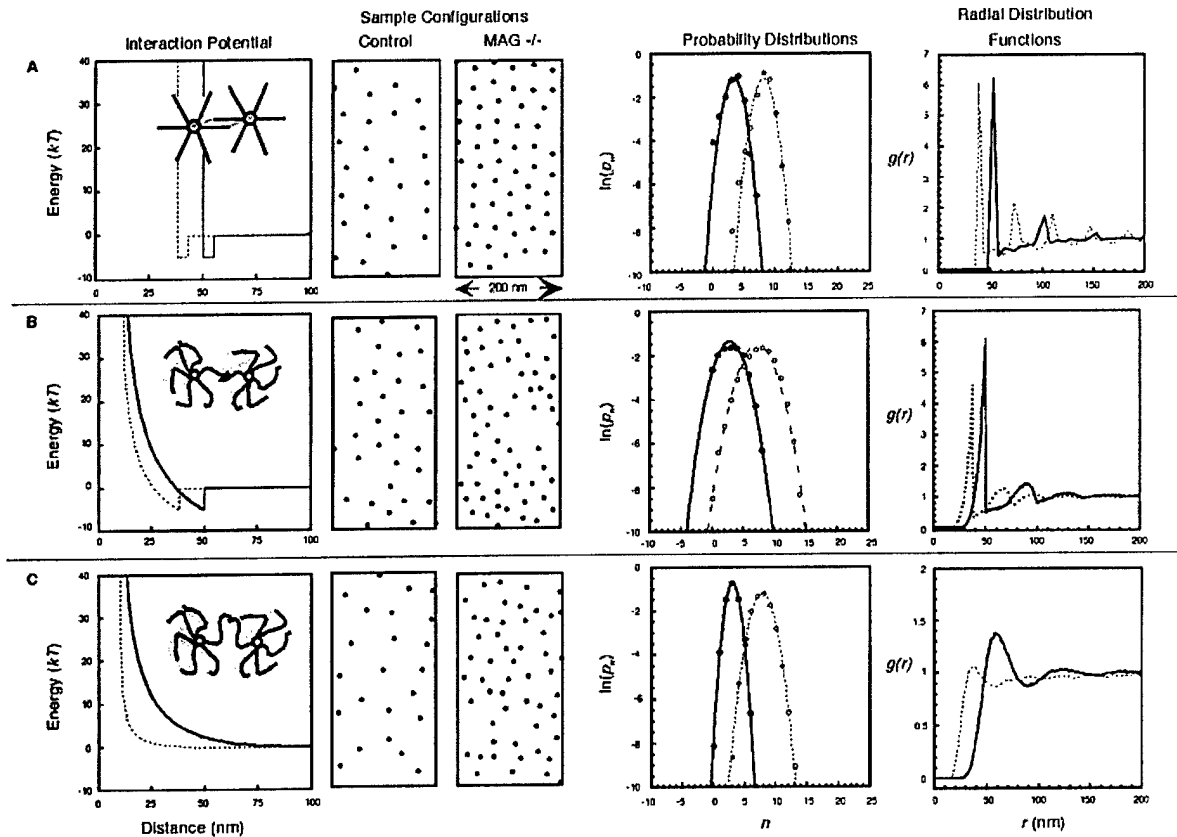
Fig. 4. Monte Carlo simulations for three model NF interaction potentials: rigid cross-bridging model (**A**), soft cross-bridging model (**B**), and entropic repulsion model (**C**). The leftmost panels depict the potentials used in the simulation to represent the wild-type and MAG −/− NFs along with a schematic physical model (**insets**). Note that the width of the potential well in A is exaggerated for clarity. The next two panels show examples of configurations sampled during a typical simulation for each case. The next panel depicts the resulting probability distributions for the simulation with Gaussian fits, and the rightmost panel depicts radial distribution functions for each case (note scales). Solid lines and solid circles represent wild-type and dashed lines and open circles represent MAG −/− mice.

corresponding to that of the MAG −/− mice. We did not attempt to model a purely electrostatic spacing mechanism, because doing so requires the three-dimensional charge distribution (i.e., shape of the protein), which is not known. This is because under physiological ionic conditions the Debye screening length is approximately 0.5 nm, and direct electrostatic interactions are negligible on the length scale of interfilament spacings.

We first considered the cross-bridging or "rigid strut" model (Fig. 4A), in which the NF architecture results from a sidearm of one filament binding rigidly to the backbone or sidearm of an adjacent filament. We assume that there is a narrow region of binding sites along the NF sidearm, with a modest binding energy of $5kT$. The corresponding interaction potential is a narrow energy well placed at a fixed interfilament distance. We assume that the sidearms may not penetrate one another, so that at separation distances less than the strut position an infinitely steep potential is encountered. At distances greater than the strut position, the interaction potential is zero; inside the well, the NFs bind. Simulations were run at interfilament binding distances corresponding to approximate average nearest-neighbor distances in wild-type and MAG −/− mice (~38 and 50 nm, respectively) and at the appropriate respective densities (Fig. 4A). Inspection of typical configurations for each case indicates that, under this potential, the NFs are regularly spaced, with some voids that result from interfilament adhesion and clustering. The probability distributions deviate slightly from Gaussian predictions, particularly at low n; similar results have been observed in other attractive (self-associating) systems. At 1.08 and 1.10 for wild-type and MAG −/−, respectively (fractional difference of 0.019 times the wild-type value), the standard deviations of the two probability distributions are similar, unlike the case for the experimental data (Fig. 2). The radial distribution functions also differ substantially from the experimental data; the hard repulsion gives rise to a step-like increase in $g(r)$ at the strut

position and the adhesive well produces sharp, periodic spikes. When the adhesive well is reduced or removed entirely, the probability distributions more tightly follow Gaussian fits, and the spikes broaden and fall in amplitude (not shown).

To test the sensitivity of the cross-bridging simulation result to well depth (binding energy), well position (interfilament binding distance), and well width (binding range), we ran several simulations in which each of these parameters was systematically varied. These simulations produced results similar to those shown in Figure 4; we were unable to find, within a reasonable parameter space, conditions that qualitatively recapitulated the experimental results of Figure 2. We also tested potentials in which the sidearms were allowed to penetrate one another without binding, i.e., where the narrow adhesive well was retained at the position shown but the hard wall separation distance was reduced to 10 nm (the NF core diameter). These simulations produced aphysical configurations in which the cross bridge between a pair of NFs overlapped the core of a third NF (not shown), leading us to reject such potentials as inaccurate descriptions of the physical model. More sophisticated potentials that incorporate correlations of three or more NFs were also rejected because the experimental probability distributions indicate that the NF architecture arises from pairwise additive interactions.

Next, we considered a model in which the NFs interact via soft or deformable cross bridges (the "soft strut" model; Fig. 4B). Here, as in the rigid strut model, the NFs do not interact beyond separation distances corresponding to the strut position; inside the strut position, the NFs bind with energy $5kT$. However, the NFs are now allowed to approach one another more closely than the binding distance, where they remain bound but encounter an increasingly repulsive potential with closer approach. This soft repulsion represents the deformation of the cross bridge, which could result from bending of a folded protein or compression of an unfolded protein. To simulate this model, we retained the cross bridge positions of the rigid strut model, used a soft repulsive component to represent the wild-type potential, and used a shorter range, soft repulsive component for the MAG $-/-$ potential (Fig. 4B). As expected, sample configurations now reveal some NF pairs separated by distances less than the strut position. However, the attractive component still produces moderate NF clustering. Because of this, the probability distributions again deviate slightly from Gaussian predictions; the fit improves when either the repulsive component is strengthened or the attractive component is weakened (not shown). The standard deviations of the probability distributions, which were 1.7 for wild-type and 1.9 for MAG $-/-$ (a fractional difference of 0.12 times the wild-type value), do not differ as greatly as in the experimental results. The distributions are broader than those produced by the rigid strut potentials because of the greater diversity of interfilament spacings made possible by the soft repulsion. The periodic maxima in the radial distribution functions now develop gradually, a conse-

quence of the soft repulsion; however, the spikes that are not seen in the experimental data persist.

Finally, we considered the entropic repulsion model (Fig. 4C). Here, the NFs interact through a long-range (>50 nm) repulsive force generated by the thermally driven motion of the unstructured sidearms. To represent this model analytically, we used a potential based on the Alexander-DeGennes expression for polypeptide-coated hard spheres. The key physical parameter here is the effective thickness of the unstructured polypeptide layer (the "brush"); by varying this parameter in our simulation, we found that at each density, as the layer thickness is increased, the variance of the probability curve falls (not shown). This reflects the stronger interfilament interactions at greater brush thicknesses. To determine whether this model could account for the experimental data, we ran simulations at the wild-type NF density with a brush thickness of 50 nm and the MAG $-/-$ NF density with a thickness of 25 nm, estimates for highly and poorly extended sidearms (Fig. 4C). Inspection of sample configurations for each case indicates that the presence of extended sidearms is capable of generating much long-range order at low (wild-type) NF density. This is further evident in the probability distributions, which show differences in the standard deviation of the distribution for MAG $-/-$ and wild-type that are similar to those in the experiment (0.82 for wild-type and 1.3 for MAG $-/-$, a fractional difference of 0.59 times the wild-type value). The radial distribution functions show broad maxima consistent with a soft repulsive potential. The wild-type maximum is both greater in magnitude and right shifted relative to the MAG $-/-$ maximum. Moreover, the curves are notable for the absence of the sharp spikes observed in the cross-bridging model. We also performed simulations in which the brush thickness was fixed but the NF density was varied; we were unable to reproduce the experimental result at the densities of interest.

DISCUSSION

The central finding that emerges from the probability distribution analysis is that axonal NF distributions may be described in terms of pairwise additive NF–NF interactions. This is evidenced by the observation that experimental occupancy probability distributions are Gaussian. A second finding is that this analysis can detect phenotypic alterations in NF distributions associated with genetic ablation of MAG. These differences are age dependent, with phenotypic differences most prominent at 9 months. This parallels the observed developmental course of mean axonal caliber and nerve degeneration in MAG $-/-$ mice (Yin et al., 1998). Interpreting the parameters of these distributions using IT, we find that NF distributions from MAG $-/-$ mice are more densely packed yet show weaker interfilament correlations. Those differences suggest weaker pair interactions in the MAG $-/-$ axons, an interpretation supported by experimental determination of the radial distribution function. The finding that axonal NF distributions may be represented in terms of pair interactions bears at least two important consequences.

First, it enables us to conduct MC simulations in which pair interaction potentials are used, which, in turn, allows us to test the effect of interfilament repulsion and attraction on the overall structure of NF distributions and to determine which interaction potentials best account for the phenotypic changes observed in the absence of MAG. Second, it implies that the correct physical model is one in which only the relative positions of two NFs have to be known to determine the potential energy. This excludes more complex models in which the interaction potential between two NFs depends on the position of a third.

Based on these findings, we conducted MC simulations to test three models of NF–NF interactions: rigid interfilament cross bridging, soft (flexible) interfilament cross bridging, and entropic repulsion mediated by disordered sidearms. The results of the simulations show that the presence of a long-range repulsive interfilament potential between the NF sidearms best accounts for the experimentally observed NF architectures in vivo. The probability distributions calculated for a rigid cross-bridging model do not agree well with the experimental data. Furthermore, the radial distribution functions for this model have sharp spikes that are absent in the experimental data. Using a mixed potential to represent a soft cross bridge improves agreement of the simulations and data with respect to the radial distribution functions. However, the spikes that are not seen in the experimental data persist in the simulations; moreover, in both cases, the attractive component of the potential favors NF aggregation, which, in turn, produces deviations from Gaussian behavior. The purely repulsive long-range potential captures the changes in probability distributions when the magnitude of the repulsion is decreased in the MAG $-/-$ mice.

Interfilament cross bridging is widely regarded as an important regulator of interfilament spacing, based largely on the observation of such structures by EM (Hisanaga and Hirokawa, 1988; Chen et al., 2000). It is therefore somewhat surprising that a purely repulsive model of NF–NF interactions accounts for the phenotypic changes observed in the absence of MAG. One candidate cross-bridging protein is the neuronal isoform of bullous pemphigoid antigen 1 (BPAG1-n), whose gene locus encodes a rich variety of splice variants, which cross-link several cytoskeletal proteins (Leung et al., 2001). Recently, BPAG1-n was reported to cross-link microtubules (MTs) and bind and coalign NFs to the actin cytoskeleton in transfected cells (Yang et al., 1996, 1999). However, in a subsequent report from another group, the ability of BPAG1-n to bind several NF fragments was examined using fluorescence colocalization, three-hybrid analysis, and in vitro binding assays (Leung et al., 1999). These investigators found that the NF triplet bound BPAG1-n only when the sidearm of NF-H was genetically ablated. The authors hypothesized, based on these findings, that the sidearm domain blocked or otherwise interfered with binding. Similarly, NF-H and NF-M were found not to bind themselves or one another in a yeast two-hybrid screen unless the tails were removed (Leung and Liem, 1996).

Both results are consistent with the model presented here, in which the disordered sidearm domains sterically exclude binding partners. Additional data appearing to support the cross-bridging model are that transgenic mice with low axonal NF densities show clustered NFs with nearest-neighbor spacings similar to those in wild-type (Xu et al., 1996). However, these transgenic strains also have greatly increased numbers of axonal MTs (to the point, in fact, where the microtubules completely dominate the axonal cytoskeleton). Little is known about NF–MT interactions; if those interactions are highly repulsive, or if MT–MT interactions are highly attractive, then one would observe separation of the MTs and NFs into distinct phases. Indeed, BPAG1-n has recently been shown to bind and organize neuronal MTs (Yang et al., 1999). Phase separation of this type is routinely observed in synthetic polymer mixtures (Bates, 1991). Finally, there are several examples of cases in which decreases in NF density are accompanied by increases in interfilament spacing (de Waegh et al., 1992; Nixon et al., 1994; Yin et al., 1998; Martin et al., 1999). Taken together with the possibility of compensatory changes, support for the cross-bridging model by the transgenic animal studies is equivocal. A repulsive interfilament potential is also most consistent with the experimental finding that, when the axonal membrane is chemically disrupted, the NFs diffuse apart freely (Brown and Lasek, 1993).

It should also be noted that our findings do not imply that attractive interfilament interactions never exist, merely that they do not appear to play a dominant role in organizing NF distributions in the system characterized here. Moreover, the depiction of the sidearms as unstructured is not mutually exclusive with attractive interactions between the sidearms. Disordered polymers may attract one another through mutual entanglement (Doi and Edwards, 1986) or through specific chemical interactions (Zilman and Safran, 2001). These interactions have been addressed analytically only recently. They are expected to assume a more complex analytical form than the binding potentials used here; superimposition of these interactions onto repulsive potentials may in fact yield simulation results that are more easily reconciled with the experimental data.

Our analysis suggests that the observed MAG $-/-$ phenotype is the result of weaker interfilament repulsion despite higher NF density. Thus, one question that arises is the mechanism by which the strength of this repulsion might be modulated. There are several candidates for the origin of this modulation, including changes in sidearm phosphorylation and O-GlcNAc modification. Analysis of the murine NF-H sidearm sequence indicates that, although it is extremely rich in charged residues (285 of 679 residues), these residues are nearly evenly divided between cationic and anionic (147 D and E, 138 R and K); the balance is even tighter in human NF-H (155 D and E, 154 R and K). The NF-H sidearm is normally very heavily phosphorylated; for example, squid giant axon NF-H has been shown to contain more than 100 phosphates per sidearm, representing near-maximal phosphorylation of

consensus kinase targets. The phosphorylated NF sidearms have a significant net negative charge and from a polymer perspective can be viewed as a polyelectrolyte. Unstructured polyelectrolyte brushes have been well studied (Lodge and Muthukumar, 1996; Luckham, 1996; Szleifer and Carignano, 1996; Tirrell and Levicky, 1997; Zhao and Brittain, 2000). In particular it has been shown that the size (thickness) of the brush is directly dependent on the net charge of the polymer (Pincus, 1991). Increasing the charge increases intramolecular monomer repulsion, which, in turn, effectively swells the brush resulting in a longer range repulsion. In the case of NFs from MAG −/− axons, it has been shown by immunoblotting of whole nerve homogenates and immunogold staining of axonal cross sections that NF-M and NF-H sidearm phosphorylation is markedly reduced relative to wild type (Yin et al., 1998). In the polymer view, this change in phosphorylation represents a modulation in polymer charge, which would reduce the predicted repulsive potential. This reduction in repulsive potential is in agreement with the experimental and simulation results presented here and suggests a mechanism for regulating interfilament spacing (Fig. 5). Here, NFs in wild-type mice are abundantly phosphorylated and interact via a long-range entropic exclusion mechanism; absent MAG, this phosphorylation is reduced, the sidearms are consequently less extended, and the interactions are more short range. This interpretation is further supported by in vitro studies that reveal that dephosphorylation alters both sidearm hydrodynamic radius (Chin et al., 1989) and NF gel viscoelastic properties (Gou et al., 1998). We note that we are not the first to propose a model in which sidearm phosphorylation produces increased interfilament spacing through increased phosphate–phosphate repulsion; for example, de Waegh et al. (1992) invoked such a model to explain a correlation between regional phosphorylation level and interfilament spacing. We agree with these investigators that electrostatic repulsion plays a fundamental role, but our results suggest that this role is far more short ranged. Rather than directly mediating interactions between NFs, we propose that electrostatic repulsion governs structure within each NF, which, in turn, gives rise to long-range repulsion.

There is also considerable evidence that phosphorylation is an important physiologic regulator of interfilament spacing. One example of this is the finding that sidearm phosphorylation is often heavy in the distal axon, where parallel NF distributions are found, and relatively light in the cell body, where NFs form a more clustered network (Nixon et al., 1994). Electron energy loss spectroscopy studies in squid giant axon have demonstrated a reciprocal relationship between NF density and phosphorylation; as NF density falls distally to the cell body, phosphorylation and axonal caliber rise (Martin et al., 1999). A recent study found coexisting populations of differentially phosphorylated NFs with dramatically different transport and morphological properties (Yabe et al., 2001); another study found regional variations in phosphorylation along single filaments (Brown, 1998). Both further support

Wild-Type

MAG -/-
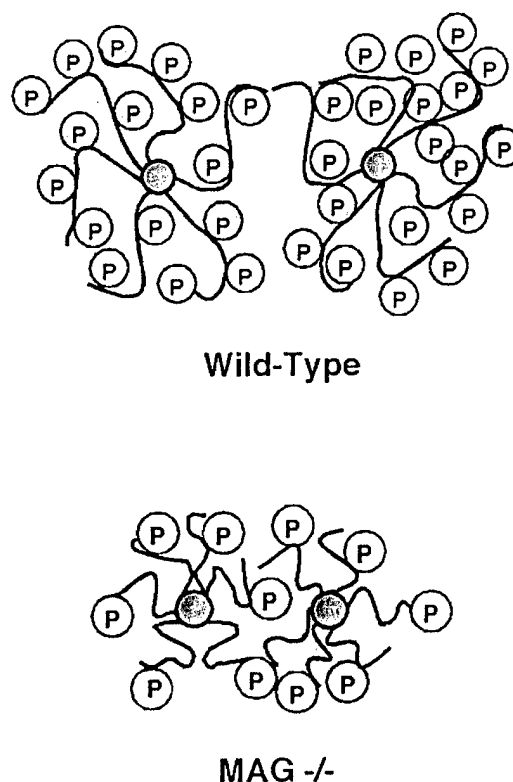
Fig. 5. Proposed biochemical mechanism for modulating interfilament spacing. Wild-type NF sidearms are extensively phosphorylated and negatively charged, producing expanded unstructured sidearms and long-range repulsion. Conversely, MAG −/− NFs are less phosphorylated, leading to weaker intrachain repulsion between monomers and a sidearm that is collapsed relative to the wild type. This in turn leads to a shorter range interfilament repulsion.

phosphorylation as a spatially localized regulator of NF architecture. In an entropic repulsion model, the highly phosphorylated sidearms produce an expanded sidearm layer that leads to mutual steric exclusion and the maintenance of interfilament spacing. Dephosphorylation reduces steric exclusion, thereby exposing potential binding sites or facilitating the formation of nonaligned NF networks.

The entropic repulsion model also bears implications for the issue of anterograde NF transport. A primarily repulsive model of NF–NF interaction would allow for transportation of individual filaments along the axon. Indeed, transport of individual NF polymers has been directly visualized in several recent fluorescence studies, one of which suggested that >97% of axonal NFs move as single filaments (Wang et al., 2000; Wang and Brown, 2001). The observation that NFs are transported individually is less compatible with a model in which NFs are highly cross-linked. Additional recent studies suggest that axonal NFs exist in highly diverse states, moving as bun-

dles under some conditions and individually under others (Yabe et al., 2001).

We have used radial distribution functions and occupancy probability distributions to analyze axonal distributions of NFs and characterize phenotypic differences between wild-type and MAG −/− mice. We show that NF distributions are governed by pair correlations, that wild-type and MAG −/− mice have distinct probability distributions, and that differences between the two are best explained by a model in which the NFs interact through a repulsive potential that weakens in MAG −/− mice. We propose that these differences in potentials are due to changes in phosphorylation. The analytical framework presented here offers a way to quantify order in NF distributions and directly relate that order to interfilament potentials. This approach may prove useful in detecting subtle changes in NF architecture in animal models of neurodegenerative disease, studying interfilament interactions in vitro, and ultimately relating intermolecular organization to interaction forces for a variety of biological macromolecules.

ACKNOWLEDGMENTS

REFERENCES

Allen MP, Tildseley DJ. 1987. Computer simulation of liquids. Oxford: Oxford Science Publications.

Bates FS. 1991. Polymer–polymer phase behavior. Science 251:898–905.

Braun J, Abney JR, Owicki JC. 1984. How a gap junction maintains its structure. Nature 310:316–318.

Braun J, Abney JR, Owicki JC. 1987. Lateral interactions among membrane-proteins—valid estimates based on freeze-fracture electron-microscopy. Biophys J 52:427–439.

Brown A. 1998. Contiguous phosphorylated and non-phosphorylated domains along axonal neurofilaments. J Cell Sci 111:455–467.

Brown A. 2000. Slow axonal transport: stop and go traffic in the axon. Nat Rev Mol Cell Biol 1:153–156.

Brown A, Lasek RJ. 1993. Neurofilaments move apart freely when released from the circumferential constraint of the axonal plasma membrane. Cell Motil Cytoskel 26:313–324.

Brown HG, Hoh JH. 1997. Entropic exclusion by neurofilament sidearms: a mechanism for maintaining interfilament spacing. Biochemistry 36:15035–15040.

Carden MJ, Trojanowski JQ, Schlaepfer WW, Lee VMY. 1987. Two-stage expression of neurofilament polypeptides during rat neurogenesis with early establishment of adult phosphorylation patterns. J Neurosci 7:3489–3504.

Chen JG, Nakata T, Zhang ZZ, Hirokawa N. 2000. The C-terminal tail domain of neurofilament protein-H (NF-H) forms the crossbridges and regulates neurofilament bundle formation. J Cell Sci 113:3861–3869.

Chin TK, Harding SE, Eagles PAM. 1989. Characterization of 2 proteolytically derived soluble polypeptides from the neurofilament triplet components nfm and nfh. Biochem J 264:53–60.

de Waegh SM, Lee VMY, Brady ST. 1992. Local modulation of neurofilament phosphorylation, axonal caliber, and slow axonal transport by myelinating schwann cells. Cell 68:451–463.

Doi M, Edwards SF. 1986. The theory of polymer dynamics. Oxford: Oxford University Press.

Galbraith JA, Reese TS, Schlief ML, Gallant PE. 1999. Slow transport of unpolymerized tubulin and polymerized neurofilament in the squid giant axon. Proc Natl Acad Sci USA 96:11589–11594.

Garde S, Khare R, Hummer G. 2000. Microscopic density fluctuations and solvation in polymeric fluids. J Chem Phys 112:1574–1578.

Geisler N, Weber K. 1981. Self-assembly in vitro of the 68,000 molecular-weight component of the mammalian neurofilament triplet proteins into intermediate-sized filaments. J Mol Biol 151:565–571.

Gou JP, Gotow T, Janmey PA, Leterrier JF. 1998. Regulation of neurofilament interactions in vitro by natural and synthetic polypeptides sharing lys-ser-pro sequences with the heavy neurofilament subunit NF-H: neurofilament crossbridging by antiparallel sidearm overlapping. Med Biol Eng Comput 36:371–387.

Hisanaga S, Hirokawa N. 1988. Structure of the peripheral domains of neurofilaments revealed by low-angle rotary shadowing. J Mol Biol 202:297–305.

Hsieh ST, Crawford TO, Griffin JW. 1994. Neurofilament distribution and organization in the myelinated axons of the peripheral nervous system. Brain Res 642:316–326.

Hummer G, Garde S, Garcia AE, Pohorille A, Pratt LR. 1996. An information theory model of hydrophobic interactions. Proc Natl Acad Sci U S A 93:8951–8955.

Leapman RD, Gallant PE, Reese TS, Andrews SB. 1997. Phosphorylation and subunit organization of axonal neurofilaments determined by scanning transmission electron microscopy. Proc Natl Acad Sci USA 94:7820–7824.

Lee VMY, Otvos L, Carden MJ, Hollosi M, Dietzschold B, Lazzarini RA. 1988. Identification of the major multiphosphorylation site in mammalian neurofilaments. Proc Natl Acad Sci USA 85:1998–2002.

Leterrier JF, Kas J, Hartwig J, Vegners R, Janmey PA. 1996. Mechanical effects of neurofilament cross-bridges—modulation by phosphorylation, lipids, and interactions with F-actin. J Biol Chem 271:15687–15694.

Leung CL, Liem RKH. 1996. Characterization of interactions between the neurofilament triplet proteins by the yeast two-hybrid system. J Biol Chem 271:14041–14044.

Leung CL, Sun DM, Liem RKH. 1999. The intermediate filament protein peripherin is the specific interaction partner of mouse BPAG1-n (dystonin) in neurons. J Cell Biol 144:435–446.

Leung CL, Zheng M, Prater SM, Liem RKH. 2001. The BPAG1 locus: Alternative splicing produces multiple isoforms with distinct cytoskeletal linker domains, including predominant isoforms in neurons and muscles. J Cell Biol 154:691–697.

Likos CN, Vaynberg KA, Lowen H, Wagner NJ. 2000. Colloidal stabilization by adsorbed gelatin. Langmuir 16:4100–4108.

Lodge TP, Muthukumar M. 1996. Physical chemistry of polymers: Entropy, interactions, and dynamics. J Phys Chem 100:13275–13292.

Luckham P. 1996. Recent advances in polymers at surfaces: The steric effect. Curr Opin Colloid Interface Sci 1:39–47.

Martin R, Door R, Ziegler A, Warchol W, Hahn J, Breitig D. 1999. Neurofilament phosphorylation and axon diameter in the squid giant fibre system. Neuroscience 88:327–336.

Nixon RA, Paskevich PA, Sihag RK, Thayer CY. 1994. Phosphorylation on carboxyl-terminus domains of neurofilament proteins in retinal ganglion-cell neurons in vivo—influences on regional neurofilament accumulation, interneurofilament spacing, and axon caliber. J Cell Biol 126:1031–1046.

Pearson LT, Chan SI, Lewis BA, Engelman DM. 1983. Pair distribution-functions of bacteriorhodopsin and rhodopsin in model bilayers. Biophys J 43:167–174.

Perelson AS. 1978. Spatial-distribution of surface-immunoglobulin on B lymphocytes—local ordering. Exp Cell Res 112:309–321.

Pincus P. 1991. Colloid stabilization with grafted polyelectrolytes. Macromolecules 24:2912–2919.

Price RL, Paggi P, Lasek RJ, Katz MJ. 1988. Neurofilaments are spaced randomly in the radial dimension of axons. J Neurocytol 17:55–62.

Price RL, Lasek RJ, Katz MJ. 1993. Neurofilaments assume a less random architecture at nodes and in other regions of axonal compression. Brain Res 607:125–133.

Romero P, Obradovic Z, Kissinger CR, Villafranca JE, Garner E, Guilliot S, Dunker AK. 1998. Thousands of proteins likely to have long disordered regions. Pacific Symp Biocomput 3:437–448.

Szleifer I, Carignano MA. 1996. Tethered polymer layers. Adv Chem Phys 94:165–260.

Terada S, Nakata T, Peterson AC, Hirokawa N. 1996. Visualization of slow axonal transport in vivo. Science 273:784–788.

Tirrell M, Levicky R. 1997. End-tethered chain molecules at liquid interfaces. Curr Opin Solid State Mat Sci 2:668–672.

Wang L, Brown A. 2001. Rapid intermittent movement of axonal neurofilaments observed by fluorescence photobleaching. Mol Biol Cell 12:3257–3267.

Wang L, Ho CL, Sun DM, Liem RKH, Brown A. 2000. Rapid movement of axonal neurofilaments interrupted by prolonged pauses. Nat Cell Biol 2:137–141.

Willard M, Simon C. 1981. Antibody decoration of neurofilaments. J Cell Biol 89:198–205.

Xu ZS, Marszalek JR, Lee MK, Wong PC, Folmer J, Crawford TO, Hsieh ST, Griffin JW, Cleveland DW. 1996. Subunit composition of neurofilaments specifies axonal diameter. J Cell Biol 133:1061–1069.

Yabe JT, Chylinski T, Wang FS, Pimenta A, Kattar SD, Linsley MD, Chan WKH, Shea TB. 2001. Neurofilaments consist of distinct populations that can be distinguished by C-terminal phosphorylation, bundling, and axonal transport rate in growing axonal neurites. J Neurosci 21:2195–2205.

Yang Y, Dowling J, Yu QC, Kouklis P, Cleveland DW, Fuchs E. 1996. An essential cytoskeletal linker protein connecting actin microfilaments to intermediate filaments. Cell 86:655–665.

Yang Y, Bauer C, Strasser G, Wollman R, Julien JP, Fuchs E. 1999. Integrators of the cytoskeleton that stabilize microtubules. Cell 98:229–238.

Yin X, Crawford TO, Griffin JW, Tu PH, Lee VMY, Li CM, Roder J, Trapp BD. 1998. Myelin-associated glycoprotein is a myelin signal that modulates the caliber of myelinated axons. J Neurosci 18:1953–1962.

Zhao B, Brittain WJ. 2000. Polymer brushes: surface-immobilized macromolecules. Progr Polym Sci 25:677–710.

Zilman AG, Safran SA. 2001. Entropically driven attraction between telechelic brushes. Eur Phys J E4:467–473.

Relating Interactions between Neurofilaments to the Structure of Axonal Neurofilament Distributions through Polymer Brush Models

Sanjay Kumar,* Xinghua Yin,[†] Bruce D. Trapp,[†] Jan H. Hoh,[*‡] and Michael E. Paulaitis[‡]

*Department of Physiology, Johns Hopkins University School of Medicine, Baltimore, Maryland 21205; [†]Department of Neurosciences, Lerner Research Institute, Cleveland Clinic Foundation, Cleveland, Ohio 44195; and [‡]Department of Chemical Engineering, Johns Hopkins University, Baltimore, Maryland 21218 USA

ABSTRACT   Neurofilaments (NFs) have been proposed to interact with one another through mutual steric exclusion of their unstructured C-terminal "sidearm" domains, producing order in axonal NF distributions and conferring mechanical strength to the axon. Here we apply theory developed for polymer brushes to examine the relationship between the brush properties of the sidearms and NF organization in axons. We first measure NF–NF radial distribution functions and occupancy probability distributions for adult mice. Interpreting the probability distributions using information theory, we show that the NF distributions may be represented by a single pair potential of mean force. Then, to explore the relationship between model parameters and NF architecture, we conduct two-dimensional Monte Carlo simulations of NF cross-sectional distributions. We impose purely repulsive interaction potentials in which the sidearms are represented as neutral and polyelectrolyte chains. By treating the NFs as telechelic polymer brushes, we also incorporate cross-bridging interactions. Both repulsive potentials are capable of reproducing NF cross-sectional densities and their pair correlations. We find that NF structure is sensitive to changes in brush thickness mediated by chain charge, consistent with the experimental observation that sidearm phosphorylation regulates interfilament spacing. The presence of attractive cross-bridging interactions contributes only modestly to structure for moderate degrees of cross-bridging and leads to NF aggregation for extensive cross-bridging.

INTRODUCTION

Neurofilaments (NFs) comprise an abundant and functionally important cytoskeletal component of large, myelinated neurons. These intermediate filaments run in parallel along the axon and occupy a large fraction of the axoplasmic volume. When the axon is cut in cross section, the transected NFs appear as a two-dimensional distribution of punctate structures with liquid-like order (Fig. 1, A and B). The observation that NFs are spaced at nonrandom distances in the axon suggests that the NFs interact with one another (Hsieh et al., 1994). Through these interactions, axonal NFs generate an ordered intracellular framework that maintains and protects axonal patency and buttresses the axon against external compressive stresses. Evidence for the importance of NFs to the mechanical properties of axons comes from structural and mechanical studies on isolated axons (McHale et al., 1995; Povlishock and Christman, 1995; Smith et al., 1999) and rheological measurements on purified NF gels (Leterrier and Eyer, 1987; Gou et al., 1998). Intracellular NF aggregation is also a central finding in several neurodegenerative diseases (e.g., amyotrophic lateral sclerosis, Parkinson's Disease), suggesting that altered interactions between NFs may participate in the pathological process (Julien, 1999).

Mammalian NFs are composed of three polypeptide subunits: light (NF-L, 61 kDa in humans), medium (NF-M, 90 kDa), and heavy (NF-H, 110 kDa) (Lee and Cleveland, 1996). The amino terminus of each subunit contains a rod domain of ~300 residues in length, which associates with the rod domains of the other subunits to form the filament "backbone." The amino terminus of each subunit also contains a head domain of ~100 residues, which, together, are thought to facilitate end-to-end association of heterotrimers to form complete filaments. The carboxy terminus of NF-M and NF-H each contains a long tail domain of more than 300 and 600 residues, respectively, which protrudes from the backbone to form the NF "sidearms." Electron microscopy (EM) of isolated NFs reveals that these sidearms extend 75–100 nm from the filament backbone (Geisler and Weber, 1981). Thus, the assembled NF has a cylindrical core–shell structure in which the core is formed by the filament backbone and the shell is formed by the extended sidearms (Fig. 1 C). These sidearms are believed to mediate interactions between the filaments.

Several distinct models have been proposed for NF–NF interactions that lead to axonal NF structure. In one model, the sidearms interact through binding or cross-bridging interactions, mediated by the sidearms themselves or by accessory factors. Support for this model comes from EM studies of axonal (Hisanaga and Hirokawa, 1988), and purified (Chen et al., 2000) NF distributions, and rheological data (Gou et al., 1998). No cross-linking agent has yet been identified; neuronal bullous pemphigoid antigen 1 (BPAG1n) was found to cross-link NFs to the actin cytoskeleton (Yang et al., 1996), although this finding was contradicted by a subsequent report (Leung et al., 1999). In

FIGURE 1 Organization of axonal neurofilaments. (A) NFs run in parallel along the length of the axon. (B) In cross section, the NF cores appear as particulate features with two-dimensional structure. (C) Individually, NFs have a core–shell structure, in which the core is formed by the backbone of the three subunit amino termini and the shell is formed by the carboxy terminal sidearms of NF-H and NF-M. (D) Charge from the constituent amino acids is locally high but globally near-neutral. Extensive phosphorylation produces significant net negative charge.

a second model, the filaments repel one another through direct, colloidal electrostatic forces. Here, the net negative charge on the sidearms is acquired through extensive phosphorylation (Fig. 1 D). This model is supported by an observed correlation between NF phosphorylation and mean interfilament spacing in vivo (de Waegh et al., 1992; Strong et al., 2001). Also, purified NF gel properties depend strongly on phosphorylation levels (Eyer and Leterrier, 1988). In the third and most recently-proposed model, the sidearms are unstructured polyelectrolyte chains, forming a hairy, polymer brush-like layer around the filament backbone. Interfilament repulsion is achieved through mutual steric exclusion by the sidearms; i.e., the sidearms function as a so-called "polymer brush." Here, electrostatic repulsion operates on a far shorter range, governing brush structure through monomer–monomer repulsion. Evidence for this model comes primarily from atomic force microscopy (AFM), in which exclusion of small particles from the filament backbone was observed, and in which repulsive forces extending up to 50 nm from the filament backbone were detected, even in high-salt buffer (Brown and Hoh, 1997; Hoh, 1998). Support for similar mechanisms has now been gathered in several other systems, including stabiliza-

tion of microtubules by microtubule-associated proteins (Mukhopadhyay and Hoh, 2001) and gating of the nuclear pore complex (Rout et al., 2000).

Several lines of sequence-based and experimental evidence suggest that it is appropriate to regard NF sidearms as unstructured polyelectrolyte chains. The human NF-H sidearm is rich in charged residues (309 of 607 total amino acids) which are nearly evenly split between anionic and cationic (155 and 154, respectively). The situation is similar for NF-M (238 charged out of 504 total amino acids), although there is considerably less balance between anionic and cationic (145 and 93, respectively). In addition to carrying intrinsic charge, NF-H (and to a lesser extent, NF-M) acquires negative charge through serine and threonine phosphorylation (Lee et al., 1988; Strong et al., 2001). Indeed, measurements with squid giant axon NFs suggest that there may be as many as 100 phosphates per NF sidearm, representing nearly maximal phosphorylation of consensus kinase recognition sites (Leapman et al., 1997). This heavy phosphorylation is critical to modulating the radius of gyration of purified sidearm domains (Chin et al., 1989), reconstituted NF gel properties (Eyer and Leterrier, 1988; Gou et al., 1998), and interfilament spacing in vivo (de-Waegh et al., 1992; Nixon et al., 1994; Yin et al., 1998; Strong et al., 2001). Both the human NF-M and NF-H sidearms are proline-rich (6.2% in NF-M and 13% in NF-H) and low-complexity (Wootton and Federhen, 1996), and are predicted to be devoid of extensive stretches of helix or sheet (Rost and Sander, 1993, 1994). All three of these properties are widely observed in sequences of polypeptides that have been experimentally demonstrated to be unstructured (Uversky et al., 2000; Romero et al., 2001). Finally, a neural network predictor has been developed to identify from databases long, disordered regions of proteins in which the training set consists of sequences from the Protein Databank that are absent in crystal structures. Screening of the entire Swiss-Prot database, which contained nearly 59,000 total sequences when the study was performed, identified the murine NF-H sidearm domain as the sixth-highest scoring sequence (Romero et al., 1998).

In addition to the AFM data discussed earlier, substantial experimental evidence indicates that the NF sidearms are unstructured. No three-dimensional atomic structure for either the NF-H or NF-M sidearm has been reported despite the availability of sequence data and expression systems for over a decade. Circular dichroism measurements show that the bovine NF-M and NF-H sidearm domains contain less than 20% helical content (Chin et al., 1983). Size exclusion chromatography demonstrates that the Stokes radius of the bovine NF-M and NF-H sidearms are 52 and 60 Å, respectively, much larger than expected for sequences of those molecular weights (Georges and Musynski, 1987). Finally, in negative-stain EM, the NF sidearms appear as extended, unfolded structures that reach out 75–100 nm from the NF

core (Geisler and Weber, 1981; Willard and Simon, 1981; Hisanga and Hirokawa, 1988).

Relating structure to interaction potentials in NF distributions

NF organization in the axon is determined by interfilament interactions. We can describe this organization by considering the distribution of NFs in an axonal cross section. The spatial distribution in cross section is quantified by the radial distribution function or two-body correlation function, (RDF, $g(r)$),which is the local density of NFs around a central NF. $g(r)$ is defined as the conditional probability of finding an NF at a distance r given an NF at $r = 0$; the probability is normalized by the average density of NFs in cross-section. The RDF is directly related to the potential of mean force (u_{MF}) for NFs in cross-section through the expression $u_{MF} = -kT \ln g(r)$, where kT is the thermal energy. The potential of mean force is defined as the interaction potential between two NFs averaged over all configurations and orientations of all other NFs in the distribution. In the dilute limit, $u_{MF} (r) = u_{12}(r)$, the pair potential between two isolated NFs. At higher NF densities, two NFs can also interact indirectly through more proximal NFs, producing long-range structure.

Several approaches allow one to relate interaction potentials to the structure of protein or particle distributions, including experimental techniques such as neutron and x-ray scattering or computational methods based on simulation and the application of integral equations (Perelson, 1978, Braun et al., 1984, 1987; Pearson et al., 1983; Pusztai and Toth, 1991; Genz et al., 1994; Toth and Baranyi, 1997). A more recently developed approach relates interparticle correlations to local density fluctuations in the configuration (Hummer et al., 1996, 1998; Garde et al., 2000). Here, one starts with an ensemble of configurations, in our case cross-sectional distributions of NFs in axons. An "observation area" of defined shape and size is randomly placed at a large number of positions in the distribution, the number of particles (n) that fall within each area is counted, and the distribution of occupancy probabilities (occupancy probability distribution, OPD) is calculated. The moments of the resulting probability distribution are related to the physical properties of the system, including density, $g(r)$, and higher-order correlation functions. In general, the nth order moment of the OPD contains information about n-body and lower order correlations. By obtaining experimental OPDs and fitting the data to the predictions of information theory, one may indirectly measure $g(r)$. In practice, this approach tends to be highly robust and relatively tolerant to poor statistics. In addition, because the central measurement involves the counting of particles within a defined area rather than the measurement of interparticle distances, wall effects may be minimized through judicious placement of observation windows.
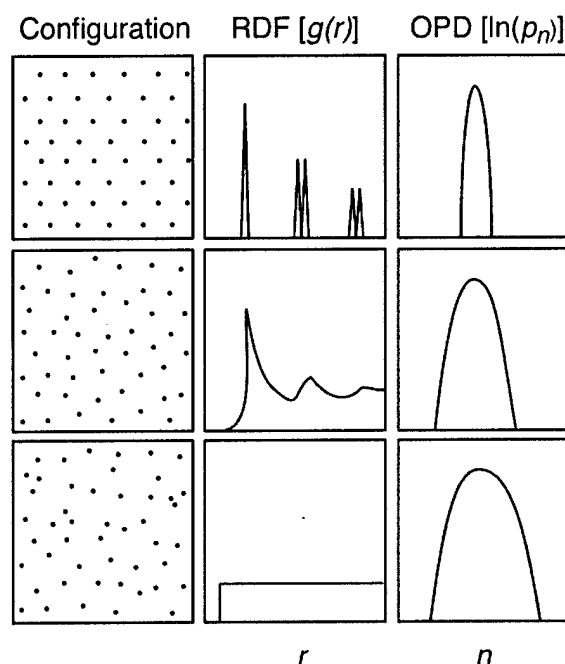

FIGURE 2 Relationship among structure, radial distribution functions, and probability distributions. The top three panels represent a crystalline arrangement, where interfilament spacings occur at precisely defined intervals. The RDF shows sharp spikes, and, for an appropriate and fixed choice of observation area, the OPD is quite narrow. The middle three panels represent a liquid-like NF distribution, in which there is order on relatively short length scales only. Broad maxima are seen in the RDF, and the OPD is broader than for the crystal. The bottom three panels represent an effectively ideal (noninteracting) NF distribution. The NFs are randomly organized, the RDF shows no structure beyond excluded volume, and the OPD is quite broad.

Measurement of the RDF directly through interparticle distances and indirectly through OPDs complement one another (Fig. 2). Direct measurement of the RDF is sensitive to changes in the pair potential but tends to be quite noisy in the absence of large pair statistics. Conversely, the OPD is not as sensitive to the interaction potential but is smooth and fairly easily interpreted even with modest statistics. Both the RDF and OPD are readily measured from particle configurations, and both may be directly compared to the results of simulation in which one imposes a pair potential. Thus, analysis of RDFs and OPDs together can provide structural insights beyond those obtained from either metric alone. We apply this complementary approach to relate experimentally observed distributions of NFs within an axon to physical models of interfilament interactions via pair potentials obtained from polymer brush theory. Specifically, we examine interaction potentials in which the sidearms are modeled as a neutral polymer brush, a polyelectrolyte brush, and a telechelic brush. Monte Carlo (MC) simulation is then used to obtain RDFs and OPDs for each model, which are compared to experiment.

THEORY

Information theory

The OPD (p_n, where $n = 0, \ldots, N$) is analyzed by defining an information entropy $\eta = \Sigma_{n=0}^{N} p_n \ln(p_n/\hat{p}_n)$. Here, $\hat{p}_n$ is a set of known (prior) distributions, which we chose to be unbiased (constant $\hat{p}_n$). The most likely p_n distribution is obtained by maximizing η under constraints that satisfy conditions imposed by the moments of the distribution. Specifically, for the zeroth moment $\langle n^0 \rangle = \Sigma\, p_n = 1$, for the first moment $\langle n^1 \rangle = \Sigma\, np_n = \pi\Delta A$, where ρ is the number density of NFs in cross section and ΔA is the observation area, and for the second moment $\langle n^2 \rangle = \Sigma\, n^2 p_n = \langle n \rangle + \rho^2 \int_{\Delta A} d\vec{r} \int_{\Delta A} g(|\vec{r} - \vec{r}'|)\, d\vec{r}'$. Including only these moments leads to a Gaussian distribution for p_n, which implies that organization in the system may be described in terms of the cross-sectional density and pair potential of mean force. Higher order correlations involving three or more NFs are not required to describe the structure. The first moment or mean of this Gaussian distribution corresponds to the NF number density in cross-section, and the variance, which is related to the second moment, provides a measure of the magnitude of the interfilament PMF. For a given density, the more tightly distributed the OPD about the mean (i.e., the smaller the local density fluctuations), the stronger the pair correlations between NFs.

Models of NF-NF interactions

The most appropriate geometry for polymer brush interactions between two NFs would be two parallel cylinders; however, to our knowledge, parallel-cylinder potentials have not been developed, reported, or experimentally tested for any of the models described here. We therefore chose sphere–sphere potentials for several reasons. First, unlike plane–plane interaction potentials, sphere–sphere potentials incorporate curvature effects. Second, many spherical potentials have been analytically derived by others, or experimentally verified, or both. Finally, based on the similarity of functional forms for these interactions, the sphere–sphere geometry may be regarded as a reasonable approximation of the cylinder–cylinder geometry (J. Israelachvili, personal communication).

All models used here were developed in the same manner. We start with an analytical expression for the free energy F_P of two brush-covered parallel plates as a function of the separation distance, D. The potential $U_P(D)$ between two such plates is $U_p = F_P - F_{P\infty}$ where $F_{P\infty}$ is the free energy of the plates at infinite separation (equivalent to twice the self-energy of a single plate). We then apply the Derjaguin approximation (Israelachvili, 1992) to convert the plane–plane interaction potential to a sphere–sphere

potential, $U_S(r)$, where r is the center-to-center separation distance between the spheres,

$$U_s(r) = \pi\alpha R_c \int_{r-2R_c}^{2L} U_p\, dD. \qquad (1)$$

Here, R_c is the radius of the hard NF core, and L is the equilibrium thickness of the sidearm (brush) layer. We also introduce α, a dimensionless constant determined empirically for each interaction potential, to accommodate the use of these expressions, which have been derived based on scaling theories. As a first approximation, we ignore variations along the axial (longitudinal) dimension of the NF. In each case, the NF cross sections were represented by two-dimensional disks, with hard-core area fractions equal to the experimentally obtained cross-sectional area occupied by the NF backbones. All of the potentials are radially symmetric. This approximation is appropriate because in vivo, NFs run in parallel with effective persistence lengths of at least several hundred nanometers. Because, as noted earlier, NF sidearms are spaced ~3–4 nm apart on the backbone, there are tens to hundreds of sidearms per persistence length projecting in a complete range of radial angles from the NF backbone. The length scale on which there are appreciable radial variations in effective sidearm density are therefore small compared to typical NF–NF separation distances; thus, radial variations in the interaction potential are neglected.

Alexander–DeGennes potential

In the Alexander–DeGennes framework, the brush is assumed to have a uniform (step) monomer density profile. The equilibrium brush thickness is determined by the relative strength of two competing forces: the osmotic pressure of the chain monomers that tends to swell and expand the brush, and chain elasticity, which acts to oppose this swelling. In the expression for the interaction potential between two brush-coated surfaces, L is a composite parameter that incorporates information about monomer dimensions and chain length. We based our potential on the expression developed by Likos et al. (2000). This potential has been found to account for structure factors for polypeptide-coated spheres obtained from small-angle neutron scattering. Here y is the dimensionless distance $(r - 2R_c)/2L$, where L is the equilibrium brush thickness,

$$\beta U_s(y) = \infty \quad \text{for} \quad y \leq 0$$

$$= \alpha_{AD} \frac{16\pi R_c L^2}{35s^3} \left[28(y^{-1/4} - 1) + \frac{20}{11}(1 - y^{11/4}) \right.$$

$$\left. + 12(y - 1) \right] \quad \text{for} \quad 0 < y \leq 1$$

$$= 0 \quad \text{for} \quad y > 1. \qquad (2)$$

Here, $\beta = 1/kT$, and s is the distance between chains on the grafting surface.

Self-consistent field potential

In the self-consistent field (SCF) description of a polymer brush, the discrete monomers are represented through a field theoretical approach. Perhaps the most widely implemented potential of this type is that of Milner et al. (1988). Starting with this expression, we developed an SCF-based interaction potential for NFs. This plane–plane potential has been adapted to the sphere–sphere geometry and used to model rheologic data for entropically stabilized particles (Mewis et al., 1989). In our simulations, we used

$$\beta U_s(y) = \infty \quad \text{for} \quad y \leq 0$$

$$= \alpha_{\text{SCF}} \left(\frac{L}{a}\right)^3 R_C N^{-1/2} s^{-2} \left(\frac{\pi^3}{12}\right)$$

$$\times \left(-\ln(y) + \frac{1}{3}(1 - y^3) - \frac{1}{30}(1 - y^6)\right.$$

$$\left. - \frac{9}{5}(1 - y)\right) \quad \text{for} \quad 0 < y \leq 1$$

$$= 0 \quad \text{for} \quad y > 1. \tag{3}$$

Here, N is the number of monomers per chain, a is the monomer length, and L is determined by the expression,

$$L = \left(\frac{12}{\pi^2}\right)^{1/3} Na \left(\frac{v}{as^2}\right)^{1/3}, \tag{4}$$

where v is the monomer volume taken to be a^3 as a first approximation, and α_{SCF} is as before.

Polyelectrolyte brush potential

To incorporate the effects of chain charge into our model, we implemented a pair potential function that follows the scaling analysis of Pincus (1991). Here, brush structure is governed by the competing influences of monomer–monomer electrostatic repulsion and osmotic pressure, which tend to swell the brush, and chain elasticity, which opposes brush expansion. The model is for two plates grafted with a uniform layer of polyelectrolytes each composed of N monomers of length a, a fraction f of which are charged, in the presence of salt concentration c_s. The disjoining (osmotic) pressure (Π) for such a system is given by

$$\beta \Pi \approx 2N^2/(s^4 c_s D^2). \tag{5}$$

To obtain the free energy, we integrate with respect to D,

$$\beta F_p = 2N^2/(s^4 c_s D). \tag{6}$$

Invoking the Derjaguin approximation as above, we find,

$$\beta U_s(y) = \alpha_{\text{PE}}[2\pi R_c N^2/(s^4 c_s)]\ln(y), \tag{7}$$

where, again, the dimensionless distance y is used, and α_{PE} is the scaling factor.

Telechelic brush potential

Telechelic brushes are composed of chemically bifunctional molecules. One end binds the grafting surface, and the other is free to bind other chains, either within the brush or in an apposing brush. Experimental studies with the surface forces apparatus show that telechelic brushes retain the long-range repulsion characteristic of polymer brushes but enter an attractive regime when the brushes are brought into contact. Thus, telechelic brushes serve as an appropriate physical model for cross-bridging interactions. For the repulsive component of the interaction potential, we retained the Pincus expression used earlier. We begin with the expression developed by Zilman and Safran (2001) for the interaction potential between two plates coated with telechelic (end-associating) brushes,

$$\beta F_P = \beta F_{\text{rep}} - \beta \epsilon N_s, \tag{8}$$

where F_{rep} is a repulsive flat-plate polymer brush interaction potential (taken here to be the expression for polyelectrolyte brushes developed above), and ϵ is the energy of association per unit area. N_s is the number of chain ends in contact per unit area, given by $N_s = 4N^{-1/2}\sigma^{5/6}(1 - u^2)u^{1/2}$, where, $u = D/(2L)$ and $\sigma = a^2/s^2$. These expressions assume that intrafilament cross bridging is far less prevalent than interfilament cross bridging and that the chains in adjacent brushes do not interdigitate. Applying the Derjaguin approximation, we find,

$$\beta U(y) = \beta U_{\text{PE}}(y)$$

$$- \alpha_{\text{tel}} \epsilon 2\pi R_c L \left[\frac{2}{3}(1 - y^{3/2}) - \frac{2}{7}(1 - y^{7/2})\right], \tag{9}$$

where $U_{\text{PE}}(y)$ is the sphere–sphere interaction potential for interacting polyelectrolyte brushes.

Choices of polymer parameters

Polymer parameters were chosen to reflect the known physical dimensions of the murine NF-H sidearm. We took $N = 679$, the number of amino acids in the tail domain of NF-H. We also set $R_c = 5$ nm and $s = 3$ nm based on estimates from EM of purified single NFs (Geisler and Weber, 1981).

METHODS

Processing electron micrographs

Electron micrographs of sciatic nerve cross-sections from 9-month-old mice were obtained as described previously (Yin et al., 1998). Each EM
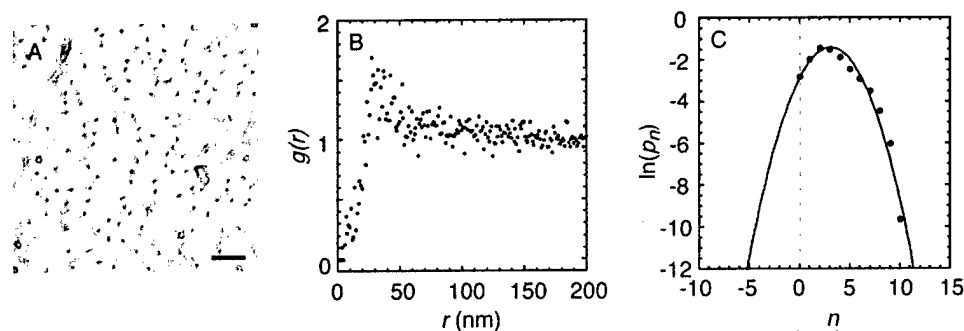
FIGURE 3 Statistical characterization of NF distributions from mouse sciatic nerve. (A) EM of mouse sciatic nerve cross section at 9 months. The NFs are the dark, pointlike structures. (Bar is 100 nm). Note that, although other cellular elements such as microtubules and organelles are shown to accurately represent the cross section, regions depleted in these elements were chosen for analysis. (B) RDF. (C) OPD for observation circle of radius 60 nm. The points represent experimentally obtained values, and the line corresponds to the predicted Gaussian fits of information theory. Each plot is a number-weighted average of EMs from six axons containing 200-1000 NFs each.

was scanned into an image file and then digitized. A rectangular area of 1–5 μm in either dimension was identified, in each case, completely within the axoplasm and relatively free of microtubules and other organelles. The position of each NF within this defined area was then identified by hand and recorded, resulting in a set of pair coordinates. These coordinates were then used to calculate OPDs and RDFs as described below. The RDF and OPD from six micrographs containing 200-1000 NFs each were weighted according to the number of NFs in each micrograph and averaged.

Monte Carlo simulation

NFs were represented as two-dimensional disks in canonical ensemble Metropolis MC simulations in which particles interacted through the radially-symmetric pair potentials described above. The disks were initially placed in a square lattice at a number density corresponding to axonal NFs. One MC move consisted of a single randomly-chosen particle displaced in both x and y within a fixed range. The total energy of the configuration was calculated assuming additivity of all pair energies. Periodic boundary conditions were enforced. A MC cycle consisted of a number of MC moves equal to the number of disks. After equilibration, as judged by constant energy and radial distribution function, distributions were accumulated every 10–15 cycles and averaged at the completion of the simulation to calculate RDFs and OPDs.

Calculation of radial distribution functions

Disk–disk distances were calculated in a pairwise manner. These distances were then binned and normalized by a factor proportional to the number of particles and the separation distance to yield $g(r)$. Calculation of $g(r)$ in a system of finite size introduces the possibility of artifacts due to the presence of walls. Several solutions have been proposed and implemented to address this, including the use of periodic boundaries (Allen and Tildesley, 1987) and normalizing against a randomly-distributed distribution (Pearson et al., 1983). After trying both of these methods, we found that periodic boundaries yielded the most robust results within reasonable computation times. Results were reproducible over a reasonable range of bin sizes, with the expected increase in noise with decreasing bin width.

Calculation of occupancy probability distributions

A circular observation area of fixed radius (60 nm unless stated) was placed at a random location within each distribution, and the particle occupancy number for each observation was recorded. This process was repeated many times (typically 10–20 times the number of particles), producing a histogram of occupancy numbers. This histogram was normalized by the number of observations to yield the OPD. In all cases, Gaussian fits were performed as parabolic fits to $\ln(p_n)$.

RESULTS

When the sciatic nerve of a 9-month-old mouse is sectioned and its constituent axons are visualized by EM, an ordered distribution of point-like structures is revealed (Fig. 3 A). Each of these structures is the cross section of an individual NF. To quantify NF organization, we calculated both RDFs (Fig. 3 B) and OPDs (Fig. 3 C). The RDF appears noisy because of the necessity for a small bin size (1 nm) in combination with the finite experimental data. The values of $g(r)$ at distances less than 10 nm approach zero, which is consistent with measurements of isolated NFs by EM that demonstrate an excluded volume diameter of 8–12 nm (Geisler and Weber, 1981). The deviation of these values from zero reflects both the noise in these $g(r)$ calculations and measurement uncertainties at small separation distances. Two key features of the RDF are the position of the first peak (r_{max}) and its magnitude (g_{max}). The most prominent feature of the RDF is a gradually developing maximum with $g_{max} > 1$ at r_{max} at 30–45 nm, consistent with previously measured distributions of nearest-neighbor interfilament spacings for mice of this age (Yin et al., 1998). The OPD, in turn, is well described by a Gaussian distribution with a mean of 2.6 and a standard deviation of 1.7. Within a robust range, the Gaussian description holds independent of the choice of observation window radius (varied between ~50 and 100 nm, not shown). Taken together, these experimental findings show order in the system that can be described using only the NF cross-sectional density and the NF–NF pair potential of mean force. This motivates our representation of the system in Monte Carlo simulations by a radially symmetric NF–NF pair potential that characterizes NF organization.
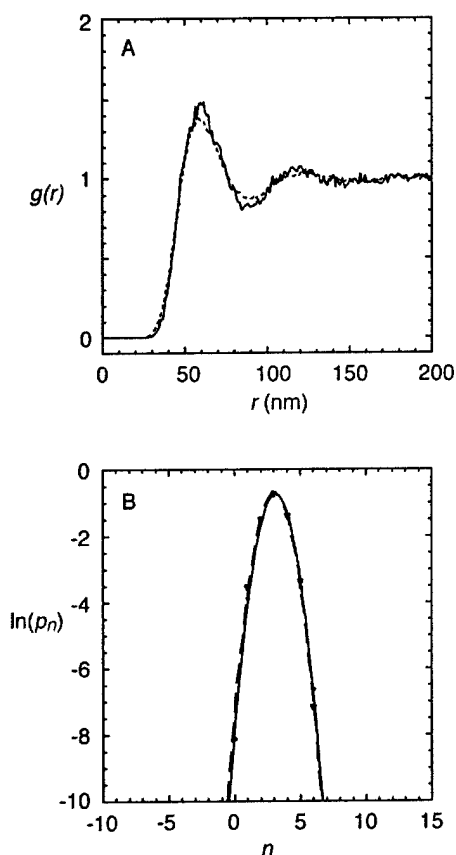
FIGURE 4 Representation of NF sidearms as neutral polymer chains. The sidearms were modeled to interact according to the Alexander–De-Gennes potential (*solid lines*) and self-consistent field potential (*dashed lines*) for neutral polymer brushes. (A) RDFs. (B) OPDs. In (B), the points represent the results from simulation, and the lines represent Gaussian fits.

We next implemented two neutral polymer brush models (Alexander–DeGennes and self-consistent field descriptions) in Monte Carlo simulations and calculated the resulting RDF (Fig. 4 A) and OPD (Fig. 4 B). Both models produce RDFs with gradually developing first peaks at 50–60 nm. It is interesting to note that the scaling parameter (α) needed to superimpose the data with the SCF potential (3×10^{-7}) was much smaller than for Alexander–DeGennes potential (0.05). These parameters are expected to differ because the Alexander–DeGennes expression is itself obtained from scaling arguments. A physical interpretation of this difference is discussed below. For both potentials, r_{max} is 10–15 nm greater than the experimentally obtained value. The value of g_{max} is in reasonable agreement with experiment. However, given the marked scatter in the experimental data, anything more than a qualitative comparison of these features of the RDFs is not possible. The experimental OPD, by contrast, is much more amenable to comparison with simulation. Both models produce Gaussian OPDs with mean occupancies of 2.7, as expected by the fixed NF density. The variances of the two OPDs
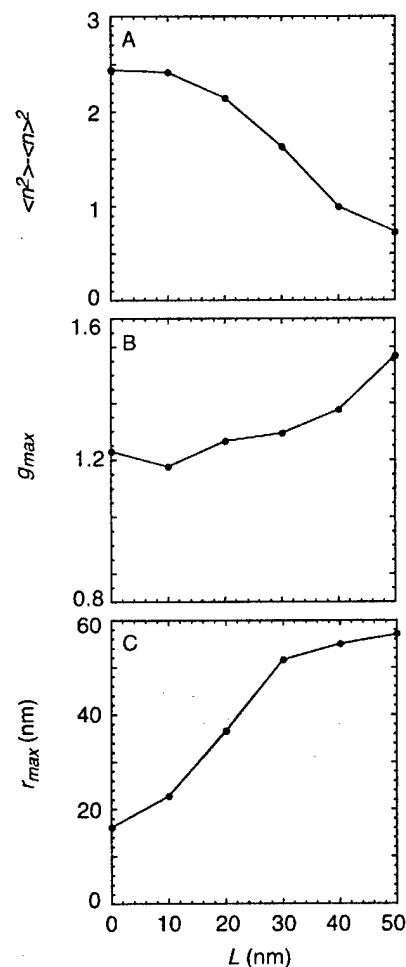
FIGURE 5 Effect of equilibrium brush thickness on structure in NF distributions. The equilibrium brush thickness (L) was systematically varied, and several descriptors of $g(r)$ and p_n were examined. (A) $\langle n^2 \rangle - \langle n \rangle^2$. For a Gaussian curve, this corresponds to the variance, which decreases with stronger interfilament correlations. (B) The magnitude of the first maximum in $g(r)$ (g_{max}). This is a metric for structure at distances corresponding to nearest-neighbor spacing. (C) The interfilament distance (r_{max}) at which the maximum value of $g(r)$ is reached. The shaded area corresponds to the range of interfilament distances covered by the first peak in the experimental RDF (shown in Fig. 1), and, as such, gives a range over which NF–NF spacing is expected to be controlled by the model.

from simulation are identical to one another but are somewhat smaller than the experimental OPD.

To examine the effects of brush properties on the NF distribution, we conducted additional simulations in which only the equilibrium brush thickness (L) was varied in the Alexander–DeGennes expression. Changes in the radial distribution functions are tracked by examining the primary peak position and magnitude in $g(r)$ and the variance of the OPD. As the brush thickness is increased, the variance of the OPD falls, a signature of stronger pair correlations and smaller local density fluctuations (Fig. 5 A). Consistent with this result are the changes in the RDFs. As the brush thickness is increased, the distribution develops structure,

and this structure shifts to greater distances (Fig. 5, B and C). At the lowest values of L, as the effective NF cross-sectional density decreases, structure disappears with g_{max} approaching the hard-sphere limit. Physiologically, r_{max} corresponds to favored nearest-neighbor interfilament spacings. The values obtained from simulation are in agreement with the range of these values observed in our system (Fig. 1), and, more generally, for a variety of axonal systems (deWaegh et al., 1992; Lee and Cleveland, 1996). Thus, changes in brush thickness can affect structure in cross-sectional NF distributions by increasing the range of inter-filament interactions and increasing effective NF density.

Because the Alexander–DeGennes potential collapses monomer properties (size, charge, etc.) into the parameter L, one cannot directly probe the effects of independently changing these microscopic parameters on brush structure. This is important to the extent that the NF sidearms acquire a substantial net negative charge from extensive serine phosphorylation of NF-H, and much evidence from studies in vitro and in vivo implicates the degree of NF-H phosphorylation as an important regulator of interfilament spacing. To explore these effects, we conducted simulations in which the NF sidearms were represented as polyelectrolytes. When all serines in the murine NF-H tail sequence are phosphorylated, it bears a fractional charge of 0.067. As the fractional charge is increased to this level, corresponding to successive phosphorylation, the RDF gains structure (Fig. 6 A). The basis for this change is the increase in equilibrium brush thickness, which rises linearly with fractional charge according to the Pincus formalism. This is illustrated by the narrower OPDs with increasing fractional charge (Figs. 6 B and 7 A), which mirrors the observed dependence when the brush thickness was directly manipulated through the parameter L in the Alexander–DeGennes potential. As the range of interfilament repulsion rises, pair correlations become stronger and local fluctuations in density are reduced. Likewise, the parameters describing the RDF change systematically. As the fractional charge is increased, we observe a graded increase in structure (Fig. 7 B) and a shift to greater favored NF–NF separation distances (Fig. 7 C). Moreover, changes in fractional charge produce changes in NF–NF spacing that correspond to the range of the first maximum in the experimental RDF (Fig. 1). According to all three metrics of NF organization, structure changes in a gradual manner over a physiologic range of phosphorylation.

The preceding results support the notion that a purely repulsive force imparts structure to NF distributions observed in axons and that a phosphorylation/dephosphorylation mechanism can control the range of this repulsion and thereby the organization of the distribution. A potential based on this physical model yields NF distributions that are consistent with experimentally measured values. We next examined the effect of superimposing attractive cross-bridging interactions onto a repulsive potential through a tele-
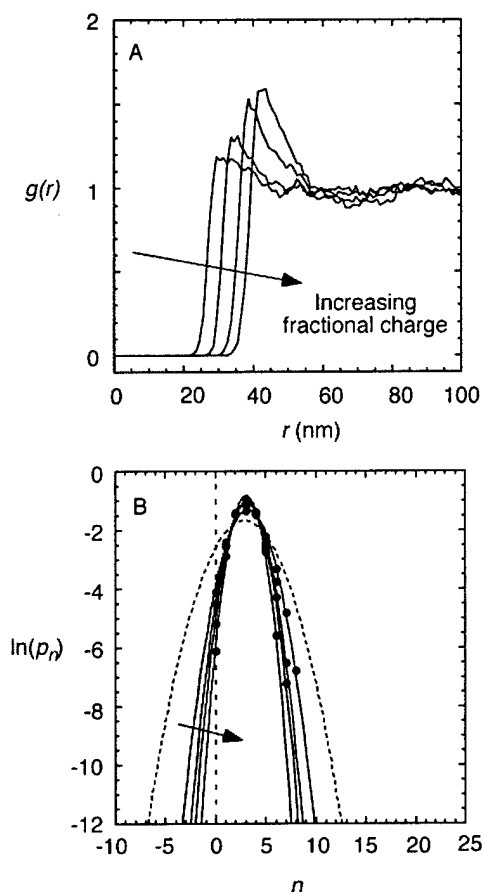

FIGURE 6   Effect of sidearm charge on structure in NF distributions. The fractional charge was increased to 0.067, corresponding to successive phosphorylation to the fully phosphorylated NF sidearm. (A) RDFs. (B) OPDs. The Gaussian for the experimental data (broken line) is reproduced here as a guide. In each case, the arrow indicates the direction of increasing fractional charge.

chelic brush model (Fig. 8). Modeling cross bridging as a telechelic brush-like interaction produces an NF–NF attractive component in the potential. The choice of this model was motivated in part by a previous report in which we represented these interactions in terms of a square-well attractive potential. There, we found that the discontinuity in the square-well potential results in prominent spikes in the RDF that are inconsistent with the experimental data (S. Kumar, X. Yin, B. D. Trapp, M. E. Paulaitis, and J. H. Hoh, submitted for publication). In molecular terms, superimposing an increasingly attractive component onto the repulsive potential is equivalent to either increasing the energy of individual cross bridges or increasing the number of cross bridges at a fixed energy. As the attractive component is increased incrementally to $\sim 30kT$, neither the RDF nor the OPD change appreciably, in contrast to the observed physiological range of change. The width of the OPD essentially remains constant. There is a small decrease in g_{max} and an increase in r_{max}, reflecting the greater sensitivity of the RDF to changes in potential.
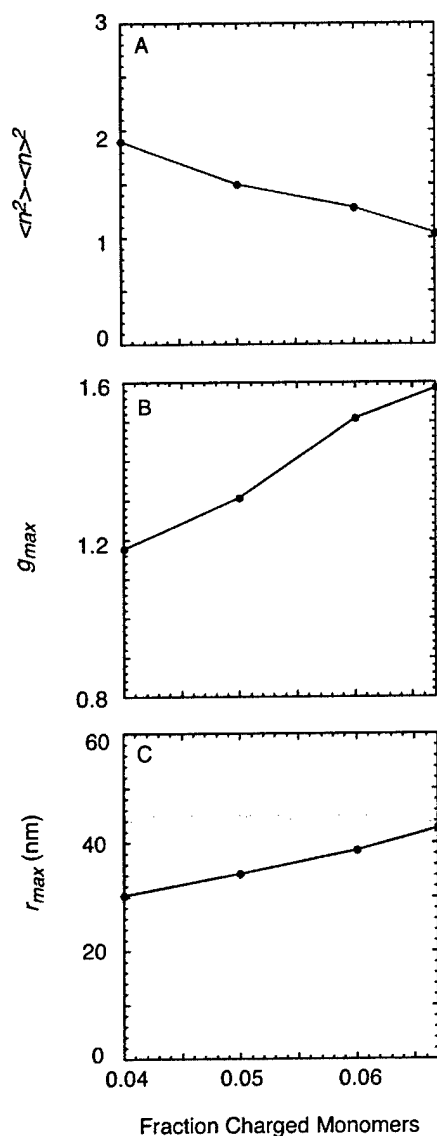
FIGURE 7 Variation of RDF and OPD parameters with sidearm phosphorylation. (A) $\langle n^2 \rangle - \langle n \rangle$, (B) g_{max}, and (C) r_{max}. The maximum charge here (0.067) approximately corresponds to complete phosphorylation of the NF-H sidearm. As the charge is increased up to this value, NF–NF pair correlations rise as a result of stronger interfilament repulsion, and the position of the favored NF–NF spacing increases. The shaded area in (C) is as described for Fig. 5.

FIGURE 8 Effect of NF–NF attractive interactions on structure in NF distributions: moderate cross bridging. The repulsive component of the interaction potential was fixed at the values corresponding to a fractional charge of 0.067, and the attractive energy was increased up to a total of $\sim 30kT$ per NF pair through a formalism in which the sidearms were treated as telechelic (associative) polymers. (A) RDFs. For modest increases in NF attractive forces, few changes are observed in the first peak of $g(r)$. (B) OPDs. In each case, the arrow points in the direction of increasing attraction. Neither the RDF nor the OPD changes appreciably in this regime of attractive energies.

As the attractive component is increased beyond 70–80kT per NF pair, an abrupt transition is observed in the RDF and OPD. g_{max} is an order of magnitude greater than that observed for cross-bridging interactions up to 30kT, and the radius corresponding to the effective excluded volume is twice the NF backbone radius ($r = 10$ nm) (Fig. 9 A). Visual inspection of a configuration sampled during the simulation reveals that this is due to extensive NF aggregation (*inset*). The OPD deviates dramatically from a Gaussian distribution, with a maximum occupancy probability at $n = 0$, which reflects the dominance of voids left as a result of

aggregation. Further, the large deviation from Gaussian behavior indicates that pair correlations in the context of the information theory framework cannot describe the organization. At these high attractive energies, the shape and magnitude of the RDF and OPD differ substantially from the experimental results, suggesting that attractive energies in this regime yield unrealistic descriptions of axonal NF organization. This justifies setting 70kT as a maximum cutoff below which the effect of NF cross bridging as a structural determinant may be examined.

We therefore varied the attractive component between 0 and 70kT and examined the effect on the parameters of the RDF and OPD (Fig. 10). There is very little change in either the variance of the OPD over this range of attractive energies (Fig. 10 A) or the position of the first peak in the RDF (Fig. 10 C). In particular, coverage of the range of r_{max} observed in the experimental RDF is poor. The primary maximum of the RDF does decrease modestly as the attractive energy is increased (Fig. 10 B). However, the observed
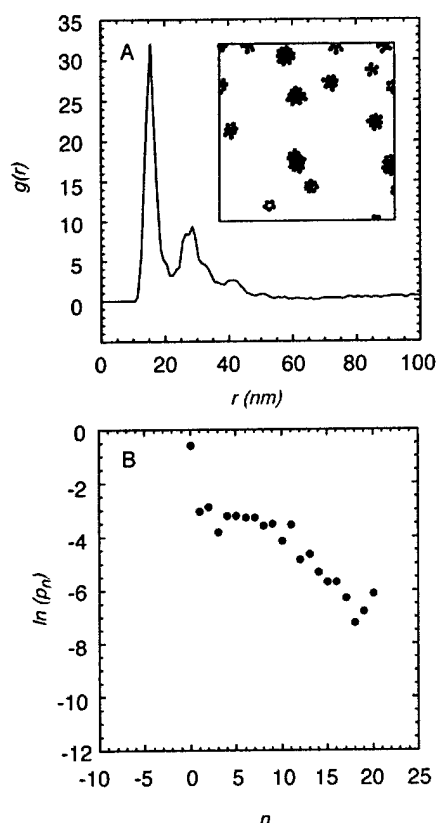
FIGURE 9 Effect of NF–NF attractive interactions on structure in NF distributions: strong cross bridging. When the NF–NF attractive energy is increased beyond 70–80kT, an abrupt phase transition occurs, leading to characteristic changes in the RDF and OPD. (A) RDF for attractive component of 150kT. Inspection of a sample configuration (*inset*) reveals NF–NF aggregation and phase separation. (B) OPD for the same pair potential. The pronounced maximum at $n = 0$ and the non-Gaussian shape reflect the large void spaces induced by NF–NF aggregation.

FIGURE 10 Variation of RDF and OPD parameters with sidearm cross bridging. Changes in NF distribution structure parameters with increases in NF–NF attraction for levels of cross bridging that are not sufficiently strong to induce aggregation. (A) $\langle n^2 \rangle - \langle n \rangle^2$. ($B$) g_{max}. (C) r_{max}. There is little change in any of the parameters over this range of attractive energies. At the highest energies, the attraction counteracts the repulsive forces and reduces NF–NF correlations. The shaded area in (C) is as described for Figs. 5 and 7.

direction of change is toward decreasing NF–NF organization with increasing cross bridging, which is opposite from that predicted by NF cross-bridging models (Gotow et al., 1994). We find that increasing attractive cross-bridging interactions in a physiologically realistic regime does not significantly influence NF organization. Where effects are seen, they regulate NF organization in a manner opposite that predicted by the underlying physical model. That is, cross bridging diminishes the organizing influence of repulsive interactions. Therefore, these results do not support the cross-bridging hypothesis.

DISCUSSION

Several key findings emerge from the analysis of NF distributions. In particular, the RDFs show first peak positions consistent with measured mean nearest-neighbor interfilament distances. The experimental OPDs are well described by a Gaussian distribution, motivating the representation of the NF distributions in terms of a density and pair potential

of mean force. The use of interaction potentials, in which the sidearms are represented as neutral polymer chains, provides RDFs and OPDs that reproduce the general features in the experimental data. All of the physical parameters in these models may be reliably estimated from existing structural data. With respect to the scaling constant α, we find that a much smaller prefactor is needed for the SCF potential to describe the data than for the Alexander–De-Gennes potential. Given the scaling arguments used to de-

termine these potentials, the disparity in prefactors is not surprising; the differences in which each model treats the monomer density profile may also play a role. Indeed, direct comparison of the compressive forces predicted by each model shows that the SCF force is both greater and more long range than the Alexander–DeGennes force (Milner et al., 1988). Simulations in which the brush thickness was systematically varied reveal that increases in brush thickness produce increases in the structure of the NF distribution. This immediately suggests that changes in sidearm expansion may serve to regulate interfilament spacing and NF organization. This notion has been invoked in the context of cross-bridging models, where the sidearms have been hypothesized to "extend" or "unfold" under increasing phosphorylation, leading to increased cross-bridging distances (Jaffe et al., 2001). However, the data presented here show that sidearm extension itself, not changes in cross-bridging dimensions, determines axonal NF structure.

The simulation results implicate phosphorylation as a mechanism for controlling sidearm expansion. As the fractional charge along the sidearm is increased through the physiologically observed range, we observe dramatic changes in NF organization both by RDFs and by OPDs. This is consistent with a mechanism in which increased sidearm phosphorylation produces an expanded brush through local electrostatic and osmotic interactions. As discussed earlier, much evidence supports sidearm phosphorylation as an important regulator of interfilament spacing. Our results support a mechanism by which phosphorylation serves as a biochemical regulator (i.e., a graded switch) that controls interfilament spacing by expanding or collapsing the sidearm brush. Cross bridging may occur between NFs, but there is no evidence here that they contribute to structure in the context of a preexisting repulsive potential. This finding is consistent with previous efforts to model cytoskeletal interactions, which suggest that soft electrostatic repulsion between dilute cylindrical particles can generate considerable long-range order (Kramer and Herzfeld, 2000), and cross-linking proteins primarily serve to stabilize the relative orientations of individual filaments rather than drive their organization (Herzfeld, 1996).

Cross-linking has been invoked as an important regulatory force for actin and intermediate filament networks (Coulombe et al., 2000, Mullins et al., 1998). An emerging theme for many of these networks is that structural and mechanical properties are controlled by many relatively low-affinity cross-links, allowing rapid changes in cell shape and viscoelasticity. Therefore, one might expect that, if cross bridging were a critical regulator of axonal NF structure, one would observe significant changes in this structure over a range of small binding energies. Instead, our simulations with telechelic brush potential functions predict only modest changes in structure for attractive energies up to $\sim70kT$. When the cross-bridging energy is increased beyond this threshold, the simulations demonstrate extensive NF aggregation.

Although it is unlikely that NFs in healthy axons ever aggregate to the extent observed here, the simulations in this regime suggest a connection between dominant attractive forces in general and mechanisms of NF pathology. Several studies show that NF aggregation in neurodegeneration is accompanied by increases in intracellular calcium concentrations (Cassarino et al., 1999), whereas others have shown that multivalent cations can induce NF aggregation in vitro (Leterrier et al., 1992). Moreover, normally repulsive polyelectrolyte brushes can be induced to attract in the presence of divalent cations (Tamashiro et al., 2001). One may therefore postulate a pathological process in which the normally repulsive NF–NF interaction is made attractive through a large, local increase in multivalent cation concentration, leading to aggregation.

In our depiction of cross-bridging interactions, we neglect cross bridging between sidearms on the same filament (i.e., intrafilament cross bridging) as a positive structural determinant. This is justified for several reasons. First, the structures reported in EM studies are largely inter- rather than intrafilament cross bridges. Second, in cases where intrafilament cross-bridging models have been invoked, such cross bridges are proposed to weaken rather than strengthen interfilament interactions by making the sidearms less available to adjacent NFs (Gou et al., 1998). Although our data do not support interfilament cross-bridging as a significant contributor to NF structure, net increases in intrafilament interactions, i.e., reductions in NF sidearm brush thickness, weaken interfilament interactions and diminish axonal NF structure.

Both the RDF and the OPD yield important structural information about the organization of NF cross-sections, although the RDFs show considerably more experimental noise than the OPDs. Several factors account for this. First, the RDF is more sensitive than the OPD to the noise produced by the relatively limited experimental sample size. Second, the OPD incorporates pair correlations through an integrated form of the RDF, via the second moment of the OPD. This integration tends to average out the noise in the RDF, leading to smooth probability distributions. An important tradeoff, however, is that the OPD tends to be less sensitive to changes in interaction potentials than does the RDF. This is evidenced by the simulations with telechelic brush models in the regime of moderate attractive energy, in which the RDF shows modest changes with increasing attraction but in which changes in the OPD are essentially negligible.

Finally, it is interesting to note that all of the repulsive potentials examined here somewhat overpredict structure, particularly at small separation distances. At least three factors contribute to this. First, at small NF–NF separations, these separations begin to approach experimental uncertainties in measuring relative NF positions by EM. Second, the

RDF is calculated by collecting a histogram of NF–NF separation distances and normalizing by a factor that is itself proportional to separation distance. Thus, these two factors tend to magnify errors in measurements of small separation distances. Third, the infinitely steep repulsion included in these interaction potentials produces artificially stringent exclusion volumes at small separations. This phenomenon has been observed in neutron scattering studies of flexible dendrimers, in which hard-wall potentials were found to substantially overpredict the first peak in the structure factor. In those studies, the Gaussian core model (GCM), a considerably softer interaction potential, was found to improve the description of the data (Likos et al., 2001). To our knowledge, GCM potentials, which explicitly incorporate all of the molecular details relevant to NFs (e.g., chain charge, grafting density), have not yet been developed or implemented for polymer brush interactions. It would be useful to fashion more physically detailed GCM expressions and to check for better agreement with experiment.

REFERENCES

Allen, M. P., and D. J. Tildseley. 1987. Computer Simulation of Liquids. Oxford Science Publications, Oxford, U.K.

Braun, J., J. R. Abney, and J. C. Owicki. 1984. How a gap junction maintains its structure. *Nature.* 310:316–318.

Braun, J., J. R. Abney, and J. C. Owicki. 1987. Lateral interactions among membrane-proteins—valid estimates based on freeze–fracture electron-microscopy. *Biophys. J.* 52:427–439.

Brown, H. G., and J. H. Hoh. 1997. Entropic exclusion by neurofilament sidearms: a mechanism for maintaining interfilament spacing. *Biochemistry.* 36:15035–15040.

Cassarino, D. S., and J. P. Bennett. 1999. An evaluation of the role of mitochondria in neurodegenerative diseases: mitochondrial mutations and oxidative pathology, protective nuclear responses, and cell death in neurodegeneration. *Brain Res. Rev.* 29:1–25.

Chen, J. G., T. Nakata, Z. Z. Zhang, and N. Hirokawa. 2000. The C-terminal tail domain of neurofilament protein-H (NF-H) forms the crossbridges and regulates neurofilament bundle formation. *J. Cell Sci.* 113:3861–3869.

Chin, T. K., P. A. M. Eagles, and A. Maggs. 1983. The proteolytic digestion of ox neurofilaments with trypsin and alpha-chymotrypsin. *Biochem. J.* 215:239–252.

Chin, T. K., S. E. Harding, and P. A. M. Eagles. 1989. Characterization of 2 proteolytically derived soluble polypeptides from the neurofilament triplet components NFM and NFH. *Biochem. J.* 264:53–60.

Coulombe, P. A., O. Bousquet, L. Ma, S. Yamada, and D. Wirtz. 2000. The 'ins' and 'outs' of intermediate filament organization. *Trends Cell. Biol.* 10:420–428.

de Waegh, S. M., V. M. Y. Lee, and S. T. Brady. 1992. Local modulation of neurofilament phosphorylation, axonal caliber, and slow axonal transport by myelinating schwann cells. *Cell.* 68:451–463.

Eyer, J., and J. F. Leterrier. 1988. Influence of the phosphorylation state of neurofilament proteins on the interactions between purified filaments in vitro. *Biochem. J.* 252:655–660.

Garde, S., R. Khare, and G. Hummer. 2000. Microscopic density fluctuations and solvation in polymeric fluids. *J. Chem. Phys.* 112:1574–1578.

Geisler, N., and K. Weber. 1981. Self-assembly in vitro of the 68,000 molecular-weight component of the mammalian neurofilament triplet proteins into intermediate-sized filaments. *J. Mol. Biol.* 151:565–571.

Genz, U., B. Daguanno, J. Mewis, and R. Klein. 1994. Structure of sterically stabilized colloids. *Langmuir.* 10:2206–2212.

Georges, E., and W. E. Mushynski. 1987. Chemical modification of charged amino-acid moieties alters the electrophoretic mobilities of neurofilament subunits on SDS polyacrylamide gels. *Eur. J. Biochem.* 165:281–287.

Gotow, T., T. Tanaka, Y. Nakamura, and M. Takeda. 1994. Dephosphorylation of the largest neurofilament subunit protein influences the structure of crossbridges in reassembled neurofilaments. *J. Cell Sci.* 107:1949–1957.

Gou, J. P., T. Gotow, P. A. Janmey, and J. F. Leterrier. 1998. Regulation of neurofilament interactions in vitro by natural and synthetic polypeptides sharing lys-ser-pro sequences with the heavy neurofilament subunit NF-h: neurofilament crossbridging by antiparallel sidearm overlapping. *Med. Biol. Eng. Comput.* 36:371–387.

Herzfeld, J. 1996. Entropically-driven order in crowded solutions: from liquid crystals to cell biology. *Acc. Chem. Res.* 29:31–37.

Hisanaga, S., and N. Hirokawa. 1988. Structure of the peripheral domains of neurofilaments revealed by low-angle rotary shadowing. *J. Mol. Biol.* 202:297–305.

Hoh, J. H. 1998. Functional protein domains from the thermally driven motion of polypeptide chains: a proposal. *Proteins Struct. Funct. Genet.* 32:223–228.

Hsieh, S. T., T. O. Crawford, and J. W. Griffin. 1994. Neurofilament distribution and organization in the myelinated axons of the peripheral nervous system. *Brain Res.* 642:316–326.

Hummer, G., S. Garde, A. E. Garcia, M. E. Paulaitis, and L. R. Pratt. 1998. Hydrophobic effects on a molecular scale. *J. Phys. Chem. B.* 102:10469–10482.

Hummer, G., S. Garde, A. E. Garcia, A. Pohorille, and L. R. Pratt. 1996. An information theory model of hydrophobic interactions. *Proc. Natl. Acad. Sci. U.S.A.* 93:8951–8955.

Israelachvili, J. N. 1992. Intermolecular and Surface Forces. Academic Press, New York.

Jaffe, H., P. Sharma, P. Grant, and H. C. Pant. 2001. Characterization of the phosphorylation sites of the squid (*Loligo pealei*) high-molecular-weight neurofilament protein from giant axon axoplasm. *J. Neurochem.* 76:1022–1031.

Julien, J. P. 1999. Neurofilament functions in health and disease. *Curr. Opin. Neurobiol.* 9:554–560.

Kramer, E. M., and J. Herzfeld. 2000. Avoidance model for soft particles. II. Positional ordering of charged rods. *Phys. Rev. E.* 61:6872–6878.

Leapman, R. D., P. E. Gallant, T. S. Reese, and S. B. Andrews. 1997. Phosphorylation and subunit organization of axonal neurofilaments determined by scanning transmission electron microscopy. *Proc. Natl. Acad. Sci. U.S.A.* 94:7820–7824.

Lee, M. K., and D. W. Cleveland. 1996. Neuronal intermediate filaments. *Annu. Rev. Neurosci.* 19:187–217.

Lee, V. M. Y., L. Otvos, M. J. Carden, M. Hollosi, B. Dietzschold, and R. A. Lazzarini. 1988. Identification of the major multiphosphorylation site in mammalian neurofilaments. *Proc. Natl. Acad. Sci. U.S.A.* 85:1998–2002.

Lees, J. F., P. S. Shneidman, S. F. Skuntz, M. J. Carden, and R. A. Lazzarini. 1988. The structure and organization of the human heavy neurofilament subunit (NF-H) and the gene encoding it. *EMBO J.* 7:1947–1955.

Leterrier, J. F., and J. Eyer. 1987. Properties of highly viscous gels formed by neurofilaments in vitro—a possible consequence of a specific interfilament cross-bridging. *Biochem. J.* 245:93–101.

Leterrier, J. F., D. Langui, A. Probst, and J. Ulrich. 1992. A molecular mechanism for the induction of neurofilament bundling by aluminum ions. *J. Neurochem.* 58:2060–2070.

Leung, C. L., D. M. Sun, and R. K. H. Liem. 1999. The intermediate filament protein peripherin is the specific interaction partner of mouse BPAG1-n (dystonin) in neurons. *J. Cell Biol.* 144:435–446.

Likos, C. N., M. Schmidt, H. Lowen, M. Ballauff, D. Potschke, and P. Lindner. 2001. Soft interaction between dissolved flexible dendrimers: theory and experiment. *Macromolecules.* 34:2914–2920.

Likos, C. N., K. A. Vaynberg, H. Lowen, and N. J. Wagner. 2000. Colloidal stabilization by adsorbed gelatin. *Langmuir.* 16:4100–4108.

McHale, M. K., G. F. Hall, and M. J. Cohen. 1995. Early cytoskeletal changes following injury of giant spinal axons in the lamprey. *J. Comp. Neurol.* 353:25–37.

Mewis, J., W. J. Frith, T. A. Strivens, and W. B. Russel. 1989. The rheology of suspensions containing polymerically stabilized particles. *AIChE J.* 35:415–422.

Milner, S. T., T. A. Witten, and M. E. Cates. 1988. Theory of the grafted polymer brush. *Macromolecules.* 21:2610–2619.

Mukhopadhyay, R., and J. H. Hoh. 2001. AFM force measurements on microtubule-associated proteins: the projection domain exerts a long-range repulsive force. *FEBS Lett.* 505:374–378.

Mullins, R. D., J. F. Kelleher, J. Xu, and T. D. Pollard. 1998. Arp2/3 complex from acantamoeba binds profilin and cross-links actin filaments. *Mol. Biol. Cell.* 9:841–852.

Nixon, R. A., P. A. Paskevich, R. K. Sihag, and C. Y. Thayer. 1994. Phosphorylation on carboxyl-terminus domains of neurofilament proteins in retinal ganglion-cell neurons in-vivo—influences on regional neurofilament accumulation, interneurofilament spacing, and axon caliber. *J. Cell Biol.* 126:1031–1046.

Pearson, L. T., S. I. Chan, B. A. Lewis, and D. M. Engelman. 1983. Pair distribution-functions of bacteriorhodopsin and rhodopsin in model bilayers. *Biophys. J.* 43:167–174.

Perelson, A. S. 1978. Spatial-distribution of surface-immunoglobulin on B lymphocytes—local ordering. *Exp. Cell Res.* 112:309–321.

Pincus, P. 1991. Colloid stabilization with grafted polyelectrolytes. *Macromolecules.* 24:2912–2919.

Povlishock, J. T., and C. W. Christman. 1995. The pathobiology of traumatically induced axonal injury in animals and humans—a review of current thoughts. *J. Neurotrauma.* 12:555–564.

Pusztai, L., and G. Toth. 1991. On the uniqueness of the reverse Monte-Carlo simulation.1. Simple liquids, partial radial-distribution functions. *J. Chem. Phys.* 94:3042–3049.

Romero, P., Z. Obradovic, C. R. Kissinger, J. E. Villafranca, E. Garner, S. Guilliot, and A. K. Dunker. 1998. Thousands of proteins likely to have long disordered regions. *Pacific Symp. Biocomput.* 3:437–448.

Romero, P., Z. Obradovic, X. Li, E. C. Garner, C. J. Brown, and A. K. Dunker. 2001. Sequence complexity of disordered proteins. *Proteins Struct. Funct. Genet.* 42:38–48.

Rost, B., and C. Sander. 1993. Prediction of protein secondary structure at better than 70-percent accuracy. *J. Mol. Biol.* 232:584–599.

Rost, B., and C. Sander. 1994. Combining evolutionary information and neural networks to predict protein secondary structure. *Proteins Struct. Funct. Genet.* 19:55–72.

Rout, M. P., J. D. Aitchison, A. Suprapto, K. Hjertaas, Y. Zhao, and B. T. Chait. 2000. The yeast nuclear pore complex: composition, architecture, and transport mechanism. *J. Cell Biol.* 148:635–652.

Smith, D. H., J. A. Wolf, T. A. Lusardi, V. M. Y. Lee, and D. F. Meaney. 1999. High tolerance and delayed elastic response of cultured axons to dynamic stretch injury. *J. Neurosci.* 19:4263–4269.

Strong, M. J., W. L. Strong, H. Jaffe, B. Traggert, M. M. Sopper, and H. C. Pant. 2001. Phosphorylation state of the native high-molecular-weight neurofilament subunit protein from cervical spinal cord in sporadic amyotrophic lateral sclerosis. *J. Neurochem.* 76:1315–1325.

Tamashiro, M. N., E. Hernandez-Zapata, P. A. Schorr, M. Balastre, M. Tirrell, and P. Pincus. 2001. Salt dependence of compression normal forces of quenched polyelectrolyte brushes. *J. Chem. Phys.* 115: 1960–1969.

Toth, G., and A. Baranyai. 1997. Conceptual and technical improvement of the reverse Monte Carlo algorithm. *J. Chem. Phys.* 107:7402–7408.

Uversky, V. N., J. R. Gillespie, and A. L. Fink. 2000. Why are "natively unfolded" proteins unstructured under physiologic conditions? *Proteins Struct. Funct. Genet.* 41:415–427.

Willard, M., and C. Simon. 1981. Antibody decoration of neurofilaments. *J. Cell Biol.* 89:198–205.

Wootton, J. C., and S. Federhen. 1996. Analysis of compositionally biased regions in sequence databases. *Methods Enzymol.* 266:554–571.

Yang, Y. M., J. Dowling, Q. C. Yu, P. Kouklis, D. W. Cleveland, and E. Fuchs. 1996. An essential cytoskeletal linker protein connecting actin microfilaments to intermediate filaments. *Cell.* 86:655–665.

Yin, X. H., T. O. Crawford, J. W. Griffin, P. H. Tu, V. M. Y. Lee, C. M. Li, J. Roder, and B. D. Trapp. 1998. Myelin-associated glycoprotein is a myelin signal that modulates the caliber of myelinated axons. *J. Neurosci.* 18:1953–1962.

Zilman, A. G., and S. A. Safran. 2001. Entropically driven attraction between telechelic brushes. *Eur. Phys. J. E.* 4:467–473.

Chapter 4. The neurofilament sidearm domain as a charged polymer: insights from gels and single filaments

The sidearms of neurofilaments are highly charged under physiologic conditions. The native sequences of NF-M and NF-H are particularly rich in lysine and glutamic acid, although as discussed earlier, the nominally positive and negative charges along the unmodified chain nearly balance one another. However, extensive serine phosphorylation of the sidearms confers an overall net negative charge. The experimental evidence reviewed earlier, together with the data presented in previous chapters of this thesis, strongly support the notion that the degree of sidearm phosphorylation is key to regulating interfilament spacing by influencing the effective volume occupied by the sidearms and thus NF-NF spacing.

Because NF sidearms contain an abundance of both positively and negatively charged residues, they may be classified as polyampholyte chains. Polyampholytes stand in contrast to classical polyelectrolytes, which contain a preponderance of same-signed charges (Bright et al., 2001; Kudaibergenov, 1999; Tamashiro et al., 2001). Synthetic polyampholytes have been studied extensively on both a theoretical level (Diehl et al., 1996; Higgs and Joanny, 1990; Kantor et al, 1992) and an experimental level (English et al., 1996; Kamiyama and Israelachvili, 1992; Nisato et al., 1990). Two key findings emerge from these studies. First, polyampholyte properties often depend strongly on ionic strength. Second, in cases where polyampholytes contain titratable groups (so-

called annealed chains), changes in pH can substantially influence polyampholyte properties. Thus, by altering intramolecular electrostatic interactions, one may manipulate the structure of polyampholyte chains and therefore the properties of the structures into which they self-assemble. In general, the specific charge distribution along the chain also plays a key role; one may consider two limiting cases. In the classical polyelectrolyte limit, where electrostatic repulsion between monomers along the chain determine properties, the chain is expected to condense with increasing ionic strength as the repulsive interactions are screened out. Conversely, in the classical polyampholyte limit, where opposite charges along the chain attract one another, the chain is expected to expand with increasing ionic strength (Ohlemacher et al., 1996). One particularly relevant example is that of β-casein, a 24-kD protein found in milk fat droplets whose carboxy terminus is highly charged. A brushlike layer of β-casein chains extends from the outer surface of each fat droplet, thus surrounding the droplet with a hydrophilic coating and emulsifying the fat. Cicuta and Hopkinson (2001) used Langmuir-Blodgett methods to study the conformational properties of β-casein as a function of buffer ionic strength and pH. They found that β-casein could expand, condense, or not change effective volume with increasing ionic strength, depending on the pH of the experiment. These changes in chain conformation are reflected in the bulk properties of β-casein films. For example, the dilational moduli of these films varies dramatically with changes in pH and ionic strength, which correlates with observations from the industrial processing of milk. Thus, changes in the magnitude of intramolecular electrostatic interactions strongly influence macroscopic properties. In a biological system, this may shed insight into macromolecular function and regulation.

NFs assemble into viscoelastic gels under appropriate buffer conditions, a process which may be facilitated by sedimentation. A small number of studies have directly examined the bulk properties of NF gels. Leterrier and colleagues (1996) examined the gelation kinetics and viscoelastic properties of NF gels using cone-and-plate rheometry. A key finding from this report is that NF gels have very large elastic moduli compared to other intermediate filaments of comparable molecular weight (e.g., vimentin). This was ascribed to extensive cross-bridging between the sidearms. Both the kinetics of gel formation and the equilibrium viscoelastic properties were found to depend on the presence of phosphoinositides, divalent cations, and actin filaments. In a later report, this group proposed a "switch" model to explain this regulation in which the sidearm of a NF either binds to its own backbone or to the sidearm of an adjacent NF; certain factors were hypothesized to alter the equilibrium between these two states (Gou et al., 1998).

The hypothesis that NF organization is influenced by the polyampholyte nature of NF sidearms predicts that interfilament interaction forces should vary with the electrostatic properties of the buffer: ionic strength, pH, and divalent cation concentration. Here, we examine those relationships and interpret our findings in terms of polyampholyte behavior. We reconstitute NFs isolated from bovine spinal cord into gels under different buffer conditions and assay for excluded volume by measuring the size of the pellet. We also perform atomic force microscopy (AFM) imaging on isolated NFs and correlate findings on the single-filament level to gel properties.

Materials and Methods

Isolation of NFs from bovine spinal cord

NFs were isolated from bovine spinal cord (BSC) as described elsewhere (Brown and Hoh, 1997; Troncoso et al., 1990). BSC was obtained from a local slaughterhouse and held on ice until processing, which began within 45 minutes of resection from the animal. BSC was then diced into 1-2 cm slices and homogenized in buffer A (100 mM MES, 1.0 mM EGTA, 0.5 mM $MgCl_2$, pH 6.5) at 1.6 mL neat buffer per g BSC. This mixture was then centrifuged at 34500 g at 4 C for 30 min. The supernatant was decanted, made 30% glycerol by volume, mixed thoroughly, and incubated at 37 C for 20 min. This mixture was then centrifuged at 158000 g for 2 h at 20 C, yielding a pellet which is a concentrated, neurofilament-rich gel. This gel was resuspended in the buffer of interest and used in experiments as described below. In some cases, the pellet was frozen in liquid nitrogen, stored at –80 C, and thawed immediately prior to use, with no detectable change in properties after 2-3 months.

Preparation of NF pellets

For studies of NF gel volume, approximately 100 μL of pellet was resuspended in 1 mL Millipore-purified water and split equally among a set of 1.5 mL Eppendorf tubes. Each tube was then centrifuged at 158000 g for 30 minutes using a tabletop microcentrifuge, the supernatant was discarded, and the resulting pellet was resuspended in the buffer of interest. Each tube was then centrifuged again and resuspended again. After 3-4 cycles of centrifugation and resuspension, the top margin of the pellet was marked and measured using a micrometer caliper. Each sedimentation was performed along with an internal standard containing the same total mass of NFs. Results are

reported as the relative pellet size which is the ratio of the pellet height for a given sample to that of the standard.

AFM imaging of single NFs

For studies of isolated NFs, approximately 2-5 µL of pellet was resuspended in 1 mL of the buffer of interest. 50 µL of this suspension was adsorbed on freshly cleaved red muscovite mica (grade V1 or V2, Asheville-Schoonmaker Mica Co., Newport News, VA) at room temperature for 15 s and washed with 5 mL of buffer. The sample was then transferred to the AFM stage for imaging. Images were obtained with a Multimode AFM with a Nanoscope III or III a controller (Digital Instruments, Santa Barbara, CA), using a glass fluid cell. Measurements were made with Olympus silicon nitride cantilevers (OMCL-TR400PSA, purchased from Digital Instruments) with lengths of 200 µm and nominal spring constants of 0.02 N/m and with Park C silicon nitride cantilevers (purchased from Digital Instruments) with lengths of 320 µm and nominal spring constants of 0.01 N/m. Prior to imaging, the microscope, sample, and cantilever were allowed to equilibrate at room temperature for at least 1 h. All images were collected in contact mode.

Enzymatic treatment of NFs

Our dephosphorylation protocol was based on previous reports (Eyer and Leterrier, 1988; Gotow et al., 1998). First, 100 uL NF pellet was resuspended in water as described above. To this suspension was added 5 µL of bovine calf intestine alkaline phosphatase (106.95 U/µl, Sigma Chemical Co., St. Louis, MO). The reaction mixture

was then incubated at 37 C for 5 h. For gel studies, the resulting suspension was

cyclically centrifuged and resuspended in the buffer of interest as described above, thus

removing enzyme via the supernatant in the process. For AFM imaging, 5 μL of the

reaction mixture was diluted into the buffer of interest and adsorbed and imaged as

described.

Results

When a suspension of NFs is centrifuged at sufficiently high speed, the NFs form

a gelatinous pellet. As the pellet size increases, the effective volume occupied by each

NF increases and the mean interfilament spacing increases.   To examine the effects of

buffer conditions and NF biochemistry on NF-NF spacing, we performed an assay for

pellet size (Figure 1). In this assay, NFs are evenly divided into several aliquots, and

each aliquot is resuspended in a buffer of defined ionic strength, pH, and divalent cation

(Ca^{++} or Mg^{++}) concentration. All aliquots are gently centrifuged together, yielding a set

of pellets containing equal amounts of NFs. The relative volumes of the pellets therefore

provide an indirect measure of interfilament spacing.

Because NF sidearms are polyampholytes, electrostatics are expected to play a

significant role in determining sidearm structure and therefore NF-NF repulsion. As a

result, NF-NF spacing should vary as a function of ionic strength. We examined this salt-

dependence over a range of buffer pH values (Figure 2).   Because there multiple

titratable groups on the NF sidearm (Glu, Lys, phosphoserine) The pH at which the

experiment is conducted strongly influences sidearm charge. Over a wide pH range (4.4,

6.8, 9.2), pellet size decreases with increasing ionic strength. In the context of the steric

repulsion model of NF organization, the corresponding decrease in NF-NF spacing with increasing salt concentration is due to condensation of NF sidearm thickness. At all three pH values, most of this decrease occurs within a concentration range of 100-150 mM. Higher salt concentrations produce little additional influence on NF-NF spacing. The steepest ionic strength dependence is observed at pH 4.4, where the NF sidearm is expected to be strongly positively charged due to protonation of lysines in the KSP domains of NF-H. Here, changing the salt concentration from 10 mM to 110 mM reduces pellet volume by 40%; conversely, at higher pH, comparable increases in salt concentrations produce more modest reductions in pellet volume (approximately 25% at pH 6.8 and 20% at pH 9.2). As the pH is increased, the sidearms are expected to acquire a progressively negative charge as the glutamate and phosphoserine residues are deprotonated.

In addition to changes in ionic strength, electrostatic repulsive forces within the NF sidearm may be directly manipulated by reducing sidearm charge. By treating native NFs with alkaline phosphatase, phosphoserine residues are dephosphorylated (Figure 3). Evidence for effective phosphorylation comes from gel electrophoresis which demonstrates a predicted shift in molecular weight of NF-H and NF-M (inset) (Eyer and Leterrier 1988; Gotow et al 1994). When dephosphorylated NFs are pelleted through a range of salt concentrations, pellet size varies only modestly. This is in contrast to native NFs, which show a steady reduction in pellet volume with increasing salt concentration. The relatively shallow dependence of NF-NF spacing on salt concentration for dephosphorylated NFs is characteristic of behavior closer to the classic polyampholyte limit, where electrostatic attraction between oppositely charged residues is balanced by

repulsion between like-charged residues. The dramatic qualitative change in the salt-dependence of gel properties with dephosphorylation underscores the importance of phosphorylation to regulating NF-NF spacing.

The polyampholyte nature of NF sidearms may be further characterized by examining the effect of divalent cations on gel behavior. In addition to their obvious physiological significance, calcium and magnesium are known to strongly influence the viscoelastic properties of NF gels in vitro (Eyer and Leterrier 1988). To probe this effect, we pelleted NFs in the presence of increasing concentrations of calcium and magnesium (Figure 4). At a total concentration of only 5 mM, Mg^{++} condenses NF pellets by approximately 22%. Increasing the concentration of Mg^{++} by a factor of 10 produces only an additional 12% reduction in pellet size (Figure 4A). Thus, small concentrations of Mg^{++} profoundly alter NF-NF spacing. These effects are reflected in the appearance of the pellets themselves (inset). Ca^{++} produces a similar degree of condensation; addition of 5 mM Ca^{++} produces a 28% reduction in pellet size (Figure 4B).

To investigate the structural origins of the effect of phosphorylation on NF gel properties, we next used AFM to image single NFs. First, native NFs were adsorbed onto mica and imaged in buffer which included either 0 mM or 100 mM NaCl(Figure 5). In these images, the NF backbones are clearly visible as snakelike filaments in a background of residual contaminants from the preparation. Surrounding each backbone is a zone of total width 100-150 nm from which these contaminants are excluded. The presence of these exclusion zones concurs with a previous report which attributed them to repulsive forces originating from the thermal motion of the unstructured sidearm domains (Brown and Hoh, 1997). Here, the exclusion zones are present at both relatively low and high

salt concentrations, suggesting they do not originate from direct electrostatic repulsion between the NFs and the contaminants. When dephosphorylated NFs are examined under the same set of buffer conditions, we observe dramatically different results (Figure 6). As with native NFs, the backbones are again prominently visible. Now, however, the exclusion zones are dramatically diminished at 0 mM NaCl (arrows) and essentially nonexistent at 100 mM NaCl.

Discussion

Several key findings emerge from our characterization of NF pellets. In particular, NF pellet volume falls with increasing ionic strength, reduced sidearm phosphorylation, and millimolar concentrations of calcium or magnesium. The size of the pellet reflects the effective volume occupied by each NF and therefore serves as an indirect measure of mean NF-NF spacing and interaction force. In terms of the entropic repulsion model of NF-NF spacing, this reduced interaction force originates from condensation of sidearm domains. Condensation or collapse of charged polymers with increases in ionic strength is characteristic of classic polyelectrolyte behavior and occurs because the added salt screens repulsive forces between charged monomers (Barrat and Joanny, 1996). This notion has been validated on several levels, including the radius of gyration of single chains (Fouissac et al., 1992), the diameter of coated spherical particles (Hariharan et al., 1998), and the thickness and interaction forces of adsorbed polymer layers (Kamiyama and Israelachvili, 1992). This is in contrast to polyampholyte-like behavior, where polymer chain volume remains constant or rises with increased ionic strength (Cicuta and Hopkinson, 2001). The most obvious origin of chain charge in the NF sidearm is the

abundance of phosphoserine residues in NF-H. Thus, one explanation for the ionic strength dependence is that phosphate-phosphate repulsion within the sidearm determines the thickness of the sidearm layer over a wide range of pH and that these repulsive forces are screened with added salt.

Further support for phosphorylation as an important regulator of NF-NF spacing comes from experiments in which the sidearms are enzymatically dephosphorylated (Figure 3). The pellet volume of dephosphorylated NFs is smaller than that of native NFs and depends much less steeply on ionic strength. This type of ionic strength dependence is more characteristic of polyampholyte behavior, where both attractive and repulsive forces within the polypeptide chain are important determinants of chain volume. This agrees well with the behavior expected from the composition of unmodified mammalian NF-H sequences, which contain closely-balanced numbers of anionic and cationic residues. Many studies have established the importance of sidearm phosphorylation to determining NF organization *in vivo*, with several finding a correlation between phosphorylation level and NF-NF spacing (de Waegh et al., 1992; Strong et al., 2000). *In vitro*, enzymatic dephosphorylation produces dramatic changes in both the gelation kinetics and viscoelastic properties of NF gels (Eyer and Leterrier 1988). In addition, thin section electron microscopy of fixed and stained NFs has shown that dephosphorylated NFs are considerably more densely packed than native NFs (Gotow et al., 1994).

The finding that NF pellets are condensed by divalent cations provides further evidence for the structural importance of phosphorylation. In synthetic polymer systems, divalent cations have been shown to produce short-ranged attractive forces, leading to

attraction between normally repulsive polymer-coated surfaces (Abraham et al., 2001). In the case of NFs, MgCl$_2$ produces profound increases in NF viscosity (Leterrier and Eyer, 1987), and AlCl$_3$ induces NF aggregation *in vtiro*. In the context of the entropic repulsion model, multivalent cations would serve to attenuate NF-NF repulsion by condensing the sidearms. At sufficiently large concentrations, multivalent cations would convert the normally repulsive NF-NF interaction into an attractive one, leading to NF aggregation in the pathological case. NF aggregation is observed by EM in the presence of high concentrations of multivalent cations (Leterrier et al., 1992; Troncoso et al., 1990). Indeed, NF sidearms have been postulated to serve as a buffer for divalent cations in healthy neurons; in neurodegenerative pathologies such as ALS, it has been proposed that large increases in intracellular calcium overwhelm the buffer system, leading to NF aggregation and ultimately cell death (Rowland and Shneider, 2001).

The AFM experiments provide direct structural support for this model of the role of phosphorylation. Native, phosphorylated NFs produce robust exclusion of contaminants even at high (>100 mM) monovalent salt concentrations, a signature of polymer brush-like behavior (Brown and Hoh, 1997). When dephosphorylated, these exclusion zones are greatly attenuated at low salt concentration and essentially ablated at high salt concentration, implying that the sidearms have condensed and therefore no longer occupy as large an effective volume. It is interesting to note that individual sidearms are never distinctly visible in any of the images presented here, even in the complete absence of exclusion zones. One reason for this is the limited lateral resolution of the AFM tip coupled with the relatively high density of NFs along the backbone; EM of single NFs show that sidearms are spaced 2-5 nm apart along the backbone, a distance

far smaller than the dimensions of a typical AFM tip (Geisler and Weber, 1981). Second, when they condense in response to changes in phosphorylation or buffer conditions, the sidearms may collapse onto the backbone. Indeed, Gou et al. (1998) propose a model in which inter- and intrafilament interactions act reciprocally to modulate the structure and mechanical properties of NF gels. While this mechanism was proposed in the context of a cross-bridging model, it could apply equally well to the entropic repulsion model.

There are several important limitations to the gel volume measurements presented here. First, the results of the assay are not directly interpretable in terms of NF-NF spacing distances; instead, trends in these distances are inferred through changes in gel volume. Second, the assay does not precisely measure a specific volume (e.g., volume per NF). This results from the geometry in which the assay is performed (pellet height along the vessel wall is used as a marker for volume), and the polydispersity of the filaments themselves. However, the relative pellet sizes are likely underestimates of actual differences in gel volume. For example, when NF gels are treated with 50 mM $MgCl_2$ (Figure 3A), gel size is reduced approximately 35% by the pellet height assay; however, inspection of the actual pellets (Figure 3A inset) suggests that the reduction in pellet size is considerably greater. At worst, then, the assay underestimates changes in interfilament spacing.

We have examined the properties of single NFs and NF gels as a function of sidearm phosphorylation and buffer conditions. In particular, we have shown that the volume of native NF gels decreases with increasing ionic strength over a wide pH range. When NFs are enzymatically dephosphorylated, this dependence becomes less steep. Native NF gel size also decreases in the presence of divalent cations at millimolar

concentrations. AFM imaging of isolated NFs reveals that native NFs produce robust molecular exclusion even at high ionic strength, a property which is markedly attenuated when the sidearms are dephosphorylated. Taken together, these results suggest that the native NF sidearm acts as a classical polyelectrolyte *in vivo* whose conformational properties are determined by the level of phosphorylation and the concentration of divalent cations. In the context of the entropic repulsion model, the degree of sidearm phosphorylation modulates the volume occupied by the NF sidearm through intramolecular electrostatic repulsion.

Figure 1. Schematic of pellet volume assay. NFs are resuspended in a buffer of given ionic strength, pH and divalent cation concentration (A). The suspension is then at 158000 g for 30 minutes, resulting in NF pellet formation (B). The resulting pellet height (arrows) is then normalized by the pellet height of an internal standard which contains the same total mass of NFs and is sedimented under identical conditions. The size of the pellet reflects mean interfilament spacing and the strength of interfilament repulsion (C). Note that in (A) the sidearms are omitted for clarity.

Figure 1
Kumar et al.

A   B   C
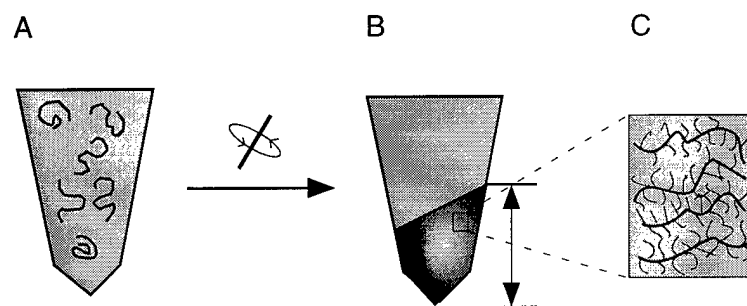
Figure 2. Effect of salt concentration on NF pellet size. (A) pH 4.4. (B) pH 6.8. (C) pH 9.2. The total salt concentration includes contributions from the MES buffer (10 mM in each case) and NaCl.
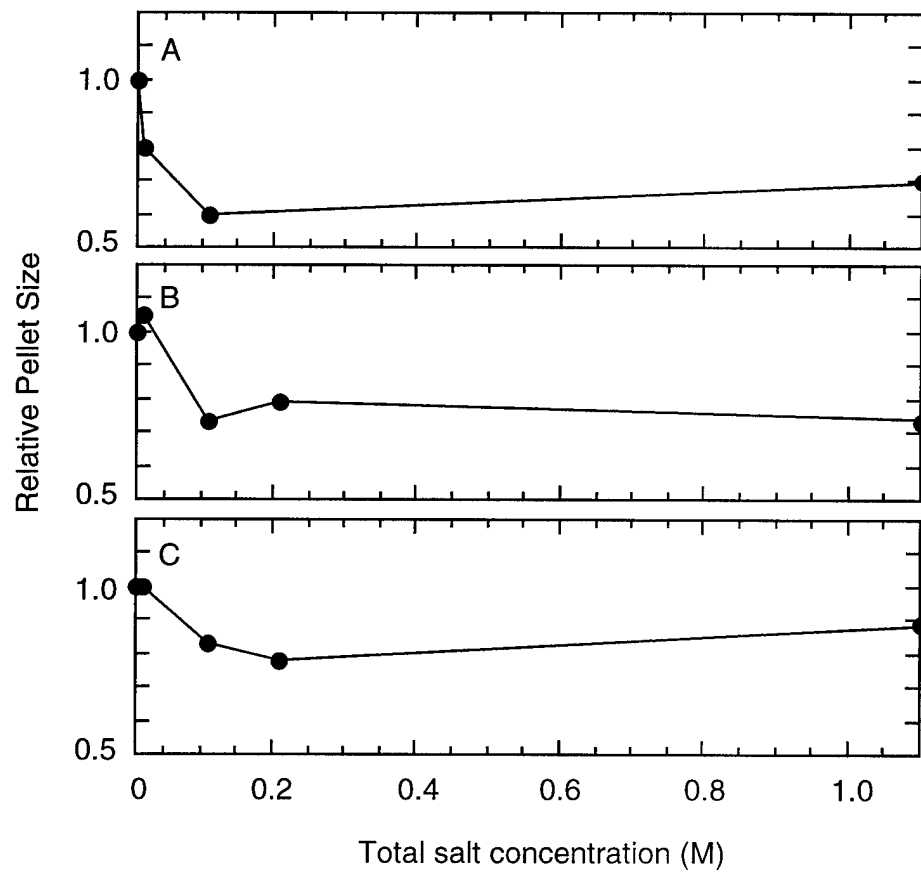
Figure 3. Effect of phosphorylation state on NF pellet size. Relative pellet sizes are shown over a range of ionic strengths for native NFs (solid line) and NFs treated with alkaline phosphatase (dashed line). SDS-PAGE is used to assess the degree of phosphorylation (inset); the right and left lanes are control and enzyme-treated NFs, respectively.
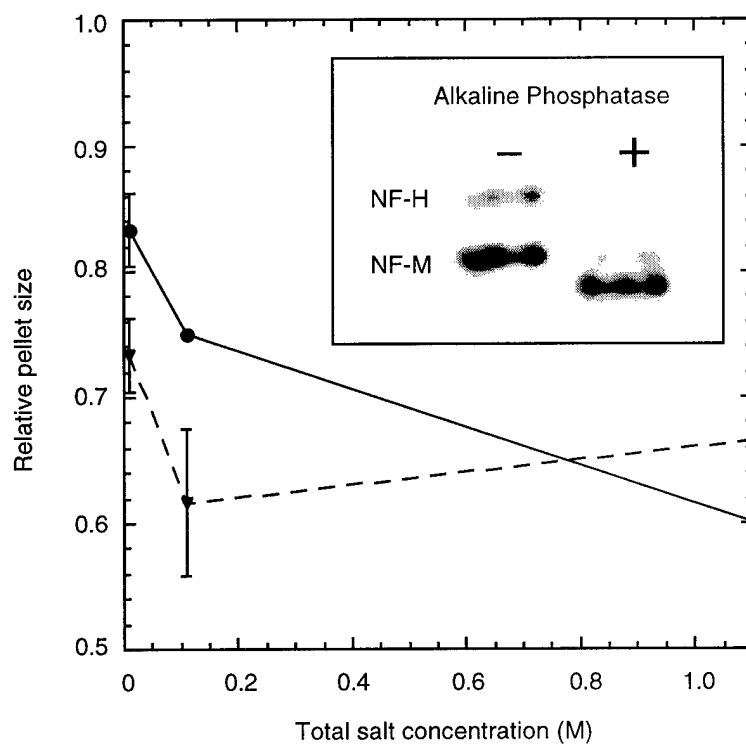
Figure 4. Effect of divalent cation concentration. Relative pellet sizes in the presence of (A) Mg^{++} and (B) Ca^{++}. The inset in (A) depicts photographs of pellets obtained at 0 mM and 50 mM $MgCl_2$ (bar is 5 mm). All experiments were performed at 1 mM MES, pH 6.8.
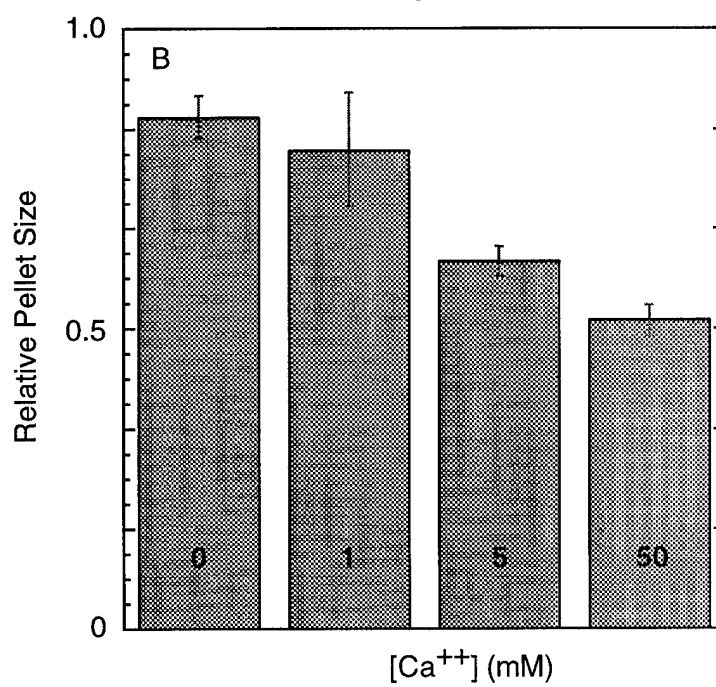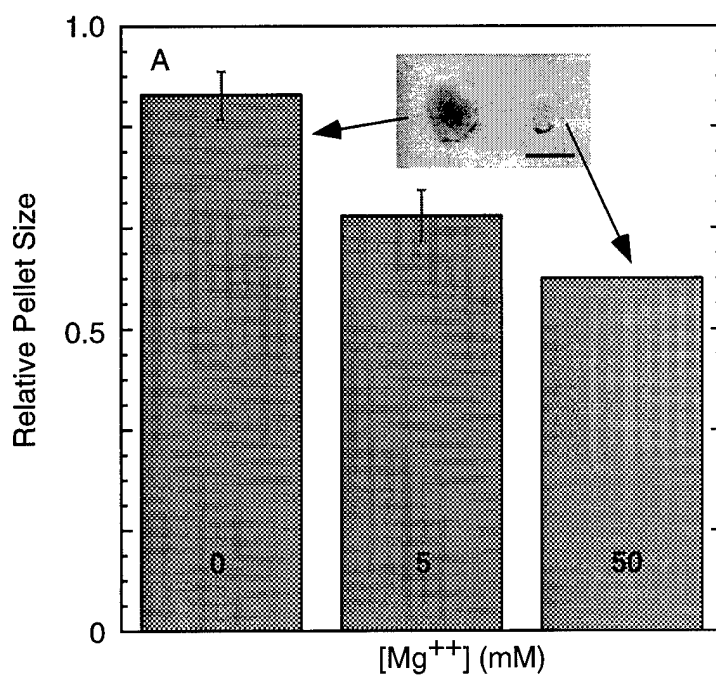
Figure 5. AFM images of native neurofilaments. The images in the right column (A-C) were taken at 0 mM NaCl, and those in the left column (D-F) were obtained at 100 mM NaCl. In addition to NaCl, each buffer contains 10 mM $MgCl_2$ and 10 mM MES, pH 6.8. Scale bar is 500 nm.
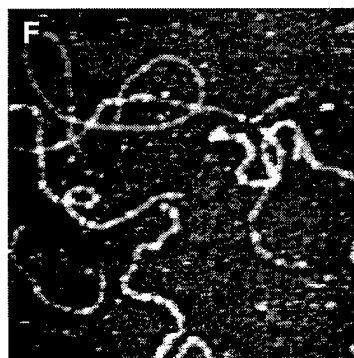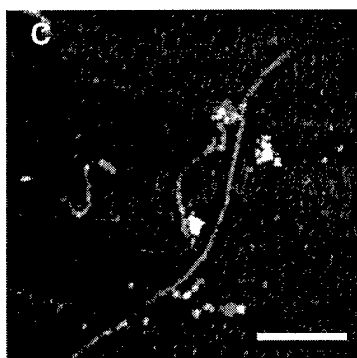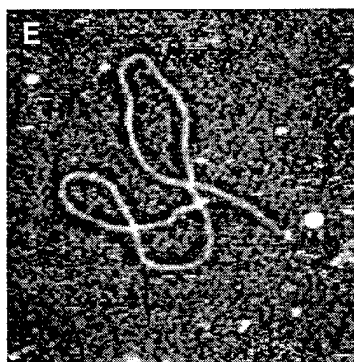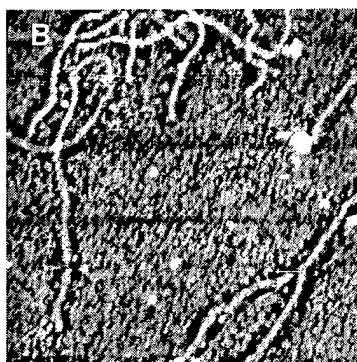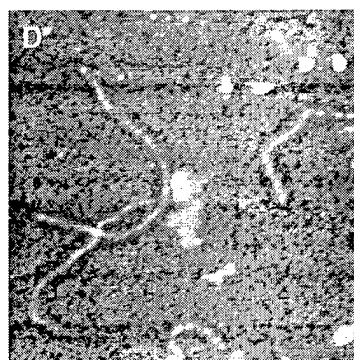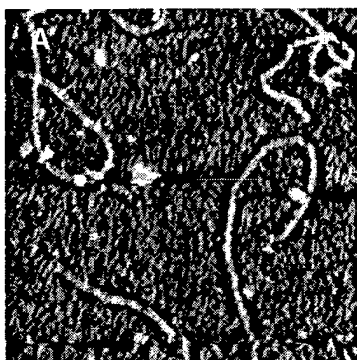
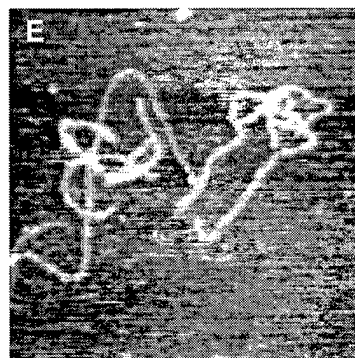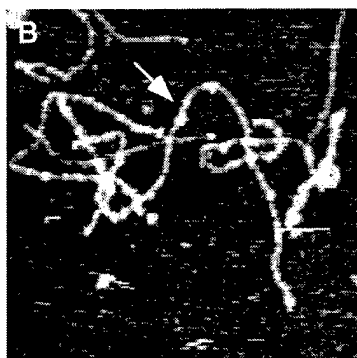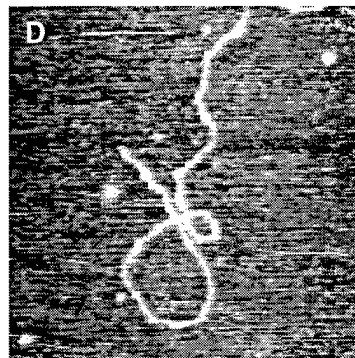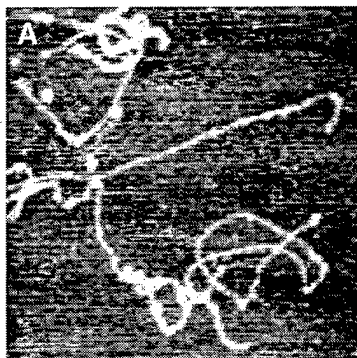0 mM NaCl   100 mM NaCl

Figure 6. AFM images of alkaline phosphatase-treated neurofilaments. The right column (A-C) corresponds to 0 mM NaCl, and the left column (D-F) corresponds to 100 mM NaCl. Areas of apparent contaminant exclusion are marked with white arrows. Each buffer also contains 10 mM MgCl$_2$ and 10 mM MES, pH 6.8. Scale bar is 500 nm.

0 mM NaCl   100 mM NaCl
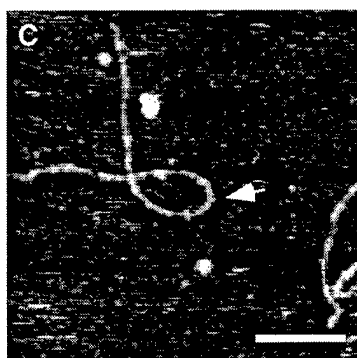
References

Abraham T., A. Kumpulainen, Z. Xu, M. Rutland, P. M. Claesson, and J. Masliyah. 2001. Polyelectrolyte-mediated interaction between similarly charged surfaces: Role of divalent counter ions in tuning surface forces. *Langmuir* 17:8321-8327.

Barrat J. L., and J. F. Joanny. 1996. Theory of polyelectrolyte solutions. *Advances in Chemical Physics, Vol XCIV* 94:1-66.

Bright J. N., T. B. Woolf, and J. H. Hoh. 2001. Predicting properties of intrinsically unstructured proteins. *Prog. Biophys. Mol. Biol.* 76:131-173.

Brown H. G., and J. H. Hoh. 1997. Entropic exclusion by neurofilament sidearms: A mechanism for maintaining interfilament spacing. *Biochemistry* 36:15035-15040.

Cicuta P., and I. Hopkinson. 2001. Studies of a weak polyampholyte at the air-buffer interface: The effect of varying pH and ionic strength. *J. Chem. Phys.* 114:8659-8670.

de Waegh S. M., V. M. Y. Lee, and S. T. Brady. 1992. Local modulation of neurofilament phosphorylation, axonal caliber, and slow axonal transport by myelinating Schwann cells. *Cell* 68:451-463.

Diehl A., M. C. Barbosa, and Y. Levin. 1996. Neutral polyampholyte in an ionic solution. *Phys. Rev. E* 54:6516-6525.

English A. E., S. Mafe, J. A. Manzanares, X. H. Yu, A. Y. Grosberg, and T. Tanaka. 1996. Equilibrium swelling properties of polyampholytic hydrogels. *J. Chem. Phys.* 104:8713-8720.

Eyer J., and J. F. Leterrier. 1988. Influence of the phosphorylation state of neurofilament proteins on the interactions between purified filaments in vitro. *Biochem. J.*

252:655-660.

Fouissac E., M. Milas, M. Rinaudo, and R. Borsali. 1992. Influence of the ionic strength on the dimensions of sodium hyaluronate. *Macromolecules* 25:5613-5617.

Geisler N., and K. Weber. 1981. Self-assembly invitro of the 68,000 molecular-weight component of the mammalian neurofilament triplet proteins into intermediate-sized filaments. *J. Mol. Biol.* 151:565-571.

Gotow T., T. Tanaka, Y. Nakamura, and M. Takeda. 1994. Dephosphorylation of the largest neurofilament subunit protein influences the structure of crossbridges in reassembled neurofilaments. *Journal of Cell Science* 107:1949-1957.

Gou J. P., T. Gotow, P. A. Janmey, and J. F. Leterrier. 1998. Regulation of neurofilament interactions in vitro by natural and synthetic polypeptides sharing lys-ser-pro sequences with the heavy neurofilament subunit NF-H: Neurofilament crossbridging by antiparallel sidearm overlapping. *Med. Biol. Eng. Comput.* 36:371-387.

Hariharan R., C. Biver, J. Mays, and W. B. Russel. 1998. Ionic strength and curvature effects in flat and highly curved polyelectrolyte brushes. *Macromolecules* 31:7506-7513.

Higgs P. G., and J. F. Joanny. 1991. Theory of polyampholyte solutions. *J. Chem. Phys.* 94:1543-1554.

Kamiyama Y., and J. Israelachvili. 1992. Effect of pH and salt on the adsorption and interactions of an amphoteric polyelectrolyte. *Macromolecules* 25:5081-5088.

Kantor Y., H. Li, and M. Kardar. 1992. Conformations of polyampholytes. *Phys. Rev. Lett.* 69:61-64.

Kudaibergenov S. E. 1999. Recent advances in the study of synthetic polyampholytes in solutions. *Adv. Polym. Sci.* 144:115-197.

Leterrier J. F., and J. Eyer. 1987. Properties of highly viscous gels formed by neurofilaments *in vitro* - a possible consequence of a specific inter-filament cross-bridging. *Biochem. J.* 245:93-101.

Leterrier J. F., D. Langui, A. Probst, and J. Ulrich. 1992. A molecular mechanism for the induction of neurofilament bundling by aluminum ions. J. Neurochem. 58:2060-2070.

Leterrier J. F., J. Kas, J. Hartwig, R. Vegners, and P. A. Janmey. 1996. Mechanical effects of neurofilament cross-bridges - modulation by phosphorylation, lipids, and interactions with F-actin. *J. Biol. Chem.* 271:15687-15694.

Nisato G., J. P. Munch, and S. J. Candau. 1999. Swelling, structure, and elasticity of polyampholyte hydrogels. *Langmuir* 15:4236-4244.

Ohlemacher A., F. Candau, J. P. Munch, and S. J. Candau. 1996. Aqueous solution properties of polyampholytes: Effect of the net charge distribution. *J. Polym. Sci. Pt. B-Polym. Phys.* 34:2747-2757.

Rowland L. P., and N. A. Shneider. 2001. Medical progress: Amyotrophic lateral sclerosis. *N. Engl. J. Med.* 344:1688-1700.

Strong M. J., W. L. Strong, H. Jaffe, B. Traggert, M. M. Sopper, and H. C. Pant. 2001. Phosphorylation state of the native high-molecular-weight neurofilament subunit protein from cervical spinal cord in sporadic amyotrophic lateral sclerosis. *J. Neurochem.* 76:1315-1325.

Tamashiro M. N., E. Hernandez-Zapata, P. A. Schorr, M. Balastre, M. Tirrell, and P.

Pincus. 2001. Salt dependence of compression normal forces of quenched polyelectrolyte brushes. *J. Chem. Phys.* 115:1960-1969.

Troncoso J. C., J. L. March, M. Haner, and U. Aebi. 1990. Effect of aluminum and other multivalent cations on neurofilaments in vitro - an electron-microscopic study. *J. Struct. Biol.* 103:2-12.